Lehrstuhl für Thermodynamik
Technische Universität München

On the Measurement and Modelling of Flame Transfer Functions at Elevated Pressure

Ewald Freitag

Vollständiger Abdruck der von der Fakultät für Maschinenwesen
der Technischen Universität München
zur Erlangung des akademischen Grades eines
DOKTOR – INGENIEURS
genehmigten Dissertation.

Vorsitzender:		Univ.-Prof. Dr.-Ing. Hartmut Spliethoff
Prüfer der Dissertation:	1.	Univ.-Prof. Dr.-Ing. Thomas Sattelmayer
	2.	Prof. Simone Hochgreb, Ph.D., University of Cambridge, U.K.

Die Dissertation wurde am 03.12.2008 bei der Technischen Universität München eingereicht und durch die Fakultät für Maschinenwesen am 14.04.2009 angenommen.

To Lucy, Gina, Sophie, Paris and Nicky

who taught me a cutting-edge attitude
to master the turns of life

If you can keep your head when all about you
Are losing theirs and blaming it on you;
If you can trust yourself when all men doubt you,
But make allowance for their doubting too;
If you can wait and not be tired by waiting,
Or being lied about, don't deal in lies,
Or being hated, don't give way to hating,
And yet don't look too good, nor talk too wise:

If you can dream - and not make dreams your master;
If you can think - and not make thoughts your aim;
If you can meet with Triumph and Disaster
And treat those two impostors just the same;
If you can bear to hear the truth you've spoken
Twisted by knaves to make a trap for fools,
Or watch the things you gave your life to, broken,
And stoop and build 'em up with worn-out tools:

If you can make one heap of all your winnings
And risk it on one turn of pitch-and-toss,
And lose, and start again at your beginnings
And never breathe a word about your loss;
If you can force your heart and nerve and sinew
To serve your turn long after they are gone,
And so hold on when there is nothing in you
Except the Will which says to them: "Hold on!"

If you can talk with crowds and keep your virtue,
Or walk with kings - nor lose the common touch,
If neither foes nor loving friends can hurt you,
If all men count with you, but none too much;
If you can fill the unforgiving minute
With sixty seconds' worth of distance run -
Yours is the Earth and everything that's in it,
And - which is more - you'll be a Man, my son!

Joseph Rudyard Kipling [Kip10]

Vorwort

Die vorliegende Arbeit entstand am Lehrstuhl für Thermodynamik der Technischen Universität München während meiner Zeit als wissenschaftlicher Mitarbeiter und Assistent, zum Teil finanziert durch das Projekt "Instability Control of Low Emission Aeroengine Combustors" (ICLEAC) im Rahmen des Growth-Programms der Europäischen Kommission.

Mein herzlicher Dank gilt meinem Doktorvater "dem Chef" Professor Dr.-Ing. Thomas Sattelmayer, dessen ansteckende Begeisterung für die Verbrennungsforschung und erfrischend pragmatische Einstellung wesentlich zu meiner Entscheidung beigetragen haben, von den "Raumfahrern" zur Energietechnik zu wechseln. Professor Simone Hochgreb, Ph.D., aus Cambridge danke ich für das Interesse an meiner Arbeit und die freundliche Übernahme des Co-Referats. Herrn Professor Dr.-Ing. Hartmut Spliethoff gilt mein Dank für die Abwicklung des Promotionsprozesses und den Vorsitz in der Prüfung.

Die Zeit am Lehrstuhl wird mir stets in angenehmer Erinnerung bleiben, vor allem durch die positive Atmosphäre, den Zusammenhalt und den freundschaftlichen Austausch unter den Kollegen. Besonders hervorheben möchte ich meinen Projektpartner Dr.-Ing. Johannes Eckstein, mit dem zusammen ich vier Jahre lang in Labor, Büro und auf Dienstreisen durch halb Europa die Höhepunkte und Herausforderungen eines anspruchsvollen Projektes erleben durfte. Seine bemerkenswerte Allgemeinbildung, sein rhetorisches Talent und nicht zuletzt sein charismatischer Humor machen ihn zu einem Kollegen wie man ihn sich interessanter nicht wünschen kann. Eine spezielle Erwähnung verdient auch unser Oberingenieur Dr.-Ing. Christoph Hirsch, der stets aufbauend und unterstützend zur Verfügung stand und aus seinem reichen Erfahrungsschatz immer einen hilfreichen Ansatz zur Lösung kniffliger Probleme anzubieten hatte.

Meine Anerkennung gebührt unserer mechanischen und elektrischen Werkstatt sowie den Herren Ruedi Tresch, Urs Dössegger und Oleg Kotliar, die es ermöglichten, den zur Erstellung dieser Arbeit verwen-

deten Prüfstand in Rekordzeit von der ersten Skizze bis zum “First Fire” aufzubauen. Auch der Laboralltag mit seinen kleinen handwerklichen Dringlichkeiten wäre ohne die hochwertige und zeitnahe Unterstützung der Werkstätten sehr mühsam geraten.

Dieser Alltag war stark geprägt von der Betriebsamkeit vieler hochmotivierter Studenten, deren unermüdlicher Einsatz das Gelingen dieser Arbeit erst möglich machte. Umso mehr freut es mich, einige von ihnen als nächste Generation von Doktoranden die Forschung weiterführen zu sehen.

Abschließend geht ein besonders herzliches Dankeschön an meine Freunde und meine ganze Familie - für ihr anhaltendes Interesse, für ihre kompromisslose Unterstützung und den manchmal dringend benötigten Rückhalt, aber auch nicht zuletzt für ihre Freude daran, erreichte Meilensteine und erzielte Erfolge anständig zu feiern!

Baden, im April 2009 Ewald Freitag

Contents

List of Figures

List of Tables

Nomenclature

Latin Characters

a	$[m^2/s]$	Thermal diffusivity
a	$[ms]$, $[mm]$	Fit constant, unit dependent on application
A	$[m^2]$	Area, surface or cross-section
A	$[-]$	CTA calibration factor
b	$[-]$	Fit constant
B	$[m^{0.45}]$	CTA calibration factor
c	$[m/s]$	Speed of sound
c_p	$[J/(kg\,K)]$	Heat capacity at constant pressure
C_1	$[ms/mm]$	Fit constant
C_2	$[-]$	Fit constant
C_3	$[-]$	Fit constant
d_a	$[ms]$, $[mm]$	Fit constant, unit dependent on application
d_b	$[-]$	Fit constant
E	$[V]$	Whetstone bridge voltage
f	$[1/s]$	Frequency
f	$[m/s]$	Riemann invariant, downstream propagating
g	$[m/s]$	Riemann invariant, upstream propagating
h	$[Js]$	Planck constant
H	$[m]$	Siren orifice height
H_u	$[MJ/kg]$	Lower heating value
I	$[-]$	Intensity
k_b	$[-]$	Fit constant
K	$[kW/K]$	CTA calibration factor
K_S	$[-]$	Stoichiometry factor
K_{OH}	$[-]$	Mixture fraction calibration factor OH* intensity
K_{u_B}	$[-]$	Mixture fraction calibration factor CTA
L	$[m]$	Length
m	$[kg]$	Mass
n	$[m]$	Tilted radial coordinate
n	$[-]$	Number of siren rotor openings

n_α, n_β, n_m	$[-]$	Order of a model polynomial
p	$[Pa]$	Pressure
$\dot{q}$	$[W/m^3]$	Heat release, heat flux per volume
$\dot{Q}$	$[W]$	Heat release, heat flux
r	$[m]$	Radial coordinate
R	$[m]$	Siren reference circle radius
R	$[J/(kg\,K)]$	Specific gas constant
R	$[\Omega]$	Electrical resistance
s	$[J/(kg\,K)]$	Specific entropy
s	$[m]$	Tilted axial coordinate
S	$[m/s]$	Flame propagation speed
S_0	$[-]$	Theoretical swirl number
t	$[s]$	Time
T	$[s]$	Oscillation period
T	$[K]$	Temperature
u	$[m/s]$	Axial velocity
U	$[-]$	Unmixedness parameter
v	$[m/s]$	Radial velocity
w	$[m/s]$	Tangential velocity
x	$[m]$	Axial coordinate
X	$[m]$	Position (vector)
V	$[m^3]$	Volume
z	$[m]$	Tilted axial coordinate
Z	$[(Ns)/m^3]$	Impedance

Greek Characters

α	$[^\circ]$	Flow angle
α_l	$[s]$	Model parameter, $l = \{1, 2\}$
β_k	$[s]$	Model parameter $k = \{1\},\ \beta_1 = \beta$
γ_m	$[-]$	Model parameter
Γ	$[m^2/s]$	Circulation
Δ	$[-]$	Difference, to be used with any variable
$\Delta\tau$	$[s]$	Time delay distribution parameter
ζ	$[-]$	Pressure drop coefficient
η	$[kg/(m\,s)]$	Dynamic viscosity

κ	$[-]$	Ratio of specific heats
λ	$[-]$	Air excess ratio
λ	$[nm]$	Wavelength
ν	$[m^2/s]$	Kinematic viscosity
ϖ	$[m^2/s^2]$	Vorticity
ρ	$[kg/m^3]$	Density
σ	$[s]$	Time delay standard deviation
τ	$[s]$	Time delay, time scale
φ	[rad]	Phase angle, angular coordinate
φ_0	[rad]	Angular width of the siren orifice
Φ	$[-]$	Equivalence ratio
ψ_0	$[-]$	Critical mass flow density
ω	$[1/s]$	Angular frequency
ω_0	$[1/s]$	Eigenfrequency, limit (angular) frequency

Subscripts

a	Outer, air
ad	Adiabatic
B	Burner
C	Combustor
cg	Center of gravity
Ch	Chemical
CTA	Related to CTA
d	Downstream
D	Higher order dynamic model
e	End, environment
E	Burner exit
exc	Excited
f	Fuel
F	Flame
G	Global
i	Inner
I	Injector
L	Laminar
L	Lance

m	Measured
M	Model
max	Maximum
OH(*)	Related to OH* chemiluminescence
PP	Related to perfectly premixed mode
rms	Root mean square, statistical fluctuation
rot	Rotational
s	Sensor
s	Along coordinate s
S	Swirl model
t	Throat, smallest flow cross section
T	Turbulent
th	Thermal
TP	Related to technically premixed mode
u	Upstream
u	Velocity related
w	Wall
W	Wire
0	Initial, reference
φ	Azimuthal
λ	Related to air excess ratio fluctuation
ϖ	Induced by vorticity
τ	Related to time delay

Superscripts

$(\,)'$	Perturbation
$(\bar{})$	Average value
$(\hat{})$	Absolute value
$(\dot{})$	Time derivative
$(\vec{})$	Vector
$(\,)^*$	Molecule in electronically excited state

Non-Dimensional Numbers

Da	$Da = \tau_T/\tau_{Ch}$	Damköhler number
M	$M = u/c$	Mach number

Re	$Re = (u\,L\,\rho)/\eta$	Reynolds number
Sr	$Sr = (f\,L)/u$	Strouhal number

Abbreviations

BC	Boundary condition
CFD	Computational fluid dynamics
CIVB	Combustion induced vortex breakdown
CTA	Constant temperature anemometry (probe)
DLN	Dry low-NOx (combustion)
FFT	Fast Fourier transformation
FTF	Flame transfer function
IB	Industrial burner
IRZ	Inner recirculation zone
LBO	Lean blow-off
LDA	Laser Doppler Anemometry
LES	Large eddy simulation
LP	Lean premixed (combustion)
LPP	Lean premixed prevaporised (combustion)
NO_x	Oxides of nitrogen
OP	Operating point
PDA	Phase Doppler Anemometry
PIV	Particle Image Anemometry
PM	Photomultiplier
PP	Perfectly premixed (combustion)
ppm	Parts per million
RQL	Rich-Quench-Lean combustion
S/D	Signal to distortion ratio
SE	Systematic error
SO_x	Sulphur oxides
TD1	Generic burner
TF	Transfer function
TM	Transfer matrix
TP	Technically premixed (combustion)

See also appendix D for an overview of the transfer function naming used throughout this work.

1 Introduction

1.1 Background

Since the commissioning of the first industrial gas turbine manufactured by Brown, Boveri & Cie for the electric grid of the city of Neuchâtel, Switzerland in 1939, gas turbine power plants have experienced an extensive technological development and are today well known for delivering clean and efficient energy. In the last decades of the past century, ever more stringent environmental regulations linked to a rising public awareness led to the development of low emission gas turbine combustors. Especially oxides of nitrogen NO_x are of special interest, since they are - together with sulphur oxides SO_x - responsible for the formation of acid rain.

The formation of NO_x is controlled mainly by the flame temperature, a fact that has a large impact on conventional non-premixed[1] combustion systems, where mixing and reaction processes are running in parallel. Since the combustion stabilises locally at regions with a stoichiometric mixture and thus the highest possible flame temperature, even globally lean mixtures as usually encountered in gas turbine engines are not effective in substantially bringing down the NO_x level.

Strategies for the reduction of nitrogen oxides include the injection of water along with the fuel into the combustor to make use of the thermal ballast of the former - the *wet* combustion concept, and sequential combustion in a rich zone followed by quick quenching and burnout in a lean zone - the RQL concept [Cor92]. However, the strategy with the highest potential that has also prevailed in the industrial gas turbine market is lean premixed or LP[2] combustion. Here, the mixing process is separated from combustion by the introduction of a mixing section upstream of the combustion chamber. In the ideal case, a homogeneous, lean mélange enters the combustor and burns at a constantly

[1] Non-premixed flames are often called "diffusion" flames. This expression is not precise though, since diffusion processes are of importance also for premixed flames.

[2] If liquid fuels are concerned, also atomisation and evaporation processes are involved and the name is extended to LPP - lean premixed and prevaporised. Another terminology for the same concept is DLN - dry low-NOx combustion.

low flame temperature. Due to the exponential dependence of NO formation on the flame temperature, the NO_x reduction potential at gas turbine typical conditions amounts to two orders of magnitude, diminishing the NO_x concentration from several hundred ppm down to single digit ppm numbers.

As a consequence of the development of LP combustors, also the cooling concept of the combustion chamber walls has changed. Instead of using the excess air to film-cool the perforated combustor liner and bring down the hot gas temperature at the entry into the turbine to acceptable levels, nearly all the air is now guided through the burner to increase the thermal ballast for NO_x reduction. The lower flame temperature does now allow a convective cooling of the combustor walls. For that purpose the air coming from the compressor passes the outer side of the combustor liner before entering the burner as sketched in figure 1.1.

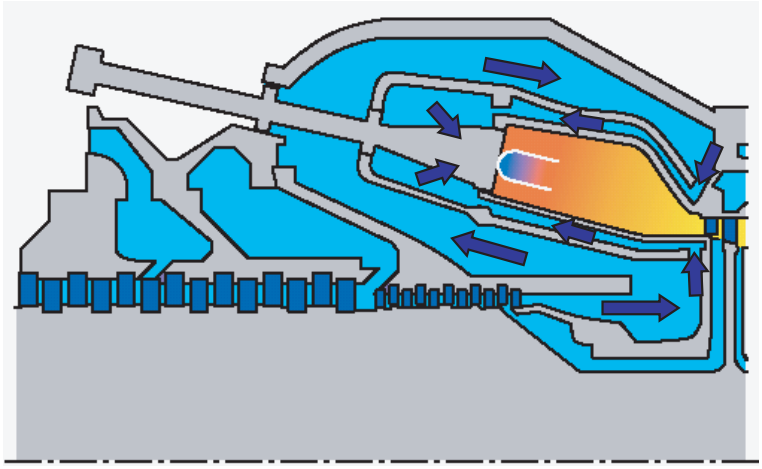

Figure 1.1: Sketch of a typical lean premixed annular combustor.

In LP combustion, the remarkable improvement concerning emissions is accompanied by drawbacks concerning the flame stabilisation - imminent dangers of lean blow-off and flame flashback into the burner - and acoustic oscillations. These oscillations are highly unwanted, since they may lead to component damage by increased mechanical load and increased heat transfer. Two effects are of predominant importance for the stronger susceptibility of LP combustors to pulsations.

- The acoustically rigid convectively cooled combustor liners instead of the perforated plates with bypass air flow substantially reduce the acoustic damping of the system and in turn increase the pulsation amplitude.

- The introduction of the mixing section leads to additional time delays for mixing and convection through the burner. As will be described later, these time delays open up new paths for the feedback loop required to establish a self-excited combustion oscillation. Also, the large total time delays of LP systems have a high tendency to couple with the first acoustic eigenmodes of the system, which are typically the strongest.

1.2 Combustion Instabilities

Thermoacoustic instabilities are self-sustained oscillations that originate from a coupling between any kind of heat transfer or heat release and the acoustics of a technical system. If the heat release is generated by a flame, the oscillation is called a combustion instability. The flame reacts to an acoustic perturbation by a fluctuation of the heat release and thus a fluctuation of the volumetric expansion that in turn is nothing else but a sound wave. That sound wave propagates through the combustor, is reflected at the boundaries and propagates back to the flame, where it again causes an acoustic perturbation. This feedback is essential and leads - for favourable conditions - to an amplification of the perturbation for every repetition of the cycle. Without feedback, the flame acts just as a once-through amplifier of turbulent noise and coherent vortex structures. The term “favourable conditions” in the context of a combustion instability denotes two requirements:

- The phase difference between the heat release and the acoustic perturbation must be favourable to generate a positive transfer of energy to the oscillation. If this requirement is not fulfilled, energy is subtracted rather than added and the oscillation is damped.

- The energy transfer to the oscillation must be larger than the losses of acoustic energy associated with the oscillation, otherwise the damping is stronger and the amplitude can not grow.

For linear systems an amplitude growth - once initiated - is not limited, since the acoustic losses grow at the same rate as does the oscillation amplitude, but not faster [Pan04]. A limit cycle can only occur if some kind of saturation mechanism sets in - that is usually related to the heat release response of the flame. The limit cycle with a stable oscillation amplitude is reached as the energy input by the thermoacoustic cycle is in balance with the acoustic energy losses.

1.2.1 The Rayleigh Criterion

A criterion for the energy transfer to the acoustic oscillation has been given by Lord Rayleigh [Str78] as early as 1878, based on experiments of Sondhauss on sound generated when transferring heat to air in glass tubes [Son50], [FJ68]. He states that the vibration will be encouraged if the heat is added at the instant of the pressure maximum, or in other words if the fluctuating pressure p' and the fluctuating heat release $\dot{Q}'$ are in phase. Vice versa, the vibration is discouraged, if the heat is added at the pressure minimum or subtracted at the pressure maximum - when p' and $\dot{Q}'$ are out of phase. More generally, the Rayleigh criterion can be expressed by integrating over time and volume [PD54]

$$\int_V \int_0^T \dot{q}'(t,V) \cdot p'(t,V)\, dt\, dV \; > \; 0 \,, \tag{1.1}$$

where T denotes the oscillation period. When the flame extension is small compared to the acoustic wavelength, the flame can be considered acoustically compact and $p'(t,V)$ reduces to $p'(t)$. Note that this simplification is not generally applicable for the heat release, since much slower convective processes are dominating the flame response and it is often observed that parts of the flame oscillate with different

phase angles. The Rayleigh criterion is then given by

$$\int_0^T \dot{Q}'(t) \cdot p'(t)\, dt \; > \; 0 \; , \tag{1.2}$$

with

$$\dot{Q}'(t) = \int_V \dot{q}'(t, V)\, dV \; . \tag{1.3}$$

Another perception of this criterion is that of a thermodynamic cycle. The addition of heat at the pressure maximum initiates a clockwise cycle and energy is fed into the oscillation. As the phase difference between p' and $\dot{Q}'$ increases from zero, the growth per cycle is reduced. A balance is reached at $\frac{1}{2}\pi$ $\left(\& \frac{3}{2}\pi\right)$ and the maximum negative growth at π - representing a counter-clockwise cycle that is absorbing energy.

1.2.2 Feedback Mechanisms

Essential for the formation of a self excited combustion oscillation is the existence of a feedback mechanism to close the loop. Figure 1.2 gives an overview of the mechanisms that can occur in a combustion system.

While turbulent noise and naturally occurring flow structures like vortex separation at edges for example can act as trigger to start an instability, they usually do not participate in the feedback cycle. Some known mechanisms are listed below.

- **Velocity perturbation:** The "classical" thermoacoustic feedback mechanism involves the heat release response of the flame to a velocity perturbation u'[3]. The generated sound wave is reflected by the downstream boundary condition, travels back and does again perturb the velocity field at the burner.

[3] Pressure perturbations p' are also involved, but are usually less important [Sch03].

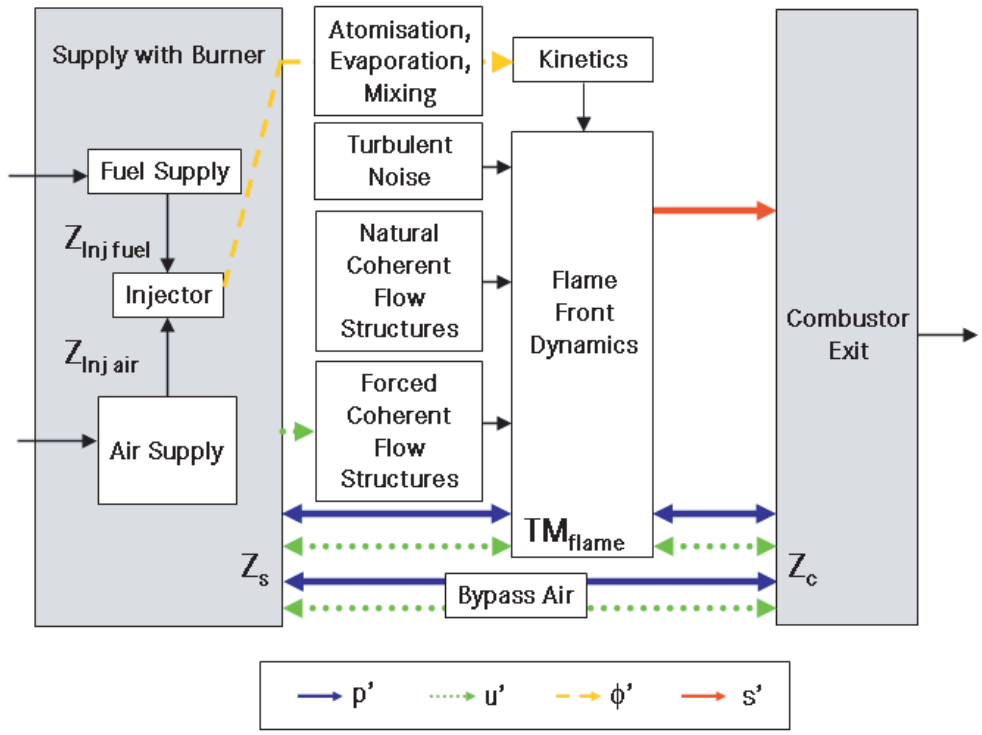

Figure 1.2: Drivers for thermoacoustic instability.

- **Equivalence ratio fluctuation:** In the usual case of fuel injection taking place in the burner, pressure and velocity perturbations at the fuel injector nozzle lead to a fluctuation of the mixture composition Φ' or λ'. This perturbation is convected through the burner and into the flame, where it leads to a modulation of the heat release both directly via the energy content of the flow and also via the flame temperature and the burning rate [KEH85], [LZ98], [RJ98], [CL03]. If liquid fuels are involved, not only the mixing, but also the processes of atomisation and evaporation can be affected by the acoustic perturbation [EFH$^+$05].

- **Forced coherent flow structures:** Acoustic perturbations at the burner can lead to the formation of flow structures that are locked to the oscillation frequency and that can affect the heat release by changing the burning rate or the flame surface area or both. A typical example is the vortex shedding often observed at backward facing steps or for bluff-body stabilised flames [SZ85], [SG92]. Extremely large oscillations amplitudes can occur if the

acoustic perturbation triggers the transition between meta-stable flow fields [FCJM05] and/or flame modes [HY04], [FES02b] sometimes observed in connection with swirl burners. For large acoustic oscillation amplitudes and depending on the oscillation frequency, ring vortex separation is observed for LP swirl burners [KB02].

- **Entropy waves:** Entropy waves s' are perturbations in the hot gas temperature generated by the heat release of the flame via equivalence ratio fluctuations. A feedback mechanism can be formed if such a perturbation is convected into a choked or nearly-choked nozzle at the combustor exit, where it is reflected as a pressure wave. Low oscillation frequencies associated with this mechanism originate from the rather low convective time delay from the flame to the combustor exit. [MC77], [PPD01], [Eck04], [EFHS06].

For the sake of completeness, bypass air injected into the combustor is also mentioned in figure 1.2. However, this is of interest mainly for non-premixed and RQL type combustors and not for LP systems.[4]

1.3 Low Order Modelling

As becomes clear from the above considerations, the reaction of the flame to perturbations is of paramount importance for the determination of the stability of a combustion system. To avoid delays and high costs associated with changes of new combustion systems at a late development stage, analytical or numerical tools are required that are able to predict the stability early in the design process. A range of analytical and numerical modelling approaches has been applied up to date, from full size, time-resolved combustor LES setups to analytical low order models in the frequency domain - [Pan04] gives a good

[4] Also LP combustors are never completely air-tight, but the amount of bypass air is typically an order of magnitude lower than in non-premixed or RQL systems. Leakages in LP systems occur for example at the separation joint of the liner segments. Moreover, bypass air can be used intentionally for additional cooling or the suppression of undesirable flame stabilisation modes or flame instabilities.

overview. While high effort numerical methods are suitable only for a limited number of cases and thus applied to investigate special aspects, especially the fast and easy to use low order models have found wide application in industry.

An acoustic low order model reduces the complexity of a system by splitting it up into a network of simple elements that are amenable to analytical treatment. Such elements comprise for example simple 1-dimensional tubular ducts, area changes, junctions/flow dividers or boundary conditions to terminate the system. The connections of these elements are formed by the acoustic variables p' and u' or, using an equivalent notation, by the Riemann invariants f and g representing the downstream and upstream propagating acoustic waves [Mun87].

$$\begin{pmatrix} p' \\ u' \end{pmatrix}_d = TM_{pu} \begin{pmatrix} p' \\ u' \end{pmatrix}_u \qquad \begin{pmatrix} f \\ g \end{pmatrix}_d = TM_{fg} \begin{pmatrix} f \\ g \end{pmatrix}_u \tag{1.4}$$

Figure 1.3: A network element with the transfer matrix in p/u and f/g notation.

Using superpositions, also 2-dimensional geometries as for example ring structures like annular combustors can be modelled. For combustion systems, the flame is considered an additional element that is included into the network model. Once all elements are defined, the stability of a system can be analysed using methods derived from control theory [SP03a], [SP03b]. An example for a simple acoustic network model of a combustion system is given in figure 1.4.

Figure 1.4: An example for a simple low order model.

Unfortunately, the knowledge on the detailed effects of fluctuations in the flow and the mixture composition field on the flame is - up to now - not sufficient to deliver reliable prediction models. For that reason, experimental methods are often used to characterise the flame behaviour and to define the flame element to be plugged into a low order model. Two methods are in use:

- **Transfer matrix:** The transfer matrix method delivers a direct acoustic description of the flame analog to equation 1.4. The matrix is determined by recording the acoustic parameters up- and downstream of the flame under external excitation for a range of frequencies, typically using the multi-microphone method [MD90], [PPSM99]. Since two independent acoustic states are necessary, the procedure is performed twice, usually with the acoustic source connected up- and downstream of the burner & flame section. Disadvantages of this method are that especially the acoustic variables in the combustor are difficult to determine [Fis04] and that the approach gives little direct information on the heat release and thus on the reaction of the flame, which might be of interest to gain a better understanding of the processes involved.

- **Transfer function:** The flame transfer function FTF relates the spatially integrated fluctuating heat release $\dot{Q}'$ to an acoustic variable - usually the velocity u' - at some location upstream of the flame, both are usually normalised with the mean quantities.

$$\frac{\dot{Q}'}{\overline{\dot{Q}}} = FTF\,\frac{u'}{\overline{u}} \tag{1.5}$$

  Since only one variable is involved on either side of the flame, this approach requires only one measurement. The closure from the heat release to the acoustic variables downstream of the flame is then provided by model assumptions developed by [Chu52] - the well known Rankine-Hugoniot relations valid for an acoustically

compact flame at low Mach numbers [PPD01].

$$u'_d = u'_u + \left(\frac{T_d}{T_u} - 1\right) \overline{u}_u \left(\frac{\dot{Q}'}{\overline{\dot{Q}}} - \frac{p'_u}{\overline{p}_u}\right) \tag{1.6}$$

$$p'_d = p'_u - \left(\frac{T_d}{T_u} - 1\right) \rho_u \overline{u}_u^2 \left(\frac{\dot{Q}'}{\overline{\dot{Q}}} + \frac{u'_u}{\overline{u}_u}\right) \tag{1.7}$$

These relations consider the flame as a flat sheet in a tube of constant cross-section, with the main driver for the downstream fluctuation being the volumetric expansion of the gas captured by the ratio of temperatures T_d/T_u.

Using additional ports in the elements, also variables like equivalence ratio Φ or entropy s to capture the corresponding mechanisms can be implemented into the network model [PPD01].

Once the network model has been obtained, its results can be utilised to find suitable strategies to minimise the pulsation behaviour - either by passive means like additional dampers, changed geometries and altered operating parameters or by active instability control, where an actuator is applied to generate perturbations of the fuel- or the air flow with a phase angle that counteracts the growth of an instability.

1.4 Goals and Work Overview

The scope of this work comprises the investigation of flame transfer functions as defined in equation 1.5.

While other parameters like flow velocity, equivalence ratio or swirl number and their influence on the flame transfer function have been investigated [Bue92], [LB04], [Fis04], [Kun04], only little information exists on their pressure-dependence [CSC+03]. For that reason, the experimental determination of FTFs at varying operating pressures is of main importance here with the goal of deriving a physical understanding of the processes involved and scaling rules to capture the pressure behaviour. A generic burner developed at the Lehrstuhl für

Thermodynamik, Technische Universität München is applied for these investigations with the benefits of a known atmospheric behaviour and a broad database of results already available.

The influence of air excess ratio perturbations λ' on the flame transfer function as described in section 1.2.2 has been modelled repeatedly [RJ98], [LZ98], [CL03], [SBG+04], but also here little data is available on the experimental side. This lack of data is mostly due to difficulties of reliably determining the heat release of a flame in the presence of mixture fraction perturbations[5]. A second goal of this work is thus to obtain a better knowledge of this topic by measuring FTFs of a burner with and without the mixture fraction influence. This investigation is performed on a different burner capable of operation in both perfectly and technically premixed mode[6].

As the last goal, a model shall be derived that is capable of reproducing the behaviour of the transfer functions measured on both burners. That model shall comprise both influences - the pressure dependence and also the mechanism of the mixture fraction perturbations.

While section 2 gives some theory and information on the modelling of flame transfer functions, the test rig designed and manufactured to achieve the goals of this work is presented in section 3. The corresponding measurement techniques are introduced in section 4. Section 5 gives the experimental transfer function results obtained for the generic burner together with some scaling rules. The application of a second burner gives the opportunity for a comparison of the two burners and their FTFs in perfectly premixed mode without any mixture fraction perturbations, this is done in section 6. Relating these data to the transfer functions obtained in technically premixed mode of section 7 enables to point out the influence of mixture fraction perturbations. Finally, the modelling efforts as described in section 8

[5] See also section 4.2.3.

[6] In the scope of this work, the term “perfectly premixed” or “PP” denotes an operation mode that generates a perfectly homogeneous fuel/air mixture without any spatial or temporal fluctuations of the mixture fraction. This is usually achieved by locating the fuel injection sufficiently far upstream of the combustor. In order to minimise the inherent risks of flame flashback and autoignition, industrial LP systems are usually designed with a rather short mixing section that does not provide full spatial and temporal homogenisation. Such a setup is called “technically premixed” or “TP” here.

split into three parts:

- The determination of a model for the transfer functions of the generic burner of section 5.
- The application of that model to the results of the second burner of section 6.
- The development of a procedure to extract the influence of the mixture fraction perturbations from the transfer functions measured in PP and TP mode and an extension of the model to include this influence.

A discussion of the linearity of the transfer functions measured on the generic burner is presented in appendix A. Appendix D provides an overview of the terminology used in this work in association with flame transfer functions.

Some useful extensions of this work giving more information on the flame structure and on low order modelling efforts can be found in [FEHS06], [FFS06], [Mor05] and [Föl06]. Especially the latter three references give some interesting results on the stability of the rig using the measured flame transfer functions, the calculated frequencies and stability limits, which match well with the observed behaviour.

2 Theory of Flame Transfer Functions

In this section, some general aspects and modelling approaches to capture the flame transfer function behaviour are introduced.

2.1 Overview

As presented in equation 1.5, the flame behaviour is characterised by a function f relating the fluctuations of a velocity u' upstream of the flame to the heat release $\dot{Q}'$.

$$\frac{\dot{Q}'}{\overline{\dot{Q}}} = f\left(\frac{u'}{\overline{u}}\right) \tag{2.1}$$

Since that behaviour usually depends on the oscillation frequency, a Fourier-transformation can be used to transfer equation 2.1 into the frequency domain.

$$\frac{\dot{Q}'(\omega)}{\overline{\dot{Q}}} = FTF(\omega)\left(\frac{u'(\omega)}{\overline{u}}\right) \tag{2.2}$$

In this relation, $\dot{Q}'(\omega)$ and $u'(\omega)$ denote the complex perturbations and $FTF(\omega)$ is defined as the (complex) flame transfer function.

Assuming sinusoidal waveforms, the perturbations can be conveniently expressed by a pointer rotating in the complex plane with a (real) amplitude denoted by a hat $\hat{}$ and a phase angle φ.

$$\begin{aligned} \dot{Q}'(\omega) &= \hat{\dot{Q}}(\omega)\, e^{i\omega t + i\varphi_{\dot{Q}}(\omega)} \\ u'(\omega) &= \hat{u}(\omega)\, e^{i\omega t + i\varphi_{u}(\omega)} \end{aligned} \tag{2.3}$$

The transfer function is thus given by

$$FTF(\omega) = \frac{\hat{\dot{Q}}(\omega)}{\hat{u}(\omega)} \frac{\overline{u}}{\overline{\dot{Q}}}\, e^{i\left[\varphi_{\dot{Q}}(\omega) - \varphi_{u}(\omega)\right]}\,, \tag{2.4}$$

with the amplitude determined by the ratio of the perturbation amplitudes and the phase by the difference of the perturbation phases.

$$\begin{aligned} \widehat{FTF}(\omega) &= \frac{\hat{\dot{Q}}(\omega)}{\hat{u}(\omega)} \frac{\overline{u}}{\overline{\dot{Q}}} \\ \varphi_{FTF}(\omega) &= \varphi_{\dot{Q}}(\omega) - \varphi_u(\omega) \end{aligned} \tag{2.5}$$

The same procedure is usually also applied to measure the transfer function. The harmonic excitation u' and the response $\dot{Q}'$ are determined at a defined frequency, and the flame transfer function is formed according to equations 2.5. Note that also other excitation signals can be used - a step function or a mixture of frequencies for example representing an excitation with a larger frequency content. Compared to the pure tone excitation these signals have the advantage of accelerating the process, while the signal to noise ratio and thus the quality usually becomes worse.

One fundamental global characteristic of a flame transfer function is a time delay τ in the heat release response with respect to the excitation. The flame reacts at a time t to a perturbation in the burner occurring at a time $t - \tau$.

$$\frac{\dot{Q}'(t)}{\overline{\dot{Q}}} = f\left(\frac{u'(t-\tau)}{\overline{u}}\right) \tag{2.6}$$

This time delay does usually have a convective character - acoustic velocity perturbations follow the flow separation at the burner exit and are convected into the flame with the flow velocity. Substituting $\varphi_{\dot{Q}} = -\omega\tau$ into equation 2.5 and defining the phase reference $\varphi_u = 0$ gives

$$\varphi_{FTF}(\omega) = -2\pi\frac{\tau}{T} \quad \text{with} \quad \omega = \frac{2\pi}{T}\,. \tag{2.7}$$

Hence, the constant time delay τ causes a negative gradient in the FTF phase as the oscillation period T decreases for a rising excitation frequency. Note that the time delay is a global characteristic,

local deviations from this behaviour induced by other effects can be quite large, as will be shown in later sections. The most important consequence of this behaviour is that τ controls the phase of the heat release - and has thus a major impact on the stability of the combustion system according to Rayleigh's criterion represented by equation 1.1.

For a perfectly homogeneous fuel-air mixture without spatial and temporal variations, the behaviour in the low frequency limit can be derived from equations 2.5 and 2.7. The flame reacts quasi-steady and any fluctuation in the mixture flow is translated into an equal fluctuation of the heat release:

$$\frac{\hat{\dot{Q}}(\omega)}{\overline{\dot{Q}}} = \frac{\hat{u}(\omega)}{\overline{u}} \tag{2.8}$$

and

$$\lim_{\omega \to 0} \widehat{FTF}(\omega) = 1 \ . \tag{2.9}$$

A similar limit can be obtained for the phase. Since the time delay between heat release and excitation becomes negligible compared to the oscillation period T, the transfer function phase vanishes.

$$\lim_{\omega \to 0} \varphi_{FTF}(\omega) = 0 \tag{2.10}$$

At the other end of the frequency spectrum, the dispersion of the fluctuations becomes large and the ability of the flame to follow the perturbations decreases. As a consequence, the FTF amplitude shows a tendency towards zero.

$$\lim_{\omega \to \infty} \widehat{FTF}(\omega) = 0 \tag{2.11}$$

For intermediate frequencies, one or more amplitude peaks > 1 are often recognised, especially for flames stabilised by a highly swirled flowfield. That point has been subject to an intensive discussion not settled yet, with physical explanations ranging from coherent vortex

shedding over entrainment of diluent gases to dynamic turbulence behaviour and vorticity transport [LB03], [SBG+04], [HSP+05]. One common agreement seeming to arise is that combustion dynamics are controlled by convective rather than direct acoustic transport of perturbations into and within the flame. Also, the dispersion of these perturbations within premixer and combustor plays an important role [Sat00].

An experimental determination of the FTF is usually obtained by taking the luminescence signal of the excited OH (OH*) molecule within the flame as the measure for heat release, whereas the velocity is recorded either directly via hot wire anemometry or the acoustic velocity is obtained from multiple microphone measurements. The FTF is then determined in discrete frequency steps with an external excitation of the system generated by loudspeakers or a siren.

The definition of the flame transfer function as the response of a fluctuating heat release to fluctuating fluid parameters - as well as the concept of low order modelling of combustion systems - dates back to the work of Merk in the 1950s [Mer56a], [Mer56b], [Mer57a], [Mer57b], [Mer58]. Early experimental works on flame transfer functions focus mainly on simple laboratory type burners and flames [Mer56c], [Mug80], [GLR+78], but also turbulent jet flames [BG70] and burners firing industrial boilers [Had71], [Had73] are investigated.

With the advent of LP technology and the corresponding deterioration of combustion stability, the concepts of stability modelling, including the measurement of flame transfer functions, received more attention. Büchner [Bue92], [BHL93] and his successors measured FTFs on LP swirl burners. They come to the conclusion that the amplitude peak observed for swirled flames is due to the periodic entrainment of ambient gas and a corresponding enhancement of the flame chemiluminescence intensity [BK97] - even for the case of a confined combustion chamber. All their transfer functions are measured at very high excitation levels of the burner velocity up to $u'_B \approx \overline{u}_B$, with the result of saturation effects like periodic ring vortices being generated that influence both amplitude and phase behaviour. An application of these transfer functions for the linear analysis required by a low order

network model is thus questionable, but they might be useful when investigating the saturation behaviour of the transfer function and the limit cycle of a self-excited oscillation.

Khanna [Kha01], [KVSB02], measured flame transfer functions on a swirl stabilised burner and does also find a global amplitude peak and amplitudes approaching zero for high frequencies. His experiments include a parameter variation of swirl number, burner flow velocity and equivalence ratio. These variations lead to an altered global phase gradient and to changes in magnitude and frequency of the global amplitude peak. He also investigates the differences obtained in perfectly and partially premixed mode, with the latter FTFs showing a higher variability in the amplitude plot and strong bends in the phase. Khanna does also apply parametric models to characterise the behaviour of the measured functions, however without claiming to capture the underlying physics. Such an approach is useful in the context of his work on active instability control, where only a formal description of the flame behaviour is needed to feed the controller.

Fischer [Fis04] investigated a generic swirl burner under perfectly premixed conditions with a variation of equivalence ratio, flow velocity and swirl number. The FTFs do generally show the anticipated behaviour with amplitude peaks and a global phase decline. Especially the swirl variation yielded some interesting results. With an increase of the swirl number, the global amplitude peak exhibits a strong rise at low frequencies, while the phase shows a substantial deviation from the global gradient at the same frequency. For a low swirl number associated with a weakly stabilised flame, a rise of the FTF amplitude is observed at high excitation frequencies that is in contradiction with the usual low-pass behaviour. Fischer detected a Strouhal scaling for the burner velocity - the FTFs plotted over a dimensionless frequency Sr formed with the excitation frequency f, the burner diameter d and the burner flow velocity u_B

$$Sr = \frac{f \cdot d}{u_B} \tag{2.12}$$

delivered identical amplitude and phase plots for varying burner ve-

locity. For the variation of equivalence ratio, the above scaling did not work perfectly though.

Kunze [Kun04], [KHS04] continued the work of Fischer and investigated the same generic burner, but mounted in an annular combustor instead of a single burner rig. The main difference is found in the high frequency region, where the amplitude increase for low swirl numbers already observed in Fischer's results is more pronounced. An explanation of this behaviour is found in the burner-burner interactions of an annular combustion chamber, where the same swirl direction of neighboring burners leads to an increased dissipation of angular momentum and thus to a further reduction of the effective swirl number.

A more general scaling rule than equation 2.12 is given by Lohrmann [LB04]. He uses the flame length L_F defined as the axial distance from the burner exit to the location of the maximum heat release (OH*-intensity) instead of the burner diameter as input for his Strouhal scaling.

$$Sr = \frac{f \cdot L_F}{u_B} \tag{2.13}$$

With this definition he is able to scale the phase plots of the preheating temperature and equivalence ratio variations for his burner. The influence of operating conditions is reduced to their influence on the flame length, and a proportional relation between flame length and global phase gradient τ_G is assumed.

$$\tau_G \propto \frac{L_F}{u_B} \tag{2.14}$$

It can thus be concluded that in order to scale a flame transfer function with an operating parameter, the dependence of the flame length on that parameter is the most important information to be acquired.

Besides the experimental determination of the flame response to an acoustic excitation, the same information can in principle also be obtained from a numerical CFD analysis. Examples for such a procedure are given in [GHK+04], [GP07], [TVP03], [ZDB03] and [SLBF05].

However, the uncertainties involved and the numerical efforts for such a procedure are still high. An intermediate approach is the determination of complex time delay distributions by CFD that can then be used in FTF time delay models [FPRS01].

While experimental efforts have led to some success in the description of flame transfer functions, a general modelling approach to capture the detailed flame dynamics for a broad range of combustion systems and including the possible feedback mechanisms outlined in section 1.2.2 is not available. However, simplifications are often possible, since not all mechanisms need to be considered for all applications. An overview of the modelling approaches applied to date can be found in [Lie03].

A very basic consideration links the instantaneous heat release of the flame $\dot{Q}$[7] to the fuel massflow $\dot{m}_f$ consumed at that instant

$$\dot{Q} = \dot{m}_f \cdot H_u \ , \tag{2.15}$$

with H_u being the lower heating value of the fuel. The only requirement associated with this relation is a complete chemical conversion of the fuel to end products of the reaction. Further analysis of that equation leads to a decomposition of the fuel massflow into a flame propagation speed S, the associated flame surface area A, the mixture density ρ and the fuel content of the mixture expressed by the air excess ratio λ[8] and the stoichiometry factor K_S.

$$\dot{Q} = S \cdot A \cdot \rho \cdot \frac{1}{\lambda} \cdot \frac{H_u}{K_S} \tag{2.16}$$

In the linearised form with small perturbations, equation 2.16 is then

[7] Strictly seen, the energy content of the system during reaction is constant (for an adiabatic system), only a conversion of chemical into thermal energy takes place. The terminology of an energy flow $\dot{Q}$ is thus somewhat misleading. However, for technical applications the conception of heat being transferred into the system is more easy to handle than the conversion of species and often sufficient.

[8] The air excess ratio is the reciprocal value of the equivalence ratio, $\lambda = 1/\Phi$. Both terms are used in this work.

written as

$$\frac{\dot{Q}'}{\overline{\dot{Q}}} = \frac{S'}{\overline{S}} + \frac{A'}{\overline{A}} + \frac{\rho'}{\overline{\rho}} - \frac{\lambda'}{\overline{\lambda}} \,. \tag{2.17}$$

For flows of low Mach number, the density fluctuation can usually be neglected [SBG+04].[9] If a perfectly homogeneous mixture with $\lambda' = 0$ is considered, equation 2.17 reduces to

$$\left.\frac{\dot{Q}'}{\overline{\dot{Q}}}\right|_{u'_B} = \left.\frac{S'}{\overline{S}}\right|_{u'_B} + \left.\frac{A'}{\overline{A}}\right|_{u'_B} \,. \tag{2.18}$$

A heat release perturbation resulting from a modulation of the burner flow u'_B can thus be interpreted as a combination of a fluctuation of the propagation speed and the associated flame surface area. This relation is used as a starting point for numerous modelling approaches aiming at the determination of a flame transfer function. Especially laminar flames have been investigated extensively, since the laminar flame propagation speed can be considered independent of velocity perturbations $S'_L = 0$ and the flame response is then solely controlled by a variation of the surface area A. The response of the surface area to velocity perturbations can be modelled using a kinematic approach that captures the modulation of the flame surface propagating into a jet exiting the burner, an example for such a setup is given in the illustration of figure 2.1.

For simple geometries, analytical transfer functions can be derived using this modelling approach. A recent example is the work of Schuller [SDC03], earlier contributions exist - amongst others - from Ducruix et al. [DDC00], Dowling [Dow99], Fleifil et al. [FAGG96] and Boyer & Quinard [BQ90]. These models usually deliver a transfer function that has the character of a low-pass filter with amplitudes quickly decreasing for a rising frequency. However, Schuller [SDC03] points out that

[9] Note that this assumption is based on the nominal impedance of travelling waves relating pressure and velocity fluctuations $p' = \rho c u'$. The relation of relative density to velocity fluctuations is then identical to the Mach number M, as seen from $\frac{\rho'/\overline{\rho}}{u'/\overline{u}} = \frac{1}{\kappa}\frac{p'}{u'}\frac{\overline{u}}{\overline{p}} = \frac{1}{\kappa}\rho c\frac{\overline{u}}{\rho RT} = \frac{1}{\kappa}\rho c\frac{\overline{u}}{\rho}\frac{\kappa}{c^2} = M$. This consideration does however not necessarily hold for standing waves, where a large pressure amplitude and a vanishing velocity is encountered in a velocity node.

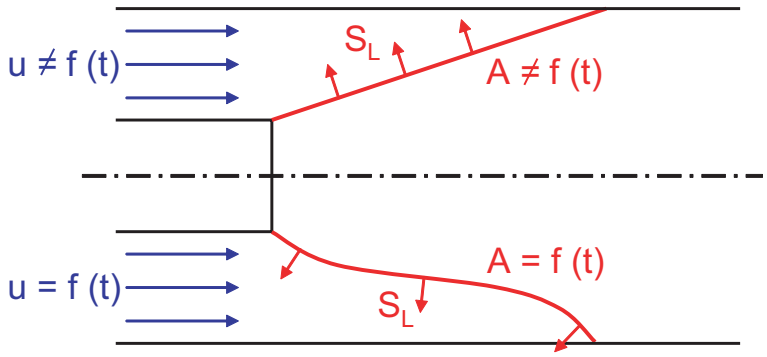

Figure 2.1: V-Flame kinematic model. Flame front propagating with S_L into the mixture flow. Upper half: without perturbations, lower half: mixture flow perturbed as a function of time.

for V-type flames - as illustrated in figure 2.1 - also amplitude peaks with a magnitude > 1 are possible. That peak amplitude is found to rise with a decreasing half-angle of the flame surface with respect to the incoming flow - in other words for long, weakly stabilised flames.

An interesting aspect of the kinematic description of the flame surface is its dependence on the "history" of the perturbation. Since the flame is anchored at a certain point and the integrity of the flame front must be maintained, the perturbed flame surface does not only depend on an instantaneous velocity $u(t_i)$, but also on the velocities $u(t_{i-j})$ at any time $i-j$ in the past.

When considering turbulent flames, the simplification of a constant flame speed independent of flow perturbations does no longer hold, which renders a purely kinematic approach as presented above unfeasible. In general, the turbulent flame speed S_T is a non-trivial function of turbulence parameters like the length scale L_t or the turbulent fluctuation velocity u_T that usually also change along the flame front. An analytical treatment with a decomposition into S_T and A is thus often not possible and the combined response

$$\left.\frac{\dot{Q}'}{\overline{\dot{Q}}}\right|_{u'_B} = \left.\frac{(S_T \cdot A)'}{\overline{(S_T \cdot A)}}\right|_{u'_B} \tag{2.19}$$

needs to be determined from an experiment or a CFD solution.

However, for large Damköhler numbers $Da \gg 1$ and high turbulent fluctuation intensities $u'_T \gg S_L$ - conditions that are representative for gas turbine combustion - a proportional rise of S_T with u_T can be assumed [Sch95]. Using that relation, Schuermans [SBG+04] proposes a model that links the heat release response of the flame entirely to fluctuations of the turbulent burning speed without any flame surface area perturbation.

$$\left.\frac{\dot{Q}'}{\overline{\dot{Q}}}\right|_{u'_B} = \left.\frac{S'_T}{\overline{S_T}}\right|_{u'_B} \tag{2.20}$$

With the second assumption of u_T being proportional to the acoustic velocity perturbation, he is able to link the flame response to the burner velocity. The flame transfer function is then reduced to a time delay (distribution) between burner and flame[10].

In the following sections, some modelling approaches of interest for gas turbine combustion and for this work are introduced. A convenient circumstance is that these models can be superposed - and thus used as a "toolbox" as required by the specific application.

2.2 Analytical Models

One group of FTF models that is widely used due to its simplicity aims at mapping the flame behaviour in the form of closed mathematical relations. Such relations can be derived from the underlying physics or - for more complex cases - from an interpretation of experimental results.

A simple example[11] for such a model is the characteristic time delay of a flame transfer function mentioned in equation 2.6, this model was proposed by Crocco and Cheng [CC56] as early as 1956 as a result of their research on combustion instabilities in liquid rocket engines. With the application of this model, the transfer function in

[10] See also next section.

[11] Most of the examples presented in this section have been adapted from the work of Pankiewitz [Pan04], who gives a good overview.

the frequency domain is defined solely by the time delay τ between heat release and velocity.

$$FTF(\omega) = e^{-i\omega\tau} \tag{2.21}$$

The constant amplitude of that model is not consistent with the experiment though, where usually a low-pass behaviour is observed that leads to a diminishing amplitude for high frequencies. Such a behaviour is obtained when the time delay is modelled as a distribution instead of a single value - an assumption that makes sense, since the flame has a finite extension and any perturbation is subject to dispersion processes between burner and flame. Sattelmayer [Sat00] for example derives the following relation for a rectangular probability distribution $\Delta\tau$ around the time delay τ.[12]

$$FTF(\omega) = e^{-i\omega\tau} \frac{e^{i\omega\Delta\tau} - e^{-i\omega\Delta\tau}}{2\,\Delta\tau\, i\omega} \tag{2.22}$$

A similar expression is used by Polifke [PKS01] for a Gaussian time delay probability distribution with a standard deviation σ.

$$FTF(\omega) = e^{-i\omega\tau - \frac{1}{2}\omega^2\sigma^2} \tag{2.23}$$

Figure 2.2 shows a Bode diagram of these two models with the same time delay τ and $\Delta\tau = \sigma$ together with the pure time delay of equation 2.21.

If the higher order dynamic behaviour of a flame shall be modelled, also the time-derivatives of the influence parameters need to be taken into account. In the time domain, this results in a differential instead of an algebraic equation. An example thereof is a function given by Bloxsidge [BDL88] that is derived from the experimental observations of Langhorne in an aeroengine afterburner application [Lan88].

$$\frac{1}{\omega_0}\frac{1}{\overline{\dot{Q}}}\frac{d\dot{Q}'(t)}{dt} + \frac{\dot{Q}'(t)}{\overline{\dot{Q}}} = \frac{u'(t-\tau)}{\overline{u}} \tag{2.24}$$

[12] In [Sat00], also a more general expression for a trapezoidal probability distribution is derived. Equation 2.22 does thus represent a simplification.

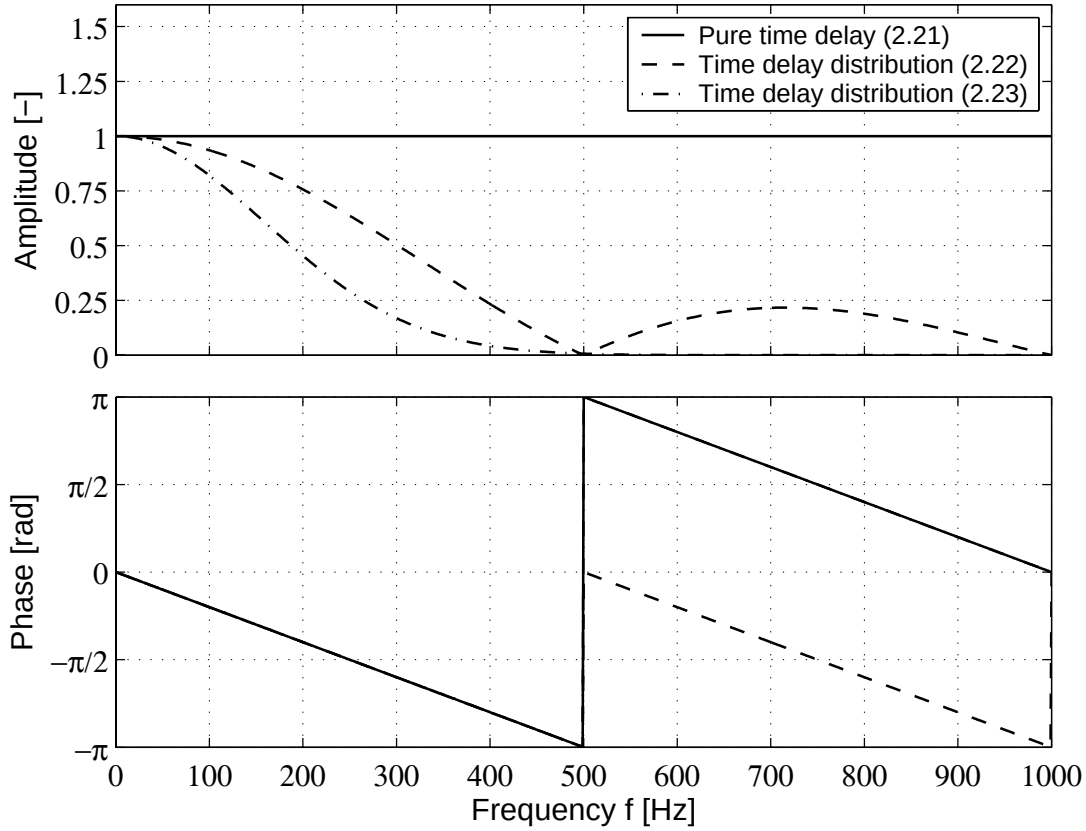

Figure 2.2: Examples for time delay distribution models as of equations 2.22 and 2.23 compared to the pure time delay of equation 2.21. Parameters: τ = 1 ms, $\Delta\tau$ = 1 ms.

This equation represents an extension of the simple time delay, where also the rate of change of the heat release is considered. Since the Fourier transform of a time derivative d/dt gives $i\omega$ in the frequency domain, the transfer function extracted from equation 2.24 is represented by

$$FTF(\omega) = e^{-i\omega\tau} \frac{1}{1 + \dfrac{i\omega}{\omega_0}} \,. \tag{2.25}$$

In the low frequency limit this relation approaches the simple time delay model of equation 2.21, whereas above the limit frequency ω_0 the second term in the denominator becomes dominant and the amplitude is reduced with rising frequency. The behaviour of the second term is well known from control theory as a low-pass filter of first order.

Of the equations presented up to now, none is able to reproduce an amplitude peak with a magnitude > 1 as observed in the experimental FTFs. To achieve that, an extension of the order of the polynomial in ω to at least 2 is required.

$$FTF(\omega) = e^{-i\omega\tau} \frac{1}{1 + \frac{i\omega}{\omega_{0,1}} + \left(\frac{i\omega}{\omega_{0,2}}\right)^2} \,. \tag{2.26}$$

Analog to equation 2.24, the term with $(i\omega)^2$ does now represent the second time derivative of the heat release fluctuation. A comparison of the first and second order models according to equations 2.25 and 2.26 against the pure time delay is given in figure 2.3.

A model of the latter type was utilised for example by Lenz [Len80] to fit his data. Dowling [Dow97] did also apply a model using the second time derivative, but expressed in partial fractions as the product of two terms with additional time constants τ_1 and τ_2.

$$FTF(\omega) = e^{-i\omega\tau} \frac{1}{(1 + i\omega\,\tau_1)\,(1 + i\omega\,\tau_2)} \tag{2.27}$$

Although equations 2.27 and 2.26 can be related by

$$\frac{1}{\omega_{0,1}} = \tau_1 + \tau_2 \tag{2.28}$$

and

$$\frac{1}{\omega_{0,2}} = \sqrt{\tau_1\,\tau_2}\,, \tag{2.29}$$

the solutions of 2.27 represent only a subset of the solutions of 2.26 with τ_1 and τ_2 being real numbers. Especially an elevated amplitude with values > 1 as shown in figure 2.3 can not be generated by equation 2.27, since the necessary condition of

$$\frac{1}{\omega_{0,1}} < \frac{2}{\omega_{0,2}} \qquad \text{or} \qquad \tau_1 + \tau_2 < 2\sqrt{\tau_1\,\tau_2} \tag{2.30}$$

can not be fulfilled for $\tau_1, \tau_2 \in \mathbb{R}$. That criterion can be derived by substituting equation 2.28 into 2.29 and solving for τ_1 or τ_2. If complex numbers for τ_1 and τ_2 are permitted, elevated amplitudes can be generated. In that case, τ_1 and τ_2 represent a conjugate-complex pair of poles in the complex plane.

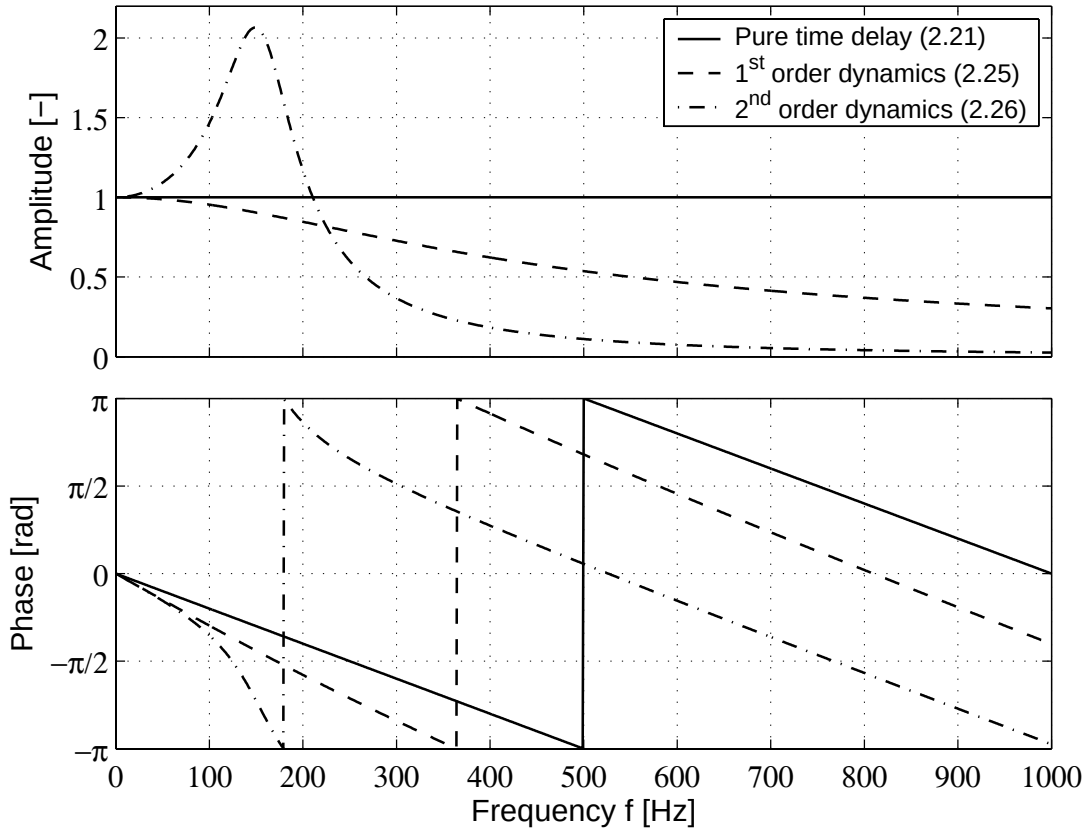

Figure 2.3: Examples for first and second order dynamics models as of equations 2.25 and 2.26 compared to the pure time delay of equation 2.21. Parameters: $\tau = 1$ ms, $1/\omega_{0,1} = 0.5$ ms, $1/\omega_{0,2} = 1$ ms.

In terms of control theory, equation 2.25 represents a PT_1 behaviour (with time delay). Equations 2.26 and 2.27 do then characterise a PT_2 element (with time delay). As seen in equation 2.27, the latter can be decomposed into a serial arrangement of two PT_1 elements. If these elements are able to store and exchange energy - as for example a mass and a spring in the mechanical analogy - an amplified oscillation with a transfer function amplitude exceeding a value of 1 can be generated. Such a case is then characterised by alternating signs of the imaginary

part of τ_1 and τ_2, as expressed by

$$\mathrm{Im}(\tau_1) + \mathrm{Im}(\tau_2) = 0 \; . \tag{2.31}$$

Although PT_1 and PT_2 elements as described above have been numerously applied in flame transfer function models to match a measurement or to produce the desired behaviour, a clear physical explanation of the mechanism leading to an amplification has not been provided yet. That deficiency is also not resolved in this work, and analytical derivations leading to such models are not presented here. However, the good fit with experimental data found in this work and in literature gives rise to the conjecture that a mechanism does exist and needs to be identified.

Following Pankiewitz [Pan04], the higher order dynamics extension FTF_D of the time delay can be represented in a more general fashion by a rational function of the form

$$FTF_D(\omega) = \frac{\sum_{k=1}^{n_\beta} (\beta_k \, i\omega)^k + 1}{\sum_{l=1}^{n_\alpha} (\alpha_l \, i\omega)^l + 1} \tag{2.32}$$

with n_α being the order of the heat release and n_β the order of the burner velocity fluctuation. Together with a description of the time delay distribution FTF_τ according to equation 2.22 or 2.23, the transfer function is written as

$$FTF(\omega) = FTF_\tau(\omega) \cdot FTF_D(\omega) \; . \tag{2.33}$$

To finally account for eventually occuring different time lag and higher order dynamic mechanisms, equation 2.33 may be extended by a superposition of n_m terms according to

$$FTF(\omega) = \sum_{m=1}^{n_m} \gamma_m \cdot FTF_{\tau,m}(\omega) \cdot FTF_{D,m}(\omega) \tag{2.34}$$

with

$$\sum_{m=1}^{n_m} \gamma_m = 1 \ . \tag{2.35}$$

The benefit of such a model is twofold. If the underlying physics are understood, both the order of the model and the associated parameter values $\tau, \Delta\tau, \alpha_l, ...$ can be derived from theoretical considerations - as for example the determination of a time delay distribution from the flowfield of a burner and/or the flame appearance.

In the other case, the physical mechanisms leading to an observed flame behaviour are not known, as it is often the case for the higher order dynamics part (equation 2.32). For such a case, expression 2.34 can still be fitted to any experimentally determined flame transfer function to derive an analytical expression for further use in stability modelling or as an input for active instability control. Pankiewitz [Pan04] for example succeeded in reproducing a measured transfer function of Fischer [Fis04] with a high degree of accuracy by applying equation 2.34 with a second order dynamics part.

A clear disadvantage of the latter approach is that - depending on the level of detailing required and thus on the order of the model - the number of fit parameters quickly exceeds an acceptable limit. Khanna [Kha01] for example reports a requirement for 8^{th} or higher order models to fit his measured FTFs. On the other hand, a model that is fitting well on a not fully understood measured FTF may provide valuable hints on the physical processes involved, since for that case the mathematical relations are obviously captured and just need to be filled with a physical meaning.

2.3 Swirl-Induced Velocity Fluctuations

In this section, a rather new flame transfer function modelling approach developed by Hirsch et al. is introduced. This method postulates a modulation of the flame heat release by a velocity perturbation along the flame front that results from a fluctuation of the azimuthal

vorticity in the combustor flowfield. The latter is generated from swirl perturbations within the burner that are caused by the acoustic excitation and subsequently transported into the flame by convection. An overview of the concept together with the equations required for the application of this model is given here, for more details on the derivation the reader is referred to [HSP+05].

The current method is closely related to the mechanisms responsible for the occurrance of vortex breakdown in the combustor that is usually utilised to stabilise the flame in a gas turbine combustor. Following a derivation of Darmofal [Dar93], the vorticity equation can be written as

$$\frac{D\varpi_\varphi}{Dt} = \frac{v\,\varpi_\varphi}{r} + \frac{1}{r^3}\frac{\partial\left(\Gamma^2\right)}{\partial x} \quad \text{with} \quad \Gamma = w\,r\ . \tag{2.36}$$

As seen from this relation, azimuthal vorticity ϖ_φ is created if an axial gradient of the circulation Γ is encountered. Since in an ideal flow the isolines of vorticity are parallel to the streamlines, such a gradient is necessarily generated at the burner exit, where the flow is forced radially outward by the centrifugal forces. As illustrated on the right side of figure 2.4, the radial increase of axial circulation combined with the outward bending of the streamlines creates a negative axial gradient of Γ and thus negative azimuthal vorticity.

According to the law of Biot-Savart, the rotational part of the flow field $\vec{u}_{rot}$ at a location $\vec{X}_0$ in the flow field is induced by the vorticity $\vec{\varpi}$ at all other locations $\vec{X}$.

$$\vec{u}_{rot}(\vec{X}_0) = -\frac{1}{4\pi}\int_V \frac{\left(\vec{X}_0 - \vec{X}\right)\times\vec{\varpi}(\vec{X})}{\left|\vec{X}_0 - \vec{X}\right|^3}\,dV \tag{2.37}$$

Thus, negative axial velocity will be induced on radii smaller than a given streamline, which further stagnates the flow and increases the streamline divergence. The latter further intensifies the vorticity through the second "stretching" term of equation 2.36, and this positive feedback results in the experimentally observed abrupt vortex

breakdown with the formation of an inner recirculation zone (IRZ).

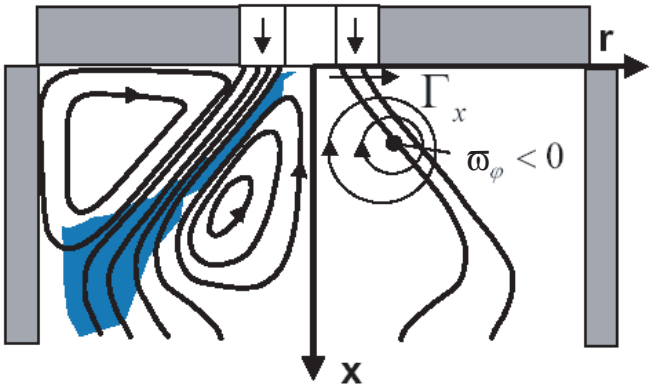

Figure 2.4: Sketch of a typical combustor flowfield with streamlines. Left: Azimuthal streamlines with vortex breakdown and reaction zone. Right: Generation of negative azimuthal vorticity with diverging streamlines. Illustration taken from [HSP+05].

Also seen in figure 2.4 is the typical stabilisation region of the flame in the shear layer between the IRZ and the jet of reactants exiting the burner.

The flame transfer function model now proposed is based upon the same mechanism described above that leads to vortex breakdown. An acoustic velocity excitation of the burner flow u'_B leads to a fluctuation of the swirl circulation Γ'. While this fluctuation is convected along the streamlines through the combustor, it generates perturbations of the azimuthal vorticity ϖ'_φ that in turn induce secondary velocity fluctuations u'_ϖ at the flame front via the Biot-Savart law. Similar to a direct velocity perturbation, the secondary perturbations are also assumed to modulate the heat release. To obtain the net effect, u'_ϖ is integrated over the reaction zone, weighted with the heat release density. The resulting effective global perturbation u'_F is then related to the excitation u'_B to derive a formal transfer function.

For the simplified analysis approach used here, the vorticity equation 2.36 is evaluated along a conical streamline - as illustrated in figure 2.5 - where an average streamline starting from an average radius r_0 is assumed to be representative. The half-angle α of the swirling conical

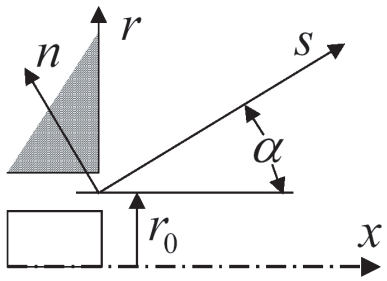

Figure 2.5: Model coordinates. Illustration taken from [HSP+05].

flow from the burner annulus can be approximated with reasonable accuracy from the theoretical swirl number S_0 and the assumption of a solid body vortex profile within the burner

$$\tan\alpha \approx 1.6\, S_0\, \frac{r_a\left(r_a^3 - r_i^3\right)}{r_a^4 - r_i^4}\ , \tag{2.38}$$

where r_a and r_i represent the outer and the inner radius, respectively, of the burner annulus. In order to reduce the complexity of the expression, the vorticity equation 2.36 is transformed into the n, s coordinate system of the streamlines, yielding the following expression.

$$\frac{\partial\varpi_\varphi}{\partial t} + u_s\frac{\partial\varpi_\varphi}{\partial s} - \varpi_\varphi\frac{u_s\sin\alpha}{r_0 + s\sin\alpha} = -\frac{\sin\alpha\,\frac{\partial\left(\Gamma^2\right)}{\partial n} - \cos\alpha\,\frac{\partial\left(\Gamma^2\right)}{\partial s}}{\left(r_0 + s\sin\alpha\right)^3} \tag{2.39}$$

By making use of the constant circulation Γ along the streamline ($\partial/\partial s = 0$) and again assuming a solid body vortex profile in the radial direction

$$\Gamma = \frac{w_0}{r_0}\, r^2 \tag{2.40}$$

that leads to

$$\frac{\partial\left(\Gamma^2\right)}{\partial n} = \frac{4\,\Gamma^2}{r\cos\alpha} \tag{2.41}$$

for the radial gradient of the circulation, the following vorticity equa-

tion is obtained.

$$\frac{\partial \varpi_\varphi}{\partial t} + u_s \frac{\partial \varpi_\varphi}{\partial s} - \varpi_\varphi \frac{u_s \sin\alpha}{r_0 + s\sin\alpha} + \frac{4\tan\alpha\,\Gamma^2}{(r_0 + s\sin\alpha)^4} = 0 \qquad (2.42)$$

That equation may now be solved for ϖ_φ to obtain the distribution of azimuthal vorticity along the streamsurface provided that the initial and boundary conditions as well as the velocity $u_s(s)$ and vorticity $\Gamma(s,t)$ distributions along that streamsurface are known. A good approximation of the velocity distribution - in agreement with the measured velocity profile of [Wäs05] - is given by a hyperbolic decrease with the radius that transforms into

$$u_s(s) = \frac{u_{s,0}\; r_0}{r_0 + s\sin\alpha} \qquad (2.43)$$

for the n, s coordinate system.

For the steady-state case, the circulation Γ along the streamline is constant and equal to the value at the burner exit. To obtain the (linear) transfer function, small perturbations Γ' are impressed on equation 2.42 that cause fluctuations ϖ'_φ. A linearisation of the latter equation is thus performed - neglecting fluctuations of the transport velocity u_s - that yields

$$\frac{\partial \varpi'_\varphi}{\partial t} + u_s \frac{\partial \varpi'_\varphi}{\partial s} - \varpi'_\varphi \frac{u_s \sin\alpha}{r_0 + s\sin\alpha} + \frac{8\tan\alpha\,\Gamma\,\Gamma'}{(r_0 + s\sin\alpha)^4} = 0\ . \qquad (2.44)$$

The input Γ' to this equation can be derived from solving the transport equation

$$\frac{\partial \Gamma'}{\partial t} + u_s \frac{\partial \Gamma'}{\partial s} = 0\ . \qquad (2.45)$$

For a harmonic oscillation at the burner exit the following expression is obtained.

$$\Gamma'(s,t) = \hat{\Gamma}\, e^{i\omega t}\, e^{-i\frac{\omega s}{u_s}\left(1+\frac{s\sin\alpha}{2\,r_0}\right)} \quad \text{with} \quad \omega = 2\pi f \qquad (2.46)$$

Equation 2.46 is valid if the swirl generator is located at the burner

exit and the perturbation of the acoustic velocity is in phase with the perturbation of vorticity. For lean premixed swirl burners, this is however not the usual case. An offset of the swirl generator in the upstream direction to allow for a mixing section is usually encountered. That offset leads to a time delay τ_S in the transport of the circulation perturbation from the swirler to the burner exit. Since this transport of vorticity is a convective process, the time delay can be estimated from the burner flow velocity and the offset distance.

For such a case, the circulation perturbation at the burner exit corresponds to the perturbation at the swirl generator at an earlier instance, and equation 2.46 is modified to[13]

$$\Gamma'(s,t) = \hat{\Gamma}\, e^{i\omega(t-\tau_S)}\, e^{-i\frac{\omega s}{u_s}\left(1+\frac{s\sin\alpha}{2\,r_0}\right)} \,. \tag{2.47}$$

This equation along with the velocity distribution of equation 2.43 can now be substituted into equation 2.44 to derive a numerical solution of ϖ'_φ.

Since the azimuthal vorticity ϖ_φ at a location z along the streamsurface induces secondary velocity u_ϖ at any location s within the entire flame domain, the Biot-Savart law is evaluated from the burner exit $s = 0$ to the end of the reaction zone s_e.

$$u'_\varpi(s,t) = \frac{1}{4\pi} \int_0^{s_e} \frac{(z-s)\,\varpi'_\varphi(z,t)}{|z-s|^3}\, dz \tag{2.48}$$

Effectively, that integral is split into the two parts before and after s to obtain

$$u'_\varpi(s,t) = -\frac{1}{4\pi} \int_0^{s} \varpi'_\varphi(z,t)\, dz + \frac{1}{4\pi} \int_s^{s_e} \varpi'_\varphi(z,t)\, dz \,. \tag{2.49}$$

In order to derive a singular value u'_F representative for the global

[13] Note that a dispersion of the swirl wave in the mixing section of the burner is not taken into account here. For that purpose, a model analog to equations 2.22 or 2.23 can be applied. See also [HSP+05].

flame response, u'_{ϖ} is integrated over the reaction zone together with the local magnitude of the heat release as a weighting factor.

$$u'_F(t) = \frac{1}{\overline{\dot{Q}}} \int_0^{s_e} \frac{d\overline{\dot{Q}}}{ds}\, u'_{\varpi}(s,t)\, ds \tag{2.50}$$

The local magnitude of the heat release can be determined from an assumed heat release distribution or from a measurement of the reaction zone of the flame, typically by flame imaging.

Finally, the resulting time series for $u'_F(t)$ are Fourier-transformed and the flame transfer function in the frequency domain $FTF_S(\omega)$ is obtained in the usual manner by relating u'_F to the acoustic velocity perturbation at the burner u'_B and by normalising with the average values.

$$FTF_S(\omega) = \frac{u'_F(\omega)}{\overline{u}_F} \frac{\overline{u}_B}{u'_B(\omega)} \tag{2.51}$$

Since the direct influence of the burner velocity perturbation - the supply of the flame with combustible mixture - is not included in the presented modelling approach, FTF_S does not represent a standalone transfer function model. An extension is required that captures the response of the flame to the direct velocity perturbation. For that purpose, any one of the models introduced in section 2.2 or determined in another way can be utilised. In the most simple case, such a model would comprise just a pure time delay according to equation 2.21. The final transfer function is then derived from a superposition of the swirl transfer function FTF_S and the time delay model FTF_τ.

$$FTF(\omega) = FTF_\tau(\omega) + FTF_S(\omega) \tag{2.52}$$

In other words, the vorticity perturbations can be considered to "ride on top" of a velocity perturbation generated within the burner.

For the derivation of the model presented here, a swirl burner with an annular flow duct and a solid body vortex profile have been drawn on. This restriction is by no means necessary, other geometries and

vortex types can be implemented by modifying the driving equations accordingly. Also, the integration path along a streamline approximated here by a conical surface can be refined using details from an experimental or numerical investigation of the flowfield.

2.4 Mixture Fraction Fluctuations

Up to now, only perfectly homogeneous mixtures have been considered in the presented flame transfer function models. LP burners for gas turbine engines, however, have only a finite mixing length available to minimise the risks of flashback and self-ignition, a typical sketch is given in figure 2.6. Such a setup inherently bears the risk of creating a feedback mechanism for self-excited oscillations via the generation of mixture fraction perturbations that modulate the flame response.

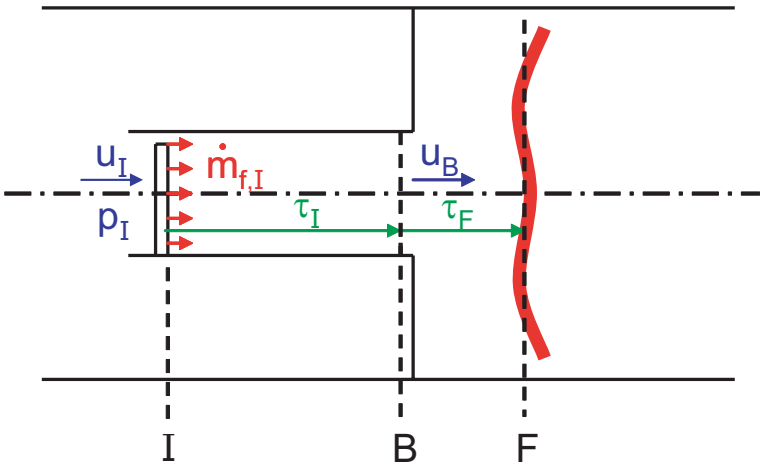

Figure 2.6: Sketch of a typical LP burner to outline the generation and transport of mixture fraction perturbations.

The mechanism for the generation of such a perturbation is quite simple. Acoustic velocity u'_I and/or pressure p'_I fluctuations at the fuel injector I modulate the air- and fuel flow and thus the local air excess ratio λ_I. This inhomogeneity is then transported with the local flow velocity through the mixing section of the burner and into the flame, where it modulates the heat release. Due to the rather low convection velocity, large time delays can build up that can significantly influence

the transfer function phase and thus the stability of the system.

In the linearised form and neglecting air density fluctuations, the air excess ratio at the injector can be written as

$$\frac{\lambda'_I}{\overline{\lambda}} = \frac{u'_I}{\overline{u}_I} - \frac{\dot{m}'_{f,I}}{\overline{\dot{m}}_f} \,. \tag{2.53}$$

The fuel mass flow at the injector will be controlled by the pressure drop Δp over the fuel orifices; an expression for $\dot{m}_{f,I}$ may be derived from the Bernoulli-equation.

$$\dot{m}_{f,I} = A\sqrt{\frac{2\,\Delta p\,\rho_f}{\zeta}} \tag{2.54}$$

Generally, Δp is defined from the instantaneous pressure upstream (u) and downstream (I) of the fuel orifice.

$$\Delta p = (\overline{p}_u + p'_u) - (\overline{p}_I + p'_I) \tag{2.55}$$

Another linearisation does then yield

$$\frac{\dot{m}'_{f,I}}{\overline{\dot{m}}_f} = \frac{p'_u}{2\,\overline{\Delta p}} - \frac{p'_I}{2\,\overline{\Delta p}} \,. \tag{2.56}$$

For a large pressure drop, the fuel supply system may be considered acoustically decoupled with $p'_u = 0$. If $\Delta p \gg p'_I$ also the acoustic pressure fluctuation in the burner can be neglected and the fuel flow is considered "choked" - independent of any acoustic perturbation.

The convective process to the burner exit B and further on to the flame F can be modelled analog to equation 2.21, the respective time delays result from the convection distance and the flow velocity.

$$\frac{\lambda'_B}{\overline{\lambda}} = \frac{\lambda'_I}{\overline{\lambda}}\, e^{-i\omega\tau_I} \tag{2.57}$$

$$\frac{\lambda'_F}{\overline{\lambda}} = \frac{\lambda'_B}{\overline{\lambda}}\, e^{-i\omega\tau_F} \tag{2.58}$$

Also, the dispersion of the mixture fraction perturbations may be included by extending the above equations with the expressions from equation 2.22 or 2.23.

Once the mixture fraction perturbation has arrived at the flame, the modulation of the heat release can be described by the relation developed in equation 2.17, again with the simplification of neglecting density fluctuations.

$$\left.\frac{\dot{Q}'}{\overline{\dot{Q}}}\right|_{\lambda'_B} = \left.\frac{S'(\lambda_F)}{\overline{S}}\right|_{\lambda'_B} + \left.\frac{A'(S)}{\overline{A}}\right|_{\lambda'_B} - \left.\frac{\lambda'_F}{\overline{\lambda}}\right|_{\lambda'_B} . \tag{2.59}$$

Note that the direct influence of the energy content of the reactant flow $\lambda'_F/\overline{\lambda}$ is not the only path to modulate the heat release. Important for the evaluation of equation 2.59 is also the dependence of the burning rate S on the air excess ratio, especially for very lean mixtures close to the blow-off limit this path becomes strong. With the flame speed depending on the equivalence ratio, also the surface area A couples to the fluctuation via the reaction front kinematics discussed in section 2.1.

Despite the additional complexity, the reaction front kinematics approach is still successful for a laminar flame front, where the mixture fraction can be considered the only parameter influencing S_L. The correlation between S_L and λ required for the closure of the model is then determined from experimental data available in literature. A kinematic model of a simple geometry laminar flame front including the effect of mixture fraction perturbations is given in [CL03]. An experimental validation is not available though. For turbulent flames, the challenges discussed in the context of equation 2.19 do also apply here and an straightforward solution is not available.

The modulation of the heat release by mixture fraction perturbations as given in equation 2.59 may be expressed in form of a flame transfer function FTF_λ by relating it to the fluctuation of the air excess ratio at the burner exit B. This procedure is in analogy to equation 2.18, where the heat release from a velocity perturbation has been related

to the velocity perturbation at the burner exit.

$$FTF_\lambda = \frac{\left.\frac{\dot{Q}'}{\overline{\dot{Q}}}\right|_{\lambda'_B}}{\frac{\lambda'_B}{\overline{\lambda}}} \tag{2.60}$$

Note that FTF_λ captures solely the effect of the mixture fraction. The total heat release of the flame is obtained by combining equations 2.18 and 2.59 to

$$\left.\frac{\dot{Q}'}{\overline{\dot{Q}}}\right|_F = \left.\frac{\dot{Q}'}{\overline{\dot{Q}}}\right|_{u'_B} + \left.\frac{\dot{Q}'}{\overline{\dot{Q}}}\right|_{\lambda'_B}, \tag{2.61}$$

and can be expressed in terms of two transfer functions as

$$\left.\frac{\dot{Q}'}{\overline{\dot{Q}}}\right|_F = FTF_u \frac{u'_B}{\overline{u}_B} + FTF_\lambda \frac{\lambda'_B}{\overline{\lambda}}. \tag{2.62}$$

As seen from this expression, the influence of mixture fraction fluctuations FTF_λ can be considered an extension of the flame transfer function obtained for a perfectly homogeneous mixture FTF_u.

While equation 2.61 represents the total consumption of fuel by the flame, the total amount of fuel supplied at the burner exit may be determined from a consideration similar to equation 2.16 at the burner exit B leading to

$$\left.\frac{\dot{Q}'}{\overline{\dot{Q}}}\right|_B = \frac{\dot{m}'_{f,B}}{\overline{\dot{m}}_f} = \frac{u'_B}{\overline{u}_B} - \frac{\lambda'_B}{\overline{\lambda}}. \tag{2.63}$$

Such a relation is useful to derive a boundary condition for the transfer functions in the low frequency limit $\omega \to 0$, since $\left.\frac{\dot{Q}'}{\overline{\dot{Q}}}\right|_F$ and $\left.\frac{\dot{Q}'}{\overline{\dot{Q}}}\right|_B$ must be identical for that case. In terms of fluctuations at the injector nozzle and using a pure time delay model to account for the convective

transport, equation 2.63 may be written as

$$\frac{\dot{m}'_{f,B}}{\overline{\dot{m}}_f} = \frac{u'_B}{\overline{u}_B} - \left(\frac{u'_I}{\overline{u}_I} - \frac{\dot{m}'_{f,I}}{\overline{\dot{m}}_f} \right) e^{-i\omega\tau_I} \ . \tag{2.64}$$

The mechanism of mixture fraction fluctuations was first mentioned by Keller [KEH85] in the context of the generation of entropy waves. Other substantial contributions exist from Richards and Janus [RJ98], the group around Lieuwen and Zinn [LZ98], [CL03], Scarinci et al. [SF00] and the combustion group at the ABB/ALSTOM research center, e.g. [SPP99], [PPD01].

Typically, a major reduction of the relevance of a self-excited instability caused by this mechanism can be achieved by increasing the dispersion of the fuel and thus reducing the amplitude of λ' [FPRS01], [Sat00]. By this measure, the fuel consumption of the flame is distributed over a range of phase angles with respect to the Rayleigh criterion and the energy fed into the oscillation cycle is reduced. Practical solutions to achieve a well dispersed mixture include axially staged fuel injection, axially staged air injection and strong shear gradients in the burner flow. A good example for a successful implementation of such a strategy is given by Scarinci et al. [SFD04].

Another way of influencing the sensitivity of the system to the generation of mixture fraction perturbations is through changing the injector nozzle and/or the fuel line impedance [RR05], [GSM+05]. By that measure, the fuel massflow $\dot{m}'_{f,I}$ as a reaction to the acoustic pressure at the nozzle can be controlled and along with $\dot{m}'_{f,I}$ amplitude and phase of the fuel fraction perturbation. Taking this concept one step further, also an active control of the combustion oscillation can be realised by modulating the fuel flow to the burner using a servo valve [LDH90], [SVK+98]. While an increase of the dispersion can only attenuate an oscillation caused by the mixture fraction mechanism itself, impedance matching and active control bear also the potential of inhibiting pulsations resulting from other feedback mechanisms by destructive interference - “fighting fire with fire”.

3 High Pressure Combustion Facility

In 2003, a facility capable of both combustion tests at elevated pressure and external excitation for thermoacoustic investigations was designed, manufactured and commissioned by the Lehrstuhl für Thermodynamik in close cooperation with Tresch+Kieliger Engineering and Apparatebau Dössegger of Egliswil, Switzerland. Most of the investigations described in this work were performed using that high pressure rig. The operational capabilities of the rig are given as follows.

Combustor pressure:	10 (40) bar
Preheating power:	128 kW
Preheating temperature:	450 (500) °C
Air massflow:	300 g/s
Fuel massflow:	15 g/s
Thermal power:	750 kW

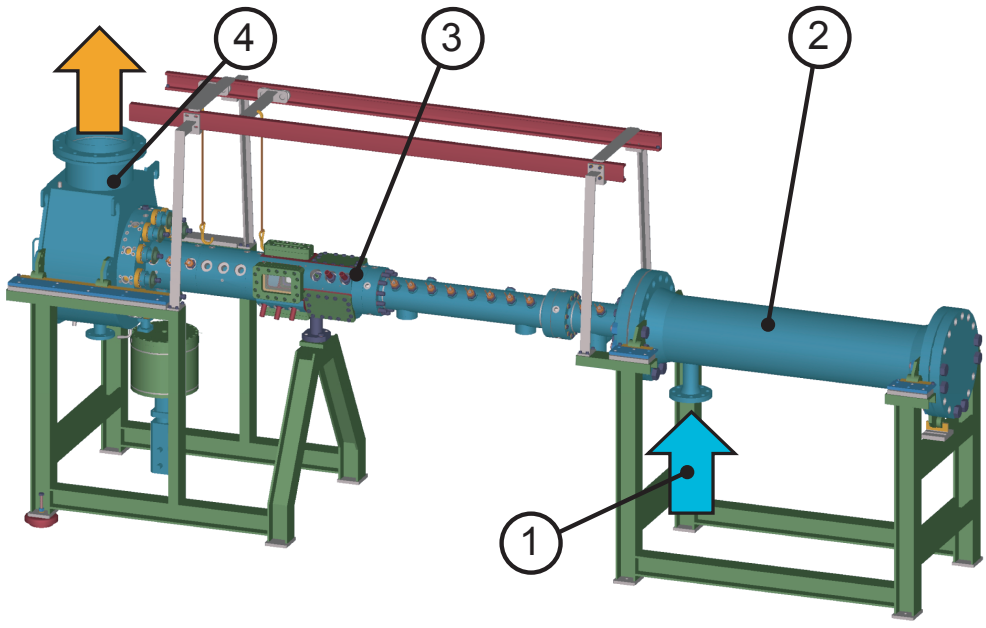

Figure 3.1: High pressure combustion test facility.

The pressure vessel as described in the next subsection is capable of withstanding pressures up to 40 bar, whereas the limitation in the air supply line of the laboratory allows only operation up to 10 bar.

A future upscale in the infrastructure could therefore enable a full exploit of the rig. For the full pressure rating of 40 bar, the wall temperature and thus also the temperature at the burner is limited to 450°C. 500°C apply for the reduced pressure of 10 bar.

Figure 3.1 gives an overview of the test rig. The combustion air (1) enters an electrical air preheater (2) consisting of four sequentially arranged heating elements, each delivering 32 kW of power. The preheater features a double-walled design with the benefits of small heat losses and a cold outer wall not requiring insulation. A surveillance thermocouple is mounted after each of the heating elements, the maximum temperature allowed is 600°C. The preheater is directly connected to the pressure vessel (3), where all combustion-related equipment is mounted. After leaving the combustor and expanding through a set of valves, the exhaust gas is cooled by water injection to less than 250°C, collected in an exhaust manifold (4) and disposed of through a chimney.

3.1 Pressure Vessel

The main part of the test rig is represented by the section exposed to high pressure and temperature as shown in figure 3.2. One common practice in the design of pressurised combustion rigs is to build double walls - a thick and cool outer wall to carry the pressure load, a hot thin walled inner liner and a secondary cooling airflow in between. This standard design bears disadvantages in accessibility and suffers from badly defined acoustics within the thin-walled, not absolutely tight inner liner. Since acoustic investigations represent an important part of this work, the common double-walled design was disregarded and a robust and acoustically well-defined single wall solution was chosen. The low temperatures needed for mechanical integrity are achieved by water-cooling the combustor walls, this has on the other hand the disadvantage of wall boundary conditions not fully representing the high wall temperatures encountered in a gas turbine engine.

To prevent the condensation of the water formed during combustion at

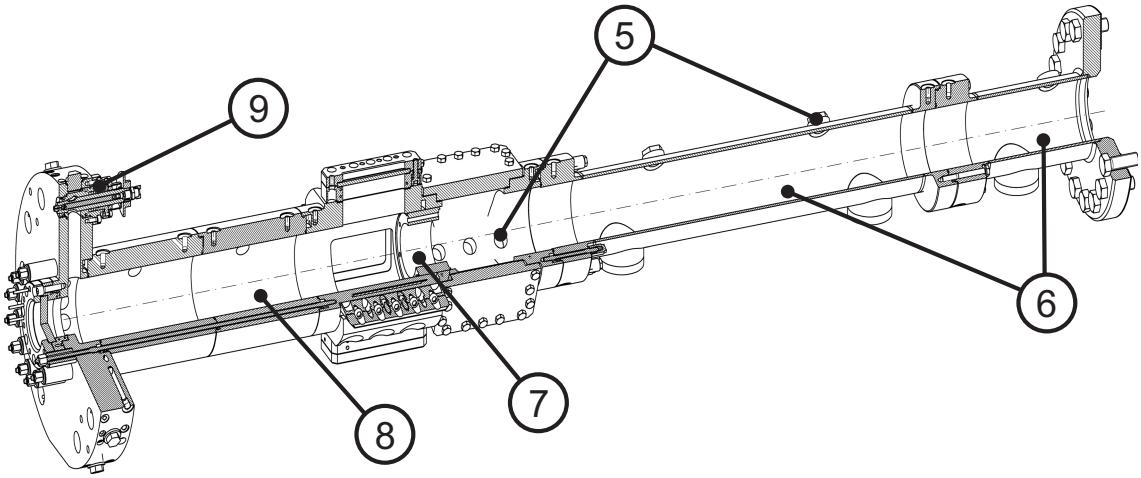

Figure 3.2: Cross section of the pressure vessel without burner.

the inner walls of the pressure vessel, the cooling water is preheated to a temperature of about 90°C. Pre-loading the whole circuit to a pressure of about 15 bar prevents cavitation on the suction side of the pump and raises the boiling temperature to about 220°C to prevent the formation of local vapor pockets that could lead to a collapse of the cooling circuit.

A set of over 50 uniform access ports (5) is distributed all over the pressure vessel. Originally intended for mounting dynamic pressure transducers, these ports are besides that also used for flame surveillance, fuel supply, seeding, ignition, pressure tappings and gas analysis. The diameter of 30 mm (G1" thread) is large enough to accommodate a large variety of sensors and thus enables great flexibility for measurement access.

3.1.1 Supply Tube

The preheater is connected to a supply tube (6) consisting of two modules, one 400 mm and the other one 953 mm long. The inner diameter of both tubes is 146 mm. Main purpose of the supply tube is to allow a simple measurement of the acoustic state upstream of the burner using the multi-microphone method. It is therefore designed with an undisturbed inner geometry and equipped with multiple access ports

that can accomodate dynamic pressure sensors. For an optimisation of the acoustic excitation amplitude the long module can also be removed. In the scope of this work, that was not necessary though.

For setups with perfect fuel/air mixing, the fuel gas is injected directly at the entry into the supply tube. A fuel lance with multiple injection holes and vortices generated as the combustion air exits the transition piece from the preheater provide a good initial spatial distribution of the fuel. Small scale homogenisation is achieved as the mixture travels down the supply tube. Possible temporal modulations of the equivalence ratio generated by the siren exciation can be virtually excluded since the excitation level in the supply tube is generally very low and even for the lowest excitation frequency of 10 Hz the convective wavelength is of the same order of magnitude as the tube diameter, indicating a rapid decay of any perturbation.

3.1.2 Window Module

The window module (7) represents the heart of the pressure vessel and the whole rig, since it accomodates both burner and flame - the former mounted in the upstream part and the latter stabilised in the downstream section. Large rectangular access ports allow an observation of the flame through quartz glass windows and a convenient supply of the burner with fuel, cooling water and cooling air through one cover plate.

A symmetrical design concerning connection interfaces to supply tube and combustor modules as well as the burner mount allows a rotation of the module by 180° around the vertical axis. This is to make use of the different arrangement of the access ports on the two halves: In "conventional mode" two large windows 150 x 90 mm^2 and two small windows 150 x 10 mm^2 provide conventional optical access to the flame as well as the application of all kinds of light sheet techniques in the vertical center plane of the combustor (see figure 3.3 left). In the rotated "PDA mode", the combustor is accessible through two large windows with an angular offset of 115°, which is optimal for Phase Doppler Anemometry. Since the large access interfaces on both sides

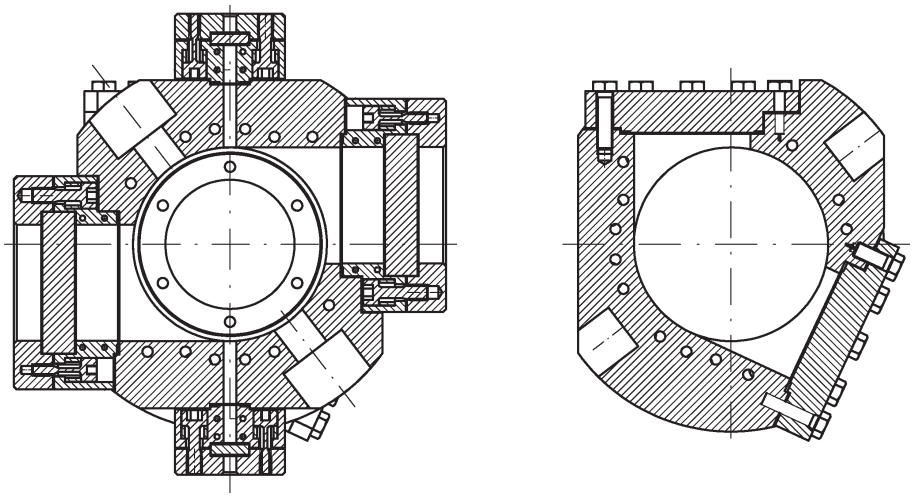

Figure 3.3: Cross sections through the window module in conventional mode. Left: combustor side, right: burner side, view from downstream.

are identical, windows and cover plates are compatible and the burner media supply is not affected by the orientation mode of the window module. In the scope of this work, the window module is operated in conventional mode only.

The arrangement of the large windows allows an undisturbed observation of one half of the flame. Since the inner diameter of the combustor amounts to 150 mm, an additional window overlap of 2 x 15 mm exists that can be used for measurement techniques requiring a laser beam crossing the combustor. The large windows are water-cooled, this option also exists, but is not used for the cover plates. Both large and small windows are equipped with a purging air system to cool the inner side of the glass and to keep it free of seeding particles in the case of LDA or PIV measurements. Since this purging air has an undesirable effect on the overall stoichiometry of the flame, it is not used here.

Also visible in figure 3.3 are the holes for the water-cooling system of the window module and the subsequent combustor modules. Three circular collector channels at the upstream and downstream end as well as in the middle of the module distribute the water to the cooling holes oriented parallel to the central axis. Inserts plugged into the combustor side holes to increase flow velocity result in both enhanced

cooling and an even distribution of the cooling water due to a high pressure drop.

A pin on the lower side of the window module forms the axial fixing of the pressure vessel. This makes sure that thermal expansion at the side windows is negligible and an offset correction of camera images recorded through the side windows is not necessary.

3.1.3 Combustor

Similar to the supply tube, the combustor (8) is rather long to allow the determination of the acoustic state downstream of the flame by a measurement of the dynamic pressure at several axial locations. Of the two 250 mm long tube modules following the combustor side of the window module, one can be omitted to gain flexibility in combustor length. Again like the supply tube, the inner diameter is undisturbed throughout the combustor. A useful side-effect of the long combustor is that cold air from the siren injected into the rear part can not reach and adversely affect the flame. This has been verified in a commissioning test.

The rear part of the combustor is designed in a rather unconventional way. The valve support disk forming the last module has 12 holes of 30 mm diameter guiding the exhaust gases radially outward to 11 pressure valves, where the gas is expanded into the collector manifold. This leaves the rear combustor wall free for a circular window with a diameter of 90 mm that can be conveniently used to observe the entire flame and not only a part of it as through the side windows. Like the side windows, the rear window is equipped with a water-cooling and an air purging system. The one radial hole that is not connected to a valve is used to inject the siren bypass air as described in section 3.2.

A set of bolts is used to tie the combustor modules together. Special high-performance springs allow for the thermal expansion of the pressure vessel while providing sufficient axial force to maintain the sealing of the modules under pressure. Guiding the cooling water through the bolt holes prevents overheating and thermal failure of the bolts. The

cooling water is led radially outwards through the valve support disk parallel to the exhaust gas, thus preventing overheating of the disk.

3.1.4 Pressure Valves

The 11 valves (9) are responsible for setting the pressure in the combustor by adjusting the exit cross section according to the settings of combustion air flow and equivalence ratio. As soon as the critical pressure ratio is reached, the flow velocity within the exit cross section equals the speed of sound, resulting in an extremely high thermal load on the valve. Thus, an individual cooling of both the valve seat and the valve needle using cold high-pressure water was implemented. A high water pressure raises the boiling temperature and prevents a collapse of the cooling due to vapor pockets formed within the channel. The water used for cooling the needle does not circulate, but is injected into the hot gas flow at the downstream end of the needle. This is done to simplify the design of the needle and - more importantly - to cool the exhaust gas flow down below the temperature limit of 250°C imposed by the exhaust silencer.

To maintain a certain operating point, small adjustments of the valve position have to be made continuously. This is very inconvenient and time-consuming, since the valve position has to be set manually. Thus, another procedure was developed using the secondary air flow through the siren duct to fine-tune the operating point, as described in the next section.

3.2 Siren

To be able to generate acoustic excitation within the pressure vessel, a siren has been developed. This device generates acoustic energy by periodically blocking and releasing the air flow through an orifice using a rotating disk with rectangular openings (see figure 3.5). The frequency of the excitation is defined by the speed of the rotor multiplied by the number of openings in the rotor while the amplitude is

set by the air flow through the device.

Unlike designs implemented for other test rigs at the Lehrstuhl für Thermodynamik, the siren for this rig is not mounted in-line with the supply tube to directly excite the combustion air, but is connected to the pressure vessel from below and uses a secondary air flow into the rig to generate the acoustic excitation (see figures 3.1 and 3.4). In this configuration, air at ambient temperature can be used for excitation and the device does not have to deal with both high preheating temperature and high pressure.

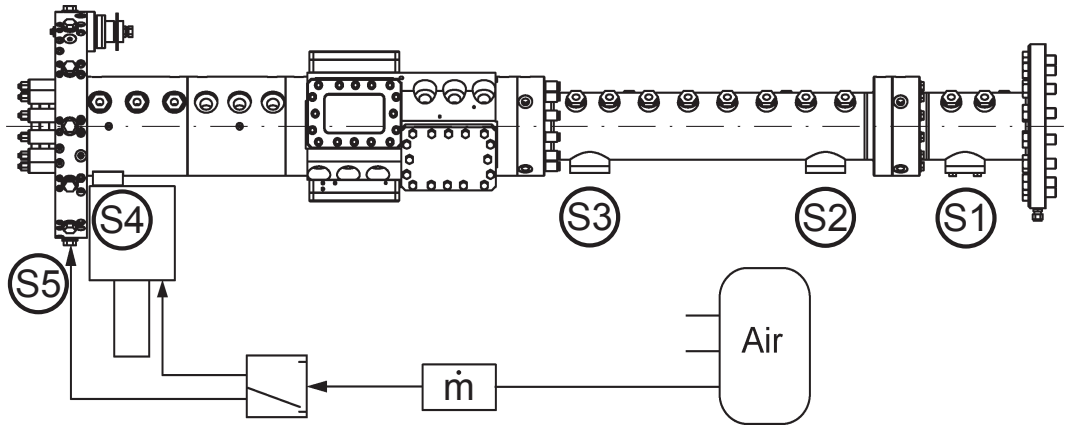

Figure 3.4: Scheme of the siren air massflows.

Siren ports have been implemented both upstream and downstream of the burner to be able to excite the combustion system at different locations. A total of five connection ports exist where the siren can be mounted to the pressure vessel - two in the downstream part of the combustor and three in the supply tube. While for purely acoustic measurements to determine the burner transfer matrix the siren was also connected to port S1, only port S4 was used in the combustion experiments with a setup as sketched in figure 3.4. Injecting cold air into the rear part of the combustor does not affect the combustion; preliminary tests have confirmed that the siren air can not reach and influence the flame stabilised in the upstream region of the combustor. Contrarily, the cold air is useful to reduce the exhaust gas temperature and thus the thermal load on the pressure valves. Mounting the siren to the supply tube is not as favourable, since the siren air reduces the

temperature of the total massflow arriving at the burner. For that case, a blow-off configuration has been designed with another control valve connected to the suppy tube via a T-piece and discharging the preheated air into the exhaust duct. In this configuration, the siren is mounted to the remaining branch of the T-piece and the excited siren air is periodically blocking the blow-off valve. That setup reduces the temperature reduction at the burner to a minimum at the expense of a loss of preheated air through the valve.

To achieve a constant excitation amplitude, the air flow through the siren has to be varied with the excitation frequency. Since the siren airflow injected into the combustor has to be discharged through the pressure valves, a variation does also affect the operating point of the rig, which has to be compensated manually then by readjusting the setting of the pressure valves. To eliminate this effect, a second line was implemented that bypasses the siren and connects to port S5 in the valve support disk. A remotely actuated split valve distributes the total siren massflow coming from the measurement and control cluster to the siren and bypass lines. This design yields the following advantages:

- The excitation amplitude can be conveniently set by the split valve without any influence on the total siren massflow and thus on the operating condition.
- Small drifts in the operating conditions can be easily corrected by an adjustment of the total siren massflow.
- The additional bypass air reduces the thermal load on the rear section of the combustor and on the pressure valves.

The operating pressure[14] of the siren is limited to 10 bar by the shaft sealing ring. Although this ring is a high performance element, it imposes another pressure limitation depending on the excitation frequency as given in equation 3.1. That equation is derived from a fit of the specified operating limit of the sealing ring that in turn originates

[14] Referring to the combustor pressure.

from a limit in the friction power loss.

$$p\,[bar] < 12600\,f\,[Hz]^{-1.17} \tag{3.1}$$

Some key performance figures of the siren are given below:

Pressure:	10 bar
Air massflow:	300 g/s
Temperature:	100 °C
Number of rotor holes:	8
Excitation frequency:	800 Hz
Motor speed:	6000 rpm
Motor continuous power:	3 kW
Total orifice area:	220 mm^2

3.2.1 Siren Contour and Excitation Quality

Compared to loudspeakers, a siren generates excitation amplitudes that are orders of magnitude higher. On the other hand the stability of the frequency is not as good and usually higher harmonics are produced along with the base signal that reduce the signal to distortion ratio S/D. Since difficulties have been encountered with a preliminary design, some thoughts are presented below that have led to an improvement in S/D from about 1 to about 10 for the final siren design.

It is assumed that the excited waveform correlates with the open area of the orifice. To generate a sinusoidal excitation signal, the orifice contour has to be sinusoidal as well, since the integration of the contour sine does again give a sine for the open area[15] [Fre00].

In practice, the orifice contour is a double-sine shape that is projected onto the reference circle to take the rotational movement into account, as sketched in figure 3.5. The angular width φ_0 is determined by the number of holes n on the rotor according to $\varphi_0 = \frac{\pi}{2\,n}$.

[15] With a phase offset of 90° not relevant here.

$$r_{a\,(\varphi)} = R + H\cos(n\varphi) \tag{3.2}$$

$$r_{i\,(\varphi)} = R - H\cos(n\varphi) \tag{3.3}$$

This projection stretches the outer and shrinks the inner contour. Integration over φ gives the influence of the deformation on the open area outside a and inside i the reference circle.

$$\begin{aligned} A_{a\,(\varphi)} &= \frac{1}{2}\int_{-\varphi_0}^{\varphi}\left(r_{a\,(\varphi)}^2 - R^2\right)d\varphi \\ &= \frac{RH}{n}\left[\sin(n\varphi)+1\right] + \frac{H^2}{4}\left[\varphi + \frac{\pi}{2n} + \frac{1}{2n}\sin(2n\varphi)\right] \end{aligned} \tag{3.4}$$

$$\begin{aligned} A_{i\,(\varphi)} &= \frac{1}{2}\int_{-\varphi_0}^{\varphi}\left(R^2 - r_{i\,(\varphi)}^2\right)d\varphi \\ &= \frac{RH}{n}\left[\sin(n\varphi)+1\right] - \frac{H^2}{4}\left[\varphi + \frac{\pi}{2n} + \frac{1}{2n}\sin(2n\varphi)\right] \end{aligned} \tag{3.5}$$

It is evident that the projection imposes a distortion (2^{nd} term) on the linear solution (1^{st} term) that causes a deviation from the pure sine and thus generates higher harmonics. Fortunately, the distortion is equally large on both outer and inner side

$$A_a = \frac{2}{n}RH + \frac{\pi}{4n}H^2 \tag{3.6}$$

$$A_i = \frac{2}{n}RH - \frac{\pi}{4n}H^2 \tag{3.7}$$

so that the total area is unperturbed.

$$A = A_a + A_i = \frac{4}{n}RH \tag{3.8}$$

This result shows that it is vital to shape the orifice as a double-sine, the outer or the inner contour alone would generate higher harmonics in the excitation signal.

The above assumption of the acoustic waveform correlating with the

open orifice area works best for a rather high pressure drop over the orifice approaching the critical pressure ratio. For that case, acoustic pressure fluctuations are too small to generate an undesirable modulation of the pressure drop and the high flow velocity has an additional effect of acoustically decoupling upstream and downstream side of the orifice. A measurement campaign to investigate different siren geometries [Gün05] confirmed that finding. Especially at high frequencies a too small pressure drop leads to a strong distortion of the sine signal with amplitudes of the higher harmonics sometimes exceeding the amplitude of the base signal.

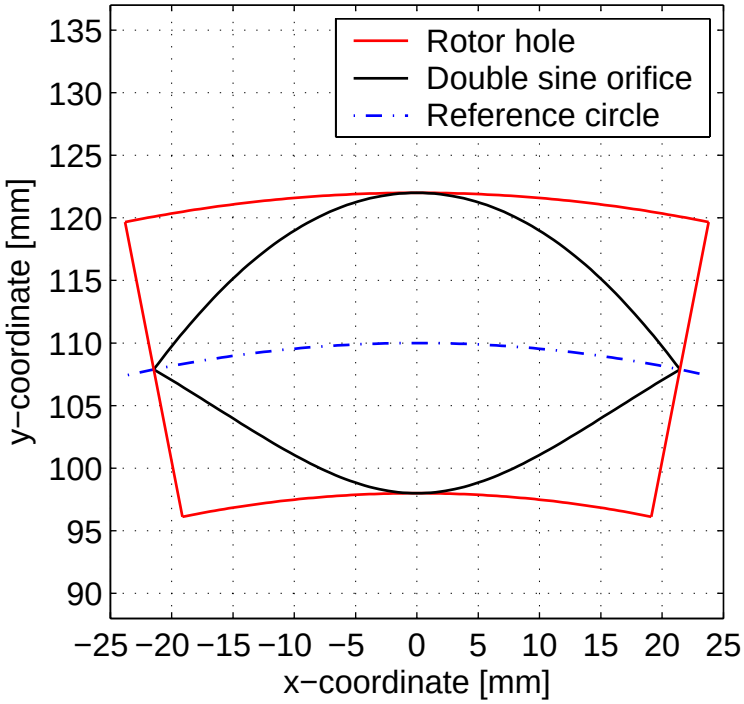

Figure 3.5: Double-sine shaped siren orifice, $R = 110$ mm, $H = 12$ mm, $n = 8$.

Another design feature that has been found to influence the signal quality is the length of the adapter tube connecting the siren to the pressure vessel. For this reason the adapter was redesigned to the shortest possible length with the largest possible inner diameter.

In the low frequency limit, a perturbation of the excitation signal can occur when the pressure upstream cannot be sustained for the long opening duration of the orifice. This case does also result in higher

harmonics of the signal. To reduce that effect, a large volume of about 12 liters upstream of the orifice acting as a buffer and an air connection line with a large diameter have been implemented into the siren design. For the sake of completeness it shall be mentioned that the buffer volume together with the siren orifice acts as a Helmholtz oscillator with an eigenfrequency around 50 Hz. This effect appears in the experiments, but is not of major importance.

3.3 Burners

Two different lean premix (LP) burners have been investigated within the scope of this work. The main interest lies on the TD1 burner developed at the Lehrstuhl für Thermodynamik with a generic design, well known characteristics and a considerable amount of experimental data already available.

Since this burner cannot be operated in technically premixed mode[16], another burner derived from an industrial aero-engine design was investigated in parallel. After some modifications, this burner can be operated with both kerosene and natural gas and in both perfectly and technically premixed mode. It is thus used to draw conclusions from comparisons of the different operating modes. On the other hand, the industrial burner is less suited for high quality transfer function measurements due to its complex design, high burner exit flow velocity and a very high turbulence level.

3.3.1 Generic TD1 Burner

The TD1 burner applied here is a variant derived from a generic design already available at the Lehrstuhl für Thermodynamik that has been subject to a number of theoretical and experimental investigations at atmospheric pressure. Several adaptations have become necessary to achieve high pressure capability, which comprise mainly cooling and design issues. Nevertheless, the geometry of the flowpath upon entry

[16] See footnote on page 11

into and within the burner has not been changed, and comparability to earlier results is thus maintained.

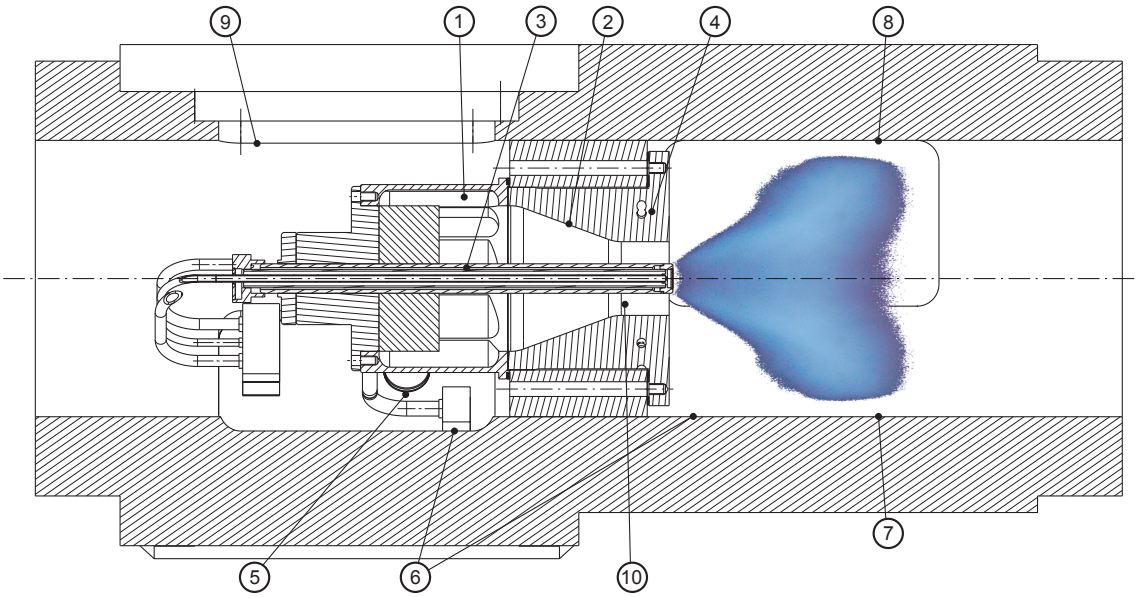

Figure 3.6: Cross section of the generic TD1 burner with a typical flame.

A cross section through the TD1 LP burner is shown in figure 3.6. The homogeneous mixture of combustion air and natural gas generated upstream at the entry into the supply tube enters the burner through the slots of the swirl generator (1). These tangentially oriented slots are 64 mm long and end at an inner diameter of 79 mm, they generate the swirl needed for flame stabilisation. Disks can be inserted into the swirl generator to block a portion of the open area of the slots. This leads to a higher flow velocity for a given mass flow, thus increasing the ratio of tangential to axial momentum or in other words the swirl number. Only one swirl configuration was investigated within the scope of this work with a disk of 32 mm length blocking half of the length of the swirl slots[17]. The associated swirl number was determined numerically ([Kie00], [Kun04]) and amounts to 0.6. After leaving the swirl generator, the mixture is accelerated in a converging nozzle (2) with a cylindrical downstream tube of 40 mm diameter.

A lance (3) with a diameter of 16 mm is inserted into the burner to

[17] Consult [Fis04] for transfer functions with swirl number variation.

avoid flashback along the axis. To prevent the lance from overheating at high pressure and thermal power, an air cooling system of the lance tip has been implemented. The pressurised air is guided to the lance tip and back out of the lance within concentrical tubes, this way the loop is closed and the flame stoichiometry is not affected. Another feature of the lance is a pilot gas system discharging into the air flow through 8 holes in the lance tip. Piloting is needed to achieve a stable ignition - the pressure peak in the combustor associated with the quick temperature rise upon ignition does otherwise drive the flame upstream into the supply tube. Although the pressure peak is also occurring in pilot mode, no combustible mixture propagates upstream of the lance tip so that flashback into the supply tube is impossible and the flame is stabilised reliably in the combustor. After ignition and before starting any measurement, a switchover to full premixed mode is performed. No pilot gas is used during normal operation that could adversely affect the chemiluminescence emission of the flame through local perturbations of the equivalence ratio.

The front wall (4) of the burner is water-cooled to be able to manage the high thermal load at elevated pressure conditions. Typical front wall temperatures range from 100°C near the cooling channels to about 700°C on the outer rim. Parts facing the flame like the front wall are manufactured from stainless steel 1.4841, while the upstream parts of the burner are made of brass for easy machining. A thermocouple (5) is used to determine the burner temperature shortly before entry into the swirler and two of the G1" access ports within the window module accomodate the pressure taps (6) to monitor absolute pressure (upstream side) and burner pressure drop. A spark plug for ignition (7) and a flame detector (8) are mounted within two access ports on the combustor side. A second flame detector within the supply tube (9) triggers an automatic emergency procedure in case of flame flashback. All supply lines for cooling and pilot gas enter the pressure vessel via one cover plate on the upstream side of the window module.

To measure the flow velocity and its fluctuation due to acoustic excitation, a constant temperature anemometer (CTA) is inserted into

the burner. Its location is 22 mm upstream of the burner exit in the middle of the slot between lance and burner nozzle (10). At this location, the signal strength is good due to the high flow velocity, the turbulence level is low enough and the distance to the flame is sufficiently large to exclude an influence by flame radiation. The probe is mounted radially through a bore that passes both pressure vessel and burner nozzle. The sensitive probe tip is retracted into the protective mounting hole for ignition and can be replaced by a dummy rod when not needed.

3.3.2 Industrial Burner

The industrial burner (IB) is a generic design derived from an aero-engine kerosene LP burner with a simple airblast atomiser. This burner was modified to make it compatible with the high pressure rig and with gas operation.

Figure 3.7 shows a sketched cross section through the industrial burner mounted in the high pressure rig. The burner consists of three main parts - a fuel nozzle (1), a swirler (2) and a mixing tube (3). The main purpose of the nozzle is to atomise the liquid fuel at its tip using the momentum of the surrounding airflow. Since atomisation is not necessary in natural gas operation, the function of the nozzle is reduced to provide a defined starting point for the mixing process. To account for the much lower density of natural gas, the nozzle orifice has been enlarged. However, the initial fuel velocity in gas operation is still much larger than in kerosene operation, which also changes the flowfield in the mixing tube.

In addition to the atomisation air around the burner axis that is not swirled, a second air inlet ring exists around the atomisation air with a set of blades generating the swirl. This ring is located upon entry into the 120 mm long mixing tube. An area contraction with a sharp edge (4) at the tube exit aims at reducing the boundary layer thickness to prevent flame flashback along the wall into the mixing tube.

Similar to the TD1 design, the burner front wall (5) is water-cooled

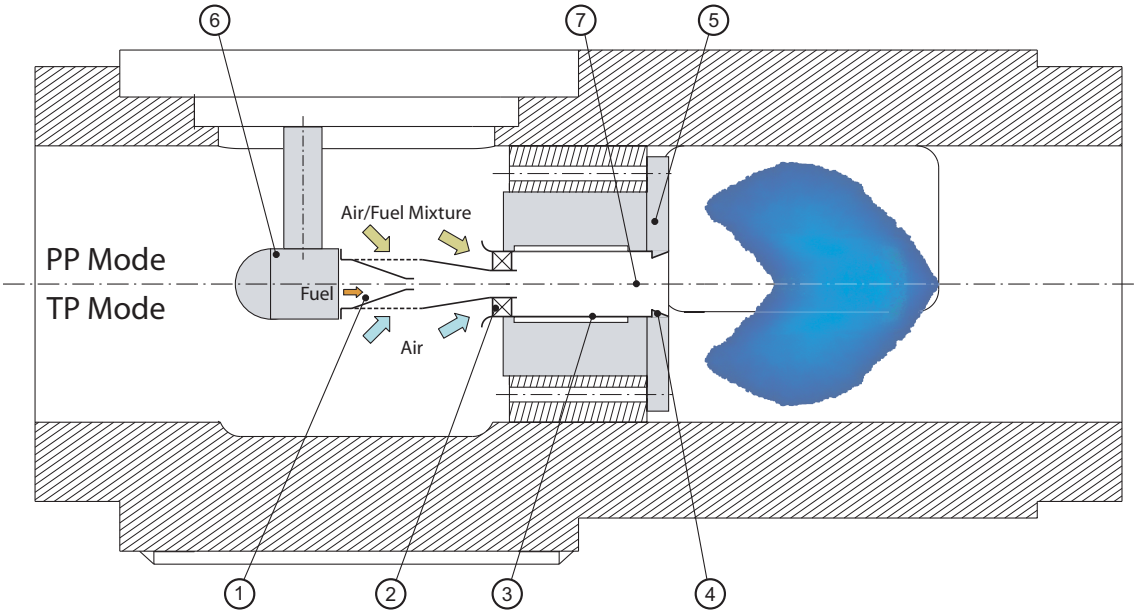

Figure 3.7: Cross section of the industrial burner with a typical flame.

and the head carrying the fuel nozzle (6) is air-cooled to protect the O-ring seal. To avoid cold walls, a double walled design with an air insulation layer is chosen for the mixing tube. Materials are stainless steel 1.4841 for the front wall facing the flame and stainless steel 1.4301 for the rest.

This burner can be operated in both technically (TP) and perfectly (PP) premixed mode. The technically premixed mode uses the nozzle for injecting the fuel into the burner, only the burner length is available for mixing.

In PP mode, the gas injection is the same as for the TD1 burner and takes place at the entry into the supply tube - at a distance from the burner that is sufficient to perfectly homogenise the fuel air mixture. The fuel nozzle is mounted but not used, this leads - compared to TP mode - to a different flow distribution between atomiser and swirl duct due to the missing momentum of the fuel jet. Similar to the pilot gas in the TD1 burner, the TP mode is required here for ignition to prevent flashback. The switchover to PP mode takes place after a stable TP flame is established.

The CTA is inserted into the mixing tube at the same axial distance to

the burner exit as for the TD1 burner. Unlike the TD1, the industrial burner produces a high level of turbulence in the mixing tube due to the strong shear forces in the mixing region of the two flows entering the burner. This high turbulence limits the operating range of the CTA to about 3 bar in TP and less than 4 bar in PP mode - exceeding this limit results in a broken CTA wire. An optimum ratio of signal to turbulent noise is achieved at the burner axis, for that reason the hot wire is located there (7).

3.4 Operating Conditions

The main focus of the investigations within the scope of this work lies in a variation of the operating pressure p_B defined as the pressure upon entry into the burner. Of minor interest are a variation of the flame (combustor) temperature T_C via a change of the air excess ratio λ and a variation of the flow velocity in the burner u_B.

To achieve a comparability of the results for varying pressure it is vital to keep other key parameters like the burner flow velocity or the flame temperature constant. The flame temperature is governed by the preheating temperature measured at the burner entry T_B and the air excess ratio λ. Since

$$u_B^2 = \frac{2\,p_B\,\frac{\Delta p_B}{p_B}}{\zeta\,\rho_B} = \frac{2R}{\zeta}\,T_B\,\frac{\Delta p_B}{p_B}\ , \tag{3.9}$$

the burner flow velocity u_B does for constant T_B only depend on the relative pressure drop over the burner $\Delta p_B/p_B$. A convenient circumstance is the independence of $\Delta p_B/p_B$ from the massflow $\dot{m}_B$ through the burner for rigs with a sonic orifice downstream of the combustor. This can be shown when substituting the gas-dynamics equation for a critical flow through an orifice

$$p_B \approx p_C = \frac{\dot{m}_B}{\psi_0\,A_t\,\sqrt{\frac{2}{R\,T_C}}} \tag{3.10}$$

into

$$\frac{\Delta p_B}{p_B} = \frac{\zeta R}{2A_B^2}\, T_B\, \frac{\dot{m}_B^2}{p_B^2} \tag{3.11}$$

derived from equation 3.9. The result

$$\frac{\Delta p_B}{p_B} = \zeta\, \psi_0^2\, \frac{1}{A_B^2}\, \frac{T_B}{T_C}\, A_t^2 \tag{3.12}$$

makes clear that for given temperatures of burner T_B and flame T_C the relative pressure drop does only depend on the open area of the orifice A_t and thus only on the setting of the pressure valves. For rig operation this means that (in the ideal case) the pressure valves have to be adjusted only once to achieve the desired relative pressure drop. The massflow through the burner can then be employed to set the pressure level according to equation 3.10 without affecting the burner flow velocity.

The above procedure still holds when replacing the manual fine tuning of the pressure valves necessary in practice by small changes of a secondary air massflow $\dot{m}_C$ through the siren/bypass duct into the rear part of the combustor as discussed in section 3.2. A constant relative pressure drop during the process of changing the pressure level is then achieved by maintaining the air split $\dot{m}_B/\dot{m}_C$ while varying $\dot{m}_B$.

Table 1 summarises the scaling rules of the combustion variables for varying pressure, as utilised in the scope of this work.

Those scaling rules are applied on the nominal operating conditions of the two burners at atmospheric pressure. An overview of the operating points where flame transfer functions have been measured is given in table 2. In the following, the first three columns are used to abbreviate the operating condition - IB-P2 for example denominates the transfer function measured using the industrial burner in perfectly premixed mode at a pressure of 2.5 bar.

[18] All pressures given in this work are absolute values. A typical atmospheric ambient pressure at the test rig location in Munich is 0.96 bar.

[19] Compared to the rest of the TD1 transfer functions, TD1-P1 at $\lambda = 1.3$ was measured at

Table 1: Pressure scaling rules.

Variable		Constant	$\propto p_B$
Burner temperature	T_B	$\surd$	–
Flame temperature	T_C	$\surd$	–
Air excess ratio	λ	$\surd$	–
Burner velocity	u_B	$\surd$	–
Burner pressure drop ratio	$\frac{\Delta p_B}{p_B}$	$\surd$	–
Air massflow burner	$\dot{m}_B$	–	$\surd$
Air massflow siren/bypass	$\dot{m}_C$	–	$\surd$
Burner pressure drop	Δp_B	–	$\surd$
Fuel massflow	$\dot{m}_f$	–	$\surd$
Thermal power	P_{th}	–	$\surd$
Air/mixture density	ρ	–	$\surd$
Reynolds number burner	Re_B	–	$\surd$

Table 2: Operating conditions for flame transfer function measurement.

Burner	Premix Mode	OP	p_B[18] [bar]	$\Delta p_B/p_B$ [%]	λ [–]	T_B [°C]	P_{th} [kW]
TD1	P	1	1.1	0.83[19]	1.3	150	68
		2	1.1	1	1.4	150	70
		3	2.2	1	1.4	150	140
		4	3.0	1	1.4	150	190
		5	2.2	1	1.47	150	134
		6	3.0	1	1.47	150	183
		7	4.0	1	1.47	150	244
		8	5.0	1	1.47	150	305
IB	P	1	1.75	6	1.2	150	60
		2	2.5	6	1.2	150	90
		3	2.8	6	1.2	150	100
		4	3.5	6	1.2	150	128
		5	4.0	6	1.2	150	144
IB	T	1	1.75	6	1.2	150	60
		2	2.5	6	1.2	150	90
		3	2.8	6	1.2	150	100

a different burner velocity setting. The latter originates from an offset of the burner differential pressure sensor that has been recognised not before completion of the measurement of the two FTFs and that biased the operating point setting.

4 Measurement Techniques

In this section, the measurement techniques applied within the scope of this work are introduced. A constant temperature hot wire probe is used to determine the velocity at the burner exit, and the chemiluminescence representing the heat release of the flame is recorded by a photomultiplier. Also, the setup and the data acquisition & evaluation procedure applied to determine the flame transfer functions are explained below. Finally, the recording and evaluation procedures of high speed camera images utilised to locally resolve the flame heat release are presented.

4.1 Velocity

4.1.1 Hot Wire Anemometry

Constant temperature hot wire anemometer (CTA) probes are used to determine the mixture flow velocity within the burner. Their functional principle is based on the cooling effect of a flow around a heated body. Such a probe consists of a thin wire that is welded to the tips of two needle-shaped prongs, as illustrated in figure 4.1, right.

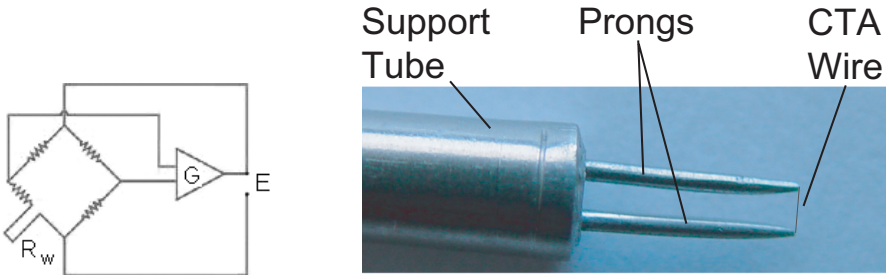

Figure 4.1: Left: Whetstone bridge, R_W = wire resistance, E = bridge voltage. Right: Image of the CTA probe.

The wire is connected to one arm of a Wheatstone bridge - see figure 4.1, left - and heated by an electrical current. A servo amplifier (G) keeps the bridge in balance by controlling the current to the sensor so

that the resistance R_W - and hence the temperature - is kept constant, independent of the cooling imposed by the fluid. For this setup, the bridge voltage E represents the heat transfer to the flow and is thus a direct measure of the velocity. The combination of the sensor's low thermal inertia and the high gain of the servo loop amplifier gives a very fast response to fluctuations in the flow, and temporal resolutions on the order of kHz are achievable.

A formulation for the heat transfer from a thin wire to a fluid for anemometry purposes was originally derived by King [Kin14], later refined by Collis and Williams [CW59] and is now widely used [CB76], [TSI].

$$\dot{Q} = K \left[A + B \left(\frac{\rho u}{\eta} \right)^{0.45} \right] \left[\frac{T_s + T_e}{T_e} \right]^{0.17} (T_s - T_e) \tag{4.1}$$

In equation 4.1, K, A and B denominate constants obtained from a calibration of the hot wire probe, T_s is the sensor- and T_e the gas temperature. The heat flux $\dot{Q}$ is determined from the electrical power loss in the wire by evaluating the bridge voltage E and the wire resistance R_W.

$$\dot{Q} = \frac{E^2}{R_W} \tag{4.2}$$

The probes were manufactured in-house and are capable of withstanding ambient temperatures of up to 500 °C. A Pt-Ir wire with a diameter of 10 μm was applied to the probes for all measurements. The prongs were made of an alloy with a negligible temperature coefficient[20] to avoid a drift of the Whetstone bridge at elevated ambient temperatures. A wire temperature of 350°C - 200°C above the ambient gas temperature - was applied for all measurements. For further details on the CTA setup consult [Sch05], [Wol05] and [Kon05].

[20] CrFeAl 135

4.1.2 CTA Calibration

To determine the missing factors in equation 4.1, a calibration of the probe is required. That calibration was performed in situ and directly before each FTF measurement. A typical calibration curve as recorded for the generic TD1 burner is shown in figure 4.2.

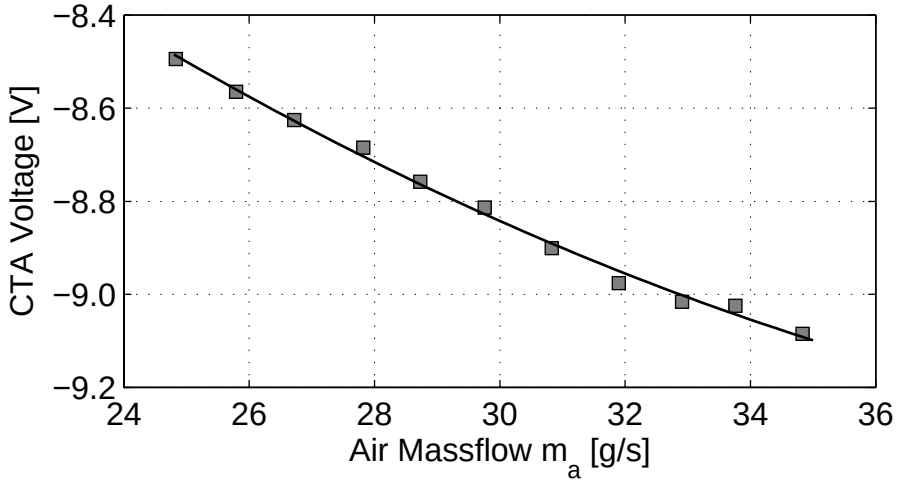

Figure 4.2: Typical example of a CTA calibration - TD1-P1.

Since only relative changes are of interest, the air massflow has been chosen as a reference. To acquire a calibration curve, the air massflow is varied by typically ±20% around the operating point, while the air excess ratio is kept constant by adjusting the fuel flow accordingly and the pressure is kept constant by a parallel variation of the bypass air flow. Several measurement points of bridge voltage versus air massflow are recorded during this variation, and the calibration curve is subsequently determined by a least-squares fit to these points. Since only a limited portion of the curve is mapped, a 2^{nd} order polynomial is sufficient for the fit.

While the calibration data for the generic burner is usually good, the data quality achieved with the industrial burner setup is much lower[21]. As a consequence, the uncertainty in the calibration data fit is larger, which in turn results in an uncertainty in the amplitude of the associated FTFs.

[21] See section 6.2 for the reasons behind this deterioration

4.1.3 Influence of the Mixture Fraction on the CTA Signal

In technically premixed mode, a fluctuation of the velocity at the injector nozzle does in general also generate a fluctuation of the air excess ratio within the burner. Since the hot wire probe is not only sensitive to the velocity, but also to the mixture fraction, a systematic error $u_{B,\lambda}$ is introduced that affects the measured velocity values $u_{B,m}$ in the burner.

$$u_{B,m} = u_B + u_{B,\lambda} \tag{4.3}$$

The same equation is valid for perturbations

$$u'_{B,m} = u'_B + u'_{B,\lambda} \ , \tag{4.4}$$

from which a calibration factor K_{u_B} can be defined that relates the measurement error from a mixture fraction fluctuation to the actual velocity fluctuation.

$$K_{u_B} = \frac{u'_{B,\lambda}}{u'_B} \tag{4.5}$$

The velocity error term $u'_{B,\lambda}$ of the CTA probe can be separated into two effects:

1. A modified heat transfer to the fluid due to the influence of the gas composition itself.
2. A modified heat transfer to the fluid due to a change of the temperature difference between sensor and fluid. Since ambient temperature fuel is injected into pre-heated air, the mixture temperature does change together with the air excess ratio.

Both effects can be analysed by tracking their influence on equation 4.1. While this is straightforward for the second, the first effect requires an analysis of several parameters influencing the heat transfer - density, viscosity and thermal conductivity[22] of the mixture. A nu-

[22] Also the heat capacity c_p is considered, although the variation of this parameter is very small.

merical model using fluid property data from [VDI02] has been set up to derive K_{u_B} for the operating points of interest IB-T1 to IB-T3.[23]

One factor of paramount importance for the model is the local, time-averaged air excess ratio at the location of the hot wire in the burner. A strong radial unmixedness must be assumed for the industrial burner, which can be expressed using the global average of the air excess ratio according to

$$U_\lambda = \frac{\overline{\lambda}}{\lambda(r)} \, . \tag{4.6}$$

With U_λ as main parameter and an additional variation of the sensor temperature T_s, the results of the model are presented in figure 4.3.

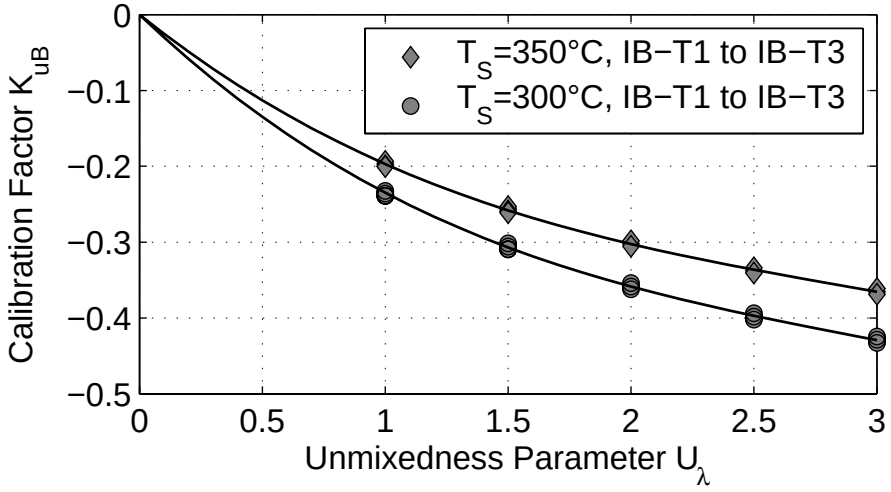

Figure 4.3: Mixture fraction calibration factor K_{u_B} over the unmixedness parameter U_λ.

Note that the pressure variation between the operating points has a negligible influence on K_{u_B}. On the other hand, the sensor temperature has a rather strong influence, a careful setting of the overheating ratio of the Whetstone bridge is thus required. The negative values of K_{u_B} denote an underestimation of the true velocity fluctuation u'_B, which is due to the mixture temperature perturbation being the dominant error effect.

[23] See [Wol05] for details.

For pure air at $U_\lambda = 0$ the velocity bias vanishes completly, while for various mixtures the curve with the nominal T_s of 350 °C is well fitted by a polynomial of 3^{rd} order.

$$K_{u_B} = -0.00786\,U_\lambda^3 + 0.0691\,U_\lambda^2 - 0.26\,U_\lambda \tag{4.7}$$

This relation is used in section 8.3.1 to eliminate the systematic error imposed by $u_{B,\lambda}$ on the measured transfer functions, with the required unmixedness input being estimated in section 7.1.

4.1.4 Pressure Influence on the CTA Signal

In the case of acoustic excitation that is of interest here, not only the burner velocity is fluctuating, but also the ambient pressure at the location of the hot wire probe. These pressure fluctuations could distort the measurement and are thus investigated here.

Basis for the subsequent sensitivity analysis is again equation 4.1 for the heat flux from the heated wire to the surrounding gas in the channel. This equation is now perturbed by small fluctuations of the ambient conditions

$$\begin{aligned}\overline{\dot{Q}} + \dot{Q}' = K \left[A + B \left(\frac{(\bar{\rho} + \rho')(\bar{u} + u')}{\eta} \right)^{0.45} \right] \\ \left[\frac{T_s + \overline{T_e} + T_e'}{\overline{T_e} + T_e'} \right]^{0.17} \left(T_s - \overline{T_e} - T_e' \right)\end{aligned} \tag{4.8}$$

A first order Taylor series approximation and neglecting the product of ρ' and u' leads to

$$\begin{aligned}\overline{\dot{Q}} + \dot{Q}' \;=\; & K \left[A + B \left(\frac{\bar{\rho}\bar{u}}{\eta} \right)^{0.45} \left(1 + 0.45 \frac{\rho'}{\bar{\rho}} + 0.45 \frac{u'}{\bar{u}} \right) \right] \left[\left(\frac{T_s}{\overline{T_e}} + 1 \right)^{0.17} \right. \\ & \left. -0.17 \left(\frac{T_s}{\overline{T_e}} + 1 \right)^{-0.83} \frac{T_s}{\overline{T_e}} \frac{T_e'}{\overline{T_e}} \right] \left(T_s - \overline{T_e} - T_e' \right) \; .\end{aligned} \tag{4.9}$$

Some algebra and again neglecting the products of perturbations gives the following normalised equation.

$$\frac{\dot{Q}'}{\overline{\dot{Q}}} = 0.45 \frac{B\left(\frac{\bar{\rho}\bar{u}}{\eta}\right)^{0.45}}{A + B\left(\frac{\bar{\rho}\bar{u}}{\eta}\right)^{0.45}} \left[\frac{\rho'}{\bar{\rho}} + \frac{u'}{\bar{u}}\right] - \left[\frac{\overline{T_e}}{T_s - \overline{T_e}} + 0.17\frac{T_s}{T_s + \overline{T_e}}\right] \frac{T_e'}{\overline{T_e}} \tag{4.10}$$

Since acoustic waves represent isentropic changes of the thermodynamic variables, the linearised isentropic relations can be used to replace density and temperature with pressure fluctuations.

$$\frac{\rho'}{\bar{\rho}} = \frac{1}{\kappa}\frac{p'}{\bar{p}} \quad \text{and} \quad \frac{T_e'}{\overline{T_e}} = \frac{\kappa - 1}{\kappa}\frac{p'}{\bar{p}} \tag{4.11}$$

The term in equation 4.10 comprising A and B is ≈ 1, since A is small compared to the rest. For the operating conditions discussed in this work, the bracketed factor scaling the temperature fluctuation amounts to ≈ 2.2. All this together gives the sensitivity of the relative heat flux - representing the measured voltage - to fluctuations in both acoustic velocity and pressure.

$$\frac{\dot{Q}'}{\overline{\dot{Q}}} = 0.45\frac{u'}{\bar{u}} - 0.31\frac{p'}{\bar{p}} \tag{4.12}$$

Equation 4.12 gives the same order of magnitude for both acoustic variables and thus a strong measurement distortion. However, this is put into the right perspective when considering typical relative fluctuation levels for the generic burner - 0.05 for the velocity set per definition by the constant siren excitation level and 0.001 for the pressure, respectively. Since now there is a difference of almost two orders of magnitude, the distortion from the acoustic pressure can be neglected. Also, equations 4.10 and 4.11 could be used to correct the measurements for any case where the dynamic pressure is not negligible.

Unlike the TD1, the pressure amplitudes can not be neglected for the industrial burner. Especially for high excitation frequencies, the velocity and pressure amplitudes are of the same magnitude, or even a dominance of p' is encountered. Unfortunately, p' for these cases can only be estimated and is not known in amplitude and phase. A correction as mentioned above can thus not be performed.[24]

4.2 Heat Release

In the scope of this work, the heat release of the flame is determined by measuring the chemiluminescent emissions of the OH* radical formed in the reaction region of the flame. Section 4.2 gives some background information and introduces the calibration necessary to find the correlation between chemiluminescence emissions and heat release.

4.2.1 OH*-Chemiluminescence

The term "chemiluminescence" refers to the emission of light from a chemical reaction. This radiation is emitted in the form of a photon when a molecule returns from an electronically excited state - usually denoted by a * - to the energetic ground state. In a hydrocarbon flame, several species act as emitters, most commonly used for measurements are OH*, CH*, C_2* and CO_2*. While large molecules like CO_2* tend to emit a broad spectrum that is hard to separate from noise and other radiation sources, the small molecules OH*, CH* and C_2* exhibit emission profiles with strong, narrow peaks and are thus preferredly utilised for measurements. The hydroxyl radical OH* used here has its main emission peak at a wavelength λ of 308 nm [Gay74], [WLTS98]; the advantages of applying this species are its strong emission peak and the wavelength in the ultraviolet range with little emission noise from other species.

$$OH^* \longrightarrow OH + \frac{h}{\lambda}, \quad \lambda = 308\text{nm} \tag{4.13}$$

[24] See section 6.2 and appendix C for further details on this topic.

In terms of tracking the heat release, the concentration of the formyl radical HCO is an excellent indicator, but very hard to detect experimentally [NPMW98]. New research suggests that the formation of the OH* radical is linked to HCO according to

$$HCO + O \longrightarrow CO + OH^* \,. \tag{4.14}$$

This link and experimental results of many researchers have led to the conclusion that chemiluminescent- and especially OH* emissions are a good measure for the heat released by the flame for perfectly premixed conditions [PHS68], [Lan88], [CKL98].[25] Especially the work of Haber [Hab00], [HVSK00a], [HVSK00b], [HV03] is of importance here, he derives a linear relationship between the heat release and the OH* chemiluminescence.

Nevertheless, the OH* chemiluminescent radiation shows also a strong sensitivity on the flame temperature and thus on the air excess ratio. This behaviour is due to a strong temperature-dependence of the probability for collisional quenching of the excited species with other molecules [GC86]. The latter effect is - next to photon emission - the second and most frequently occurring mechanism of removing the excess energy from the excited species.[26] In this work, that effect has to be taken into account for the technically premixed operating points, which feature both spatial and temporal inhomogenities of the mixture fraction.

Following the usual procedure, the time-resolved OH* chemiluminescence radiation integrated over the flame volume is recorded here to determine the flame transfer functions [Bue92], [LBZK03], [Fis04], [Kun04]. A photomultiplier is applied to convert the light emission into an electrical signal, while a narrow-band interference filter restricts the incident light spectrum to the main OH* peak at 308 nm. Due to the precise linearity of the photomultiplier, its output voltage is always proportional to the incoming radiation.

[25] Some results of Najm et al. [NPMW98] indicate that also OH* emissions as a measure for heat release should be used with caution, more research on this topic might thus be beneficial.

[26] A third mechanism is the chemical reaction with other species. However, the associated reaction rates are small enough to consider this mechanism negligible for the application within flames [DV92].

4.2.2 Photomultiplier Calibration

Since only relative changes are of interest here, a calibration has to be applied to map the OH* radiation intensity to the actual heat release of the flame. This is done parallel to the CTA calibration by varying the burner air flow $\dot{m}_a$ at constant pressure and constant air excess ratio. Again, the air massflow is taken as a reference, the link to the heat release rate is then given by the fuel mass flow.

$$\dot{Q} \propto \dot{m}_f \propto \dot{m}_a \tag{4.15}$$

An example for a typical calibration curve is given in figure 4.4. As found by other researchers and mentioned above, also here the OH* intensity is related to the heat release by linear trend. The calibration curve can thus be reduced to a constant gradient $dI/d\dot{m}$ around the operating point.

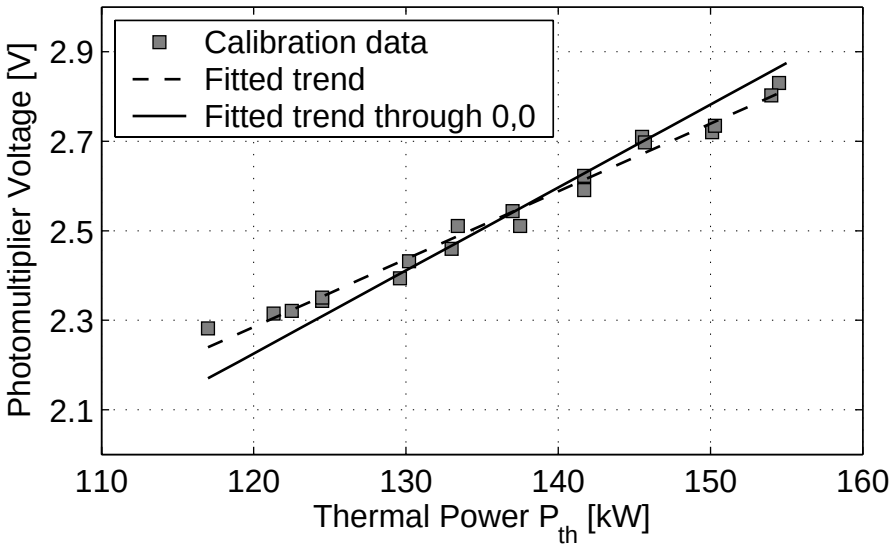

Figure 4.4: Typical example of a standard photomultiplier calibration - TD1-P3. Dashed line: fitted trend, solid line: fitted trend through the coordinate origin.

Note that the fitted trend line does usually not cross the coordinate origin, which indicates that heat release and OH* intensity are not strictly proportional. Nevertheless, the evaluation of the flame transfer functions has shown that the assumption of a strictly proportional

behaviour - as illustrated by the solid line in figure 4.4 - gives better results with a lower variability in the FTF amplitude and a better compliance with the required criterion of an amplitude value of 1 in the low frequency limit.[27] For this reason, the non-proportionality is considered an error and the gradient of all photomultiplier calibrations has been modified accordingly before evaluating the FTFs. This new procedure reduces the calibration to one recording at the operating point, the gradient can then be easily derived from this one point and the coordinate origin.

A comprehensive explanation for this effect has not been found yet, but a trend to a reduction of the gradient mismatch for rising pressure and thermal power could be a hint towards non-adiabatic effects induced by the heat losses of the flame to the walls. An influence of the radiation from the walls is unlikely, but cannot be excluded. Another possible explanation might be found in a superposition of the radiation signals of OH* and CO_2^*, since also the radiation of the CO_2^* molecule contributes to the measured intensity in the wavelength window of the interference filter around 308 nm.

4.2.3 Mixture Influence on the OH*-Chemiluminescence

As mentioned in section 4.2.1, the flame temperature and thus also the air excess ratio has a strong influence on the OH* radiation of the flame. That influence is important for the technically premixed cases of this study, since both temporal and spatial variations of the air excess ratio are expected during the flame transfer function measurement.

In the low frequency limit, the relation of flame intensity and air excess ratio can be characterised by additional calibration curves. Since the mixture fraction is influenced by a variation of both air and fuel flow, two additional calibration types are possible. Table 3 gives an overview.

[27] Details on the influence of the proportional calibration with the curve through the coordinate origin on the FTFs can be found in appendix B.

Table 3: Different types of photomultiplier calibration.

Type	$\dot{m}_a$	$\dot{m}_f$	λ
A	var	var	const
B	var	const	var
C	const	var	var

- Type A represents the standard calibration used for both PP and TP mode FTFs. Since the air excess ratio is constant, the curve captures the influence of the thermal power only.
- For type B, only the air flow is varied and the thermal power remains constant. Thus, this calibration type represents just the air excess ratio influence.
- Type C is combination of the two and represents a superposition of the influences of mixture fraction and thermal power.

All three calibrations have been recorded at constant pressure for the TP mode operation conditions IB-T1 to IB-T3, an example of the result is given in figure 4.5.

The diametrically opposed behaviour of the intensity on the different variables becomes clear in figure 4.5a. While a positive perturbation of the burner velocity increases the intensity in the premixed case with constant λ, the same perturbation causes a reduction if the fuel flow is kept constant. Note that in the context of interpreting the flame intensity as a measure for heat release the sensitivity on a mixture fraction fluctuation must be considered a systematic error. An accordingly large error of the FTFs can thus be expected in TP mode.

Moreover, the influence of the mixture fraction at the chosen operating points is stronger than the influence of the heat release, as visualised in figure 4.5b. The former will thus dominate the global behaviour of TP mode measurements that use the chemiluminescence signal as a measure for heat release.

Using the calibration data presented here, the model derived in section 8.3.1 allows to remove the influence of the air excess ratio from the

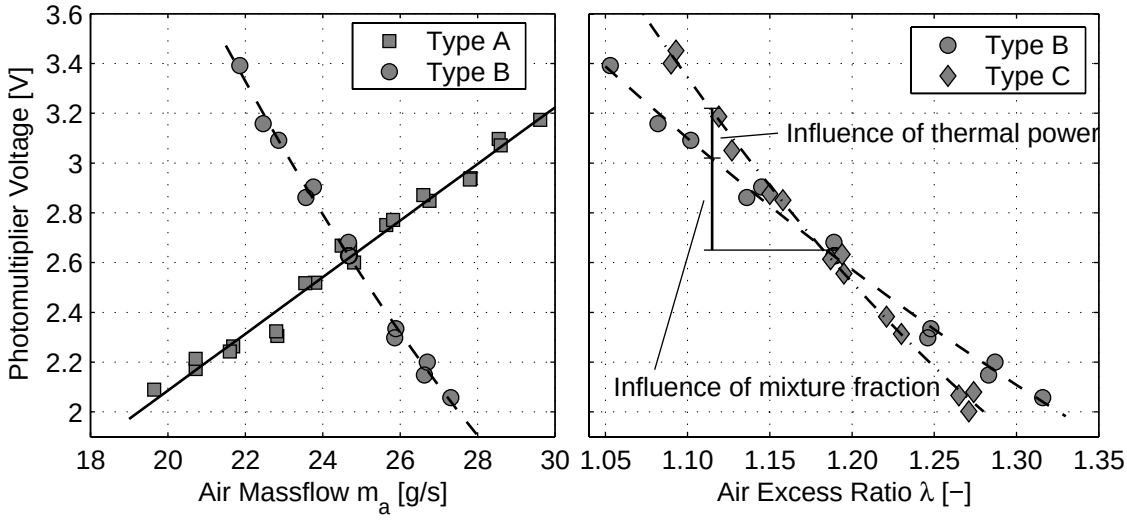

Figure 4.5: Photomultiplier calibration type A, B and C for IB-T1 over a) (left): air massflow / burner velocity and b) (right): air excess ratio. The intersection denotes the operating point.

measured flame transfer functions and to isolate the desired behaviour of the heat release rate.

4.2.4 Pressure Influence on the OH*-Chemiluminescence

Little data exist on the pressure-dependence of flame OH* chemiluminescence, one good source is, however, the work of Higgins et al [HML+01]. Their measurement data fit well to a power law relating the intensity to the pressure for constant thermal power $\dot{Q}$.

$$\frac{I_{OH^*}}{\dot{Q}} \propto p^{-0.86} \tag{4.16}$$

The strong decrease of the intensity with pressure is attributed to increased collisional quenching of the OH* molecules at higher pressure.

An investigation of the pressure dependence was also performed in this work by slowly varying the operating conditions from TD1-P2 to TD1-P4 at constant burner flow velocity and constant photomultiplier gain setting. The results are presented in figure 4.6.

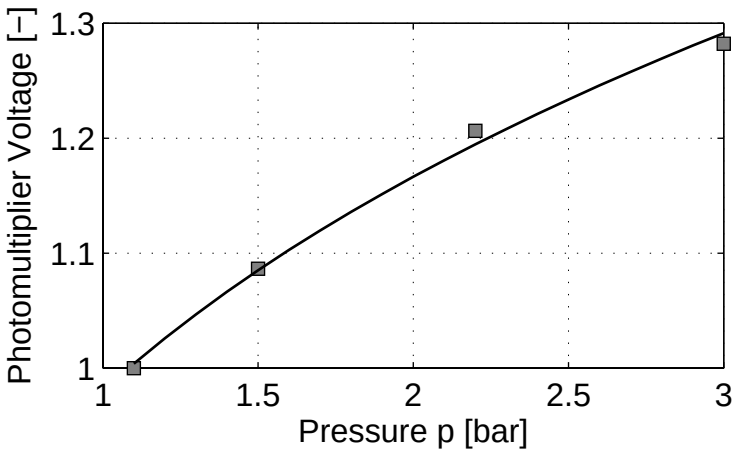

Figure 4.6: OH* intensity over pressure, recorded with constant photomultiplier gain and constant burner velocity from TD1-P2 to TD1-P4.

Also here, a power law gives a good fit to the measured data.

$$I_{OH^*} \propto p^{0.25} \tag{4.17}$$

Since the thermal power $\dot{Q}$ of the flame is also increased during the measurement procedure, the influence of $\dot{Q}$ must be compensated to get the pure pressure-dependence.

$$I_{OH^*} \propto p^{0.25} \cdot \dot{Q}^{-1} \propto p^{-0.75} \tag{4.18}$$

This result is now in good agreement with equation 4.16, taking the limited range of pressure investigated here into account. In terms of linearised fluctuations, the measured intensity relates to the heat release of the flame and the pressure fluctuation at the flame location according to

$$\frac{I'_{OH^*}}{\overline{I}_{OH^*}} = \frac{\dot{Q}'}{\overline{\dot{Q}}} - 0.75\frac{p'}{\overline{p}} \, . \tag{4.19}$$

Considering this strong dependence, pressure fluctuations at the flame location should be minimised as far as possible by choosing the setup for measuring flame transfer functions accordingly. In the scope of this work, pressure fluctuations can be neglected for the generic TD1 burner, but not for the industrial burner.

4.3 Transfer Function Measurements

For the flame transfer function measurements, the CTA probe is mounted into the burner nozzle and the photomultiplier is located at the downstream window of the combustor with an unobstructed view on the flame. The axial position of the hot wire probe is the same for both generic and industrial burner - 22 mm upstream of the burner exit, see figures 3.6 and 3.7 for details. To avoid a damage of the delicate wire, the CTA probe is retracted into a protected parking position during ignition, shutdown and transient rig operation.

A signal conditioning unit and a PCI board with 8 sequentially scanned channels and 200 kHz total sampling frequency are used for data acquisition. Parallel to the CTA and photomultiplier voltages, a rectangular reference signal is recorded that is generated from pulses provided by the siren motor encoder and used to synchronise the individual signals with the excitation and to trigger the data acquisition. Before starting the FTF measurement, the calibration data of CTA and photomultiplier are stored in the data acquisition software for direct evaluation of the data acquired during the measurement process.

In detail, the recording and evaluation procedure at each excitation frequency is as follows:

1. Acquisition of 10000 samples of the reference, CTA and photomultiplier signals at a frequency of 10 kHz per channel, triggered by the reference signal.

2. Online Fast Fourier Transform (FFT) of all acquired signals with a resolution of 1 Hz.

3. Detection of the true excitation peak within $\pm$ 1 Hz around the nominal excitation frequency.

4. Evaluation of amplitude and phase of each signal at the detected true excitation frequency.[28]

[28] At this step, also the phase error induced by the sequential sampling of the data acquisition channels is corrected.

5. 100 repetitions of steps 1 to 4 and vector averaging of the signals to eliminate stochastical fluctuations.

6. Evaluation of the FTF amplitude as the ratio of normalised photomultiplier amplitude and normalised CTA amplitude as well as the FTF phase as the difference in phase between photomultiplier and CTA according to equation 2.4.

The frequency dependence of the FTF is evaluated from 10 to 400 Hz in discrete steps of 10 Hz. A constant excitation amplitude of $u'_B/\overline{u}_B = 5\%$ is usually maintained throughout the measurements to guarantee a sufficient distance to the background noise level on one hand and to avoid non-linearities expected at high excitation amplitudes on the other hand.[29] Occasionally, checks of the CTA and photomultiplier calibration have been performed after the FTF measurement, which exhibited no significant deviations.

4.4 High Speed Camera

Since the photomultiplier tube records the luminescence of the entire flame, the FTF results can be interpreted as the spatial average of the flame behaviour. To locally resolve the flame chemiluminescence, an intensified high speed camera equipped with the same type of interference filter as applied for the photomultiplier measurements has been employed. This camera observes the flame via the side window. Due to the large amount of collected data it is not generally applied, but used only for investigations of details of special interest.

Within the scope of this work, the camera is applied for two types of investigations:

- Stationary images without siren excitation are recorded to characterise the flames of the different setups and to determine flame lengths. For this task, the high speed device is used like a conventional camera without special triggering. Typically, 10 - 100

[29] For the industrial burner, an excitation amplitude of $u'_B/\overline{u}_B = 5\%$ could not be achieved. Typical values are in the range of 1 to 4%

individual images are averaged to obtain a meaningful flame characterisation. Examples for this type of image are found in sections 5.1, 6.1 and 7.1.

- Phase triggered images of the flame during a number of oscillation cycles are obtained while the camera recording cycle is locked to the siren excitation. These images allow a resolution of the detailed flame dynamics at some frequencies of interest. The detailed recording and evaluation procedure is given below, applications are found in section 5.3 and appendix A.

For all investigated cases, the sampling frequency of the camera is related to the actual excitation frequency by directly triggering the camera sensor with a second reference signal. This second signal has 16 times the excitation frequency and is generated from the same siren encoder signal as the original reference, thus providing the same phase relation - see figure 4.7. As the result of this procedure, 16 images are recorded per excitation period, independent of the excitation frequency. Also, errors from not perfectly synchronised frequencies of camera and siren are avoided. Since every 16^{th} image represents the same excitation phase angle, ensemble averaging to determine phase resolved flame images can be easily performed. The start trigger for the camera is - identically to the conventional data acquisition - supplied from the original reference signal.

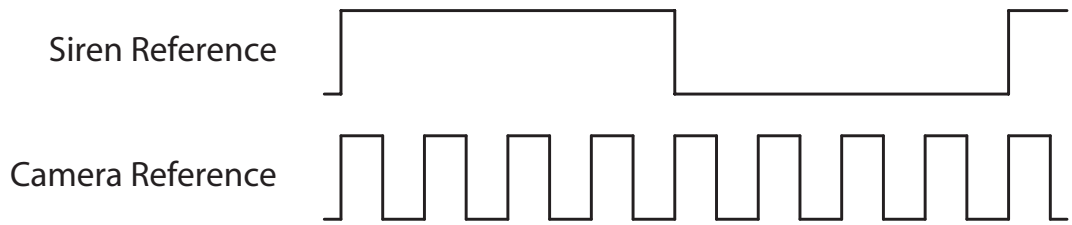

Figure 4.7: Scheme of the camera trigger signal.

For any operating point[30], 5 x 60 excitation periods or 4800 images are recorded together with reference, CTA and photomultiplier sig-

[30] An operating point in this contect denotes the usual operating conditions and one single excitation frequency.

nals. All images have been cropped to show only the lower half of the flame with the burner exit in the upper left corner and the upper rim being the combustor central axis. The image dimensions are also kept constant - 150 mm long and 70 mm high.

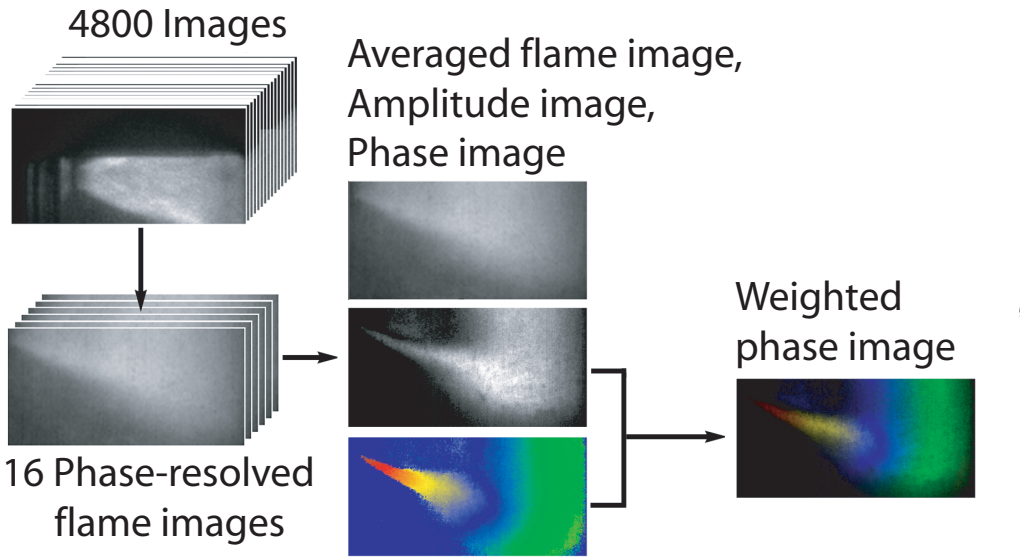

Figure 4.8: Camera image processing.

The further processing of these images is shown in figure 4.8. Cropping and ensemble averaging produces 16 phase resolved images. Applying a sine-fit for each pixel of those images similarly to the approach described in [Aue05] gives three results:

1. The average intensity value of the pixel.
2. The intensity amplitude of the pixel.
3. The phase difference between the respective pixel and the reference signal.

From these results, a locally resolved flame transfer function can be calculated for each pixel or for any arbitrary collection of pixels. Like for the global FTFs, the CTA signal serves as a reference, which is especially important for the phase. While the averaged image gives an impression of the general flame appearance and can be used to

derive the flame length, the amplitude image shows the regions of activity within the flame, with the brightness being proportional to the intensity oscillation amplitude. The corresponding phase image represents the respective pixel phase angles utilising a color code from red ($-\pi$) via yellow, blue (0) and green back to red ($+\pi$). For the sake of clarity, regions with a very low amplitude have been colored uniformly blue. Finally, weighted phase images are derived that show both results in one plot - the phase is encoded by the color-coding and the amplitude by the brightness.

5 FTFs of the Generic Burner - Pressure Influence

In this section, the flame of the generic TD1 burner is characterised and the measured flame transfer functions are presented. The FTFs are subsequently analysed and a scaling law is developed to describe their global behaviour with changing pressure and equivalence ratio.

5.1 Characterisation of the TD1 Burner

The TD1 flame has an almost conical form with an anchor point at the outer rim of the lance tip (see figures 3.6 and 5.1). In the downstream part beginning at a length of about one burner diameter, the flame cone widens to form the main reaction zone with the intensity maximum lying at a distance of about two burner diameters from the nozzle exit.

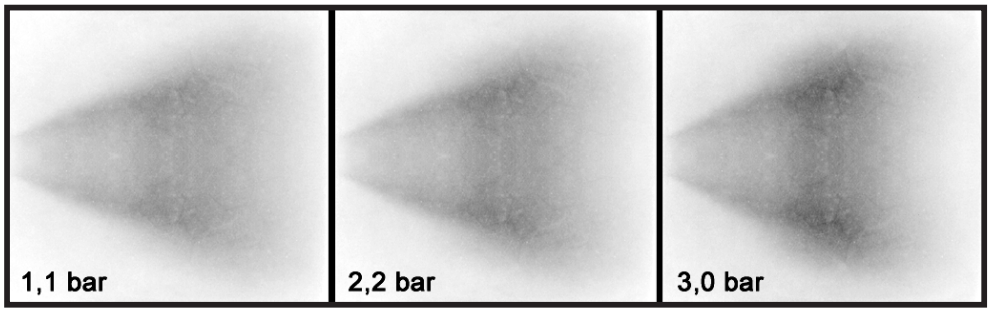

Figure 5.1: Averaged images of the stationary TD1 flame for different pressures at an air excess ratio of 1.4, TD1-P2 to TD1-P4. Burner located on the left side of the images, brightness inverted.

Stabilisation of the flame is achieved predominantly via the inner recirculation zone (IRZ) transporting hot product gas and highly reactive intermediate species back to the burner exit to constantly ignite the fresh mixture entering the combustor there. Vortex breakdown of the swirled mixture flow is responsible for forming this inner recirculation zone. The flame is stabilised in the shear layer between the IRZ and

the conical mixture flow into the combustor. Stabilisation starting also on the outer rim of the mixture flow is observed only for high flame temperature and at high pressure. Interestingly, this operating region is associated with high amplitude self excited combustion oscillations (see figure 5.5). The frequency of this instability lies at about 360 Hz and is linked to the axial $\lambda/2$ combustor mode.

5.1.1 Flame Length

In order to understand the measured flame transfer functions it is reasonable to first have a closer look on the flame appearance and its behaviour under varying operating conditions. Especially the flame length and its variation with pressure and equivalence ratio is an interesting parameter and thus analysed here in more detail.

In figure 5.2, the axial distributions of the flame intensity related to the images of figure 5.1 are shown.[31]

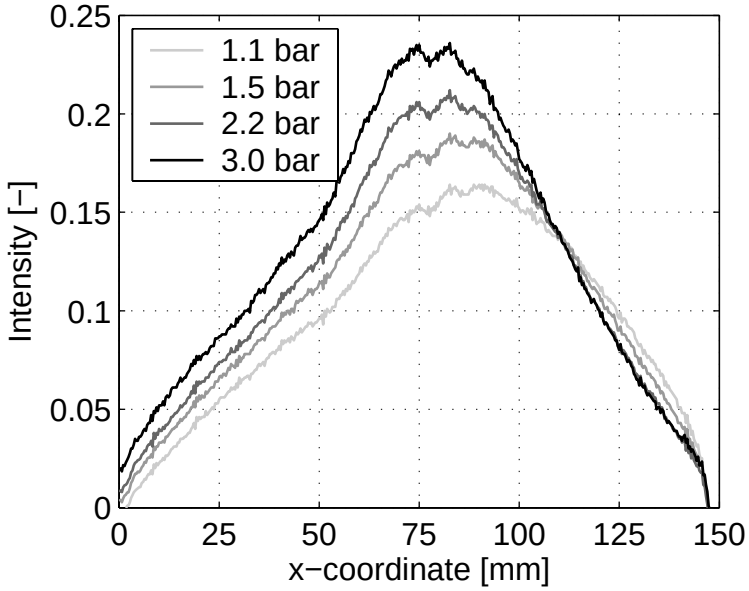

Figure 5.2: Axial distribution of the flame OH* intensity, TD1-P2 to TD1-P4.

[31] Additional stationary flame images have been recorded at 1.5 bar & $\lambda = 1.4$ and are also evaluated here.

These plots were derived from a pixel-based integration of the flame image along the lateral coordinate y according to

$$I(x) = I_i = \sum_{j=1}^{y_{max}} I_{ij} \ . \tag{5.1}$$

The plots reflect the appearance of the two flame regions from figure 5.1 - an almost linear intensity rise in the conical flame region close to the burner exit and an overproportional rise towards the maximum intensity in the main reaction zone further downstream.

Several definitions can be applied to characterise the flame length, two of them are of interest here:

- The axial location of the intensity maximum x_{OHmax} is determined by fitting a polynomial of high order to the respective plot of figure 5.2 and setting its first derivative to zero. A specific characteristic of this definition is that it focuses on the main reaction region and thus represents the dominant part of the flame.
- The axial location of the flame center of gravity x_{cg} is derived from a pixel-based integration of the flame image

$$x_{cg} = \frac{\sum_{i=1}^{x_{max}} \left(x_i \sum_{j=1}^{y_{max}} I_{ij} \right)}{\sum_{i=1}^{x_{max}} \sum_{j=1}^{y_{max}} I_{ij}} \ . \tag{5.2}$$

  This expression is useful since it accounts for the entire flame in contrast to only a specific region of the flame.

From both figures 5.1 and 5.2, a reduction of the flame length L_F with rising pressure becomes apparent. This length change is quantified in figure 5.3 using the center of gravity definition. For $\lambda = 1.4$, these points scale with pressure according to

$$L_F \mid_{\lambda=1.4} \ = \ x_{cg} \mid_{\lambda=1.4} \ \propto \ p^{-0.089} \ . \tag{5.3}$$

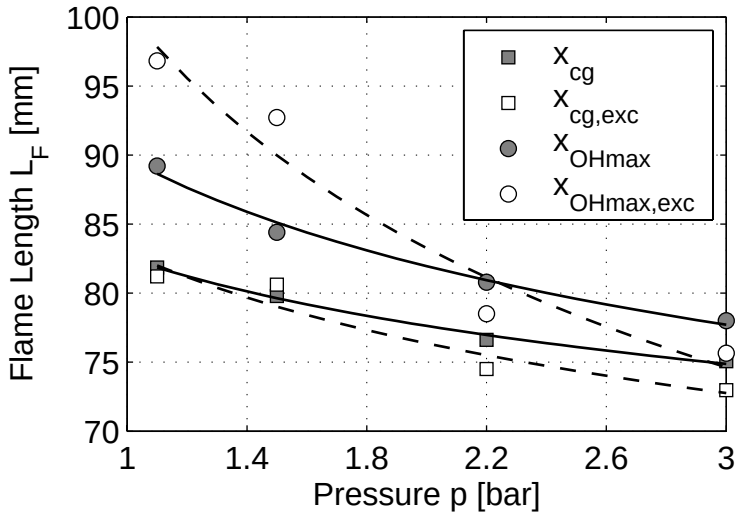

Figure 5.3: Pressure-dependence of the flame length, TD1-P2 to TD1-P4. Solid lines: without excitation, dashed lines: with excitation.

An analog evaluation of the images recorded for operating points TD1-P5 to TD1-P8 at $\lambda = 1.47$ gives a smaller pressure dependence.

$$L_F \mid_{\lambda=1.47} \; = \; x_{cg} \mid_{\lambda=1.47} \; \propto \; p^{-0.054} \tag{5.4}$$

Note that the pressure exponent of the flame length becomes larger when the siren excitation is applied[32], the values plotted in figure 5.3 are averaged over three different excitation frequencies.[33] The larger pressure gradient in the excitated case can be explained by a higher heat transfer to the combustor walls, as shown in section 5.1.2.

$$L_{F,exc} \mid_{\lambda=1.4} \; = \; x_{cg,exc} \mid_{\lambda=1.4} \; \propto \; p^{-0.119} \tag{5.5}$$

Also plotted in figure 5.3 is the variation of the maximum intensity location x_{OHmax} with pressure, with and without siren excitation.

$$\begin{aligned} L_{F,} \mid_{\lambda=1.4} \; &= \; x_{OHmax} \mid_{\lambda=1.4} \; \propto \; p^{-0.131} \\ L_{F,exc} \mid_{\lambda=1.4} \; &= \; x_{OHmax,exc} \mid_{\lambda=1.4} \; \propto \; p^{-0.270} \end{aligned} \tag{5.6}$$

[32] Excitation level $u'_B/\overline{u}_B = 5\%$

[33] Note also that L_F with siren excitation exhibits a larger scatter around the fitted trend. This can be explained by an additional dependence of L_F on the excitation frequency. Averaging over the three available individual frequency values seems to be not sufficient.

Here, the pressure gradient is larger than for the center of gravity, indicating that the main reaction zone shows a stronger response to pressure and the conical flame region remains almost constant. Note especially the strong response of x_{OHmax} to the siren excitation.

As a conclusion it can be stated that the scaling of the flame length with pressure does strongly depend on the definition of the flame length and also on the siren excitation. A leaner mixture does generally decrease the pressure dependence of the flame length.

5.1.2 Heat Loss

In this section, an estimate of the pressure influence on flame length is derived to explain the behaviour presented above. This can be achieved when considering L_F inversely proportional to the turbulent flame speed S_T - following [LB04] - and applying a model for S_T, for example after [Sch95]:

$$S_T = S_L + u'_{rms} \left(1 + \frac{1}{Da^2}\right)^{-\frac{1}{4}} . \tag{5.7}$$

Since turbulence parameters like L_T or u'_{rms} and the Damköhler number Da as the ratio of turbulent and chemical time scales do not scale with pressure

$$Da = \frac{\tau_T}{\tau_{Ch}} = \frac{L_T \, {S_L}^2}{u'_{rms} \, a} \approx \frac{L_T \, {S_L}^2}{u'_{rms} \, \nu} \sim \frac{p^0 \left(p^{-0.5}\right)^2}{p^0 \, p^{-1}} = p^0 , \tag{5.8}$$

the only influence on S_T and thus on the flame length is imposed by the laminar flame speed S_L that scales with $p^{-0.5}$ for the almost pure methane used as fuel[34] [Tur00]. The second term in equation 5.7 is usually dominant, allowing only a small influence of S_L. For an adiabatic methane flame, the length should thus increase slightly with

[34] Note that other fuels might have a different pressure dependence of the burning rate. According to a model of Turns [Tur00] and experimental data from Westbrook and Dryer [WD81], propane and other longer-chained hydrocarbons for example have a pressure exponent of S_L around -0.1.

pressure.[35]

On the other hand, the observed reduction in flame length becomes clear when the rather large thermal losses from the flame to the water-cooled combustor walls are accounted for. Since thermal power P_{th} scales with p^1, but the convective heat transfer $\dot{Q}_w$ only with approximately $p^{0.8}$ ($Re^{0.8}$), the relative heat loss $\dot{Q}_w/P_{th}$ to the walls decreases with increasing pressure. This heat loss to the walls has been measured quantitatively for the given operating points by evaluating the massflow of the combustor cooling water and the water temperature directly before and after the wall section facing the flame [Kon05, Lau05], the respective data points are given in figure 5.4.

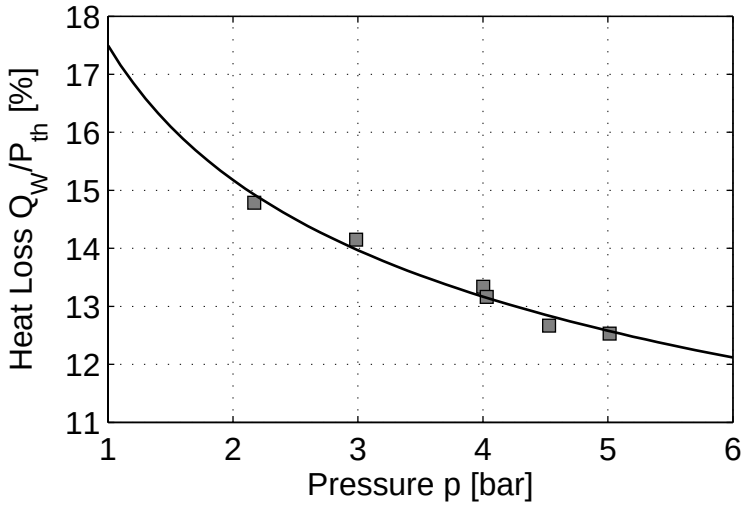

Figure 5.4: Heat loss of the TD1 flame to the combustor wall.

According to these data, the heat loss scales with $p^{-0.21}$, which is in very good agreement with Nusselt's theory of turbulent heat transfer. A simple energy balance gives the influence of this changing heat loss on the non-adiabatic flame temperature now rising with pressure. The heat loss has been modelled by reducing the heat release of the flame $\dot{Q}_F$ by the percentage of thermal power that is lost.

$$\frac{\dot{Q}_F}{H_u} = \frac{P_{th} - \dot{Q}_w}{P_{th}} \tag{5.9}$$

[35] Also other models lead to very similar results, as outlined in [PBP+03].

Equation 5.9 can now be applied to determine the actual flame temperature T_F, whose influence on laminar flame speed S_L is known [Tur00, Pet00]. An evaluation of equation 5.7 gives the turbulent flame speed S_T, which is considered inversely proportional to the flame length [LB04] and does thus deliver (calculated) values for L_F. The Damköhler number necessary for that step is derived from equation 5.8 with experimentally determined turbulence parameters L_T and u'_{rms} [Wäs05]. This procedure leads to flame length results that closely resemble the empirical scaling law of equation 5.3. The last two columns of table 4 demonstrate that agreement.

Table 4: Heat loss and flame length scaling with pressure, TD1-P2 to TD1-P4. L_F refers to x_{cg}, without siren excitation.

p $[bar]$	$\dot{Q}_w/P_{th}$ [%]	T_F $[K]$	S_L $[m/s]$	S_T $[m/s]$	$L_{F,\,calculated}$ [%]	$L_{F,\,measured}$ [%]
1.1	17.2	1704	0.163	2.31	100.0	100.0
2.2	14.9	1736	0.128	2.45	94.4	94.0
3.0	14.0	1749	0.114	2.52	91.8	91.5

Note that the downstream part of the flame, where the maximum intensity is located (see figure 5.1), lies closer to the walls and is thus stronger affected by the heat loss than the upstream conical part. This gives a good explanation for the stronger response of the maximum intensity location to pressure variations when compared to the flame center of gravity.

For the case with siren excitation, the heat transfer to the walls is enhanced and the flame temperature variation with pressure becomes larger. As a consequence, the variation of the flame length with pressure does also increase, as observed in figure 5.3.

5.1.3 Operating Range

Figure 5.5 gives an overview of the operating margins encountered with the TD1 burner at a relative pressure drop around 1 %. This

pressure drop lies well between the operating limits concerning flashback at low burner velocities and lean blow-off (LBO) at high velocities. At LBO, the high shear stress in the interaction region between the IRZ and the fresh mixture flow leads to quenching and the flame loses its anchoring position at the lance. A subsequent stabilisation of the flame at a position further downstream, where the burning velocity equals the flow velocity, was observed only occasionally and for a short time period. The relative pressure drop of 1 % corresponds to a mean-flow burner velocity of about 35 m/s and leaves sufficient velocity margins necessary for CTA and photomultiplier calibration prior to the FTF measurement.

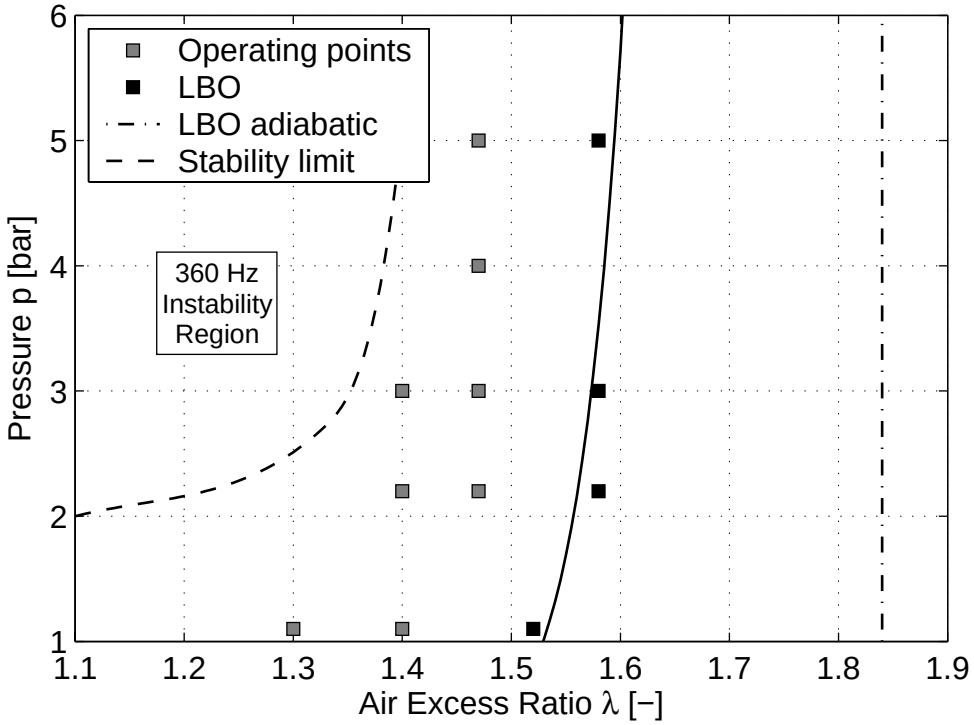

Figure 5.5: TD1 operating points with LBO and stability limits.

In order to achieve practical relevance, the operating points should lie at an air excess ratio well within the lean regime. A preliminary investigation was therefore performed to get an idea of the air excess ratio where lean blow-off occurs for the present system, the results are plotted in figure 5.5. A shift of the LBO air excess ratio towards leaner mixtures is observed for rising pressure. This appears unusual,

since the air excess ratio values are too low and no or only a very small pressure dependence of the LBO limit is commonly experienced. Nevertheless, the observed phenomenon can again be related to the thermal losses to the well cooled combustor walls. The same energy balance as used above for the flame length correlation can be employed to derive a power law for LBO with pressure that agrees with the measured data.

$$\lambda_{LBO} = 1.529\, p\,[bar]^{0.026} \tag{5.10}$$

The encountered LBO limits can thus be translated into a theoretical adiabatic LBO limit at $\lambda = 1.84$ ($\phi = 0.54$) that is independent of pressure. The associated adiabatic flame temperature $T_{F,ad}$ of 1630 K does now agree well with common experience.

For the above reasons, it seemed favourable to choose FTF operating points with about constant distance to the LBO limit, these are also plotted in figure 5.5. Two series of flame transfer functions have been measured, at an air excess ratio of 1.4 and 1.47, respectively, and from 1.1 to 5 bar. An overview of the operating points is given in table 2.

5.2 Flame Transfer Functions of the TD1 Burner

A single FTF at 1.1 bar and $\lambda = 1.3$ has been measured twice for a reproducibility check[36] with the result that reproducibility and quality of the measured transfer functions can be considered very good.

Figure 5.6 shows the flame transfer functions TD1-P2 to TD1-P4 measured at an air excess ratio of $\lambda = 1.4$ with pressure varying from 1.1 to 3 bar. Some properties typical for transfer functions in perfectly premixed mode can be detected in the plots:

- In the low frequency limit, the amplitude plot must approach a value of 1, this is required to fulfill the energy balance. In parallel, the phase plot approaches a value of 0. All dynamic processes occurring in the flame are much faster than the changes imposed

[36] See appendix B for details.

by the excitation and the system reacts in a quasi-steady manner.

- The amplitude plot shows one or more peaks typical for swirl burners and a decline towards high frequencies.
- A global decline in the phase plot is observed that stems from a global convective time delay between the velocity excitation of the mixture recorded within the burner nozzle and the flame response at a further downstream position.

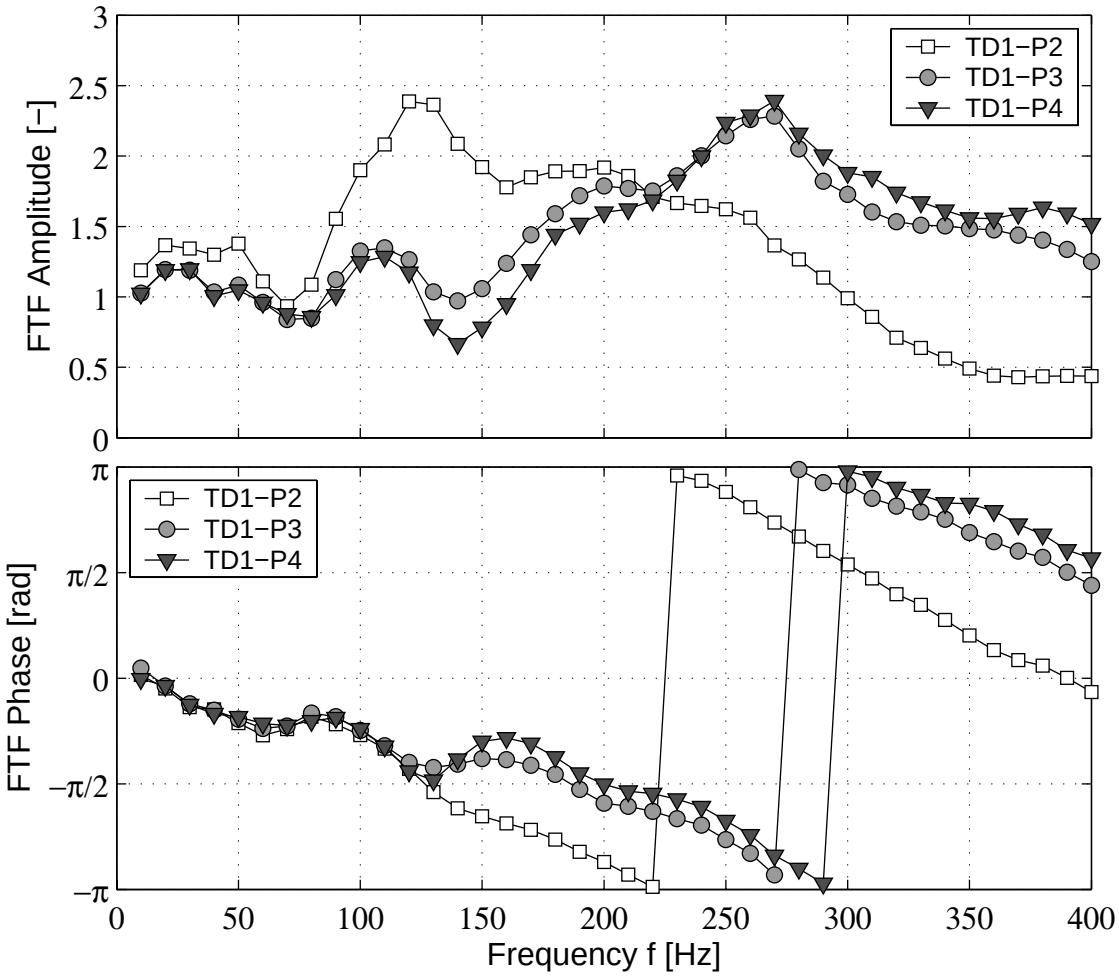

Figure 5.6: Amplitude and phase of the FTFs TD1-P2 to TD1-P4 at $\lambda = 1.40$.

The general appearance of the amplitude plot is similar for all three transfer functions with local peaks at about the same frequency. Nevertheless, there are also differences, especially in the magnitude of the

local peaks and in the high frequency behaviour. The second peak at 120 Hz is well developed for the lowest pressure of 1.1 bar, but decreases rather strongly for higher pressures. On the other hand, the expected low amplitudes for high frequencies above 300 Hz are found for 1.1 bar, but not for higher pressures. In this frequency region, the FTF amplitude increases with rising pressure. It can thus be stated that in addition to the local peaks appearing at the same frequency independent of pressure there is a broad global peak that shows a shift to higher frequencies with rising pressure.

A look at the related phases in figure 5.6 unveils some interesting results. As expected, the phases start at a value of 0 in the low frequency limit and also show the expected decrease with frequency. For all investigated pressures, the phases behave almost identical up to a limit frequency of 120 Hz, where a phase increase of the plots related to the higher pressures occurs. Only the phase of the 1.1 bar FTF continues to decline almost linearly, while the plots related to higher pressure exhibit an upwards oriented deviation from linearity, whose magnitude rises with pressure and leads to a relative phase difference of almost $\pi/2$ between the plots for 1.1 and 3 bar at 160 Hz. Above that frequency, the "normal" behaviour of an almost linear decrease can be observed for all pressures, with a slight tendency towards steeper slopes for lower pressures. This slope difference is in line with the decreasing flame length upon rising pressure and can be explained by the smaller convective time delay from the hot wire location to the dominant zone of reaction within the flame.

Prior to the separation point of the phases at 120 Hz, another phase increase appears between 60 and 90 Hz. Interestingly, this deviation from a constant gradient does not lead to a pressure dependent behaviour. Also interesting is that both deviations lie at a frequency where the amplitude plot shows a minimum.

When considering Rayleigh's criterion for instability [Str78], the observed phase deviation leading to large phase differences at elevated frequencies induces a change of behaviour with rising pressure that can dramatically influence the stability of combustors, either turning a stable system unstable or vice versa. Should the phase difference

reach a value of π, an inversion of the stability behaviour is not only possible, but inevitable. Note that this does not necessarily mean that self-excited pulsations will actually occur for a once stable system, since Rayleigh's criterion is necessary for instability, but not sufficient. One point also interesting here is that transfer function amplitudes larger than 1 occur for high pressures in this frequency region - acoustical fluctuations are amplified - which promote rather than avoid instability.

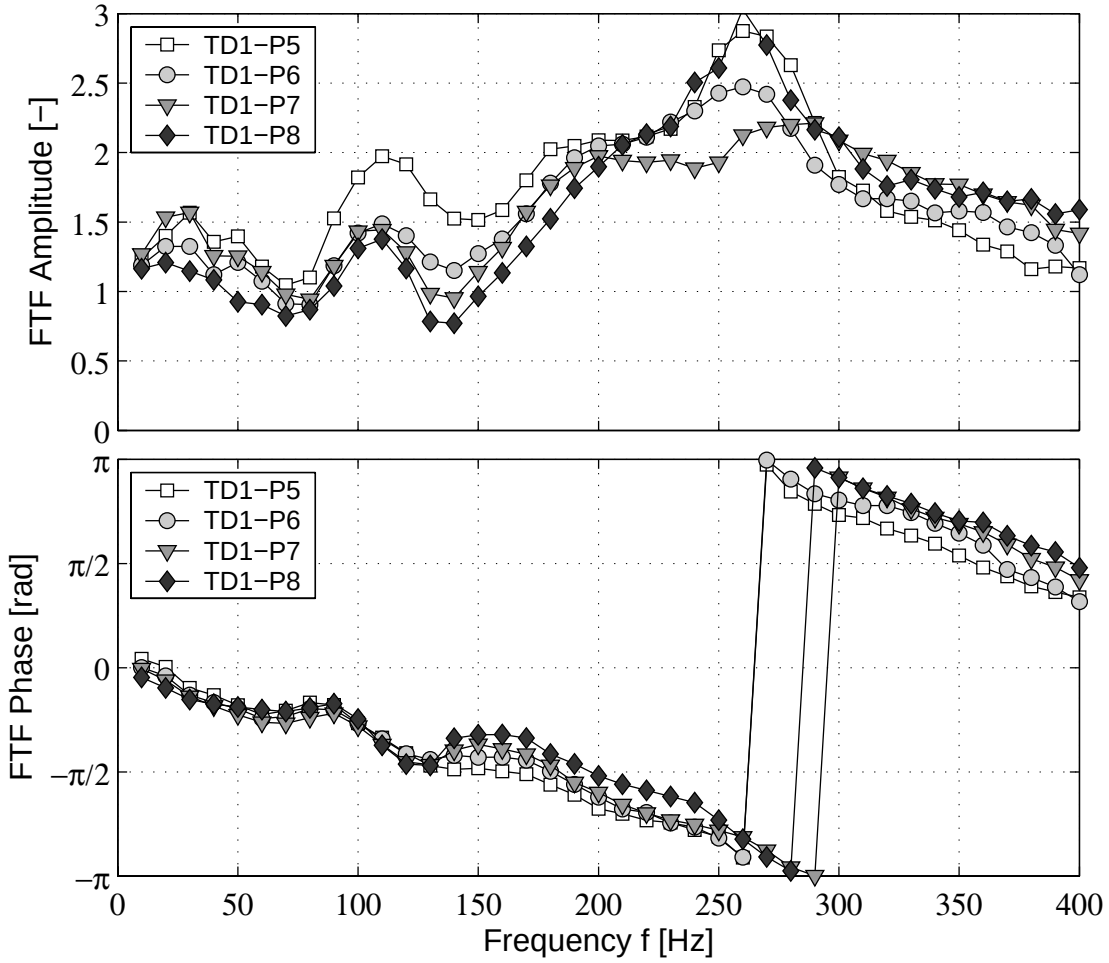

Figure 5.7: Amplitude and phase of the FTFs TD1-P5 to TD1-P8 at $\lambda = 1.47$.

For the present configuration of the rig, such an instability does indeed occur, as seen in the operating map of figure 5.5. The reduced FTF phase values and the increasing amplitude observed around 360 Hz for rising pressure and equivalence ratio move the system across a stability

limit with the result that a large amplitude self-excited combustion oscillation emerges. This behaviour has been confirmed by an acoustic low order model of the rig that is using the measured flame transfer functions as input [Föl06], [FFS06].

The amplitude and phase results for the operating points with a leaner mixture of $\lambda = 1.47$ are presented in figure 5.7. No qualitative change with respect to $\lambda = 1.4$ is observed in both amplitude and phase plots. Again, a tendency towards lower amplitudes for low frequencies and higher amplitudes above 300 Hz can be found with rising pressure. The conclusion is also the same - a global amplitude peak shifting to higher frequencies with rising pressure.

When comparing the phase plots for identical pressures at both air excess ratios above 120 Hz, a tendency towards more distinct phase deviations can be found for the richer mixture. This is an indication that not only the pressure, but also the equivalence ratio has an influence on the phase behaviour at high frequencies. However, the separation frequency of 120 Hz is unchanged, as is the frequency of the first phase deviation without separation at 60 Hz. Generally, the pressure-dependency tends to decrease for the higher air excess ratio and the phases show a slightly steeper decline that can be related to an increased flame length for the leaner mixture.

5.3 Heat Release Distribution

The flame transfer functions of the generic TD1 burner presented in section 5.2 have shown that a global description of the FTF behaviour - especially the phase plot - is not sufficient, since it can not capture local deviations like the pressure-dependent phase deviation at 120 Hz. Models derived in section 8 can reproduce these local deviations, but they deliver smooth changes with operating conditions and can not explain the observed behaviour of identical phase plots up to 120 Hz for all investigated conditions and the subsequent sudden separation of the plots above that limit frequency. Obviously, additional flame dynamics effects exist that are not captured by the modelling efforts.

In this section, the above effect is adressed by spatially resolving the flame dynamics using high speed camera images. The post-processing procedure of these images is described in section 4.4.

5.3.1 FTF Behaviour at the Pressure-Dependent Phase Deviation

Two questions arise from the pressure-dependent phase deviation at 120Hz, as presented in figures 5.6 and 5.7:

1. What is the reason for the phase deviation to occur?
2. Why does this behaviour depend on pressure?

One information important for understanding that phase deviation can be extracted from the raw data of the FTF measurement. When investigating the original phases of CTA and photomultiplier signal as shown in figure 5.8, it becomes clear that, for a given frequency, the CTA phase shows almost no change with pressure, but the photomultiplier does.[37] This means that the reason for the pressure dependence of the phase must lie in the OH*-chemiluminescence signal and thus in the heat release response of the flame. For that reason, high-speed camera images have been recorded in the frequency regime around the phase deviation and evaluated to obtain more detailed information.

Figure 5.9 shows amplitude and phase images as described in section 4.4 recorded for operating points TD1-P2 and TD1-P4 with 1.1 and 3 bar pressure, both at an air excess ratio of $\lambda = 1.4$. Also plotted are the weighted phase images that combine both informations into one image. In order to reveal the effects that lead to the pressure dependency of the phase deviation, the excitation frequency has been set to 120 Hz in one case, where the phases are almost identical, and 160 Hz in the other case, where the maximum deviation is observed. Note that with amplitude and phase images (together with the averaged

[37] Note that both CTA and photomultiplier signals exhibit a "bulge" at the frequency of interest and not a monotonic decline. This behaviour is not unusual, it is observed several times in the measured frequency range.

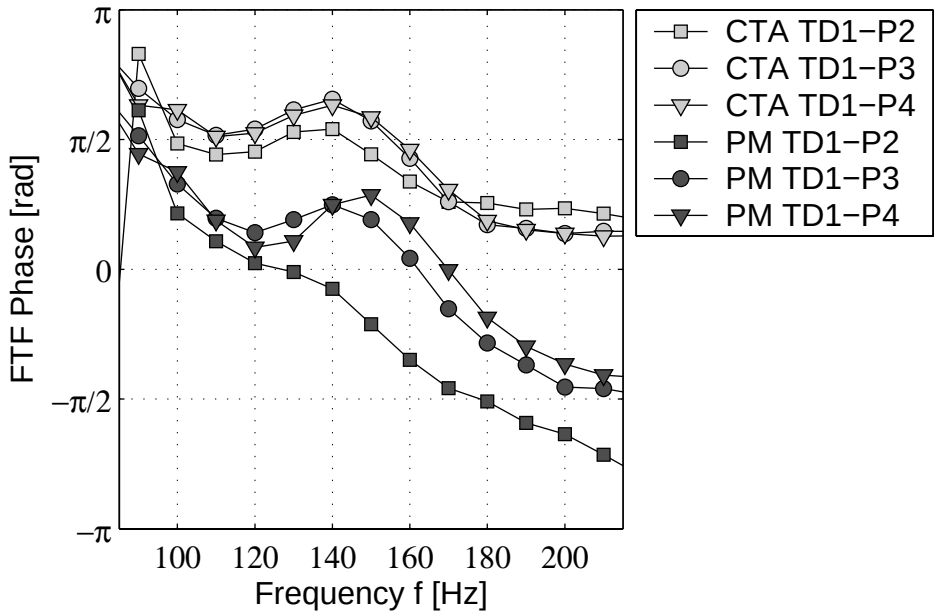

Figure 5.8: Phases of CTA and photomultiplier signals at operating points TD1-P2 to TD1-P4.

pixel values), a FTF can be determined for any pixel in the image or for any region of connected pixels within the image[38].

In the amplitude image, two active regions can be identified within the flame that include almost the complete flame activity - a "far field" in the right - downstream - part distributed almost evenly over the combustor radius (marked with a red circle) and a "near field" conically extending from the burner exit and having its maximum near the middle of the images (marked in blue). In order to answer the two questions stated above, the behaviour of these two regions with changing pressure and frequency is discussed below.

Far field: The far field region is large and strong at 120 Hz for both pressures and disappears almost completely at 160 Hz. For the higher pressure, this region shifts slightly towards the burner exit. An important finding is that the phase value associated with the far field region does not change with rising pressure.

[38] To obtain a FTF for a group of pixels, the vector average of the individual pixel data - intensity amplitude and phase - needs to be obtained. A separate averaging of amplitude and phase data would lead to erroneous results.

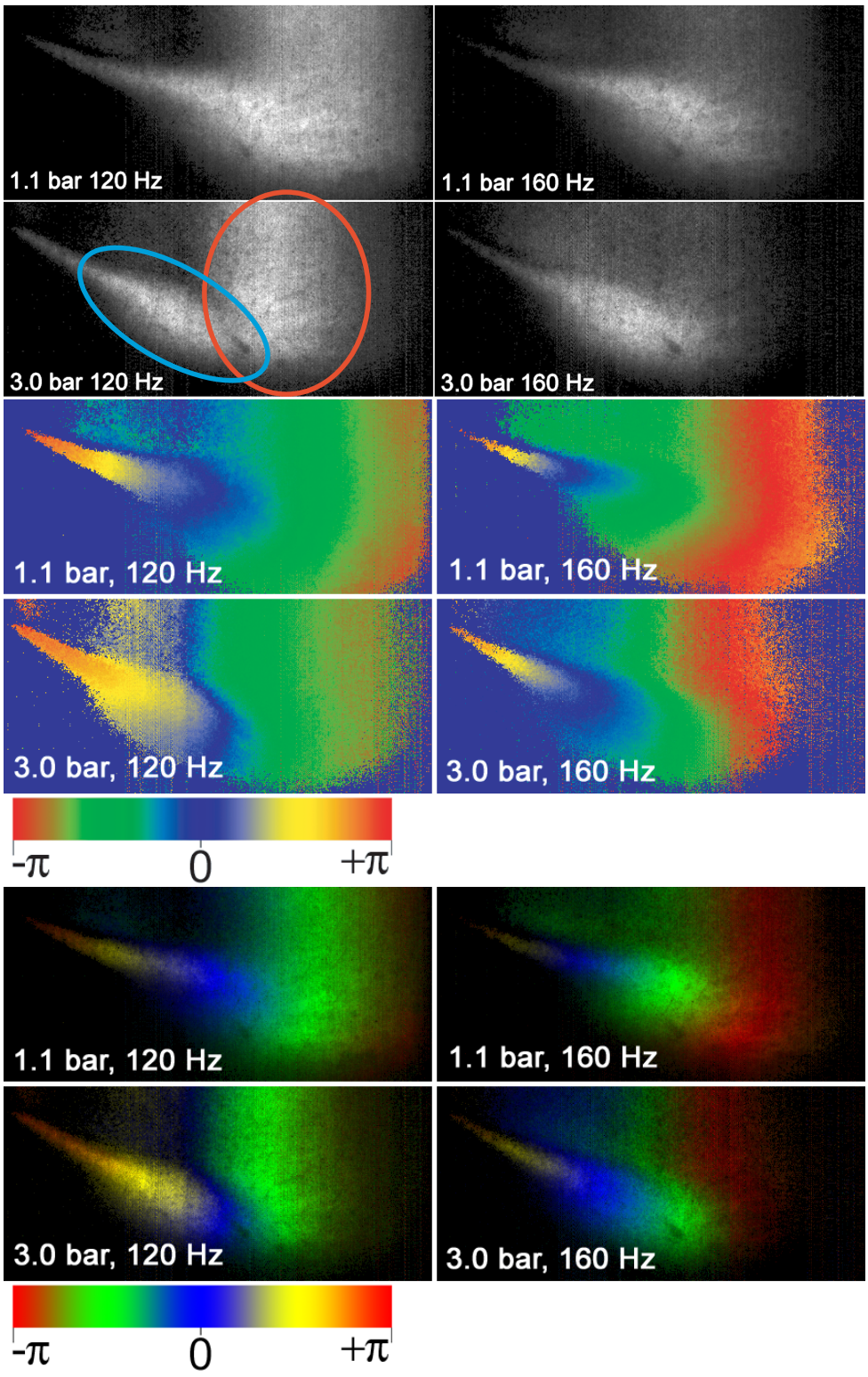

Figure 5.9: Amplitude (above), phase (middle) and weighted phase (below) images for operating points TD1-P2 and TD1-P4 at $\lambda = 1.4$.

Near field: A closer look unveils the different behaviour found for the near field. This region becomes slightly stronger with rising pressure and shows a distinct upstream shift towards the burner exit that results in a clear separation of the two regions for 3 bar, while they are partially overlapping for 1.1 bar. More important, as the activity region moves upstream, also the phase values associated with the activity region change. Unlike the far field region, the near field does not disappear for 160 Hz and begins to dominate instead. The upstream shift with pressure is also clearly visible for 160 Hz. Another interesting fact is that for 120 Hz the near field region oscillates with opposite phase to the far field, which implies that changes of relative strength of both do only affect the amplitude, but not the phase angle of the total signal.

These observations can now explain the frequency- and pressure behaviour at frequencies near the phase deviation.

120 Hz: At 120 Hz and low pressure, the far field region is dominating over the near field, thus also dominating the FTF phase. Although the near field becomes stronger with rising pressure, the far field remains dominant even for 3 bar, thus fixing the phase to a value that is independent of pressure. Due to the opposite phase of the near field its stronger contribution should reduce the amplitude of the FTF for rising pressure. The FTF amplitude plots in figure 5.6 do indeed confirm this behaviour.

160 Hz: For 160 Hz, the far field region disappears and only the near field remains. At low pressure, this has no major effect on the phase, since the active region of the near field is located at nearly the same axial position where the far field has been previously. Note that the shift in phase color within the active region from green ($-\pi/2$) to green/red ($-3\pi/4$) for increasing frequency is due to the "normal" phase decline generated by the convective time delay. At high pressure, the disappearance of the far field region for 160 Hz generates a major upstream shift of the activity maximum. Thus, other phase values are now associated with the activity region that correspond to a smaller convective time delay from the burner exit and thus also smaller phase differences between the velocity and OH* signals. The

result is the observed deviation in the FTF phase plots towards values around $-\pi/4$.

For the analysed frequencies around the phase deviation the phase behaviour has been demonstrated to depend on the interaction of the two activity regions and, most importantly, on the sudden disappearance of the far field. One question is now if this also holds for all other frequencies. An observation supporting this assumption is that the phase plots keep their pressure-independent behaviour below 120 Hz and their different slopes above 160 Hz. This indicates that the far field region can be found for other frequencies below 120 Hz and will not appear above 160 Hz. Further high speed camera series have been recorded[39] to answer this question and the corresponding amplitude plots are shown in figure 5.10. In these images, the far field region indeed can be found at 20 and 80 Hz, but not at 160 and 320 Hz.

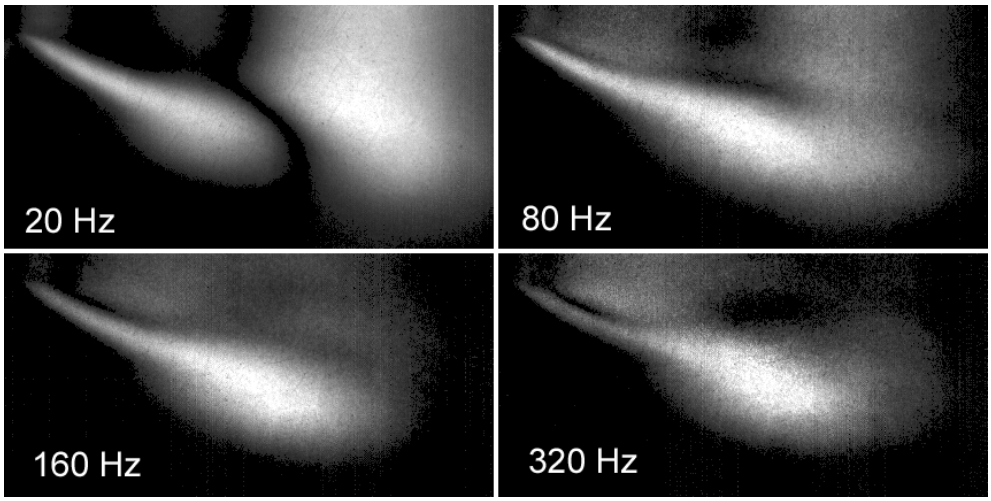

Figure 5.10: Amplitude images for for different frequencies, operating point TD1-P6 at 3 bar and $\lambda = 1.47$.

Interestingly, the relative strength of near and far field depends on the excitation frequency. The image at 80 Hz in figure 5.10 - unlike the images for 20 Hz in figure 5.10 and 120 Hz in figure 5.9 - shows that the far field is not well established and the near field is the dominating reaction zone with a location of the intensity maximum closer to the

[39] This time for the higher air excess ratio of 1.47

burner exit. From figure 5.9 one would then conclude that a larger FTF phase value should be determined at this frequency, which indeed can be seen in form of a bulge in the FTF phase plot. This confirms that the phase behaviour of the flame transfer function does for all pressures and frequencies mainly depend on the axial location of the dominant region of activity within the flame and the phase value at this location. The influence of parameters like pressure and burner temperature & velocity then reduces to their influence on location and strength of the regions of highest activity.

5.3.2 Origin of the Pressure-Dependent Phase Deviation

After the phenomenological description in the previous section, the origin of the far field activity region and the pressure-dependent phase deviation is discussed here.

5.3.2.1 Flame Length Fluctuation

Consider the left half of figure 5.11, where two averaged flame images and the corresponding flame envelopes[40] at the phase angle of the maximum and minimum OH*-chemiluminescence intensity have been plotted. The respective excitation frequency is 20 Hz - and associated with a strong far field region. At that low frequency, the oscillation period is much larger than the convection time through the flame - the flow field & the flame appearance are quasi-stationary and all locations within the flame oscillate at about the same phase angle. Also, the phase difference of the flame intensity with respect to the CTA reference signal - the FTF phase - is close to zero. As clearly seen in the images, the large flow velocity at the intensity maximum causes a large flame length, and vice versa for the intensity minimum. The combination of the two flame envelopes also shown in figure 5.11 points out an area in the rear part of the flame that has been shaded light grey. Since this area does closely resemble the appearance of the far field region seen in the previous figures, it can be concluded that the far field activity region originates from a length fluctuation

[40] The flame envelope is a line of constant intensity in the flame image that separates the (visible) reaction region from the non-reacting environment.

of the flame.[41] This finding is supported by the respective phase plot also shown in figure 5.11, which points out that the far field region oscillates at the global phase angle of the flame transfer function.

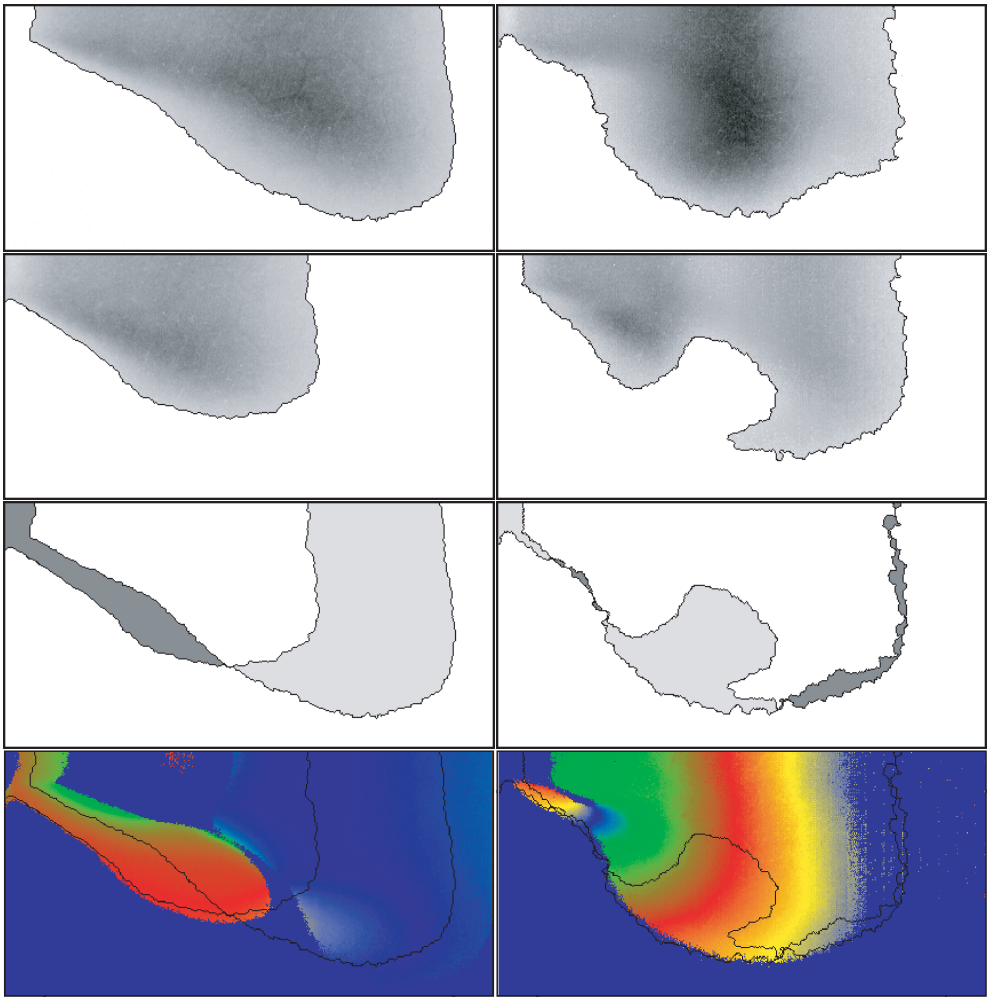

Figure 5.11: Flame images and flame envelope under excitation for 20 Hz (left) and 320 Hz (right), brightness inverted. First row: averaged flame image at phase angle of maximum OH* intensity, second row: averaged flame image at phase angle of minimum OH* intensity, third row: combination, fourth row: corresponding phases. Operating point TD1-P6, excitation amplitude 22% (left) and 27% (right).

[41] Note that the images of figure 5.11 have been recorded at a high excitation amplitude of >20% to clearly visualise the effect. However, a lower excitation level does only change the intensity fluctuation amplitude, but not the overall appearance. This is shown in more detail in appendix A.

Also seen in the combination of the flame envelopes is an area shaded dark grey in the conical near field region. This area is cleared for the phase of the highest flow velocity & flame intensity, which results from a downstream shift of the flame anchoring point at the lance and a slightly lower cone angle. Since the maximum intensity amplitude in this area occurs at the phase of the global intensity minimum, it shows a red color in the phase plot that represents a phase angle shifted by 180° with respect to the far field activity region. Note that this 180° offset is independent of the excitation frequency. For other frequencies, the phase values might change, but the 180° offset between near and far field remains. That effect can be observed in the 120 Hz plot of figure 5.9 for example.

Since the dark grey area in the left half of figure 5.11 is much smaller than the light grey far field, the latter is dominating the global FTF behaviour. Due to the 180° phase offset the global phase angle is not altered by the dark grey activity region, only the FTF amplitude is reduced.

From the above findings it can be concluded that any displacement of the flame or any change in flame shape caused by the acoustic excitation produces regions of activity in the intensity amplitude images, with every single region tending to have a uniform phase angle. The far field activity region is the most prominent one of those, having its origin in a fluctuation of the flame length.

5.3.2.2 Convective Velocity Perturbations

Now consider the plots on the right half of figure 5.11. These have been recorded at a frequency of 320 Hz, where the near field activity region is dominant and the far field has disappeared. The behaviour observed here represents the “classical” flame response as it is understood by many researchers. The acoustic field within the combustion system leads to velocity perturbations at the burner exit that are convected through the flame along the mean flowfield. These perturbations can consist of fluctuations of axial velocity, radial velocity and/or swirl circulation. On its path along the flame front, the velocity perturbation modulates the heat release either directly via fluctuating turbulence

parameters [SBG+04] or indirectly via the induction of secondary velocities by a fluctuating vorticity [HSP+05] as introduced in section 2.3. Due to the low convection velocity, different regions of the flame oscillate at different phase angles, while the phase changes gradually towards more negative values along the convection path. The location of the activity maximum is basically defined by the location of the global flame intensity maximum, and the phase value at this point represents the global flame behaviour. Thus, a linear phase decline over frequency is encountered for a fixed position of the activity maximum.

Like for the 20 Hz case, also at 320 Hz a high excitation amplitude has been chosen for a clear visualisation of the effects.[42] Especially the gradual phase change as a result of the convective transport of the velocity perturbations can be clearly identified in the phase plot. Note also that despite of the high excitation amplitude the flame length remains about constant. The heat release activity is located close to the region of the flame intensity maximum instead and appears as a true intensity fluctuation together with a radial fluctuation of the flame front due to coherent vortex formation at this high amplitude.

5.3.2.3 Superposition

A superposition of the flame length fluctuation and the conventional convective velocity perturbations gives the results observed in figure 5.9 for a siren excitation frequency of 120 Hz. In the downstream flame region, the far field caused by the flame length fluctuation is strong and can be easily distinguished from the conical near field.

In the upstream flame region extending from the burner exit to the location of highest intensity, a superposition of the activity regions related to the convective velocity perturbation[43] and the flame length fluctuation[44] result in a complex amplitude and phase behaviour. Furthermore, fluctuations of the radial extension of the flame front in the region close to the burner[45] lead to a radial variation of the phase

[42] Unlike the 20 Hz case, the excitation amplitude does have an additional effect here (see also appendix A) - a rising amplitude increases the radial and decreases the axial extension of the activity region. However, this phenomenon does not affect the above findings.

[43] See section 5.3.2.2.

[44] See section 5.3.2.1, referring to the dark grey area in the left half of figure 5.11

[45] These are especially strong for excitation frequencies that lead to a strong fluctuation of the

values.

All these effects contribute to a complex phase behaviour in the region close to the burner exit. Note that already Kunze [Kun04] observed strong deviations from the global FTF phase at locations close to the burner when performing axially resolved FTF measurements for a very similar burner. However, his explanation of this behaviour based on long time delays in the outer recirculation zone seems outdated in the light of the observations presented here.

5.3.3 Conclusions

With the findings of section 5.3.2, the origin of the pressure-dependent phase deviation becomes clearer. Up to the limit frequency of 120 Hz, the FTF behaviour is governed by a superposition of the flame length fluctuation and the conventional convective transport of perturbations from the burner, with the former being the dominant mechanism. Since that mode is rather insensitive to flame length variations induced by the operating conditions, the phase plots of the measured FTFs are almost identical. As soon as the flame length fluctuation disappears and the convective transport of perturbations becomes dominant at and above 120 Hz, the FTF phases are controlled by the flame length that is in turn sensitive to the operating conditions. As a result of that change, the phase plots exhibit a distinct deviation from linearity depending on pressure and equivalence ratio.

The above findings do also have some implications concerning the scaling of flame transfer functions. Only in the case of negligible sensitivity of the active zones - near and far field, driven by the mechanisms described above - to operating parameters like pressure there is no influence of those parameters on the transfer function. An example for such a behaviour in this study is the negligible pressure dependence of the FTF phase plots up to a frequency of 120 Hz.

A more complex case is that the activity pattern is not constant, but self-similar. In that case, global scaling laws for operating parameters

swirl number and thus of the flow angle upon exit from the burner.

can be applied as postulated by Lohrmann [LB04]. Self-similarity in this context means that one unique pattern can be generated by applying geometrical or intensity scaling. An example for this case in the current study is the FTF phase slope scaling with pressure for frequencies above 160 Hz. As only one region of activity exists in this frequency regime, the slope change is clearly attributed to the observed upstream shift.

However, as soon as the activity pattern changes qualitatively, self-similarity is lost and global scaling laws will fail, as demonstrated here for the phase deviation at 120 Hz depending on the operating parameters. These findings do not only apply to pressure scaling, but to any operating parameter influencing the flame activity pattern.

5.4 Pressure Scaling

In this section, a scaling law is developed to quantify the changes with pressure observed in the FTF plots. For that investigation, the focus lies on the phase, the amplitude behaviour is not considered. Of main interest is the phase gradient changing with pressure and the question whether this change can be correlated with the flame length as derived in section 5.1. Also, the air excess ratio is considered, but it is of minor interest due to the rather small variation of λ in the tests.

A simple fit is applied to quantify the time delay leading to the global phase gradient of the FTF. For that purpose, the FTF phase decline is approximated by a least squares-fit of a straight line starting at the origin of the phase plot - see figure 5.12. This model represents a constant time delay τ_G between flame and excitationthat is given by the FTF phase gradient

$$\tau_G = -\frac{1}{2\,\pi}\frac{\partial\varphi}{\partial f} \quad . \tag{5.11}$$

Note that this model delivers a first order approximation - the global phase behaviour over frequency - and can not account for local deviations. As seen in figure 5.12, the phase plot lies above the line for low

frequencies and crosses to the lower side for high frequencies[46]. That trend occurs for all FTFs measured and indicates that even the global phase behaviour is not linear in the investigated frequency range - a point that will be reconsidered in section 8.1.2.

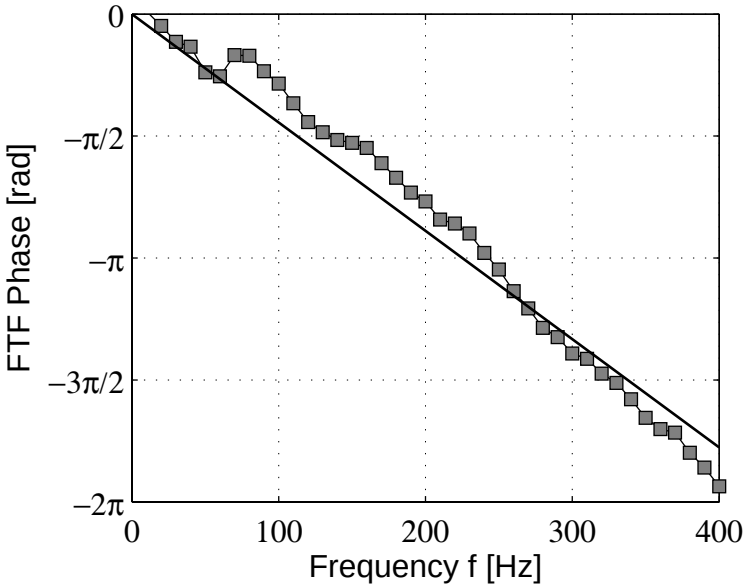

Figure 5.12: FTF phase at TD1-P1 with the phase decline approximated by a simple global time delay model.

The least-squares fit time delay from the phase plot has been evaluated for all recorded TD1 FTFs, the results are plotted in figure 5.13. From that figure can be seen that the changes of the time delay become smaller when proceeding towards higher pressure and that the decline is almost linear, when plotted in a double-logarithmic diagram. Taking this into account, a power law of the form

$$\tau_G(p) = a_\tau \, p^{-b_\tau} \quad \text{with} \quad 0 < b_\tau < 1 \tag{5.12}$$

has been found to provide the best fit for the measured points.[47] This is an encouraging result pointing out that in order to identify the time delay at realistic engine pressures of up to 35 bar, one does not necessarily have to reach that pressure in dynamic combustion tests,

[46] This behaviour can also be found in the work of other researchers, e.g. in figure 11 of [LB04].
[47] The values of a_τ and b_τ are given in table 5.

but only approach it up to a sufficiently small factor. Due to the degressive nature of the power law (negative exponent), the largest part of the time delay reduction takes place in the lower range of the pressure scale. Taking the data at $\lambda = 1.47$ as example, the time delay between 1 and 35 bar reduces from 100% to 55%. At 10 bar, the time delay has already dropped to 68% - a coverage of less than 30% of the pressure range gives more than 70% of the time delay reduction to be expected at the full operating pressure.

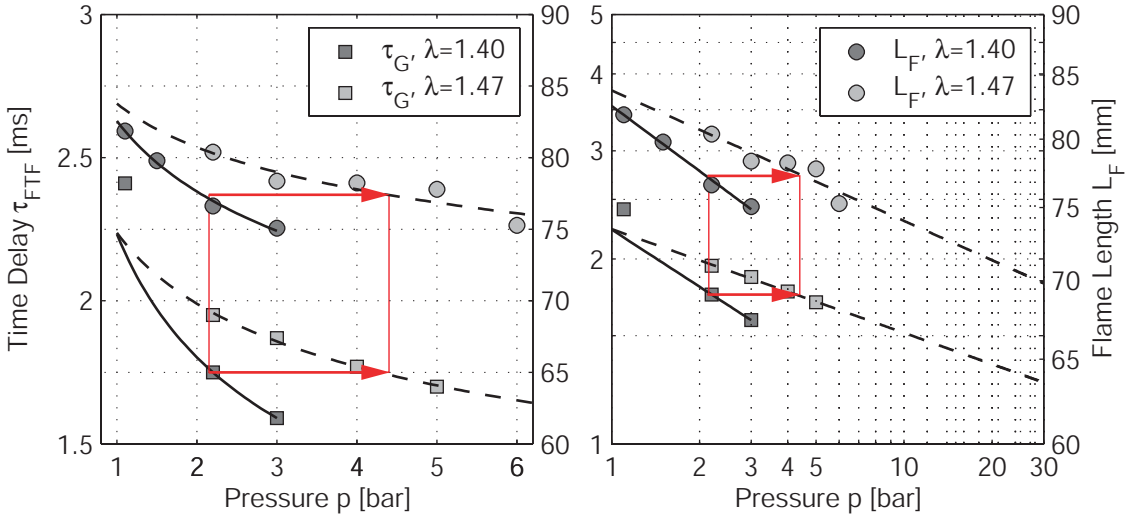

Figure 5.13: Global time delay from FTF phases and flame length over pressure. Left: linear plot, right: log/log plot. TD1-P2 to TD1-P8. Data points of table 6, power law fits according to equations 5.12 and 5.13, fit parameters of table 5.

The power functions for both measurement series at $\lambda = 1.4$ and $\lambda = 1.47$ resulting from a least-square fit of the evaluated points have also been plotted in figure 5.13.[48] Generally, the observed behaviour meets the expectations derived from the stationary investigation in section 5.1. Rising pressure reduces the relative heat loss to the walls, increases the flame speed and does thus also lead to a reduced flame length and a lower time delay in the transfer function. The explanation concerning the air excess ratio is straightforward - a leaner mixture

[48] Note that the point at TD1-P2 has been plotted, but not included into the power law fit. This point is considered questionable due to the large deviation of the FTF amplitude plot (figure 5.6) when compared to the other operating points. This behaviour will be reassessed in section 8.1.3, figure 8.7.

results in a reduced flame speed and a rising time delay. An interesting observation is the strong influence of the air excess ratio - an increase of 5% from 1.4 to 1.47 at 3 bar leads to a time delay increase of 17.6%. Even more interesting is the circumstance that these differences grow larger with rising pressure and decreasing time delays, which is caused by the different exponents b.

It is now interesting to see if the global time delay scales with the flame length, as it is often assumed (e.g. [LB04]). For that purpose, the stationary flame length results determined using x_{cg} of equation 5.2 have been plotted into figure 5.13. In analogy to equation 5.12, also the flame length L_F can be expressed in terms of a power law.[49]

$$L_F(p) = a_{L_F}\, p^{-b_{L_F}} \quad \text{with} \quad 0 < b_{L_F} < 1 \tag{5.13}$$

As seen in figure 5.13, the trends of time delay and flame length with pressure do indeed correlate very well. Also, the behaviour of τ_G and L_F with changing air excess ratio is very similar. These similarities are demonstrated by the red arrows drawn into both figures - the same flame length results in the same time delay, independent of pressure or air excess ratio.

As found in section 5.1.1, a whole range of pressure gradients of the flame length exists, depending on the definition applied and on the amplitude of the acoustic excitation. Interestingly, the variation of the location of the maximum flame intensity x_{OHmax} with siren excitation exhibits a pressure exponent that is almost identical to the exponent of the global FTF time delay τ_G.[50] In other words, τ_G scales almost proportionally with x_{OHmax}. On the other hand, the pressure dependence of the flame length using the center of gravity definition is much smaller - regardless of the siren excitation level. This leads to the conclusion that x_{OHmax} is the best suited parameter when it comes to correlating flame lengths and flame transfer function features - which is consistent with the finding of section 5.3.1: The global FTF phase behaviour is coupled to the dominant flame activity region.

[49] As for the time delay, the exponents a_{L_F} and b_{L_F} are given in table 5. Note that b_{L_F} can also be found in equations 5.3 and 5.4.

[50] See figure 5.3 and compare the exponent of equation 5.6 (with excitation) to table 5.

The good correlation of the global FTF time delay and the flame length indicated by the red arrows in figure 5.13 can now be utilised to derive a relation between the two parameters. Such a relation could be useful to determine the global time delay from an averaged stationary flame image recorded at high operating pressures, where a full flame transfer function measurement might become very difficult.

Before relating τ_G and L_F, the influence of the mixture fraction on the two parameters is included in the scaling laws, so that only one equation is sufficient to describe the behaviour with varying p and λ.

The influence of λ is accounted for by a linear variation in the exponent of the pressure scaling law of equations 5.12 and 5.13. This procedure does per definition give the same pressure exponents as found for the former equations.

$$\tau_G(p,\lambda) \;=\; d_{a,\tau}\, p^{-d_{b,\tau}-k_{b,\tau}\lambda} \tag{5.14}$$

$$L_F(p,\lambda) \;=\; d_{a,L_F}\, p^{-d_{b,L_F}-k_{b,L_F}\lambda} \tag{5.15}$$

In that formulation, d_a, d_b and k_b are now the empirical fit parameters to match the measured data points, as compared to a and b before. The coefficients d_b and k_b for both τ_G and L_F can be determined from the two exponents b of equations 5.12 and 5.13 at $\lambda = 1.4$ and $\lambda = 1.47$.

$$\begin{aligned} -b_\tau \,|_{\lambda=1.4} &= -d_{b,\tau} - k_{b,\tau}\lambda \\ -b_\tau \,|_{\lambda=1.47} &= -d_{b,\tau} - k_{b,\tau}\lambda \end{aligned} \tag{5.16}$$

$$\begin{aligned} -b_{L_F} \,|_{\lambda=1.4} &= -d_{b,L_F} - k_{b,L_F}\lambda \\ -b_{L_F} \,|_{\lambda=1.47} &= -d_{b,L_F} - k_{b,L_F}\lambda \end{aligned} \tag{5.17}$$

A convenient fact here is that the factor $d_{a,\tau}$ does not depend on the air excess ratio in the small range of λ investigated.[51]

[51] A range extension concerning equivalence ratio measurement points is suggested if the latter parameter is of further interest.

Relating equations 5.14 and 5.15 does now lead to a formulation that allows a conversion between flame length and global FTF time delay

$$\frac{\tau_G(p,\lambda)}{L_F(p,\lambda)} = C_1\, p^{C_3\,(1+C_2\lambda)}\ , \tag{5.18}$$

with the constants C_1 to C_3 defined as

$$C_1 = \frac{d_{a,\tau}}{d_{a,L_F}} \tag{5.19}$$

$$C_2 = \frac{k_{b,\tau}}{d_{b,\tau}} = \frac{k_{b,L_F}}{d_{b,L_F}} \tag{5.20}$$

$$C_3 = d_{b,L_F} - d_{b,\tau}\ . \tag{5.21}$$

In equation 5.18, the factor C_3 represents the different pressure gradients of τ_G and L_F. Note that the factor C_2 can be derived from both time delay and flame length.

Table 5 summarises the factors a and b found from the individual least-squares fits of equations 5.12 and 5.13 to the measured data as well as the coefficients derived for equations 5.14 to 5.21.

Table 5: Coefficients for power law pressure scaling of flame length and global time delay. Use bar as pressure unit in equations 5.12 to 5.21.

	λ [−]	a [ms] [mm]	b [−]	d_a [ms] [mm]	d_b [−]	k_b [−]	C_1 [ms/mm]	C_2 [−]	C_3 [−]
τ_G	1.4	2.233	0.309	2.235	3.111	-2.001	0.0269	-0.639	-2.316
	1.47	2.237	0.169						
L_F	1.4	82.55	0.089	83.16	0.795	-0.504			
	1.47	83.77	0.054						

In addition, table 6 shows the underlying measurement data as well as the respective results of the fitted power law of equations 5.14 and 5.15 together with an extrapolation to operating conditions beyond the range of the experimental investigations.

Table 6: Measured and calculated flame length and global time delay. The power law calculation refers to equations 5.14 and 5.15.

			Measurement		Power Law	
OP	λ [−]	p [bar]	τ_G [ms]	L_F [mm]	τ_G [ms]	L_F [mm]
TD1-P1	1.30	1.1	2.22		2.13	81.7
-	1.30	2.2			1.53	73.4
-	1.30	3.0			1.32	70.0
TD1-P2	1.40	1.1	2.41	81.9	2.17	82.3
-	1.40	1.5		79.8	1.98	80.0
TD1-P3	1.40	2.2	1.75	76.6	1.76	77.2
TD1-P4	1.40	3.0	1.59	75.1	1.61	75.0
-	1.47	1.1			2.20	82.3
TD1-P5	1.47	2.2	1.95	80.4	1.95	80.0
TD1-P6	1.47	3.0	1.87	78.4	1.85	78.7
TD1-P7	1.47	4.0	1.77	78.2	1.75	77.5
TD1-P8	1.47	5.0	1.70	77.8	1.69	76.7
-	1.47	6.0		75.3	1.63	76.0
-	1.47	10			1.49	74.0
-	1.47	20			1.32	71.4
-	1.47	30			1.23	70.0

That extrapolation of the FTF phase gradient can also be checked by recording stationary flame images at further operating points and comparing the measured flame length against the extrapolation. An advantage of this procedure is that a FTF measurement - that might become very difficult at high pressures - is not necessary and equation 5.18 can be utilised to derive the global phase gradient at the extrapolated pressure.

5.5 Summary and Conclusions

A characterisation of the TD1 flame was performed prior to the actual FTF measurements and yielded some interesting results.

- A slight decrease of the flame length with pressure has been observed. This behaviour can be attributed to rather large heat

losses of the flame to the cool combustor walls that lead to a pressure dependency of the diabatic flame temperature and to an increasing turbulent burning velocity with pressure. The same effect is found to affect the LBO characteristics.

- For a quantification of the flame length variation with the operating conditions, the definition of the flame length is important. The axial location of the maximum flame intensity for example shows a stronger variation with pressure than the flame center of gravity that takes the entire reaction zone into account.
- The flame length variation with pressure generally increases if siren excitation is applied.

The following statements can be made about the flame transfer functions.

- The procedure to record flame transfer functions was found to work remarkably well. A very good reproducibility was achieved and normalisations with arbitrary values as often reported are not necessary.[52] All FTFs show the behaviour typical for swirled flames with one or more amplitude peaks and a global phase decline due to the time delay between burner and flame.
- A broad global amplitude peak is observed between 150 and 300 Hz that shifts to higher frequencies for rising pressure and richer mixtures.
- Deviations in the phase gradient occur that correlate with the local amplitude behaviour and lead to a "wavy" phase plot.
- Up to a limit frequency of 120 Hz the phase plots of all operating conditions are almost overlapping. At that limit a substantial separation of the phases in the form of a deviation from the linear phase decline takes place. The magnitude of this deviation depends on operating conditions like pressure and equivalence ratio. At frequencies above that deviation, the phases exhibit

[52] See also appendix B.

an almost constant decline with frequency that is reduced with rising pressure along with the reduced flame length.

- An analysis of the locally resolved heat release distribution using a high speed camera provides an explanation for the phase behaviour observed. Up to the limit frequency of 120 Hz, a fluctuating flame length is the dominant mechanism of the heat release oscillation. Since the heat release perturbation associated with this flame length fluctuation is insensitive to operating conditions, the phase plots up to 120 Hz are almost identical. Above that limit, the "conventional" convective transport of perturbations through the flame is the dominant mechanism, and the phase gradient varies as the flame length is influenced by the operating conditions.

- The above finding can be generalised: Only as long as the heat release pattern of the flame is qualitatively unchanged, global scaling laws can be derived to describe the influence of operating parameters on the flame transfer function. In the other case, a global scaling law is not sufficient and a more detailed description is needed to capture the flame dynamics.

- The distinct phase differences at high frequencies can severely influence the stability of a system. For the present configuration of the rig, a self-excited combustion instability occurs at high pressures and rich mixtures. Low order modelling using the rig geometry and the measured FTFs does confirm this instability.

- To characterise the phase behaviour with changing operating conditions, a power law scaling of the global time delay was found to give a good fit. This is an encouraging result since it points out that in order to identify the transfer function at realistic engine pressures of up to 35 bar, one does not necessarily have to reach that pressure in dynamic combustion tests, but only approach it up to a sufficiently small factor.

- The identified scaling laws reveal that the global FTF time delay scales almost proportionally (same pressure exponent) with the flame length defined as the distance from the burner exit to

the location of the maximum flame intensity. This finding results from the FTF phase being controlled by the phase of the dominant flame activity region. As the latter is (above 120 Hz) located at the flame intensity maximum, the global FTF phase is controlled by the flame length defined as the distance to that maximum. For a constant burner velocity, the observed flame length variation with pressure results in a proportional scaling of the global phase drop and time delay.

- Since the scaling laws of flame length and global FTF time delay are similar, their pressure- and equivalence ratio behaviour can be related and the easier to determine flame length can be used to gain information on transfer functions at high pressures without actually measuring them.

A general conclusion from these results is a rather small direct influence of operating conditions like pressure or equivalence ratio on the global appearance of the flame transfer function of the generic burner. Most variations can be attributed to the indirect influence of the non-adiabatic combustor via its effect on flame temperature and flame length. Nevertheless, interesting features as for example the pressure-dependent phase deviation are observed that exhibit distinct changes of the behaviour over a comparably small variation of the operating conditions.

Additional investigations with a varying siren excitation amplitude have been performed to analyse the linearity of the measured flame transfer functions and potential saturation effects. The results of these experiments are presented in appendix A.

More information on the reproducibility and quality of the measured transfer functions can be found in appendix B.

6 FTFs of the Industrial Burner - Burner Influence

In this section, the comparison of the industrial burner to the generic TD1 burner is of main interest. For that purpose, flame shape & behaviour and flame transfer functions are presented and compared to the TD1. Again, the flame transfer functions were measured at different pressures, but a variation of the air-fuel mixture fraction was omitted.

6.1 Burner and Flame Characterisation

All results given in section 6 were obtained in perfectly premixed mode using the same gas injection location far upstream of the burner as for the TD1. The only difference in the gas supply is a reduced injection hole size matched to the lower gas flows of the industrial burner to achieve the same injection pressure drop and thus the same mixing behaviour of air and gas. Also, potential effects of the fuel line acoustics due to a different pressure drop are eliminated by the matched hole size.

Compared to the TD1, the industrial burner is smaller in size and is operated at a lower thermal power ratio of about 36 kW/bar vs. 60 kW/bar for the TD1. Burner flow velocity, equivalence ratio and preheating temperature are similar to the TD1, the results are thus well comparable in terms of operating conditions. Also, the theoretical swirl number S_0 amounts to the same value of 0.6. However, due to a higher pressure drop coefficient the relative pressure drop values are larger. A summary of the operating points is given in table 2.

One major difference of the industrial burner to the TD1 is a bimodal combustor flowfield associated with two meta-stable flame modes illustrated in figure 6.1. Although the swirl number is about the same as for the TD1, the mixture flow of the industrial burner does usually not generate a vortex breakdown at the area step from the burner exit to the combustor. Thus, no central recirculation bubble is formed and

the flow exits the burner in the form of a swirled free jet [FES02a]. The flame does then stabilise at a rather large distance from the burner, where the jet velocity has diminished to a value equal to the turbulent flame speed. This "lifted" flame mode is associated with a high burner flow velocity, low combustor pressure and a low flame temperature. The flame itself is distributed over a large volume and shows a low intensity blue colour. Due to the weak stabilisation, the lifted flame exhibits a strong sensitivity on all operating parameters influencing the equilibrium position.

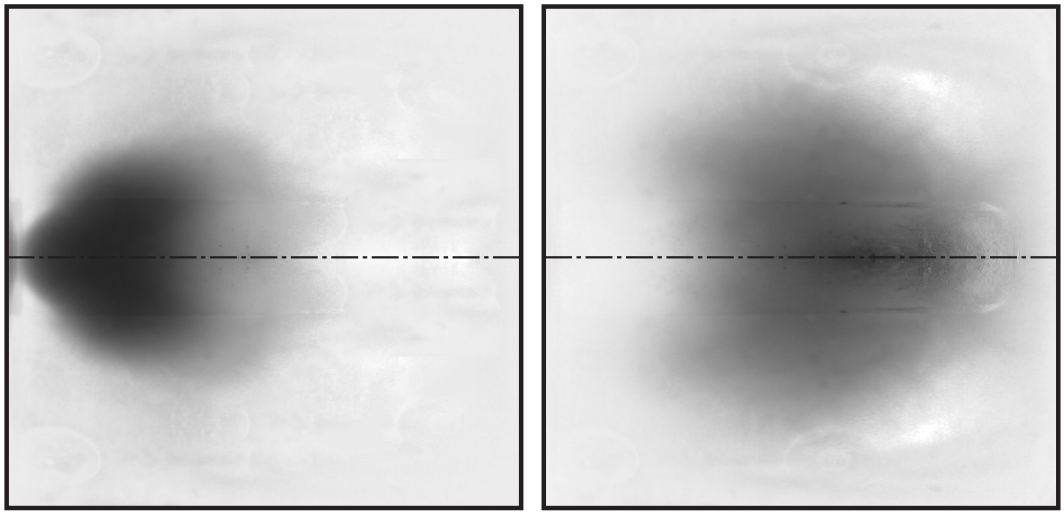

Figure 6.1: Anchored (left) and lifted (right) flame mode of the industrial burner, single images taken at the same operating point with $p = 5.5$bar, $\Delta p/p = 1\%$ and $\lambda = 1.05$. Burner located on the left side of the images, brightness inverted.

At high flame temperatures and low flow velocities, another flame mode appears that is located close to the burner exit, more compact and brighter. This "anchored" mode shows the typical conical shape associated with the occurence of a central recirculation zone induced by vortex breakdown. Due to this recirculation zone, the anchored flame is well stabilised and its position is independent of flow velocity or mixture composition changes. Interestingly, the anchored mode does only occur at elevated pressures above 3 bar.

A rather large region exhibiting sudden transitions from one mode

to the other separates the operating regimes of the two flame modes. These transitions occur with a frequency in the range of 1 - 10 Hz and are completed within about 1 ms[53]. Within the transition region, the residence time of one mode is governed by the distance to the respective limit conditions. At low frequencies, siren excitation can trigger the flame mode transition [Sch04].

Concerning the measurement of flame transfer functions, the well-stabilised anchored mode is the preferred choice. However, since stable anchored conditions without transitions to the lifted mode and providing a safe distance to the flashback limit could not be achieved, all FTFs of the industrial burner were obtained in the lifted flame mode. The boundary between lifted flame and transition region is for all investigated pressures located at about $\Delta p/p = 4\%$ and $\lambda = 1.2$. Adding a safety margin to this boundary leads to the operating points for the industrial burner setup given in table 2.

Averaged flame images for varying pressure at the air excess ratio and burner velocity of the FTF operating points are given in figure 6.2. Note the strong variation of the intensity and the location of the flame root despite of the constant flow velocity and adiabatic flame temperature. The reason for that strong variability of the flame root position is considered the same as it was described in section 5.1 for the TD1 burner - a large heat loss to the cold combustor walls leads to a flame temperature far from adiabatic conditions. Compared to the TD1, this effect is even stronger due to the larger flame surface in contact with the walls and due to the lower thermal power. As a result of the missing aerodynamic stabilisation, not only the flame length is affected here by the non-adiabatic reaction process, but also the flame root location. With rising pressure, the relative heat loss decreases and the (diabatic) flame temperature rises, leading to a higher flame speed and in turn to a shorter flame located closer to the burner. Unfortunately, the limited optical access does not allow a quantification of the flame length. Especially for operation at low pressure the largest part of the flame is located downstream of the side window.

[53] Note the similarities of the transition between the two flame modes encountered here with the “Combustion Induced Vortex Breakdown” described in [FKS04] and [KFS03]

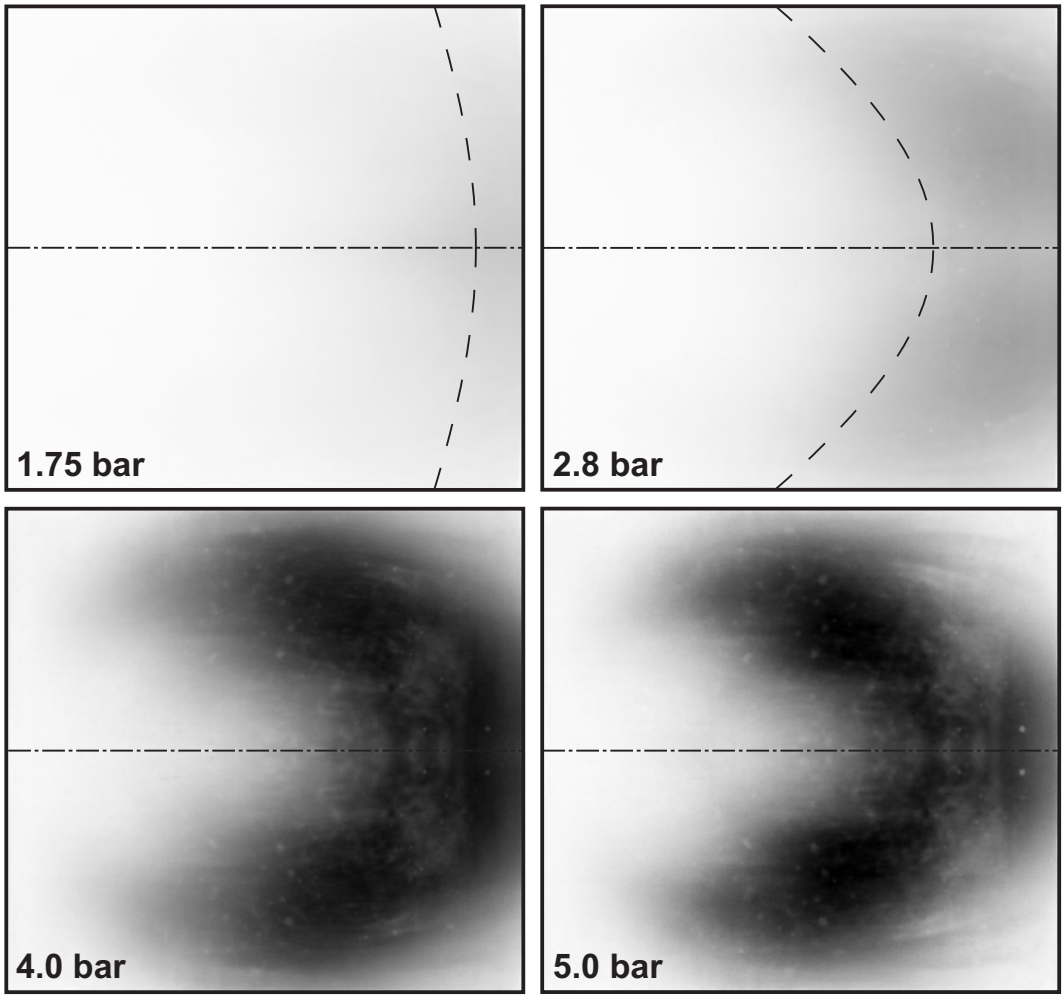

Figure 6.2: Flame location and appearance in PP mode for various pressures, $\Delta p/p$ = 6% and $\lambda = 1.2$. Images averaged over 15-30 individual recordings, constant camera settings. The dashed line indicates the upstream flame envelope for the low intensity images at low pressure. Burner located on the left side of the images, brightness inverted.

A similar behaviour with a strong variation of flame intensity and flame root location is observed for operation with different air excess ratios. This is expected, since the diabatic flame temperature is the main driver. Due to the large heat loss the maximum air excess ratio achieved is even lower than for the TD1 - flame extinction takes place in the range of $1.3 \leq \lambda \leq 1.4$.

The spatial distribution of the heat release, respectively the flame intensity, resembles the appearance of the free jet exiting the burner.

Along the axis, high axial flow velocities occur that push the flame far down into the combustor. In the rim regions of the jet, the velocity is much lower and the flame is stabilised closer to the burner. Note also the increasing curvature of the flame root towards higher pressures. This is a result of the jet diameter increasing with the distance into the combustor and of the relative heat losses in the near-wall regions decreasing with rising pressure.

6.2 Flame Transfer Functions

The flame transfer function measurement setup for the industrial burner is the same as for the TD1, with a hot wire probe mounted in the mixing tube close to the burner exit[54] and a photomultiplier tube looking at the flame through the rear window.

Unlike the TD1, the industrial burner features a complex flow field within the mixing tube with a high level of turbulence induced by the shear layer between the unswirled inner and the swirled outer flow path. The turbulent velocity fluctuations are typically one order of magnitude larger than the coherent fluctuations generated by the siren excitation, which leads to several difficulties. Despite the averaging over a large number of samples, an error induced by turbulent noise remains in the CTA signal and thus in the flame transfer function, this becomes apparent in the rather large scatter of the FTF amplitude plots. Moreover, the turbulence deteriorates the CTA calibration by introducing a scatter in the points defining the calibration curve and thus an uncertainty in the calibration curve itself. Finally, the high turbulence level constitutes a mechanical stress on the CTA wire, limiting the operational range to below 4 bar in perfectly premixed mode. The lowest degree of turbulence is found on the axis of the mixing tube, for this reason the CTA probe is located there.

Another difficulty associated with the complex flowfield of the industrial burner is its behaviour under excitation. While for very low frequencies the relative excitation $u'/\overline{u}$ is constant over the mixing tube

[54] See also figure 3.7

radius, a variation of $u'/\overline{u}$ over the radius is observed for frequencies above about 50 Hz.[55] This effect originates from the different dynamic response of the two flowpaths to the acoustic excitation. As a consequence, especially for high frequencies the measured FTFs might not stand for the global dynamic behaviour of the burner, but only for a part of it represented by the flow at the axis. A correct treatment of this effect would require an averaging over the mixing tube radius for every frequency investigated during the FTF measurement - an unfeasible effort for the scope of this work. Nevertheless, the measurement position at the axis does again give the best representation of the global behaviour.

A last source of uncertainty is a rather low average excitation amplitude $u'/\overline{u}$ of about 2% at the hot wire measurement position within the burner achieved with the industrial burner setup. This is mainly due to the lower burner cross section and the higher flow velocity that increase the impedance at the burner exit[56] and tend to locate an acoustic velocity node at the CTA measurement position. Associated with this effect is a pressure antinode at the flame location, leading to pressure amplitudes about one order of magnitude higher than experienced for the TD1 setup.

As a consequence of the effects described above, the quality of the IB flame transfer functions can not be considered as high as the quality of the TD1 FTFs. Especially the uncertainty in the CTA calibration generates an additional error in the already sensitive amplitude plots. Analog to the FTFs for the TD1 burner, the amplitude plots are corrected by a photomultiplier scaling factor as derived in section 4.2.2 to compensate amplitude deviations. However, this compensation is small compared to the errors introduced by the CTA. The resulting amplitudes for the operating points given in table 2 are shown in figure 6.3.

The global amplitude behaviour of all FTFs measured in PP mode on the industrial burner is similar. All plots start approximately at a

[55] This effect was measured by radially traversing the CTA probe. See [Wol05] for details.

[56] Note that the velocity in the mixing tube is only slightly higher than the velocity in the generic burner. The higher flow velocity at the burner exit mentioned here is a result of an area contraction at the exit as sketched in figure 3.7.

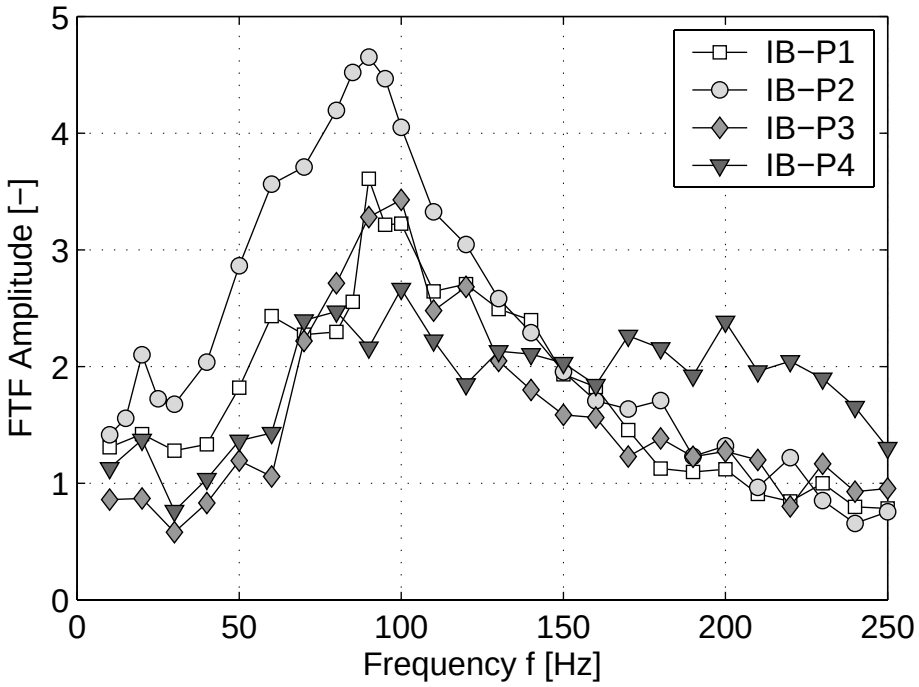

Figure 6.3: Flame transfer function amplitude plots for the industrial burner, perfectly premixed mode, operating points as specified in table 2.

value of 1 , reach a global peak at about 90 Hz and show a subsequent decline towards high frequencies. Note that no obvious change of the peak frequency is observed within the investigated pressure range comprising a factor of 2.3 - this is in line with the TD1 results also showing very little variation of the global peak frequency. Its absolute value of 90 Hz is however much lower than for the TD1, while the peak amplitudes tend to be larger. Another similarity to the TD1 is the high frequency amplitudes rising with pressure. This effect could also be related to very low excitation amplitudes in that range at high pressures though. Compared to the TD1, the amplitude plots are missing the local peaks and minima at low frequencies, with an exception being some indications of peaks below 50 Hz, especially for operating point IB-P2. The absence of those local peaks makes the global maximum appear more dominant.

The corresponding phase plots presented in figure 6.4 do again show the common decline with frequency starting from a phase value of 0 in the low frequency limit. Due to the flame location far downstream of

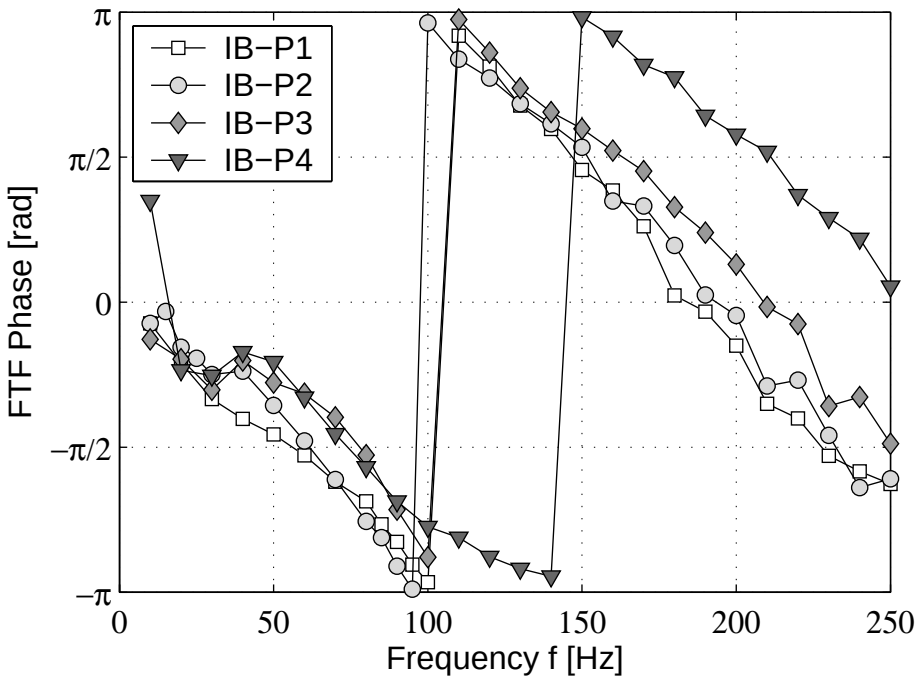

Figure 6.4: Flame transfer function phase plots for the industrial burner, perfectly premixed mode, operating points as specified in table 2.

the burner exit, the global time delay associated with the phase gradient is larger than for the TD1, even though the burner exit velocity is higher. When comparing the phase gradients of figure 6.4 to the flame locations of figure 6.2, a close correlation can be found. With rising pressure, the flame is located closer to the burner exit and the global FTF phase gradient decreases.

Interestingly, the pressure-dependent deviation of the phase from the linear decline investigated in section 5.3 is also found here, but with a limit frequency around 30 - 40 Hz. Like for the TD1, this effect is accompanied by a local peak followed by a minimum in the amplitude plot. The similar behaviour of the two burners concerning the phase deviation indicates a common mechanism causing the effect. This appears remarkable when considering the significant differences of the flame appearance of the two burners.

One unexpected effect is found in the phase plots of all measured IB transfer functions. Above a limit frequency of 250 - 300 Hz, the phase plots lose their negative gradient with frequency and start rising

again. That behaviour is found to be an error resulting from the low excitation amplitude, a more detailed analysis is given in appendix C. In this section, the FTF plots have been reduced to the frequency range where meaningful data are obtained.

Table 7: FTF global time delay for the industrial burner in PP mode.

OP	Pressure [bar]	$\tau_{G,PP}$ [ms]
IB-P1	1.75	5.24
IB-P2	2.5	5.12
IB-P3	2.8	4.62
IB-P4	3.5	3.70

A summary of the global FTF time delays for the investigated operating points is given in table 7. Despite the strong variation in the global time delay $\tau_{G,PP}$ with pressure caused by the changing flame location, the amplitude peak remains almost fixed at a frequency of about 90 Hz. A similar result, but less visible due to the smaller variation in $\tau_{G,PP}$ is found for the TD1[57]. A correlation of the amplitude peak frequency with the flame standoff distance or the FTF time delay can thus be excluded for the cases investigated in this work. This result is not in line with results from literature, e.g. Lohrmann [LB04], who uses a Strouhal number derived from the axial distance burner exit - flame intensity maximum to scale his transfer functions.

These results suggest that the mechanism generating the global amplitude peak at around 90 Hz can be considered independent from the global phase decline. The rather unusual low swirl number of both industrial and generic burner and the amplitude results not fitting the literature give rise to the assumption that the mechanism generating the global amplitude peak in both configurations is associated with the rather long and weakly stabilised flame and some kind of internal dynamics within it.

[57] See also section 8.1.3

6.3 Summary and Conclusions

The main focus of section 6 was to compare the FTF behaviour of the industrial burner to the generic setup investigated in section 5. Operating conditions and some basic parameters like flow velocity and swirl number are similar for the two burners, one major difference however is the lifted flame of the IB setup. A complex burner flowfield and a high level of turbulence deteriorate the FTF quality for the industrial burner.

Local low frequency amplitude peaks and minima are much weaker than observed for the TD1, and occur at very low frequencies. Nevertheless, some other similarities do exist:

- With rising pressure the global FTF time delay derived from an averaged phase gradient exhibits a strong decline that can be attributed to an observed upstream shift of the flame.
- A global amplitude peak is observed like for the TD1, the peak frequency however is lower by a factor of 3 - around 90 Hz vs. 260 Hz - and the maximum amplitude lies higher at a value of around 4. Also similarly to the TD1, the global peak frequency is almost independent of pressure. This is remarkable, since the flame location and the associated global time delay values show a strong dependence here. A correlation of the global amplitude peak with the FTF phase gradient or the axial location of the dominant heat release region can thus be excluded. Nevertheless, an influence of the flame length can not be excluded, since the latter could not be determined in the lower pressure range.
- Like for the TD1, a pressure-dependent deviation of the phase from the linear decline is observed. Similar to the global amplitude peak frequency mentioned above, the frequency of that deviation is smaller by a factor of 3 - 40 Hz here vs. 120 Hz for the TD1.

7 FTFs of the Industrial Burner - Influence of Mixture Fraction Fluctuations

After the investigation of the industrial burner in perfectly premixed mode in section 6, this section aims at analysing the influence of mixture fraction fluctuations on the flame transfer function by operating the same burner at the same conditions in technically premixed mode and subsequently comparing the results. Consult appendix D for an overview of the naming conventions used concerning the FTFs.

7.1 Burner and Flame Characterisation

For the industrial burner in TP mode, the fuel injector nozzle at the burner head is used instead of an injection location far upstream of the burner. This has some implications on the fuel and velocity profiles in the mixing tube when compared to PP mode, as sketched in figure 7.1.

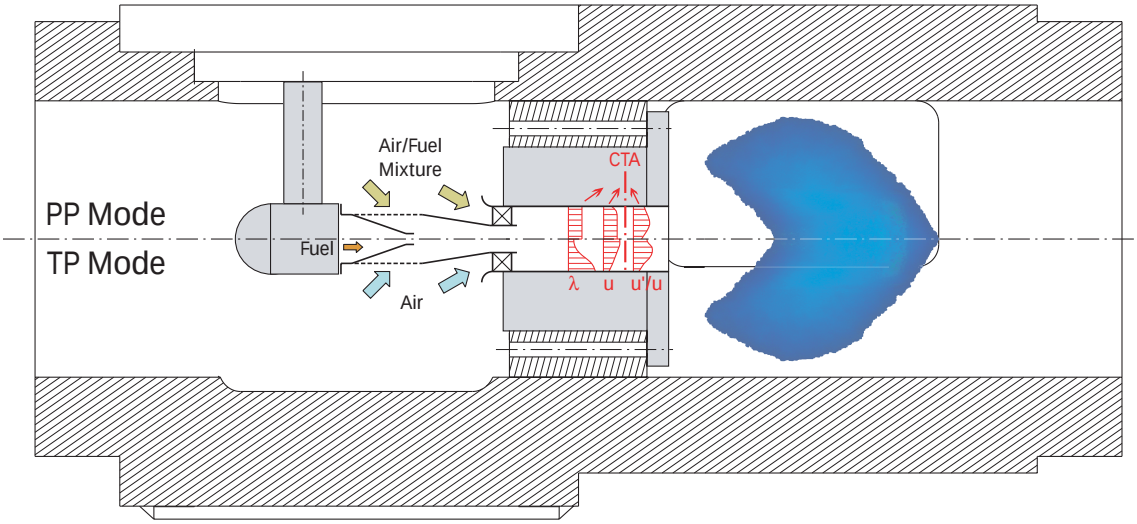

Figure 7.1: Sketch of the industrial burner in PP mode (upper half) and TP mode (lower half) with qualitative illustrations of radial profiles at the CTA location: Air excess ratio λ, axial velocity $\bar{u}$ and turbulence level $u'/\bar{u}$.

Since the injector nozzle diameter is rather small, the fuel gas is injected with a high velocity. This additional momentum increases the flow velocity in the unswirled inner duct with respect to the outer swirled ring. At the same time the turbulence level in the inner duct is substantially increased by the strong shear gradient between the fuel jet and the surrounding air. Due to the high fuel momentum at the burner axis, a radial fuel profile far from uniformity with a rich mixture at the axis and a lean wall region is generated. At the CTA location on the burner axis, the unmixedness factor according to equation 4.6 is estimated[58] to

$$U_\lambda \,|_{r=0} = 3 \; . \tag{7.1}$$

The large pressure drop caused by the high fuel gas velocity in the burner head and in the injector nozzle justifies the assumption of an acoustically stiff injection system with an impedance approaching infinity - acoustic pressure fluctuations do not affect the fuel flow through the injector.

Since the flame is lifted off the burner, the standoff distance acts as an extension of the mixing tube, and the influences of the different flow field and mixture distribution on the flame between PP and TP mode become less accentuated. Figure 7.2 shows a comparison of the flame shape and location of the two modes for varying pressure. While the flame shape is almost identical, the only apparent difference is a slightly larger flame standoff distance in TP mode. The strong dependence of the flame location on pressure does also exist in TP mode, and for low pressures the larger part of the flame does also lie beyond the range visible through the combustor side window.

The similarity of the flame shape and its position between PP and TP mode is a favourable condition for a comparison of the flame transfer functions between the two modes. Differences found in the FTFs can now be related to the effect of interest - the mixture fraction oscillations generated by the acoustic excitation.

[58] The basis for this estimation is a measurement of the radial distribution of the velocity in the mixing tube in both PP and TP mode. See [Wol05] for details.

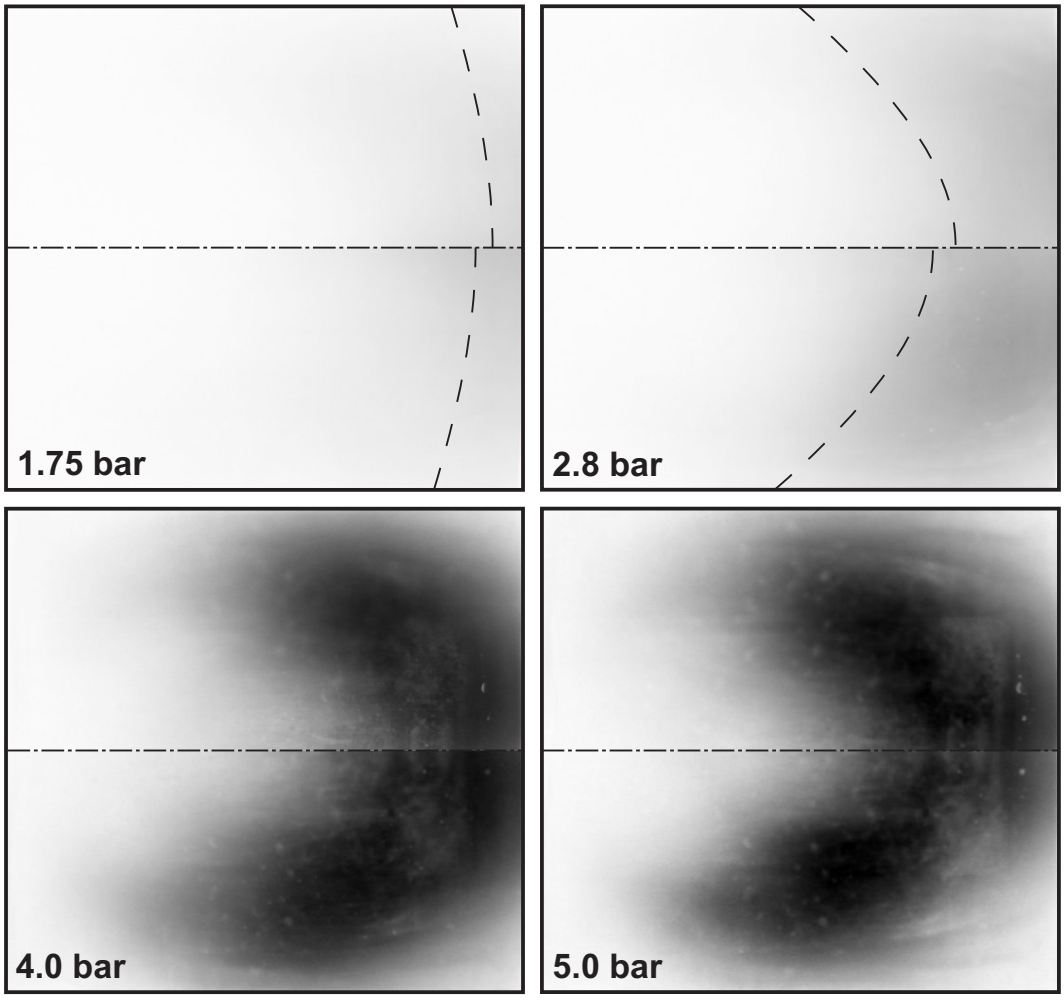

Figure 7.2: Flame location and appearance for various pressures in PP (lower half) and TP (upper half) mode.

7.2 Flame Transfer Functions

7.2.1 Low Frequency Limit

The choked fuel injection allows to characterise the low frequency behaviour of the burner in TP mode. For this purpose, equation 2.64 describing the response of the fuel massflow and thus the flame heat release to velocity and mixture fraction perturbations at both injector (I) and burner exit (B) is utilised.[59] Note that this equation does not

[59] See also figure 2.6.

account for any flame dynamics, which are anyway not important for low frequency considerations.

Since the choked fuel massflow is not influenced by the acoustic perturbations, only the air excess ratio at the injection location is modulated by the perturbation. Because the heat release within the flame is directly proportional to the fuel massflow consumed

$$\dot{Q} \propto \dot{m}_f \ , \tag{7.2}$$

the former is then also constant - provided that the convective wavelength is large enough to assume the same phase of the mixture fraction perturbation at both injector and flame. As a consequence, the amplitude of the FTF must approach 0 for very low excitation frequencies.

$$\lim_{f \to 0} \widehat{FTF}_{TP} = 0 \tag{7.3}$$

In addition, a low frequency limit can be derived for the phase.

$$\lim_{f \to 0} \varphi_{FTF_{TP}} = \frac{\pi}{2} \tag{7.4}$$

This is a necessity due to the same magnitude of u'_I and u'_B in equation 2.64. Note that for higher excitation frequencies $u'_I \neq u'_B$ is the rule rather than the exception.

Although the heat release oscillation and thus the transfer function amplitude is 0 in the above case, the mixture fraction fluctuation does still exist. Since the latter has a strong influence on the OH* chemiluminescence intensity taken as the measure for the heat release, the actually measured $TF_{OH/CTA}$ does not reflect the reality and the amplitude is not expected to approach a value of 0.

$$\lim_{f \to 0} \widehat{TF}_{OH/CTA} > 0 \tag{7.5}$$

For the cases shown in this work, the response of the chemiluminescence intensity to a mixture fraction variation is much higher than

the response to the actual heat release fluctuation, leading to large TF amplitude values in the low frequency limit.

Also due to the above consideration, the phase of the measured transfer function is expected to approach a value of π in the low frequency limit.

$$\lim_{f \to 0} \varphi_{TF_{OH/CTA}} = \pi \tag{7.6}$$

This results from the opposite phase of the velocity perturbation and the flame intensity for a pure mixture fraction oscillation - a higher velocity gives a leaner mixture and less OH* radiation.

7.2.2 Measured Transfer Functions

Compared to PP mode, no changes were made to the setup for the flame transfer function measurement. The shortcomings described in section 6 that limit the operating range and the FTF quality do also apply here and are even more severe. Due to the higher velocity and turbulence level at the CTA location, the 10 μm hot wire does not survive at burner pressures higher than 3 bar. Nevertheless, transfer functions have been measured at pressures up to 2.8 bar, which can be compared to the FTFs acquired in PP mode.

Figure 7.3 shows the resulting transfer function amplitudes for operating points IB-T1 to IB-T3. As expected from the previous section, the amplitudes do not approach 0 in the low frequency limit, but start at values ranging from 4 to 7.5, with a clear tendency of the start value to decrease with pressure. While the plots at 2.5 and 2.8 bar converge nicely towards the low frequency limit, the 1.75 bar plot does not, which indicates a measurement anomaly. A more reasonable starting value for the the 1.75 bar case would lie between 5 and 6.

The global amplitude peak at about 100 Hz observed for the PP mode is also found here, as is the subsequent decline to amplitudes below 1. Unlike the PP case, the frequency of that peak shows an appreciable variation with pressure here. For rising pressure, the peak shifts to

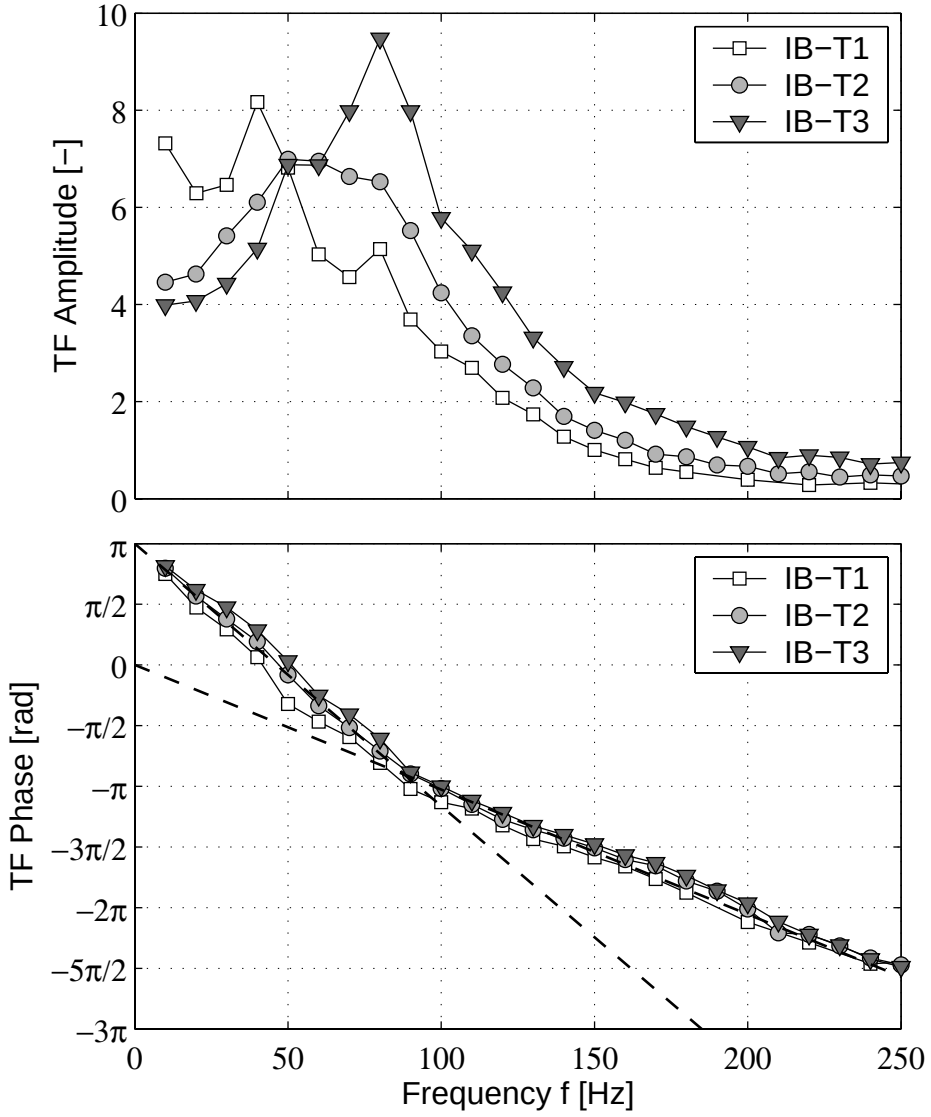

Figure 7.3: Transfer function ($TF_{OH/CTA}$) plots for the industrial burner, technically premixed mode, operating points as specified in table 2.

higher frequencies. A peak amplitude value of 9.5 is reached for the 2.8 bar case, which is considerably higher than the maximum of 4 obtained in PP mode.

The corresponding phase plots can also be found in figure 7.3. Again, the low frequency limit shows the expected behaviour and the plots approach a value of π. Like in PP mode, the phase plots exhibit a rising phase for high frequencies above 250 Hz and have been reduced to the meaningful range below that frequency. More details on this

effect can be found in appendix C. For low frequencies below 100 Hz, the phase behaviour is smoother than for the PP case and the pressure-dependent deviation of the phase from the linear decline around 40 Hz does not become apparent.

At about 90 Hz, the phase plots of figure 7.3 exhibit a bend from a large gradient below to a much smaller one above that limit frequency. Both branches are almost perfectly linear, as indicated by the dashed lines. Interestingly, the high frequency gradient intercepts the coordinate origin in the low frequency limit.

A table with the global transfer function time delay values, evaluated above and below the limit frequency, is given below. Note that the trend to lower time delay values for higher operating pressure found in PP mode (see table 7) is also observed here. As for the PP mode, this behaviour can be attributed to the flame location shifting upstream with pressure. Note also that the variation of the flame location is rather small due to the limited pressure range, as seen in figure 7.2. Thus, also the time delay values of table 8 show little variation.

Table 8: FTF global time delay for the industrial burner in TP mode. Gradients are evaluated above and below the bend at 90 Hz.

OP	Pressure [bar]	$\tau_{G,OH/CTA} < 90$ Hz [ms]	$\tau_{G,OH/CTA} > 90$ Hz [ms]
IB-T1	1.75	11.65	5.27
IB-T2	2.5	10.70	5.04
IB-T3	2.8	10.07	4.96

The observations described above and the values of $\tau_{G,OH/CTA} > 90$ Hz being very similar to the respective gradients in PP mode of table 7 lead to the presumption that the steep initial phase decline can be attributed to the influence of mixture fraction oscillations and the high frequency behaviour is the same as in PP mode.

7.2.3 Influence of the Operation Mode

A comparison between PP and TP mode using the example of the flame transfer function measured for IB-T/P2 at 2.5 bar is given in figure 7.4. Both amplitude and phase plots are indeed similar for high frequencies, which confirms that the differences of flowfield and mixture fraction profile between PP and TP mode do not have a significant influence on the dynamic behaviour. As a consequence, the difference of the transfer functions between the two modes - the hatched region in figure 7.4 - can be solely attributed to the air excess ratio fluctuation generated by the acoustic excitation.

While the TP amplitude can qualitatively follow the PP amplitude for low frequencies and keep the relative separation, a steep decline of the TP amplitude is observed beginning at a limit frequency of about 80 Hz. The two plots then quickly converge until the influence of the mixture fraction oscillation disappears completely at about 130 Hz. This low-pass behaviour can be explained by the short wavelength of the mixture fraction oscillation resulting from its convective character. As an example - with an average convection velocity of 20 m/s the wavelength at 130 Hz amounts to only 15 cm, which is about half the distance from the injector tip to the flame. Together with the spatial mixing by large velocity gradients in the mixing tube and the unconfined turbulent flow in the combustor before reaching the flame, this short wavelength leads to a strong dispersion of the mixture fraction wave and thus to a low cutoff frequency. Only for frequencies below the cutoff limit the generated perturbation can persist and affect the heat release rate in the flame.

The observed lowpass behaviour of the mixture fraction fluctuation can also explain the increase of the global amplitude peaks of figure 7.3 with pressure as well as their shift to higher frequencies. As the flame moves upstream with rising pressure, the dispersion of the mixture fraction wave is reduced and the cutoff limit is shifted to higher frequencies. As a consequence, the underlying global amplitude peak at about 100 Hz already recognised in PP mode is becoming more accentuated, leading to an increasing TP mode peak amplitude and a higher peak frequency.

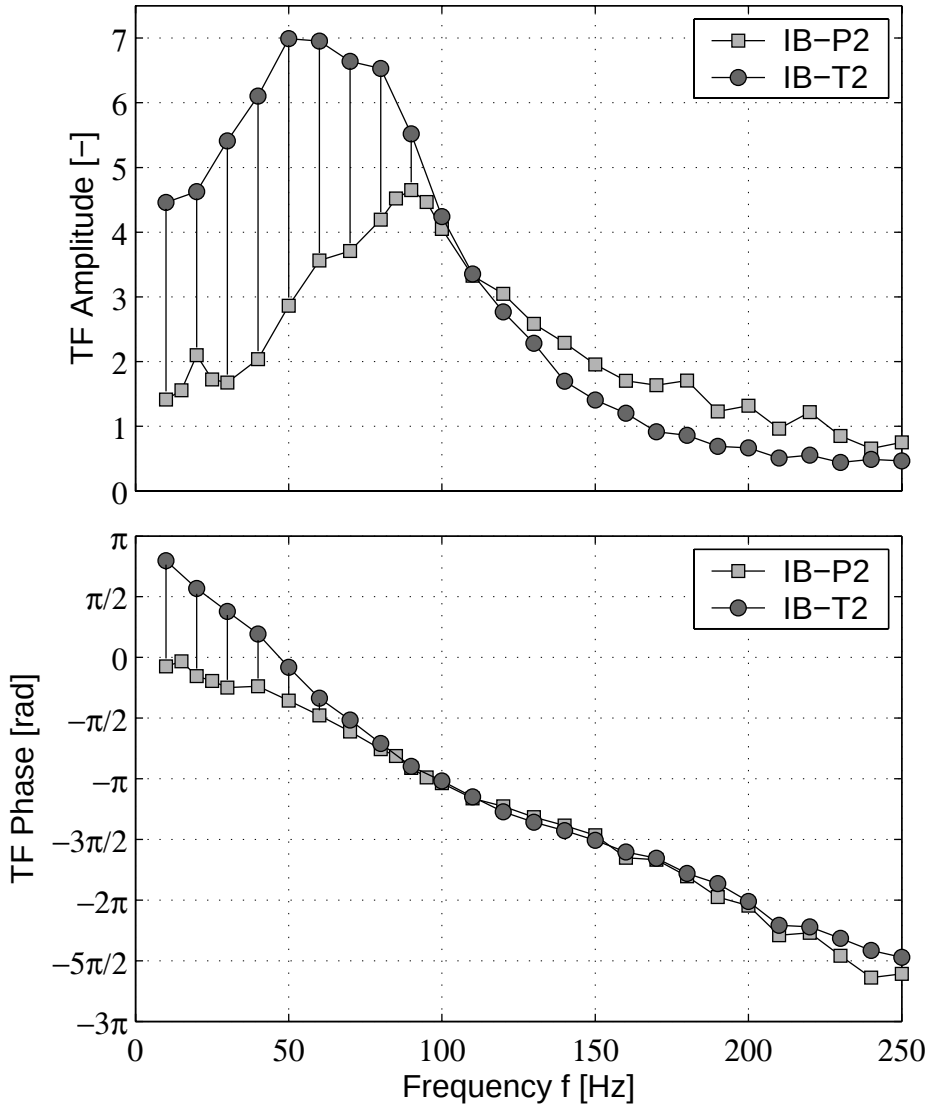

Figure 7.4: Comparison of transfer functions in PP and TP mode for IB-T/P2.

Compared to PP mode, the transfer function time delay τ_G is extended by an additional value τ_I to account for the convective delay of the air excess ratio fluctuation in the mixing tube between injector nozzle and CTA position - see also figure 2.6.[60] As a consequence, the phase

[60] Note that the hot wire probe is still located at the same position as in PP mode. The additional time delay τ_I seen in the TP mode transfer function results from a different propagation velocity of acoustic and convective waves. Since the acoustic velocities u'_B at the burner exit and u'_I at the injector are almost in phase for the rather low frequencies occurring here, the generation of a mixture fraction perturbation at the injector and the measurement of the velocity at the burner exit - the reference for the TF measurement - happen at about the same instant. However, the mixture fraction perturbation does then have to travel the additional distance from the injector to the hot wire probe with the convection velocity, which leads to an additional time delay in the

gradient of the TP mode transfer function is steeper than the PP gradient for the low frequencies where the mixture fraction oscillation is dominant. As soon as the latter has been damped out by the spatial dispersion, the TP phase bends and the PP behaviour is reproduced at higher frequencies.

Note that the measured TP mode transfer functions presented here are still influenced by the chemiluminescence and CTA sensitivity on the mixture fraction and do therefore not represent their true behaviour. A comprehensive treatment of this topic with a procedure to remove the systematic errors from the measured transfer functions to derive the true TP mode FTF is given in section 8.3.

For the sake of completeness it shall be mentioned that the transfer functions determined for this burner in TP mode with kerosene fuel instead of natural gas look very similar to the ones obtained here.[61] Especially the phases show the same behaviour observed here - a large gradient for low frequencies and a sudden bend towards lower time delays above the limit frequency. This is an indication that even with the additional complexity imposed by the liquid fuel atomisation, evaporation and only partially prevaporised (droplet) combustion the statements made above remain valid.

7.3 Summary and Conclusions

In section 7, the focus lied on a comparison of technically and perfectly premixed mode with the goal of investigating the influence of mixture fraction fluctuations generated by the acoustic excitation for otherwise identical conditions. The following conclusions can be extracted from the results:

- Despite of different flowfields in the burner in TP and PP mode due to the additional momentum of the fuel jet, the flame shape and location for the two modes are almost identical. This fact is

transfer function.

[61] These investigations were performed on a different rig at atmospheric pressure [EFS03a], [EFS03b].

the basis for a good comparability of the two modes concerning the separation of the influence of mixture fraction fluctuations.

- The measured TP mode transfer functions are almost identical to the PP mode FTFs for high frequencies. Effects originating from mixture fraction perturbations are thus limited to low frequencies up to 130 Hz. This low-pass behaviour is attributed to the short convective wavelength, the large distance from the injector to the flame and - most importantly - to the strong dispersion of the mixture fraction wave in the burner and in the upstream part of the combustor.

- The measured transfer functions do not truly represent velocity- and heat release fluctuations, as they are influenced by the sensitivity of the OH*-chemiluminescence and the CTA probe on the air excess ratio. These systematic errors lead to large amplitude values and the plots do not approach the required value of 0 in the low frequency limit.

- Those systematic errors are also responsible for a phase low frequency limit value of π instead of $\pi/2$. Starting from that value, the phases show a steep decline due to the additional convective time delay τ_I within the burner. As the mixture fraction fluctuation vanishes at the cutoff frequency of the low-pass behaviour, the phase exhibits a bend and the subsequent gradient is identical to the one in PP mode.

- Rising pressure shifts the TP mode amplitude peak to higher frequencies and results in lower phase gradients. Both effects can be attributed to the flame location moving closer to the burner exit and thus reducing the convective time delay. The reduced dispersion for higher pressures does then shift the cutoff frequency of the mixture fraction fluctuations to higher values, which leads to a larger amplification of the underlying global amplitude peak already recognised in PP mode and to a shift of the TP peak to higher frequencies.

8 FTF Modelling

In section 8.1, an analytical model is developed that can describe the measured transfer functions. This model is applied to the generic burner in section 8.1 and to the industrial burner in section 8.2, both operated in perfectly premixed mode.

In section 8.3 a procedure is introduced that allows a separation of the systematic measurement error encountered in technically premixed mode to determine the true TP mode flame transfer function. With that influence known, the FTF model is extended and can then also cover mixture fraction fluctuations.[62]

8.1 Generic Burner

The global behaviour of any flame transfer function does in a first approximation follow a time lag model, due to the convective time delay between the location of the acoustic velocity within the burner and the location of the heat release somewhere in the combustor. In the most simple form, this model comprises a constant FTF amplitude and a linear phase decline with frequency, as given in equation 2.21. This type of model has been applied in the previous sections to analyse the measured FTF phases - see equation 5.11 and figure 5.12 for example. However, as seen in the measured transfer functions, the real behaviour of the flame can differ considerably from this simple model in both amplitude and phase. Since especially the transfer function phase is a very important parameter for the stability of a combustion system, the FTF behaviour needs to be predicted in more detail.

8.1.1 Swirl Induced Velocity Fluctuations

Of the models introduced in section 2, Hirsch's [HSP+05] mechanism based on swirl fluctuation and vorticity transport is the most promising one to describe the dynamics of swirl flames and is thus applied

[62] See appendix D for an overview of the FTF naming conventions applied.

here. Unlike other approaches, his model is based on a physical analysis of the mechanism and not just on a phenomenological description. Only a few input parameters are required that can be provided from experimental observations. The disadvantage is that a numerical solution has to be found due to the differential equations involved. However, on a year 2005 personal computer this does only take a few minutes per calculation.

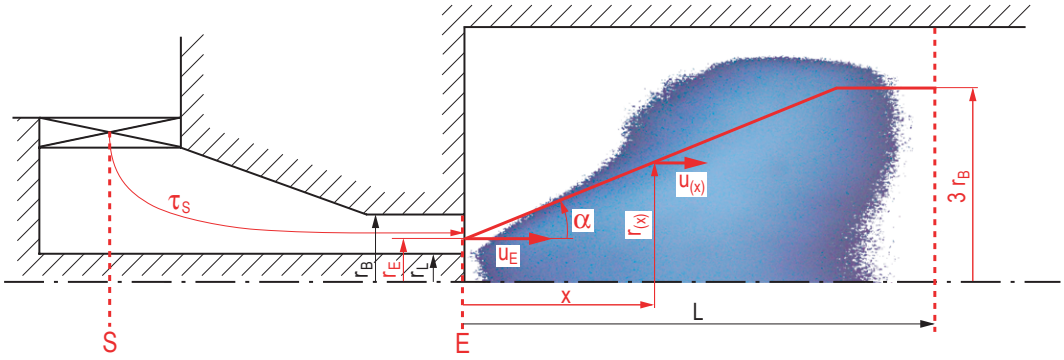

Figure 8.1: Sketch of the swirl model applied to the TD1 burner.

Figure 8.1 gives a sketch of the burner and flame geometry together with the input parameters required for the model. The corresponding parameter values are presented in table 9.

Table 9: Input parameters for the TD1 swirl model.

Parameter		Unit	Value
Burner radius	r_B	mm	20
Lance radius	r_L	mm	8
Start radius	r_E	mm	10
Flow angle	α	°	19
Integration length	L	mm	145
Swirl number	S_0	-	0.6
Swirl time delay	τ_S	ms	8.8
Average axial velocity	$\overline{u}_E$	m/s	35.3
Relative velocity perturbation	$\frac{u'_E}{\overline{u}_E}$	-	0.05

Of particular importance for the swirl model is the integration path along which the vorticity transport equation 2.44 is evaluated. This

path is approximated by a start radius r_E and a cone angle α of the flowfield after vortex breakdown. The latter has been derived from the effective swirl number S_0 according to equation 2.38 and verified by PIV measurements of Wäsle ([Wäs05]) for the same burner. Also, an analysis of the cone angle of the flame images gives a good agreement with this value. In the outer limit, the integration path has been limited to $3\,r_B$ to reflect the deflection of the streamlines by the combustor walls. This does, however, only affect the last few percent of the flame and has little influence on the results.

$$r(x) = \min\left[r_E + x\tan\alpha,\, 3\,r_B\right] \tag{8.1}$$

Along the integration path, the axial velocity is assumed to decline with the radius according to a hyperbolic law. The flowfield measurements referenced above do also verify this particular behaviour, showing a constant velocity for $r(x) < r_B$ and a hyperbolic decline for a larger radius. This is modelled as

$$\bar{u}(x) = \frac{\bar{u}_E\, r_B}{\max\left[r(x),\, r_B\right]}\,. \tag{8.2}$$

Another important parameter is the swirl delay τ_S describing the convective time delay between swirl generation at the tangential slots (S) and its arrival at the burner exit (E). This value can be calculated by integrating the local axial velocity over the burner length according to

$$\tau_S = \int_{x_S}^{x_E} \frac{dx}{\overline{u}(x)}\,. \tag{8.3}$$

The swirl time delay is responsible for the decoupling of the swirl fluctuation from the axial velocity fluctuation at the burner exit and does thus strongly influence the vortex dynamics. Note that a dispersion of the swirl wave during convection to the flame is not taken into account in this model, since the degree of dispersion is difficult to determine and damping effects are anyway taken into account by another part of the model.

With the parameters provided above, equations 2.44, 2.47 and 2.49 can be utilised to numerically calculate the induced velocity fluctuation $u'_{\varpi}(x,t)$, which is considered proportional to the local heat release fluctuation. The former is then subject to a numerical integration over the flame length L that is weighted with the averaged local heat release $\bar{\dot{Q}}(x)$ according to equation 2.50 to obtain a global measure for the heat release fluctuation u'_F. Unlike [HSP+05], the measured local heat release distribution derived from an analysis of the averaged flame images was utilised here instead of assuming a typical distribution. This is actually the only point to differentiate the individual operating points, since flowfield and velocity magnitude do not change with pressure as shown in section 3.4 and the tiny change of the flow velocity generated by the different equivalence ratios is neglected here.

To reduce the computing time, the measured heat release distribution with an axial resolution of about 0.3 mm[63] was approximated by a polynomial prior to the numerical integration. The order of the polynomial was chosen high enough to sufficiently reproduce the axial heat release distribution.[64] After integration, the resulting time series of u'_E and $\dot{Q}'_S$ (u'_F, respectively) are Fourier-transformed to derive the frequency response and evaluated in the same manner as the FTFs determined experimentally. Also, the frequency steps are chosen to match the frequencies investigated experimentally. The result is then of the form of a measured FTF

$$FTF_S(f) = \frac{\overline{u}_E}{\overline{\dot{Q}}_S} \frac{\dot{Q}'_S}{u'_E}(f) \,. \tag{8.4}$$

Figure 8.2 shows a typical result of the swirl model with amplitude and phase plotted over frequency. The amplitude plot shows two maxima and a trend of the amplitudes to decline with rising frequency. Note that the amplitude at the maxima is generally rather low - this is due to the low swirl number and the related small cone angle of the TD1 flow field in the current configuration. For a larger swirl number, the maximum amplitude shows an over-proportional rise, as expected from equation 2.44 and verified by the experiments of [Fis04].

[63] See figure 5.2 for an example.
[64] Here: 15^{th} order.

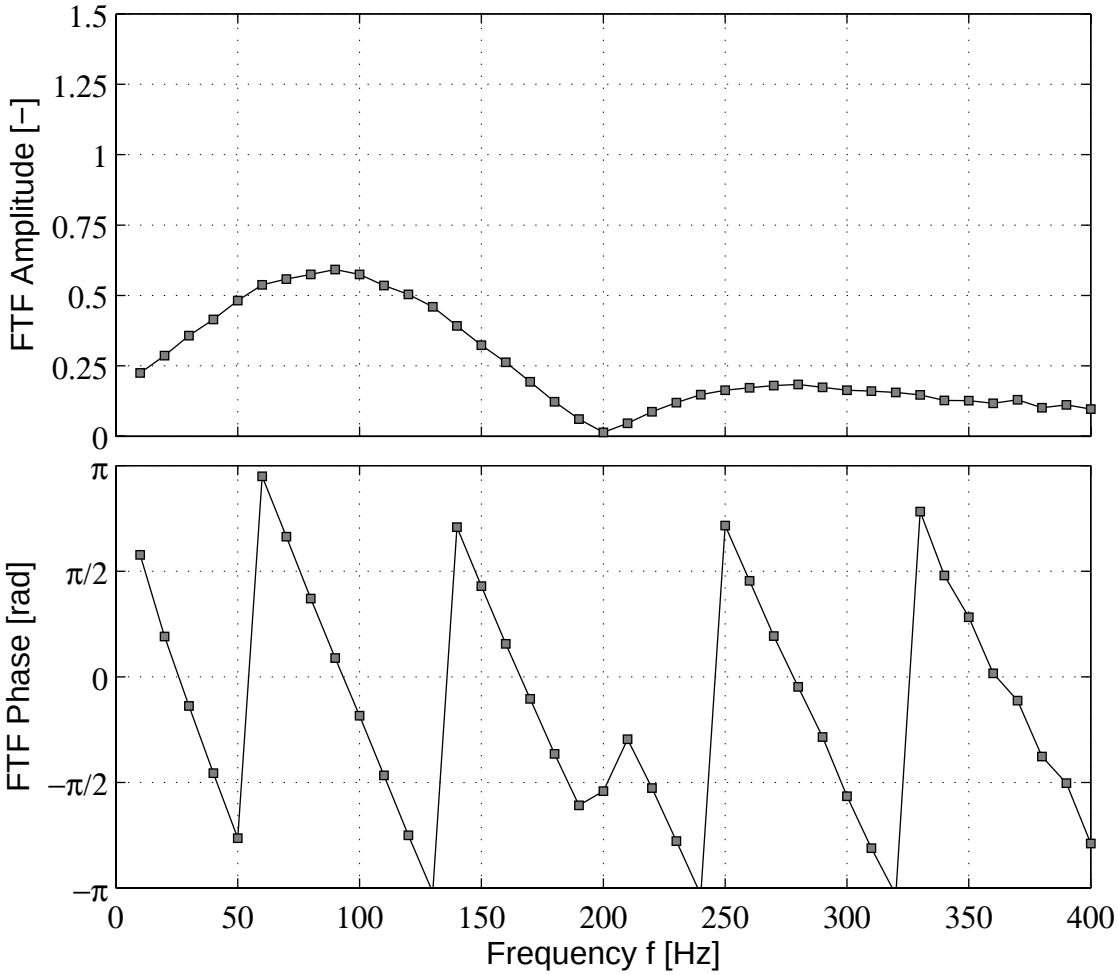

Figure 8.2: Swirl model transfer function FTF_S, operating point TD1-P1.

The phase plot in figure 8.2 shows a strong decline with frequency that is a hint towards a large time delay in the system. Indeed, the phase decline correlates roughly with the sum of the two time delays τ_S from the swirler to the burner exit and τ_G from the burner exit to the average heat release location of the flame. Especially the large value of τ_S is responsible for the strong decline seen here.

The model described up to now does only predict the heat release fluctuation $\dot{Q}'_S$ resulting from a vorticity perturbation. Since $\dot{Q}'_S$ is related to the burner velocity perturbation according to the FTF definition, the typical transfer function behaviour is not yet produced. This can be seen in the amplitude not approaching 1 and the phase not approaching 0 in the low frequency limit. A second part of the

model is thus needed to describe also the direct influence of the burner velocity perturbation on the heat release, which takes the form of a global time delay model as described in the next section. The final model is then derived from an additive superposition of the two parts, where the heat release fluctuation from vorticity can be thought of as "riding on top" of the fluctuation from the velocity perturbation.

8.1.2 Second Order Time Delay

The most simple time delay model to be applied to characterise the heat release response to a velocity perturbation at the burner exit[65] has a constant amplitude of 1 and a constant phase decline with frequency due to a single time delay parameter τ_M

$$FTF_\tau(f) = e^{-i\omega\tau_M} \quad \text{with} \quad \omega = 2\pi f \ . \tag{8.5}$$

Superposition with the swirl model does then give the complete FTF model

$$FTF_{\tau,S}(f) = e^{-i\omega\tau_M} + FTF_S(f) \ . \tag{8.6}$$

Both FTF_τ and $FTF_{\tau,S}$ are plotted in figure 8.3 together with the FTF determined experimentally for operating point TD1-P1. For the models, the time delay parameter τ_M has been set to the overall time delay determined from the experiment τ_G[66] and the respective axial heat release distribution has been used for the swirl model.

While the pure time delay model is a very rough approximation, figure 8.3 clearly shows that the superposition $FTF_{\tau,S}$ of swirl and time delay model can resolve the local peaks in both amplitude and phase plot. This is a confirmation that the approach chosen here does indeed reflect the experimental truth.

However, some deficiencies still exist. As seen in figure 8.3, a broad global peak with amplitude values ranging from 1.5 to 2 exists between

[65] See equation 2.21 in section 2.2.
[66] See table 6.

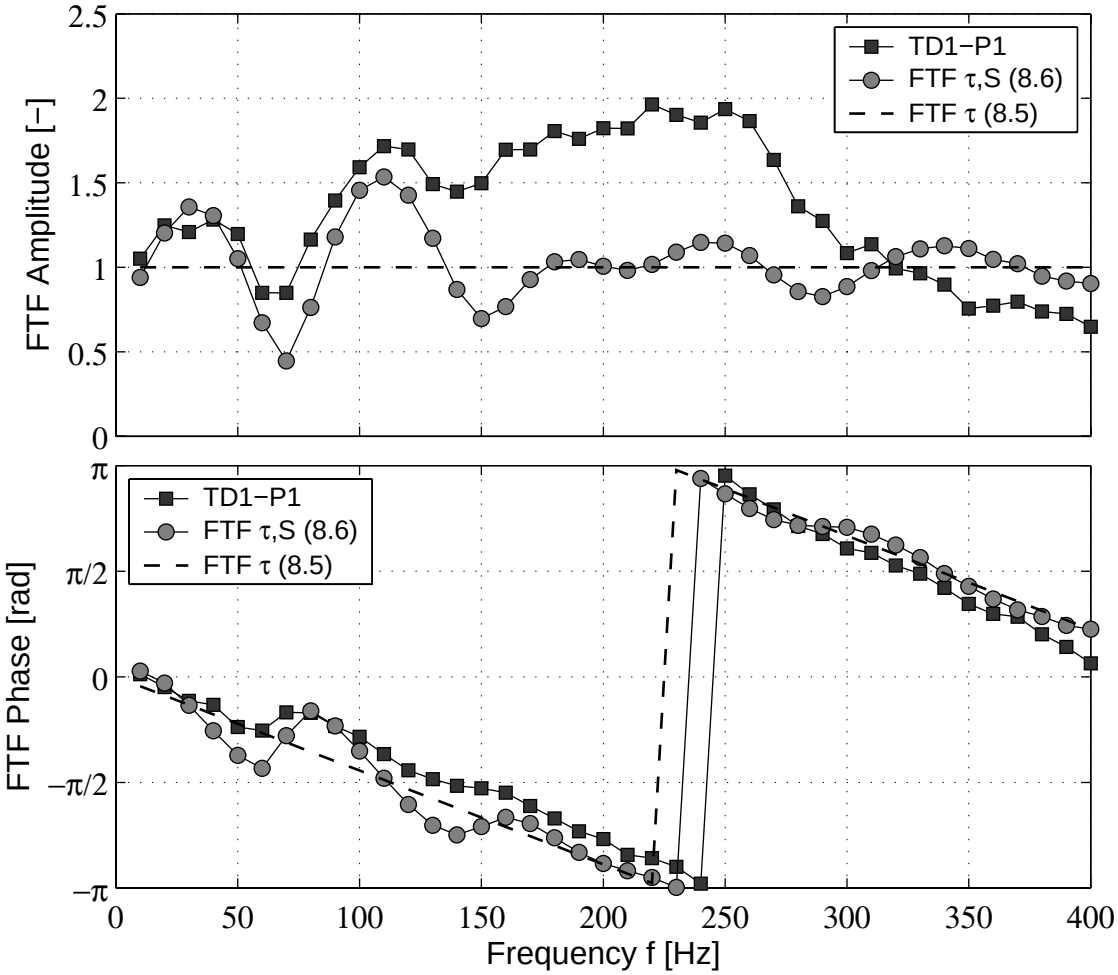

Figure 8.3: FTF_{τ} and $FTF_{\tau,S}$ compared to the experimental FTF at TD1-P1. Model time delay $\tau_M = \tau_G$.

150 and 300 Hz that cannot be resolved by the model. Also, the constant average amplitude value of 1 delivered by the simple time delay models of equations 8.5 and 8.6 does not reflect the global behaviour of low amplitudes < 1 for high frequencies. Furthermore, the measured phase values show a trend to lie above the values of the linear fit at low frequencies and vice versa for high frequencies, as already illustrated in figure 5.12. Although that trend is not very strong, it can be found in all measured transfer functions.

As a consequence of these shortcomings, an extension of the time delay model is proposed below that is able to overcome the described deficiencies and to match the modelled to the experimentally determined

transfer functions.

For this purpose, the approach utilised by e.g. Pankiewitz [Pan04] (and also Khanna [Kha01]) as described in section 2.2 is used here. He proposes an extension of the simple time lag by a higher order dynamics part that includes the influence of the time-derivatives of both the excitation variable u and the heat release fluctuation $\dot{Q}$. Using these derivatives, any flame behaviour that is characterised by linear differential equations with constant coefficients in the time domain can be mapped.

This approach enables Pankiewitz to reproduce a measured transfer function with good accuracy, with the order of the additional dynamic terms utilised being $n_\alpha = 2$ and $n_\beta = 1$.[67] However, the clear disadvantage of this method is that it quickly generates a high number of parameters whose physical interpretation might be difficult. For example, his approximation of a rather simple transfer function with two local peaks requires a set of 12 parameters. It is therefore not recommended to apply this method on a general basis. In the cases investigated in this work, the details of the transfer function behaviour are already explained with high accuracy by the swirl model. Thus, only a global description of the remaining flame dynamics is required and the number of free parameters is kept low. One weak point of that approach, however, is its empirical nature - the higher order dynamics extension proposed here is not, as for example the swirl model, based on a clear physical understanding of the underlying mechanisms.

To take the dyamic effects observed here into account, a reduced variant of Pankiewitz's time delay model is applied - consult equations 2.32 to 2.35 as a reference. From the variables of equation 2.22 or 2.23, the time delay distribution parameter $\Delta\tau_M$ is omitted, since the effects of interest can also be shown without. However, a future refined model could also include this parameter to better predict the high frequency behaviour. Also, the dynamic model of equation 2.32 is restricted to $n_\beta = 0$, this implies no qualitiative change. A corresponding reduction of n_α to values lower than 2 is however not possible. Since only one global peak needs to be modelled, a restriction to $n_m = 1$ is sufficient.

[67] See equation 2.32.

The resulting model is then - equivalently to equation 2.26 - of the form

$$FTF_{\tau,D}(f) = FTF_{\tau} \cdot FTF_{D} \tag{8.7}$$

$$FTF_{\tau,D}(f) = \frac{e^{-i\omega\tau_M}}{(\alpha_2\, i\omega)^2 + \alpha_1\, i\omega + 1}\,. \tag{8.8}$$

FTF_D represents the classical PT_2 behaviour known from control theory with a resonance peak at an eigenfrequency $\omega_0 = \frac{1}{\alpha_2}$ and a 180° phase shift at that frequency.[68] The damping parameter α_1 controls the amplitude at the eigenfrequency and the extension of the phase shift along the frequency axis. An example for such a second order time delay model is given in figure 2.3. Note especially the phase shift of 180° occurring at the frequency of the global amplitude peak.

To derive the final model, the simple time delay in equation 8.6 is replaced by the higher order dynamics model

$$FTF_{\tau,D,S}(f) = FTF_{\tau,D} + FTF_{S}(f) \tag{8.9}$$

$$FTF_{\tau,D,S}(f) = \frac{e^{-i\omega\tau_M}}{(\alpha_2\, i\omega)^2 + \alpha_1\, i\omega + 1} + FTF_{S}(f)\,. \tag{8.10}$$

This extended time delay model together with the swirl induced behaviour does now allow for a very detailed reconstruction of the measured transfer functions, as shown in figure 8.4 for the same case as earlier in figure 8.3. Both amplitude and phase plot are now matched astonishingly well, compared to the simplicity of the model extension:

- The broad global amplitude peak in the frequency range between 150 and 300 Hz is reproduced.
- The amplitude trend to values < 1 at the high frequency limit is captured.
- Even the slight tendency of the phase plot to lie above the linear fit at low frequencies and below that line at high frequencies[69]

[68] α_2 is thus referred to as resonance parameter.
[69] See figures 5.12 and 8.3 for example.

is now matched. That behaviour is associated with the phase shift of 180° generated by FTF_D at the frequency of the global amplitude peak.

These improvements are a strong hint that the extension FTF_D proposed here does indeed reflect what is happening in reality.

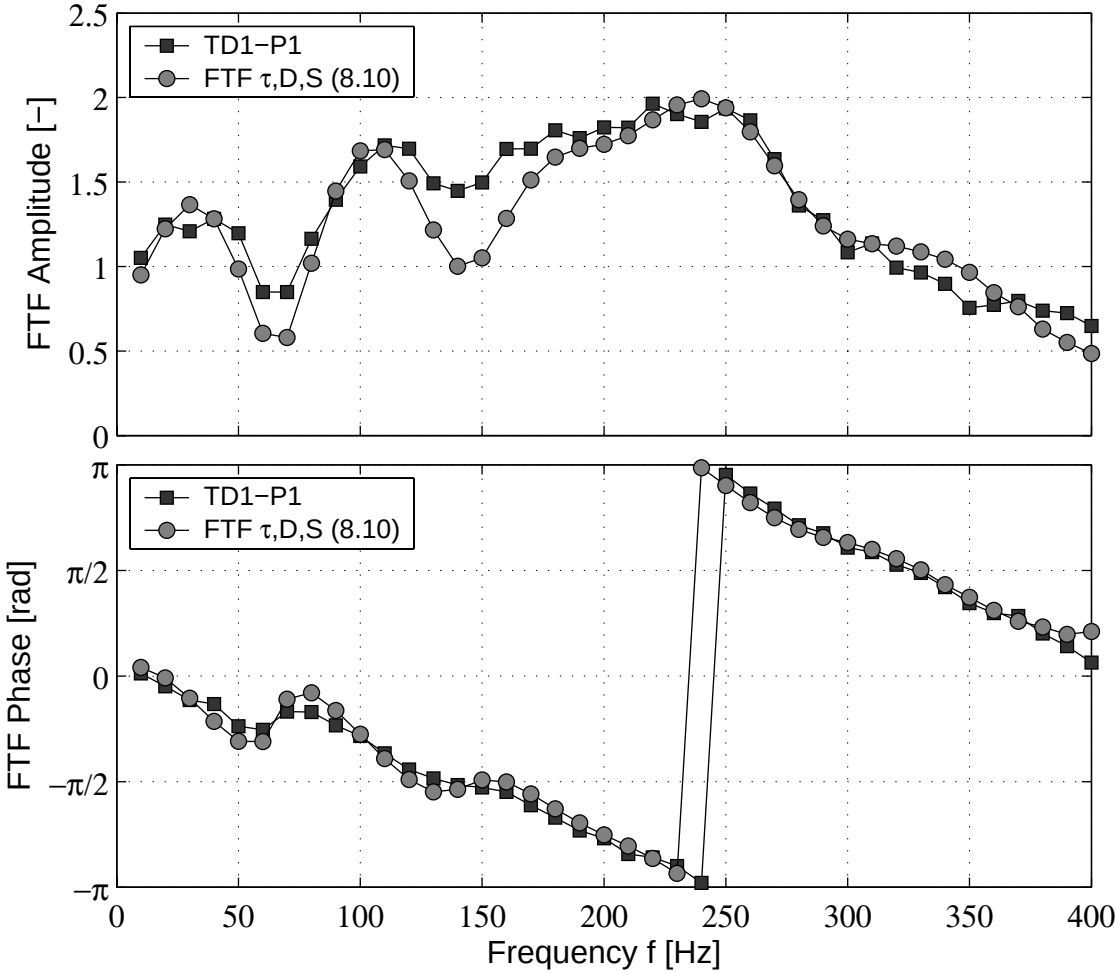

Figure 8.4: $FTF_{\tau,D,S}$ compared to the experimental FTF at TD1-P1.

Two more examples demonstrate the close coherence of the model and the experimental FTFs also at elevated pressures and different air excess ratio settings, see figure 8.5. However, one general tendency observed in the model results is an overestimation of the swirl influence in the low frequency region up to about 150 Hz. This becomes apparent in both amplitude and phase plot, where the swirl-induced

maxima and minima are overpredicted. Above that frequency, the agreement is very good.

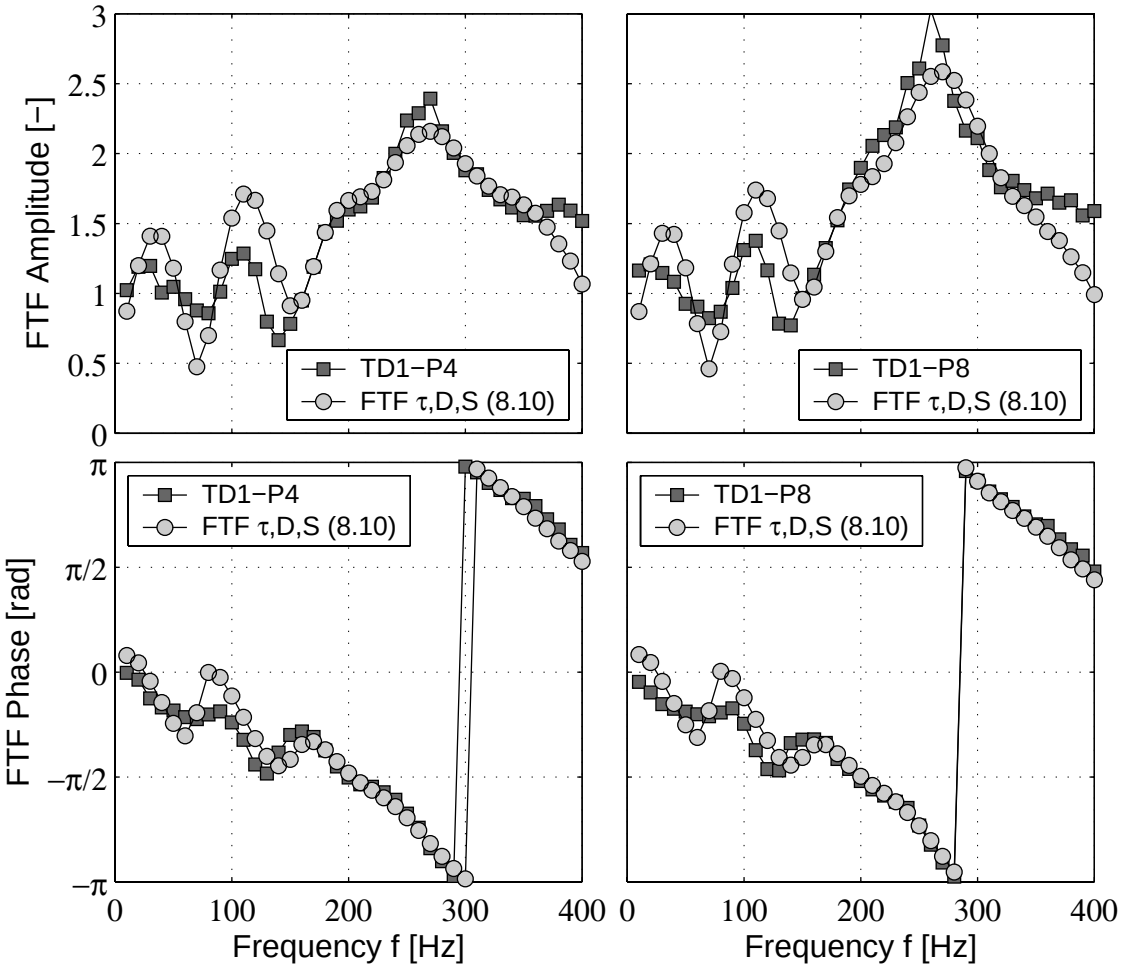

Figure 8.5: $FTF_{\tau,D,S}$ compared to the experimental FTF at TD1-P4 (left) and TD1-P8 (right).

Note that the model FTF at TD1-P1 as shown in figure 8.4 has been determined with a different swirl time delay τ_S (9.6 instead of 8.8 ms) and burner exit velocity u_E (32.1 instead of 35.3 m/s). This is necessary to account for the deviating burner pressure drop $\Delta p/p$ during the FTF measurement.[70] Not applying these corrections would result in a frequency mismatch of the local FTF features generated by the swirl model.

[70] See also table 2.

As a recapitulation of the findings of this section it can be stated that the swirl model together with a simple time delay model delivers a good approximation of the phase plot and can reproduce the local behaviour with minima and maxima of amplitude and phase. That model is however not sufficient to describe the global behaviour of the flame transfer function - a broad amplitude peak between 150 and 300 Hz, a subsequent decline to amplitudes below 1 and a phase that lies above the average gradient for low frequencies and below for high frequencies. An extension of the time delay model comprising 2^{nd} order dynamics is needed to reproduce the global behaviour as described above. The final model does then match the measured data with a very high accuracy.

The behaviour leading to the model extension described above was also observed in the results of Fischer [Fis04] and Kunze [Kun04][71] on the same burner, but only for the low swirl settings also applied here. As shown in [Fis04], raising the burner swirl number increases the low frequency amplitude peaks and reduces the amplitude at higher frequencies. The latter effect seems to be related to the compact and well stabilised flame at high swirl that reduces the degrees of freedom of local heat release fluctuations within the flame. However, one general conclusion thereof is that the necessity of applying the 2^{nd} order time delay model introduced here might be limited to cases with a low burner swirl number.

8.1.3 Pressure Scaling

After developing a model that is able to reproduce the measured FTFs it is now interesting how the model parameters scale with pressure and air excess ratio. Four parameters remain to define the FTF model - the heat release distribution as the only variable to influence the swirl part, the higher order dynamic parameters α_1 & α_2 and τ_M to characterise the time delay. Since the axial heat release distribution and thus the whole swirl part of the model is given by the flame imaging results, only the time delay and higher order dynamics parameters

[71] And also in the work of Auer [Aue05].

are investigated here. In order to determine these parameters for the individual operating points, a Matlab routine was developed that performs a least squares fit to the experimental FTF data with α_1, α_2, τ_M as variables. Table 10 gives the results.

Table 10: FTF model parameters resulting from a least squares fit to the experimental FTFs.

Operating Point	τ_M [ms]	α_1 [ms]	α_2 [ms]
TD1-P1	1.202	0.352	0.626
TD1-P2	1.183	0.408	0.727
TD1-P3	0.945	0.271	0.536
TD1-P4	0.816	0.253	0.525
TD1-P5	1.079	0.235	0.566
TD1-P6	1.028	0.258	0.553
TD1-P7	1.045	0.241	0.505
TD1-P8	0.863	0.223	0.550

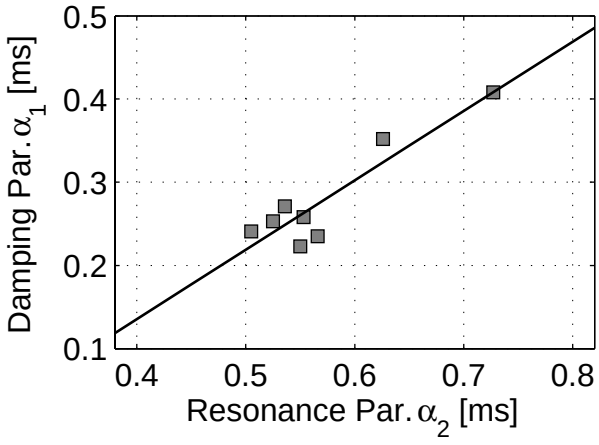

Figure 8.6: Correlation of damping parameter α_1 and resonance parameter α_2.

As a first result, a correlation between α_1 and α_2 was detected - as shown in figure 8.6 - that allows for a further reduction of the independent variables by making use of the approximation

$$\alpha_1\,[\mathrm{ms}] = 0.835\,\alpha_2\,[\mathrm{ms}] - 0.199\,. \tag{8.11}$$

As discussed in the context of equation 2.27, the PT_2 behaviour described by the parameters α_1 and α_2 can be interpreted as the result of the interaction of two PT_1 elements. Since the time constants τ_1 and τ_2 of these elements are closely related in the form of a conjugate-complex pair, also the parameters α_1 and α_2 in the equivalent formulation of equation 8.8 are connected. Expression 8.11 captures that correlation. As the 2^{nd} order dynamics model in general, 8.11 is an empirical relation, the actual parameter values can only be determined from the experiment. The underlying physics remain unclear as long as the mechanism described by FTF_D is not identified.

Since a constant peak amplitude at the eigenfrequency $\omega_0 = 1/\alpha_2$ is obtained for $\alpha_1 \propto \alpha_2$, the correlation of equation 8.11 showing an over-proportional rise of α_1 with α_2 describes a slight increase in the peak amplitude for increasing eigenfrequency.

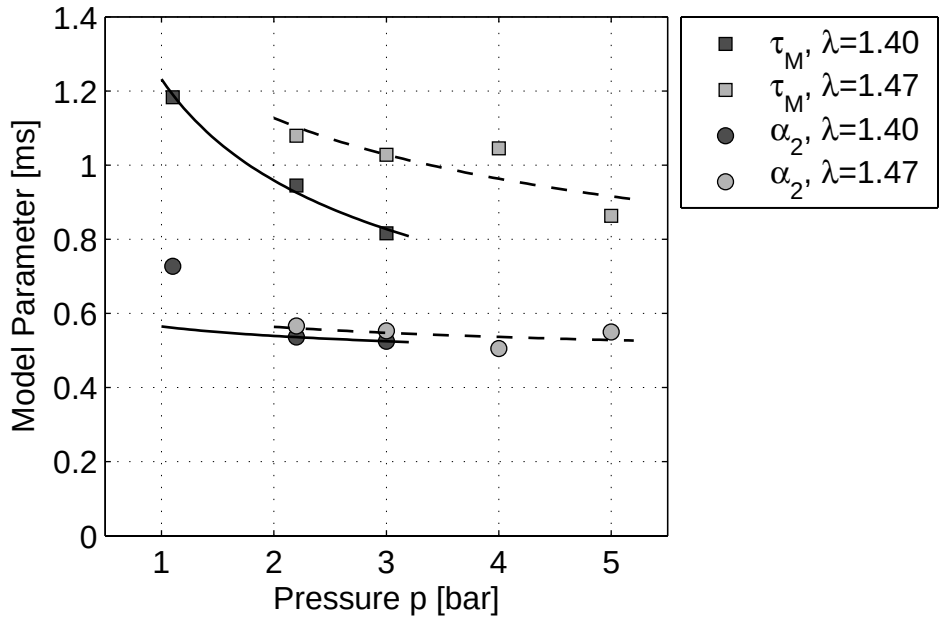

Figure 8.7: Pressure scaling of model time delay τ_M and resonance parameter α_2.

After eliminating α_1, α_2 and τ_M remain to characterise the model behaviour, both are plotted in figure 8.7 over pressure. Note the similarities to figure 5.13 - both parameters exhibit a decline towards rising pressure and decreasing air excess ratio.

Table 11: Coefficients for power law pressure scaling of model time delay τ_M and resonance parameter α_2 according to equations 8.12 and 8.13. For evaluation use the following units: bar for pressure, ms for τ_M and α_2.

Parameter	λ	a	b
τ_M	1.4	1.232	0.362
	1.47	1.319	0.227
α_2	1.4	0.565	0.067
	1.47	0.593	0.072

Similar to section 5.2, power laws analog to equation 5.12 can be found to characterise the decrease of τ_M and α_2 with pressure. The corresponding values of a and b are given in table 11.

$$\tau_M = a_{\tau_M} p^{b_{\tau_M}} \tag{8.12}$$

$$\alpha_2 = a_{\alpha_2} p^{b_{\alpha_2}} \tag{8.13}$$

In figure 5.13, the global time delay value derived for the operating point TD1-P2 at 1.1 bar and $\lambda = 1.4$ was considered an outlier, since that point lies significantly above the power law trendline. The model results derived here show that this behaviour is caused solely by a deviation of α_2, the model time delay parameter τ_M lies perfectly on the trendline. As a consequence, α_2 of TD1-P2 was not considered in the derivation of the power law for $\lambda = 1.4$.

8.1.4 Extrapolation to Realistic Engine Pressures

With the model developed so far and using some of the experimental data, it is now possible to perform extrapolations of the modelled flame transfer function to realistic engine pressure levels. A major benefit of this procedure - in comparison to the method of section 5.4 based on τ_G only - is that the extrapolation is not limited to a global time delay scaling, but can generate a transfer function comprising all details of amplitude and phase.

Similar to the pure time delay extrapolation given in table 6, the ex-

trapolation procedure derived here is applied to the series of operating points at the air excess ration of $\lambda = 1.47$. The necessary steps are summarised as follows:

1. Apply equation 5.15 and table 5 to extrapolate the flame length L_F to the pressure of interest p.
2. Scale the axial coordinate of the axial heat release distribution at one reference pressure p_{ref} with the ratio of flame lengths $L_{F,p}\,/L_{F,p_{ref}}$. This implies that the axial heat release distribution between reference and extrapolated pressure does not change qualitatively.
3. Implement the axial heat release distribution derived in step 2 into the swirl model of section 8.1.1 to generate the swirl part of the transfer function model FTF_S.
4. Apply equations 8.12 and 8.13 with the parameter values of table 11 to derive the 2^{nd} order time delay model parameters τ_M and α_2 for the extrapolated pressure.
5. Use equation 8.11 to find the damping parameter α_1 for the extrapolated pressure.
6. Build the extrapolated FTF from the two parts using equation 8.10.

Figure 8.8 shows the FTFs resulting from an extrapolation according to the above procedure for an air excess ratio of $\lambda = 1.47$. The axial heat release distribution of TD1-P8 at a pressure of 5 bar was taken as a reference, the extrapolated pressures are 10, 20 and 30 bar. Additionally, a backward application of the extrapolation procedure to a pressure of 2.2 bar was performed as a cross-check.

While the FTF behaviour at different pressures is similar at low frequencies, two general trends can be extracted from the high frequency region of the extrapolated transfer functions:

- A shift of the broad global amplitude peak between 150 and 350 Hz towards higher frequencies. The decrease of the resonance

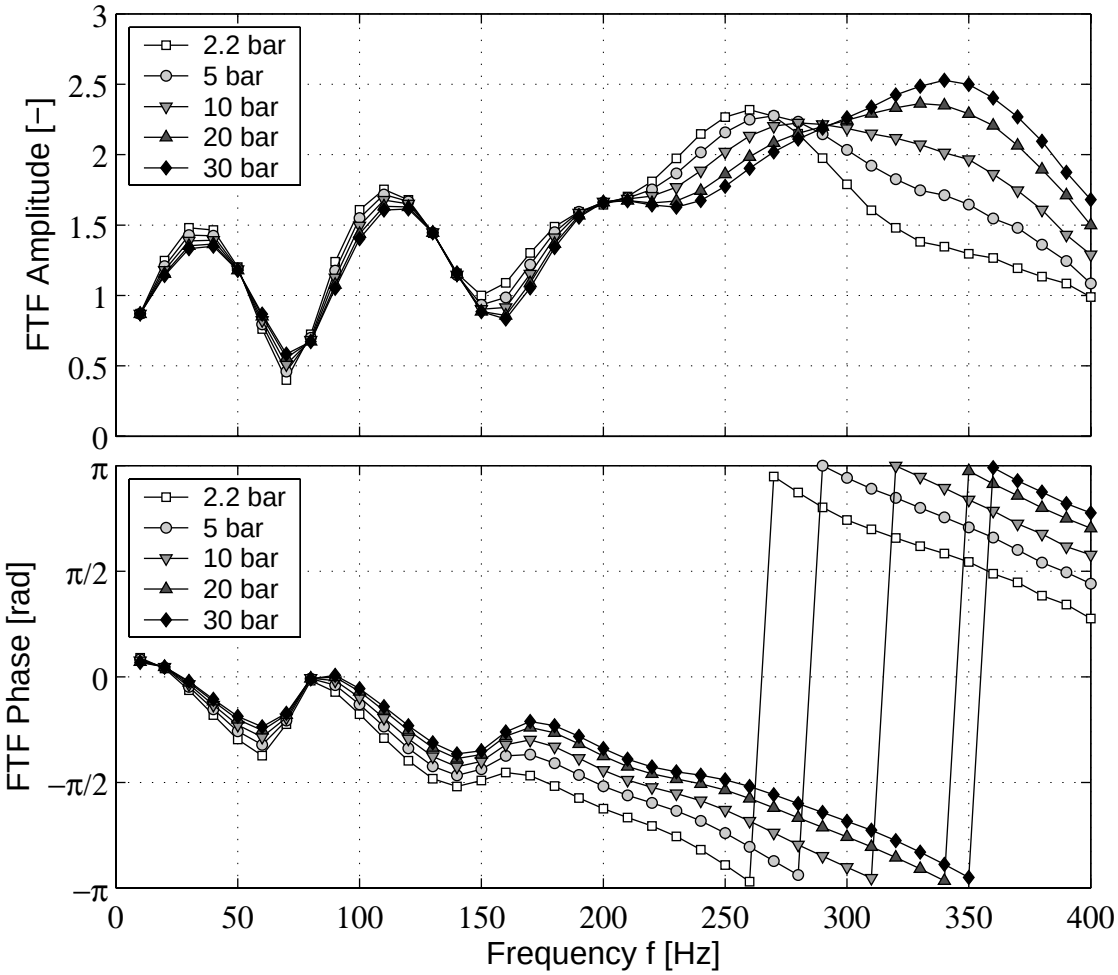

Figure 8.8: Extrapolated FTFs at $\lambda = 1.47$, Reference: TD1-P8 at 5 bar.

parameter α_2 is responsible for this behaviour. Also, the slight increase of the peak amplitudes due to the overproportional scaling of the damping parameter α_1 as indicated above is found here.

- A major reduction of the phase drop, especially at higher frequencies. This is caused by both a reduction of the time delay parameter τ_M and the above-mentioned resonance shift to higher frequencies.

Especially the second point is of major importance for the practical application, the FTF phase difference of more than $\pi/2$ observed between 2.2 and 30 bar at around 300 Hz can render a stable combustion

system unstable or vice versa. This effect is even stronger at richer equivalence ratios due to the rise of the exponents of the pressure scaling laws.

Compared to the phase plots of the experimental results shown in figures 5.6 and 5.7, the change of behaviour from almost identical phases below 120 Hz to a clear separation above that frequency is visible, but less pronounced in the model results of figure 8.8. The reason for this behaviour is probably found in additional flame dynamics not captured by the model - for example a variation of the flame length during an excitation cycle as discussed in section 5.3.

8.2 Industrial Burner, Perfectly Premixed

In this section, the model developed above is applied to the industrial burner setup and compared to the flame transfer functions presented in section 6. Again, the model consists of two parts - the swirl part and the dynamic time delay part. A sketch of the burner setup as used for the swirl part is given in figure 8.9.

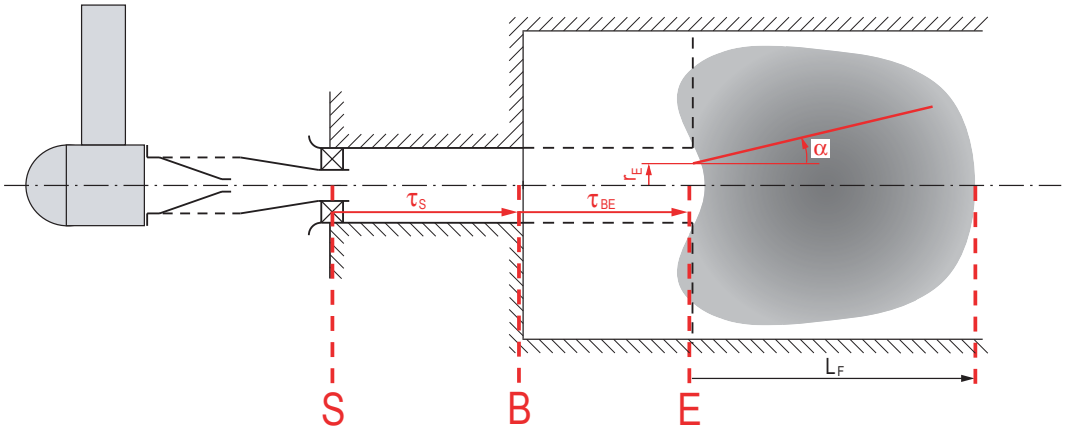

Figure 8.9: Sketch of the swirl model applied to the industrial burner.

Unlike the TD1 flame, the flame of the industrial burner investigated here is not stabilised by a central recirculation zone, but at an axial location far downstream, where the turbulent flame speed equals the axial flow velocity. This stabilisation mechanism is rather weak, and

small changes like the decreasing relative heat loss to the walls with rising pressure do significantly modify the flame position. The flowfield in the combustor has the form of a turbulent swirled jet without vortex breakdown and with weak corner recirculation zones. Due to the lower flow velocity at larger radii, the flame can propagate further upstream in the outer regions of the combustor and the flame envelope shows a characteristic V-shape as illustrated in figure 6.2. Combustion induced vortex breakdown (CIVB) does not occur in the operating regime where FTFs have been measured.[72]

After entering the combustor, the axial flow velocity decreases hyperbolically according to the following law that has been determined by a fit to PIV measurement data of the same burner acquired in a different test rig [FES02a].

$$u_B(x) = \frac{u_{B,0}}{1 + 35\,x}\,, \quad x...[\mathrm{m}] \tag{8.14}$$

Due to the large flame standoff distance of the industrial burner, a modification of the original swirl model is required. The sketch in figure 8.9 provides an overview. In the modified swirl model, the flame offset is accounted for by moving the reference plane (E) as the starting point for the integration along the streamline from the burner exit (B) to the position in the combustor where the flame root is located. For the model, the turbulent jet from the burner exit to the flame root is thus considered a part of the burner. In detail, a number of changes to the original TD1 model are required to adapt the swirl model to the new conditions:

- The swirl time delay τ_S from the swirler to the burner exit is increased to τ_{SE} by an additional amount τ_{BE} from the burner exit to the reference plane at the flame root. The latter can be determined by integrating equation 8.14 in that range.
- Due to the velocity decay in the combustor, $u_{E,0}$ instead of $u_{B,0}$ is used as an input to the numerical procedure delivering FTF_S.

[72] For high pressure and a nearly stoichiometric mixture CIVB has been observed though. The flame does then stabilise directly at the burner exit in the anchored mode illustrated in the left image of figure 6.1.

Nevertheless, the velocity reference to determine the swirl transfer function remains at (B) to ensure comparability to the experimental results.

- Similar to the velocity decay, also the swirl number S_0 and with it the flow angle α of the turbulent jet decrease along its path through the combustor due to momentum exchange with the ambient gas.
- Since parts of the flame are beyond the visible range of the side window for all investigated operating conditions, no axial flame intensity distribution can be derived from camera images. A symmetrical Gaussian distribution as used by Hirsch [HSP+05] is thus assumed. The associated flame length is estimated.

With these modifications, the swirl transfer function FTF_S for the industrial burner can be determined. Note that the quality of the current model is lower than the one for the TD1 burner due to the estimates for swirl decay and heat release intensity distribution.

As for the TD1 burner, the second part of the model is a dynamic time delay of second order. To determine the model parameters, the same least squares fit routine was applied. One extension is necessary here to obtain a good fit to the experimental data - the order of the enumerator of Pankiewitz's time delay model given in equation 2.32 is set to 1 instead of 0. This implies the introduction of an additional parameter β, whose main impact is an amplification of the amplitude at higher frequencies and an additional phase shift of $+90°$ in the high frequency limit. With the introduction of β, equation 8.10 extends to

$$FTF_{\tau,D,S}(f) = e^{-i\omega\tau_M}\frac{\beta\, i\omega + 1}{(\alpha_2\, i\omega)^2 + \alpha_1\, i\omega + 1} + FTF_S(f)\ . \qquad (8.15)$$

An example of the dynamic time delay behaviour with and without the influence of β is illustrated in figure 8.10 using the parameter values determined for TM-P1. Another extension of the model to include a time delay dispersion $\Delta\tau_M$ has been tested, but gives no significant further improvement.

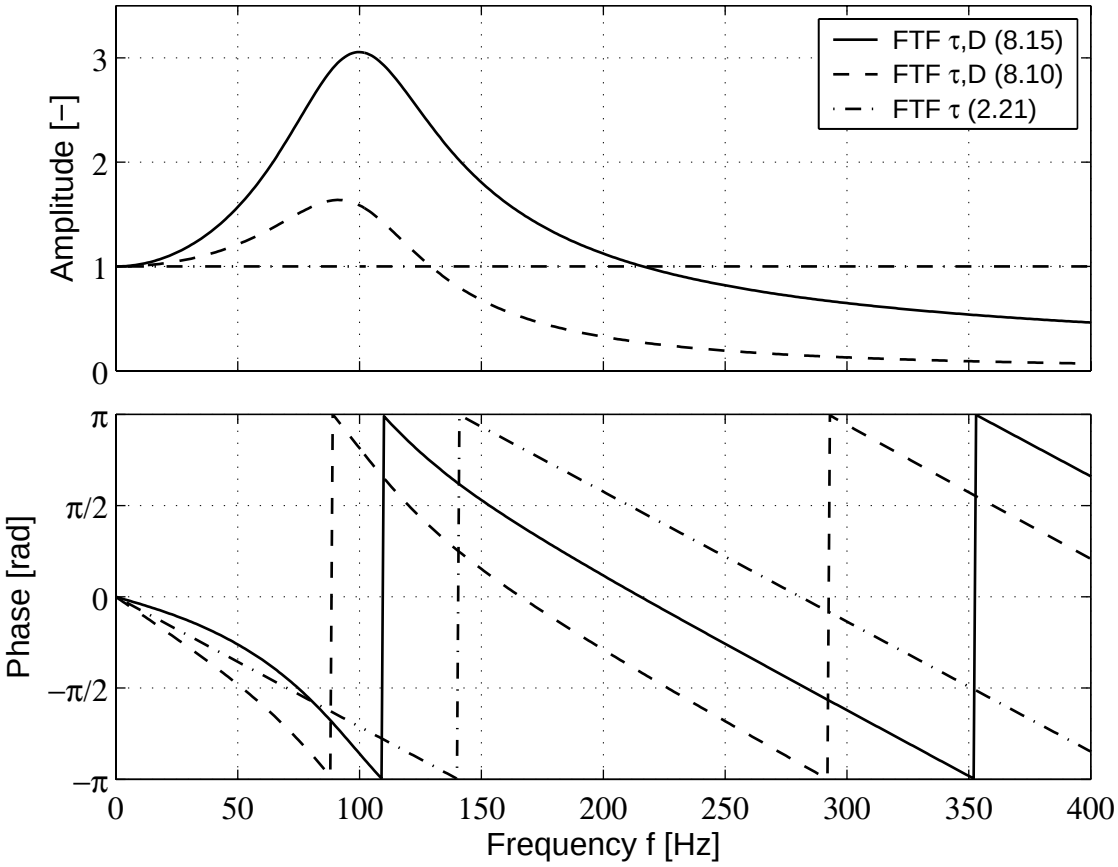

Figure 8.10: Dynamic time delay model $FTF_{\tau,D}$ with (8.15) and without (8.10) the additional parameter β. Pure time delay model FTF_{τ} as reference. Parameter values for IB-P3, taken from table 12.

In the time-domain, the now necessary additional parameter β represents an additional dependence of the fluctuating heat release on the first time derivative of the velocity perturbation du'_B/dt within the burner. The differential equation describing the flame behaviour of equation 8.15 (without the swirl part) in the time domain is then given as follows.

$$\alpha_2^2 \frac{d^2\dot{Q}'(t)}{dt^2} + \alpha_1 \frac{d\dot{Q}'(t)}{dt} + \dot{Q}'(t) = \frac{\overline{\dot{Q}}}{\overline{u}_B} \left(u'_B(t-\tau_M) + \beta \frac{du'_B(t)}{dt} \right) \quad (8.16)$$

A physical relevance of the additional term with the time derivative of the burner velocity fluctuation can not be excluded, but more likely this is a measurement artefact of the non-uniform frequency response

Table 12: Model parameter values for the industrial burner in PP mode.

Parameter	Unit	IB-P1	IB-P2	IB-P3
p	bar	1.75	2.50	2.80
$u_{B,0}$	m/s	40	40	40
$S_{B,0}$	-	0.6	0.6	0.6
τ_S	ms	3	3	3
$u_{E,0}$	m/s	8	10	11
$S_{E,0}$	-	0.16	0.2	0.22
τ_{BE}	ms	8	6	5
τ_{SE}	ms	11	9	8
L_F	mm	160	140	140
τ_M	ms	4.22	4.05	3.56
$\Delta\tau_M$	ms	-	-	-
α_1	ms	1.21	1.77	1.00
α_2	ms	1.51	2.03	1.55
β	ms	2.89	6.70	2.62

of the burner flow velocity to excitation[73]. Since the velocity measurement at the CTA location does only partially represent the burner velocity fluctuation, a systematic error in the measured FTF is likely, which in turn may cause the additional dynamics. In that case, the second order dynamics model would be the same as for the generic burner - without the additional parameter β.

A summary of the parameter values of the swirl and dynamic time delay models is given in table 12, and an example illustrating the quality of the model fit to the experimental data is presented in figure 8.11. Similar to the TD1 model, the agreement with the measurements is good. Modelling efforts for IB-P4 and IB-P5 have been omitted, since no additional findings are expected and these operating points can not be compared to the technically premixed case as discussed in the next section.

With the exception of τ_M that is decreasing with pressure as expected, the dynamic model parameters do not show a clear dependence on pressure like in the previous section. This is supposed to emanate from the low quality of the measurement data used as basis for the

[73] See section 6.2, page 116.

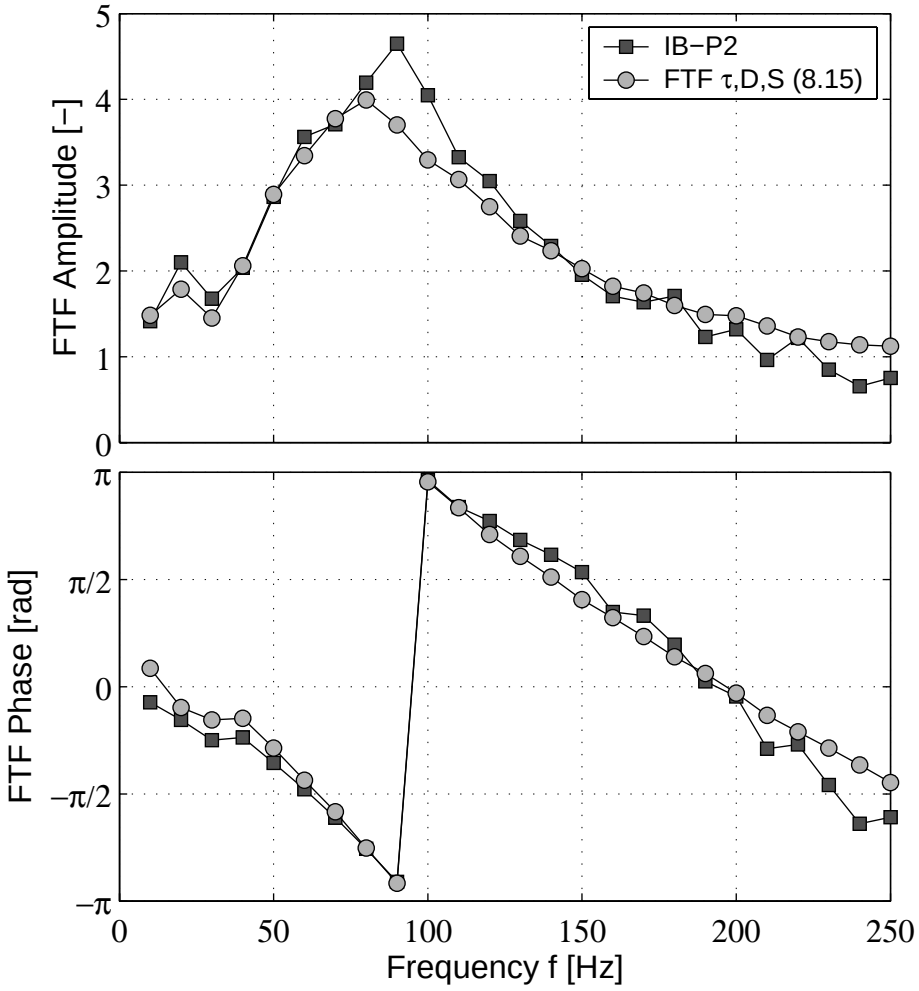

Figure 8.11: $FTF_{\tau,D,S}$ compared to the experimental FTF at IB-P2.

model fit. However, the fact that the frequency and amplitude value of the global peak at about 100 Hz is similar for all operating points indicates that the time delay model parameters are not independent and a relation between two or more of them analog to equation 8.11 exists. Compared to the TD1 model, the values of α_2 are substantially larger and generate the lower peak frequency of about 100 Hz (vs. about 250 Hz for the TD1). Although the damping parameter α_1 is also larger, the amplification caused by β overcompensates the damping, which results in generally higher global peak amplitudes in the range of 2.5 - 4.

In general, the relative importance of the swirl contribution to the model is lower than for the TD1. This is caused by the swirl decay

on the way from the burner exit to the flame root. Also, the already low amplitude of the swirl part of the model is diminished quickly with rising frequency, which limits its influence to the low frequency region below 100 Hz. The resulting transfer functions are thus clearly dominated by the global behaviour induced by the 2^{nd} order time delay. Nevertheless, the local peak and the associated deviation from the linear phase drop at about 30 Hz is well reproduced, leading to the conclusion that this feature is indeed caused by the swirl fluctuation. A comparison of the model plots for operating points IB-P1 to IB-P3 as given in figure 8.12 shows indications that the pressure dependent deviation of the phase from the linear decline at about 30 Hz, which has been pointed out in section 6.2, is also reproduced by the model.

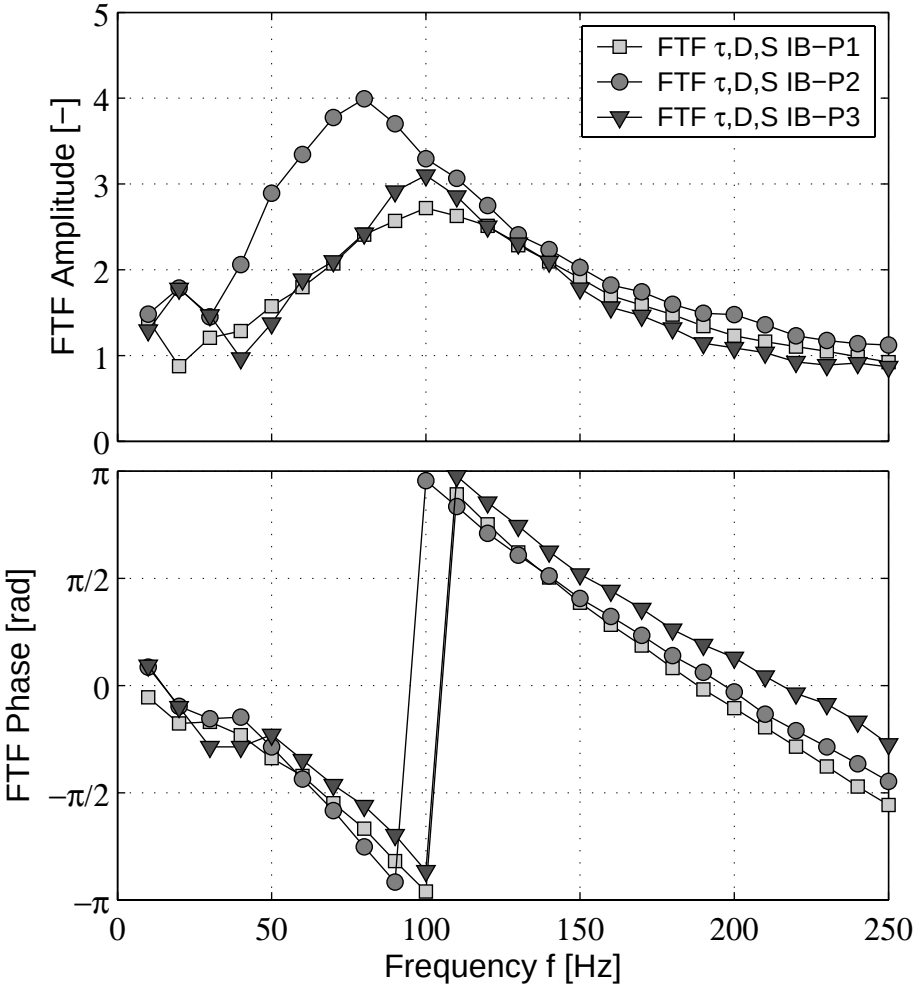

Figure 8.12: Model FTFs for IB-P1 to IB-P3.

8.3 Industrial Burner, Technically Premixed

After presenting a model to fit the measured transfer functions in the perfectly premixed case, this section discusses the mixture fraction fluctuations occurring in the transfer functions of the industrial burner in technically premixed mode as reported in section 7. A model is derived that is able to separate the systematic errors induced by the mixture fraction fluctuation on the flame OH* intensity and on the hot wire measurement[74] and to extract the true flame transfer function of the TP mode. The comparison of the PP and TP mode FTFs results in a formulation for the influence of the mixture fraction fluctuation on the flame transfer function. The knowledge of the latter does then allow to define another model for the mixture fraction influence and to predict transfer functions for the TP mode.

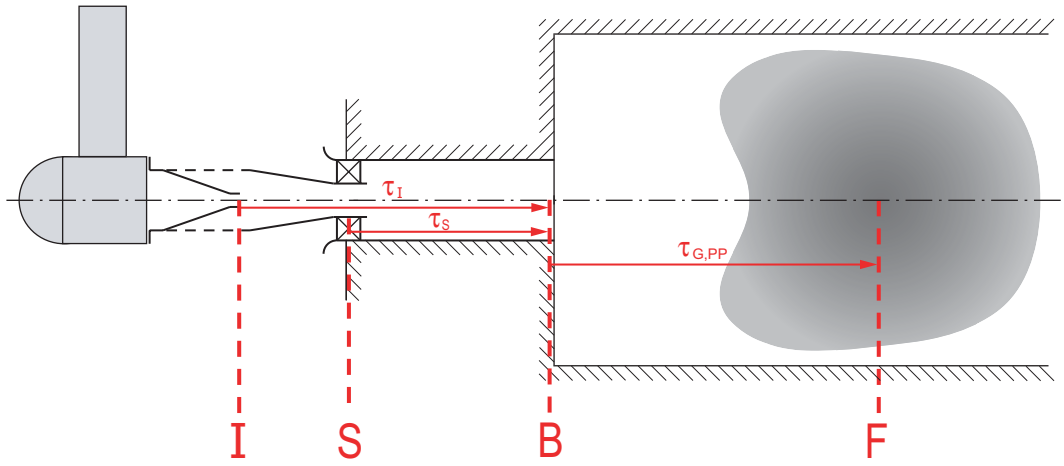

Figure 8.13: Sketch of the industrial burner in TP mode with time delays.

In technically premixed mode, fluctuations of the fuel-air mixture fraction occur due to the limited mixing length available. These fluctuations are formed by the acoustic perturbations of air and fuel mass flow at the injector nozzle and are subsequently convected to the burner exit and further on into the flame with the local flow velocity. To account for this convection process, a time delay τ_I from the injector to the burner exit is introduced. Strong shear gradients and a high level

[74] See sections 4.1.3 and 4.2.3.

of turbulence lead to a large spatial dispersion of any mixture fraction perturbation, this is modelled here by introducing a distribution of the time delay described by a characteristic dispersion parameter $\Delta\tau_I$. A sketch is given in figure 8.13.

One important assumption of the model presented here is that the mixture fraction perturbations represent an additional effect and the dynamics observed in perfectly premixed mode do also occur here. This assumption is justified by a very similar flame form and location observed in PP and TP mode, as shown in figure 7.2. The mixture fraction perturbations can then be considered to ride "on top" of the PP mode dynamics.

8.3.1 Extraction of the Influence of Mixture Fraction Fluctuations

As discussed in section 2, the heat release perturbation of the flame can be split into its components according to

$$\left.\frac{\dot{Q}'}{\overline{\dot{Q}}}\right|_{u'_B,\,\lambda'_B} = \left.\frac{(S_F \cdot A_F)'}{\overline{(S_F \cdot A_F)}}\right|_{u'_B,\,\lambda'_B} - \left.\frac{\lambda'_F}{\overline{\lambda}_F}\right|_{\lambda'_B}, \tag{8.17}$$

where the first term represents the overall response of the flame speed and its surface area to both velocity and mixture fraction perturbations. That relation can be decomposed into the contributions of velocity and air excess ratio and linked to those perturbations at the burner exit B by introducing flame transfer functions.

$$\frac{\dot{Q}'}{\overline{\dot{Q}}} = FTF_u \frac{u'_B}{\overline{u}_B} + FTF_\lambda \frac{\lambda'_B}{\overline{\lambda}_B} \tag{8.18}$$

In equation 8.18, FTF_u is equivalent to the transfer function obtained in PP mode, while FTF_λ is the extension for TP that takes the effects of a mixture fraction fluctuation at the burner into account. The transfer function of the flame heat release to the burner velocity fluc-

tuation in the technically premixed case is then expressed as

$$FTF_{TP} = \frac{\dot{Q}'}{\overline{\dot{Q}}} \frac{\overline{u}_B}{u'_B} = FTF_{PP} + FTF_\lambda \frac{\lambda'_B}{\overline{\lambda}_B} \frac{\overline{u}_B}{u'_B} \,. \tag{8.19}$$

Note that FTF_λ is scaled by the relation between velocity and air excess ratio fluctuation at the velocity measurement location within the burner, which are not necessarily the same. The identification of the mixture fraction transfer function FTF_λ can now be performed by a subtraction of the two transfer functions FTF_{TP} and FTF_{PP}.

Unfortunately, the OH* radiation intensity I used as the measure for the heat release in the experiment does not only depend on the fuel flow into the flame, but also on the air excess ratio. This latter dependence is non-linear and characterised by an exponent K_{OH}.[75]

$$I_{OH^*} \propto \frac{S_F \cdot A_F}{\lambda_F^{K_{OH}}} \tag{8.20}$$

Equation 8.20 was derived by Higgins [HML+01] from chemiluminescence measurements and is also used by Schuermans [SBG+04]. Again, a linearisation is performed that gives an expression similar to equation 8.17.

$$\frac{I'_{OH^*}}{\overline{I}_{OH^*}} = \frac{S'_F \cdot A'_F}{\overline{S_F \cdot A_F}} - K_{OH} \frac{\lambda'_F}{\overline{\lambda}_F} \tag{8.21}$$

This similarity can be used to derive

$$\frac{I'_{OH^*}}{\overline{I}_{OH^*}} = FTF_{PP} \frac{u'_B}{\overline{u}_B} + FTF_\lambda \frac{\lambda'_B}{\overline{\lambda}_B} + (K_{OH} - 1) FTF_\lambda \frac{\lambda'_B}{\overline{\lambda}_B} \,, \tag{8.22}$$

where the first two terms represent the heat release fluctuation $\dot{Q}'/\overline{\dot{Q}}$ according to equation 8.18 and the third term captures the systematic

[75] Since all operations are performed at constant operating pressure, the influence of p on the chemiluminescence intensity is not considered in the equations of this section. However, the impact of an acoustic pressure fluctuation on the OH* chemiluminescence emission and the CTA measurement is generally not negligible. That influence is presented in section 4.1.4 and 4.2.4. Furthermore, a method to directly correct the measured FTFs is found in equation C.4.

error SE_{OH} due to the sensitivity of the OH* emission on the fuel mass fraction.[76] Note that the negative sign of the K_{OH}-term in equation 8.21 is transferred into FTF_λ in 8.22. FTF_λ does thus approach a phase value of π in the low frequency limit, as demonstrated later in figure 8.14.

A second error has to be corrected in the measured CTA signal $u_{B,m}$. As shown in section 4.1.3, the CTA does not only detect the real velocity u_B, but also has a sensitivity to air excess ratio fluctuations that introduce an error signal $u_{B,\lambda}$ according to equation 4.3.

Taking both measurement deviations into account leads to an expression defining the actually measured flame transfer function in the TP case

$$TF_{OH/CTA} = \frac{I'_{OH^*}}{\overline{I}_{OH^*}} \frac{\overline{u}_B}{u'_B + u'_{B,\lambda}} , \tag{8.23}$$

or with substituting equation 8.22 to

$$TF_{OH/CTA} = \frac{FTF_{PP} + FTF_\lambda \frac{\lambda'_B}{\overline{\lambda}_B} \frac{\overline{u}_B}{u'_B} + (K_{OH} - 1) FTF_\lambda \frac{\lambda'_B}{\overline{\lambda}_B} \frac{\overline{u}_B}{u'_B}}{1 + \frac{u'_{B,\lambda}}{u'_B}} . \tag{8.24}$$

Before this expression can be evaluated, the relations between λ'_B and u'_B as well as between $u'_{B,\lambda}$ and u'_B need to be analysed. For that purpose, additional transfer functions TF are introduced. For example, the air excess ratio fluctuations at the CTA measurement position in the burner (B) and at the fuel injection position (I) link with a convective time delay (distribution) $TF_{IB,\lambda}$ according to

$$\frac{\lambda'_B}{\overline{\lambda}_B} = \frac{\lambda'_I}{\overline{\lambda}_I} TF_{IB,\lambda} . \tag{8.25}$$

The air excess ratio fluctuation at the injector can be further split up into the fluctuation of its components air velocity u_I and fuel mass

[76] K_{OH} is determined from a steady-state calibration over λ as presented in figure 4.5 (see also equation 8.38). Note that equation 8.22 is only valid if the response of heat release and OH*-intensity to a variation of the air excess ratio for any excitation frequency is the same as obtained in the steady-state calibration.

flow $\dot{m}_f$. The former is then linked back to (B) by an acoustic transfer function $TF_{IB,u}$, leading to

$$\frac{\lambda'_B}{\overline{\lambda}_B} = \left(\frac{u'_B}{\overline{u}_B} \, TF_{IB,u} - \frac{\dot{m}'_f}{\overline{\dot{m}}_f} \right) TF_{IB,\lambda} \, . \tag{8.26}$$

A similar consideration gives a replacement of the term in the denominator of equation 8.24

$$\frac{u'_{B,\lambda}}{u'_B} = K_{u_B} \, TF_{IB,\lambda} \, , \tag{8.27}$$

with

$$K_{u_B} = \left. \frac{u'_{B,\lambda}}{u'_B} \right|_{\omega=0} \, . \tag{8.28}$$

Substituting equations 8.26 and 8.27 into 8.24 results in the definition of the measured flame transfer function in TP mode

$$\begin{aligned} TF_{OH/CTA} = & \frac{FTF_{PP} + FTF_\lambda \left(TF_{IB,u} \, TF_{IB,\lambda} - \frac{\dot{m}'_f}{\overline{\dot{m}}_f} \frac{\overline{u}_B}{u'_B} \, TF_{IB,\lambda} \right)}{1 + K_{u_B} \, TF_{IB,\lambda}} \\ & + \frac{(K_{OH} - 1) FTF_\lambda \left(TF_{IB,u} \, TF_{IB,\lambda} - \frac{\dot{m}'_f}{\overline{\dot{m}}_f} \frac{\overline{u}_B}{u'_B} \, TF_{IB,\lambda} \right)}{1 + K_{u_B} \, TF_{IB,\lambda}} \, . \end{aligned} \tag{8.29}$$

In many cases, simplifications can be applied to expression 8.29. These are:

1. **Choked fuel injector**

   If the fuel pressure drop over the injector nozzle is high enough, the fuel flow is independent of any acoustic perturbation in the combustion air or in the fuel system. In other words, the acoustic impedance of the fuel nozzle $Z_f = p'_f / u'_f$ approaches infinity.

$$\frac{\dot{m}'_f}{\overline{\dot{m}}_f} = 0 \tag{8.30}$$

2. **Acoustic compactness**

   If the distance between two locations is much smaller than the acoustic wavelength for the highest frequency of interest, the acoustic variables at those locations can be considered identical. Applied to the locations of fuel injector and velocity measurement in the current case, the assumption of acoustic compactness leads to

$$\frac{u'_I}{\overline{u}_I} = \frac{u'_B}{\overline{u}_B} \quad \text{and} \quad TF_{IB,u} = 1 \; . \tag{8.31}$$

3. **Same location of fuel injector and velocity reference**

   This eliminates the transfer function between the two locations.

$$TF_{IB,\lambda} = 1 \tag{8.32}$$

For the industrial burner investigated here, simplifications 1 and 2 apply. The convective time delay between fuel injector and velocity measurement position is modelled using an expression following [Sat00]

$$TF_{IB,\lambda} = e^{-i\omega\tau_I} \, \frac{e^{i\omega\Delta\tau_I} - e^{-i\omega\Delta\tau_I}}{2\Delta\tau_I i\omega} \; , \tag{8.33}$$

where τ_I can be calculated from the average flow velocity in the mixing tube and the associated dispersion parameter $\Delta\tau_I$ is estimated to $0.2\,\tau_I$[77].

With the above considerations, equation 8.29 reduces to

$$TF_{OH/CTA} \; = \; \frac{FTF_{PP} + FTF_\lambda + (K_{OH} - 1)FTF_\lambda}{1 + K_{u_B} \, e^{-i\omega\tau_I} \, \frac{e^{i\omega\Delta\tau_I} - e^{-i\omega\Delta\tau_I}}{2\Delta\tau_I i\omega}} \; . \tag{8.34}$$

The parameter K_{u_B} represents the (normalised) maximum amplitude of the systematic error SE_{CTA} induced by the mixture ratio fluctuation

[77] See table 13 for a summary of the model parameters. Note that also the model of Polifke from equation 2.23 can be applied without qualitative changes of the results.

on the CTA measurement.

$$SE_{CTA} = K_{u_B}\, e^{-i\omega\tau_I}\, \frac{e^{i\omega\Delta\tau_I} - e^{-i\omega\Delta\tau_I}}{2\Delta\tau_I i\omega} \tag{8.35}$$

Note that K_{u_B} as defined in equation 8.28 is identical to the mixture fraction calibration factor of the CTA introduced in equation 4.5. For this reason, the actual value of K_{u_B} can be found from figure 4.3 with the unmixedness parameter of equation 7.1 as input.

In equation 8.34, the systematic error SE_{OH} of the mixture fraction fluctuation on the OH* chemiluminescence is captured by

$$SE_{OH} = (K_{OH} - 1) FTF_\lambda \,. \tag{8.36}$$

The last missing parameter K_{OH} can now be determined using the steady-state[78] calibration data of the photomultiplier. By substituting the linearised expression for the air excess ratio in dependence of air and fuel mass flows

$$\frac{\lambda'}{\overline{\lambda}} = \frac{u'}{\overline{u}} - \frac{\dot{m}'_f}{\overline{\dot{m}}_f} \tag{8.37}$$

into equation 8.21, K_{OH} is defined as

$$K_{OH} = \frac{\frac{\Delta u}{\overline{u}} - \frac{\Delta I_{OH^*}}{\overline{I}_{OH^*}}}{\frac{\Delta u}{\overline{u}} - \frac{\Delta \dot{m}_f}{\overline{\dot{m}}_f}} \,. \tag{8.38}$$

In order to syntactically distinguish between acoustic perturbations and parameter variations during calibration, a Δ instead of the $'$ is introduced in equation 8.38. As specified in table 3, three types of photomultiplier calibration are possible: (A) refers to the standard FTF calibration with constant λ, (B) denotes a λ-variation by modulating the air flow at constant thermal power and (C) is a variation of both mixture fraction and thermal power by a modulation of the fuel mass flow. Since the variations of air and fuel mass flow compensate

[78] Steady-state in this context means that the calibration process can be interpreted as an excitation that is inducing a deviation from the operating point with a frequency $f \to 0$.

each other, the standard calibration (A) is not suitable for evaluating K_{OH}. A second calibration - either type (B) or (C) - is needed, with the respective definitions derived from equation 8.38 being

$$(B) \qquad K_{OH} = 1 - \frac{\frac{\Delta I_{OH^*}}{\overline{I}_{OH^*}}}{\frac{\Delta u}{\overline{u}}} \qquad \text{or} \tag{8.39}$$

$$(C) \qquad K_{OH} = \frac{\frac{\Delta I_{OH^*}}{\overline{I}_{OH^*}}}{\frac{\Delta \dot{m}_f}{\overline{\dot{m}}_f}} \; . \tag{8.40}$$

K_{OH} is then determined from the gradient of the calibration curve $\Delta I_{OH^*}/\Delta u$ at the operating point $\overline{I}_{OH^*}/\overline{u}$, or from $\Delta I_{OH^*}/\Delta \dot{m}_f$ at $\overline{I}_{OH^*}/\overline{\dot{m}}_f$, respectively. Both calibration types have been validated in the experiment and deliver - within measurement accuracy - the same values of K_{OH}.

An alternative method of determining K_{OH} is found in the consideration that FTF_{TP} is required to approach a value of 0 for $f \rightarrow 0$ due to the fact that no fuel mass flow fluctuation and thus also no heat release fluctuation can exist for that case. With all other parameters known, K_{OH} can then be directly derived from equations 8.29 and 8.19 without the necessity of a second calibration.

Table 13: Model parameter values used for the extraction of FTF_{λ}.

Parameter	Unit	IB-T1	IB-T2	IB-T3
p	bar	1.75	2.50	2.80
K_{u_B}	-	-0.369	-0.369	-0.369
K_{OH}	-	3.24	3.52	3.31
τ_I	ms	3	3	3
$\Delta\tau_I$	ms	0.6	0.6	0.6

Table 13 gives an overview of the model parameters derived for the individual operating points of the industrial burner setup. The value of K_{u_B} is determined from figure 4.3 with the unmixedness parameter U_{λ} of equation 7.1 as input. K_{OH} as given in table 13 is the average of the two values found from the photomultiplier calibration types B

and C using equations 8.39 and 8.40, respectively. The convective time delay τ_I from the fuel injector to the CTA location is determined from an integration of the burner velocity at the axis, and the associated dispersion $\Delta\tau_I$ is estimated to $0.2\,\tau_I$.

With the experimental flame transfer functions $TF_{OH/CTA}$ and FTF_{PP} known, equation 8.34 can be utilised to calculate the direct influence of mixture fraction fluctuations FTF_λ

$$FTF_\lambda = \frac{1}{K_{OH}}\left[TF_{OH/CTA}\left(1 + K_{u_B}\, e^{-i\omega\tau_I}\,\frac{e^{i\omega\Delta\tau_I} - e^{-i\omega\Delta\tau_I}}{2\Delta\tau_I i\omega}\right) - FTF_{PP}\right] \tag{8.41}$$

and the TP mode flame transfer function FTF_{TP}

$$FTF_{TP} = FTF_{PP} + FTF_\lambda\ . \tag{8.42}$$

8.3.2 Model for the Influence of Mixture Fraction Fluctuations

With the results of the previous section it is now possible to extract FTF_λ and FTF_{TP} from the measured flame transfer functions. Both are plotted in figure 8.14 for IB-T2 together with the experimental data.

In the low frequency limit, the amplitude value of FTF_λ converges to unity and its phase to π, which correctly reproduces the necessary criterion of a vanishing flame transfer function FTF_{TP} as stated in section 7.2.1. Also, the phase of FTF_{TP} does now approach the correct value of $\pi/2$. The phase offset of π in the low frequency limit of FTF_λ is caused by the reciprocal dependence of the heat release on the air excess ratio of the mixture. Since that dependence - characterised by a negative sign in equation 8.17 - is modelled with a positive sign in the general formulation of equation 8.18, the negative sign is transferred

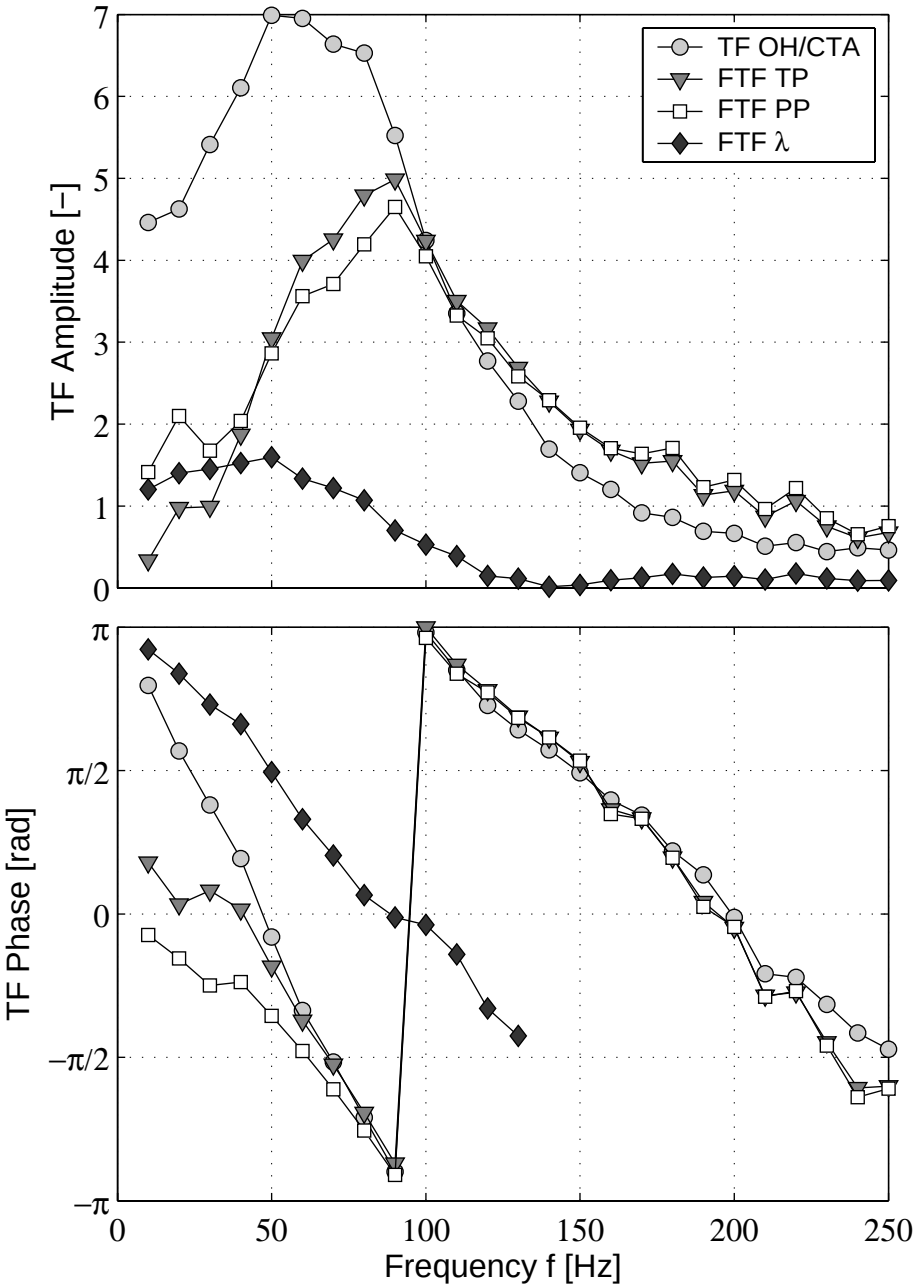

Figure 8.14: TP mode flame transfer function FTF_{TP} and mixture fraction transfer function FTF_{λ} compared to measured TP and PP mode TFs for IB-T2. Phase of FTF_{λ} not shown where correlation is lost due to low amplitude.

into FTF_{λ} and leads to the low frequency phase limit of π observed here.

For high frequencies, the amplitude of FTF_{λ} approaches zero, the

influence of the mixture fraction fluctuations vanishes and the plots of FTF_{TP} and FTF_{PP} overlap. The behaviour of FTF_λ between these bounds is characterised by an amplitude slightly rising with frequency until a limit frequency with a quick amplitude decrease is reached at around 100 Hz.

Since FTF_λ is related to the air excess ratio fluctuation λ'_B at the burner exit, where also the velocity fluctuation u'_B is measured, the convection time of either of the two perturbations into the flame is the same. Thus, also the average phase decline of FTF_λ and FTF_{PP} is the same, as observed in figure 8.14. With the additional time delay τ_I of the mixture fraction perturbation in the burner, the evaluation procedure developed in section 8.3.1 yields the correct phase behaviour of FTF_{TP} approaching the low frequency limit of $\pi/2$ and the measured phases of $TF_{OH/CTA}$ and FTF_{PP} for high frequencies.

When the amplitude of FTF_λ becomes too low at high frequencies, correlation is lost and the phase values are unstable. The phase plot in this region is therefore not shown in figure 8.14.

Compared to $TF_{OH/CTA}$, especially the amplitude of the undistorted flame transfer function FTF_{TP} does much closer resemble the behaviour of the perfectly premixed case FTF_{PP}. This effect is mainly due to the large measurement error SE_{OH} induced by a large value of K_{OH}. The influence of the velocity measurement error SE_{CTA} represented by K_{u_B} is weaker. Starting from a strong damping at excitation frequencies close to 0, the perfectly premixed transfer function is with increasing frequency either damped or amplified by the mixture fraction fluctuation, resulting in the FTF_{TP} amplitude plot located either below or above the FTF_{PP} plot. For the case reported here, the PP amplitude peak is further augmented by an in-phase mixture fraction fluctuation. After reaching the limit frequency of FTF_λ, the modulation does quickly diminish and FTF_{TP} approaches FTF_{PP}.

In figure 8.15, the error terms SE_{OH} of the OH* chemiluminescence and SE_{CTA} of the CTA are plotted together with FTF_λ. The dynamic behaviour of the latter and the OH* error is the same, as seen in identical phases and amplitudes only scaled by the factor $K_{OH} - 1$.

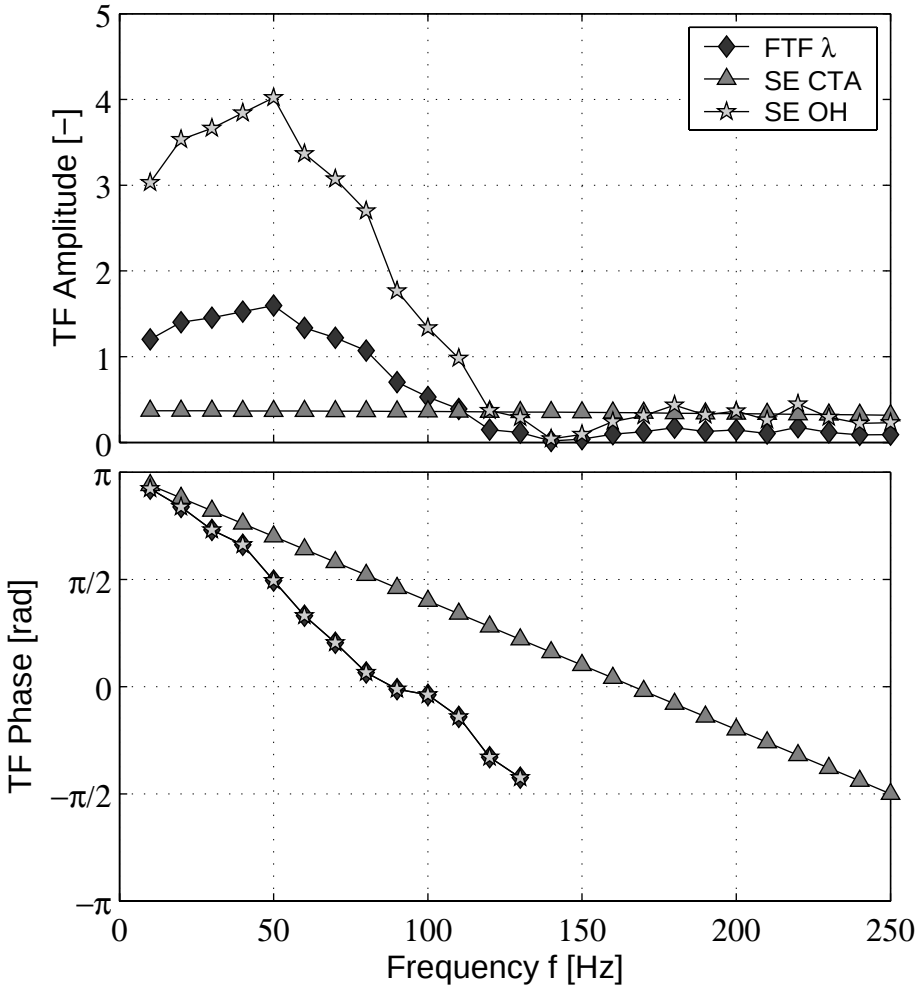

Figure 8.15: Systematic errors SE_{OH} of the flame intensity and SE_{CTA} of the hot wire probe due to mixture fraction fluctuations compared to FTF_λ for IB-T2. Phases not shown where correlation is lost due to low amplitude.

Compared to the other terms, the phase decline of SE_{CTA} is lower due to the small value of τ_I. The direct influence of the dispersion $\Delta\tau_I$ on the CTA error is small for the current setup, this becomes apparent in the almost constant amplitude of SE_{CTA}.

A comparison of FTF_λ for the three operating points investigated is given in figure 8.16. While the amplitude plots for IB-T2 and IB-T3 converge nicely towards a value of 1 with frequency approaching zero, IB-T1 shows an offset due to a large measurement uncertainty. More important, with rising pressure the amplitude plots exhibit a shift

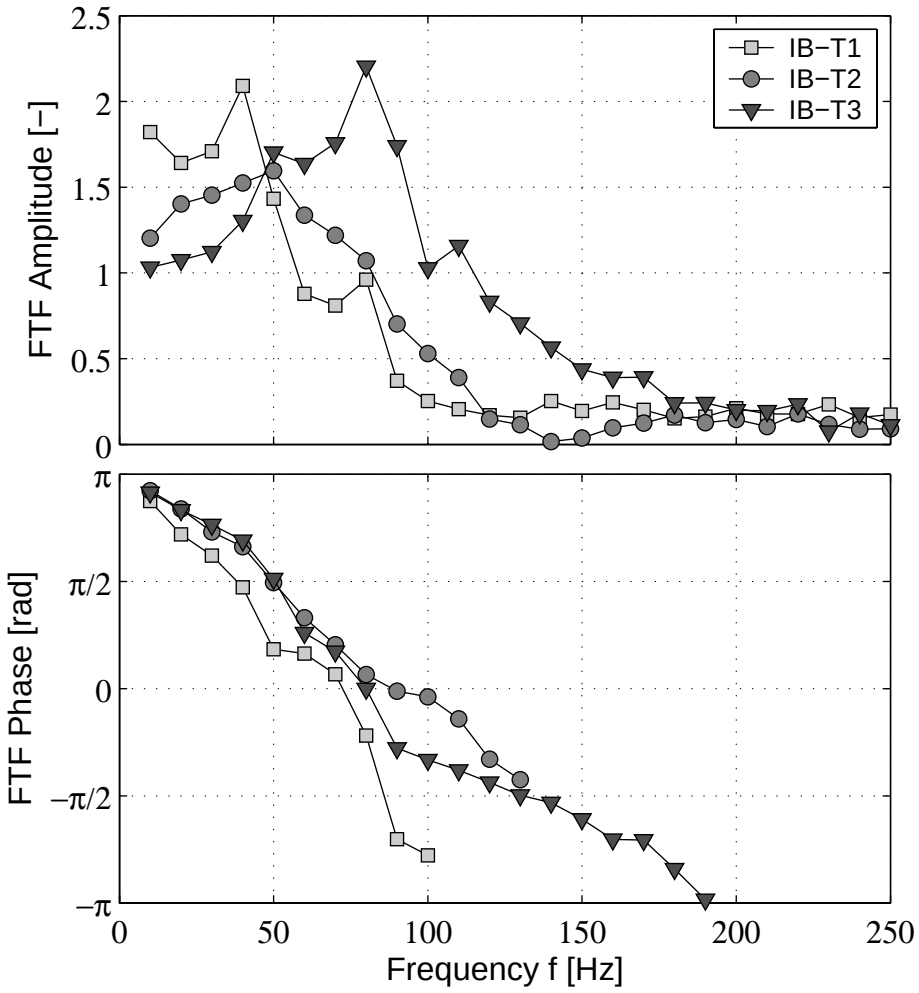

Figure 8.16: FTF_λ for IB-T1 to IB-T3. Phases not shown where correlation is lost due to low amplitude.

of the rapid decline to higher frequencies that is accompanied by a reduction of the phase drop. Both effects are caused by the upstream movement of the flame with increasing pressure that reduces both the time delay and also the dispersion of the mixture fraction wave in the combustor.

With the results presented so far in this section it is now possible to develop an analytical model $FTF_{\lambda,M}$ fitting the transfer function data of FTF_λ. This model can then be used to predict the influence of mixture fraction fluctuations on the transfer function without the necessity to actually perform a measurement of a technically premixed transfer function $TF_{OH/CTA}$ - or vice versa to determine FTF_{PP} from a

measurement of $TF_{OH/CTA}$. Such a model could have the appearance of a time delay low-pass filter similar to equation 8.8. Especially the plots of IB-T2 and IB-T3 show an amplitude rising to values larger than 1, an indication that a second order dynamics model with the potential to capture amplifications >1 is required.

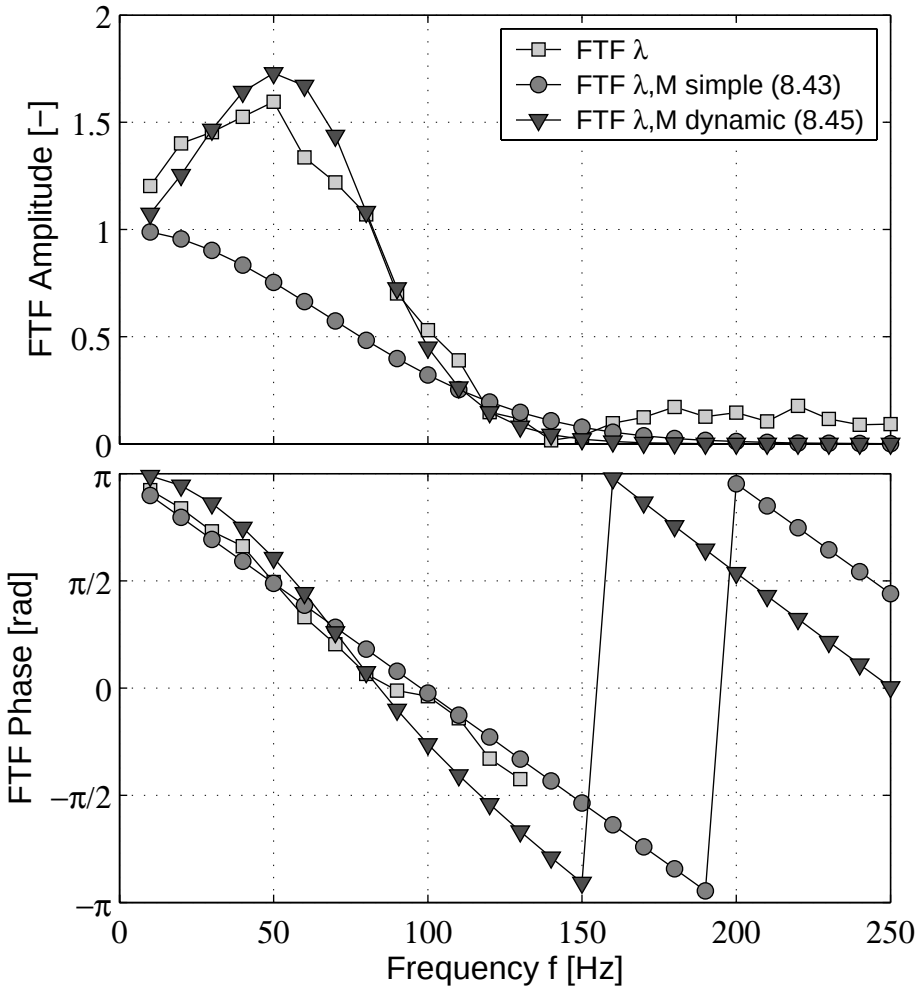

Figure 8.17: Comparison of FTF_λ for IB-T2 to a simple (equation 8.43) and a 2^{nd} order dynamic (equation 8.45) time delay model. Parameters taken from table 14. Phase not shown where correlation is lost due to low amplitude.

Figure 8.17 shows a comparison of FTF_λ to $FTF_{\lambda,M}$ determined using a simple time delay model and a time delay model with a second order dynamics extension. The simple time delay model is formulated with a dispersion term according to a proposal of Polifke [PKS01] and

Schuermans [SBG+04] similar to equation 2.23.

$$FTF_{\lambda,M} = e^{-i(\omega\,\tau_{M,\lambda}+\pi)-\frac{1}{2}\,\omega^2\Delta\tau^2_{M,\lambda}} \tag{8.43}$$

This model is preferred here to the alternative formulation of equation 2.22 due to its stronger damping of the amplitude that gives a better representation of the large dispersion of convective waves in the combustor. Note that an additional rotation of π is required to set the correct starting point in the low frequency limit. For this model, the time delay parameter $\tau_{M,\lambda}$ has been determined as the global transfer function time delay of the measured FTF in PP mode (see table 7), which represents the convection of both velocity and mixture fraction perturbation from the burner exit to the flame.

$$\tau_{M,\lambda} = \tau_{G,PP} \tag{8.44}$$

The dispersion parameter $\Delta\tau_{M,\lambda}$ has been set to 45% of $\tau_{M,\lambda}$. This value is larger than the corresponding parameter used for the convection in the burner (equation 8.33) to account for the increased dispersion resulting from strong velocity gradients and recirculation zones in the combustor region close to the burner exit.[79] These considerations deliver a good fit to the phase of FTF_λ and do also correctly reproduce the amplitude behaviour in the low frequency limit as well as for high frequencies.

However, for intermediate frequencies the predicted amplitude is too low. While the amplitude of FTF_λ extracted from the measured FTFs is rising to values larger than 1, the strong damping of the dispersion term is already affecting the amplitude of the modelled $FTF_{\lambda,M}$ (equation 8.43). Obviously, the simple time delay model is not sufficient and some additional dynamics are affecting the transfer function of the mixture fraction oscillation. Since the frequency range is the

[79] While the dispersion parameter $\Delta\tau_I$ in the burner (equation 8.33) has been estimated, the corresponding parameter $\Delta\tau_{M,\lambda}$ used here (equations 8.43 and 8.45) has been fitted to the amplitude plot of FTF_λ. That fit is necessary, since - unlike $\Delta\tau_I$ - the dispersion in the combustor has a strong influence on the amplitude of FTF_λ and a measurement or a good estimate of this dispersion does not exist. However, the fitted values as given in table 14 are reasonable. For future applications, a CFD calculation could be used to determine the time delay distribution of the mixture fraction perturbation and the corresponding dispersion parameter.

same, it seems that the same dynamics that generate the global amplitude peak for the PP mode transfer functions are also influencing the mixture fraction transfer function here - a scenario that is well conceivable. As the consequence, the same second order dynamic model extension with the same parameters as found in table 12 for FTF_{PP} is applied here, yielding

$$FTF_{\lambda,M} = e^{-i(\omega\tau_{M,\lambda}+\pi)-\frac{1}{2}\omega^2\Delta\tau_{M,\lambda}^2}\frac{\beta\, i\omega + 1}{(\alpha_2\, i\omega)^2 + \alpha_1\, i\omega + 1}\,. \quad (8.45)$$

Consequently, also the time delay parameter τ_M of the PP model found in table 12 is used to determine the mixture fraction time delay $\tau_{M,\lambda}$.

$$\tau_{M,\lambda} = \tau_M \quad (8.46)$$

After this extension, also the amplitude of FTF_λ in figure 8.17 is fitted very well. The mixture fraction transfer function FTF_λ does thus indeed seem to be subject to the same dynamics as the pure velocity transfer function FTF_{PP}. The parameters used for both models are summarised in table 14.

Table 14: Parameter values of simple time delay (equation 8.43) and second order (equation 8.45) models for FTF_λ, IB-T2.

Parameter	Unit	Simple	2^{nd} Order
$\tau_{M,\lambda}$	ms	5.12	4.05
$\Delta\tau_{M,\lambda}$	ms	2.4	3.2
α_1	ms	-	1.77
α_2	ms	-	2.03
β	ms	-	6.70

Since the second order dynamics parameters seem to apply for the mixture fraction transfer function, it is possible that also the swirl dynamics of FTF_S as determined in section 8.2 have an influence on FTF_λ. However, this statement can not be verified here due to the almost negligible magnitude of FTF_S for the industrial burner setup.

Finally, the models for the PP mode transfer function and the mixture

fraction transfer function can be combined to form a model for the TP mode transfer function analog to equation 8.42.

$$FTF_{TP,M} = FTF_{\tau,D,S} + FTF_{\lambda,M} \tag{8.47}$$

Even though the measured transfer functions suffer from the shortcomings of the industrial burner setup, the presented approach to extract and model the influence of mixture fraction fluctuations seems to be valid. Nevertheless it is recommended to confirm the findings of sections 8.2 and 8.3 with a more generic burner setup that allows a higher measurement accuracy and that generates a flame located within the bounds of the observation window.

8.4 Modelling Overview

Figure 8.18 summarises the models derived in section 8 and puts them in context with the associated FTF measurements. In this scheme, modelling efforts are coloured red, while measurements show up in black. The arrows describe the sequence of evaluation. Starting from the input parameters, the models are developed from left to right, while the analysis of the measured FTFs is organised from right to left. Only the most prominent input parameters have been shown on the left hand side to maintain simplicity. While the perfectly premixed case is mapped on the upper half of the scheme, the extension on the lower half is required for technically premixed operation.

The model for the PP mode flame transfer functions $FTF_{\tau,D,S}$ introduced in section 8.1 consists of three parts. While the global behaviour is captured by a pure time delay model FTF_τ extended by a second order dynamics part FTF_D, the local amplitude maxima and minima as well as the corresponding local features in the phase are generated by the swirl model FTF_S.

FTF_τ represents the "classical" FTF behaviour with a phase drop defined by the time delay between burner and flame τ_M and an optional dispersion parameter. FTF_D captures the higher order dynamics of the flame, leading to a global amplitude peak and an additional phase

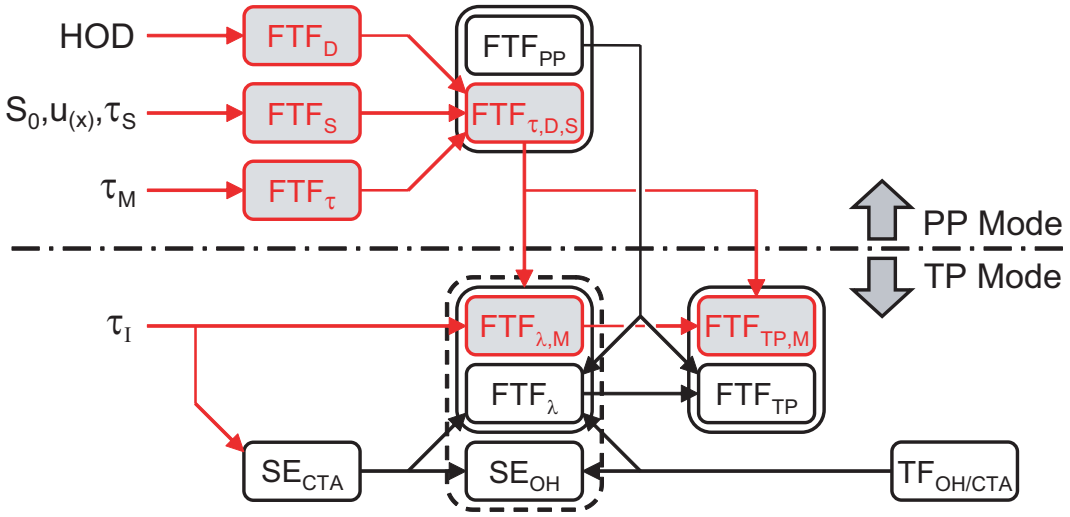

Figure 8.18: Overview of the models derived in this section and the measured FTFs. Red = Model, Black = Experimental data, HOD = Higher order dynamics. Upper half represents PP mode, TP mode needs the extension on the lower half. See also appendix D for details on the transfer function naming.

decline at the resonance frequency of that amplitude peak. Both FTF_τ and FTF_D do thus contribute to the average phase gradient τ_G of the flame transfer function. Due to insufficient knowledge of the origin of the higher order dynamics of the flame, FTF_D is fitted with empirical parameters and without a clear physical interpretation.

Unlike FTF_D, the swirl part of the model FTF_S is well supported by theory. This model captures a modulation of the flame by vorticity fluctuations that are generated by the acoustic excitation at the swirler and subsequently convected into the flame. It can not be used as a stand-alone model, but is considered to "ride on top" of the global behaviour defined by FTF_τ and FTF_D. Albeit only responsible for the local behaviour, it is FTF_S that generates the amazingly high congruence of $FTF_{\tau,D,S}$ with the details in the amplitude and phase plots of the experimental FTFs.

The model transfer function $FTF_{\tau,D,S}$ as specified above has been successfully applied to two different burners in perfectly premixed mode - a generic and an industrial burner setup. For the industrial burner,

FTF_D has been extended by an additional parameter, and parameter values differing from the generic burner have been applied.

An extension of $FTF_{\tau,D,S}$ derived in section 8.3.2 allows to determine also the transfer function in technically premixed mode $FTF_{TP,M}$. To achieve this, the influence of mixture fraction perturbations generated at the fuel injector and described by an additional transfer function $FTF_{\lambda,M}$ needs to be taken into account. The model derived for that purpose does include the convective time delay τ_I between injector and burner exit as well as the dispersion of the mixture fraction wave between injector and flame. As found in section 8.3.2, also the higher order flame dynamics of FTF_D seem to have a direct influence on $FTF_{\lambda,M}$. In figure 8.18, this is represented by a link from $FTF_{\tau,D,S}$.

Parallel to the modelling approach to determine $FTF_{\lambda,M}$, an analysis procedure is introduced in section 8.3.1 that allows an extraction of the mixture fraction influence FTF_λ and the technically premixed transfer function FTF_{TP} from the measured transfer functions in perfectly (FTF_{PP}) and technically ($TF_{OH/CTA}$) premixed mode. This procedure is needed to remove the systematic error of the mixture fraction perturbations on the OH* chemiluminescence of the flame (SE_{OH}) and on the CTA signal (SE_{CTA}).[80] The systematic OH* intensity error SE_{OH} and the true heat release response FTF_λ are subject to the same dynamics and linked by a constant scaling factor. In the scheme of figure 8.18, this is illustrated by SE_{OH} being located in the same block as FTF_λ. The undistorted TP mode flame transfer function FTF_{TP} can be easily evaluated from FTF_{PP} and FTF_λ, once the latter has been determined.

[80] Although the CTA error is actually modelled, it is displayed in black in the scheme to illustrate its affiliation to the analysis procedure of the experimental data. Also, an experimental determination of the CTA error using a calibration versus the air excess ratio is possible.

9 Summary

The scope of this work comprises the investigation of flame transfer functions at elevated pressure that can be utilised to predict thermoacoustic oscillations in gas turbine engines. For that purpose, a combustion test rig has been designed and manufactured that is capable of elevated combustor pressures of up to 10 bar. A specially developed high pressure siren provides the necessary acoustic excitation.

Firstly, the direct influence of pressure on the measurement procedure of the flame transfer function has been investigated. This investigation comprises the heat transfer to the hot wire probe - that is used to determine the acoustic velocity - and the flame chemiluminescence taken as a measure for heat release. For both signals, a quantitative analysis is presented that allows to correct the systematic error imposed by a pressure fluctuation. However, that error is found to be usually small, it becomes significant only if the relative pressure fluctuations grow to the same order of magnitude as the relative velocity perturbation.

9.1 Generic Burner

Flame transfer functions with a high quality and reproducibility have been measured for a generic burner developed in-house. An operation of this burner in perfectly premixed mode guarantees that no perturbations of the air/fuel mixture fraction can exist. The main focus of this investigation lies on the influence of pressure, a variation ranging from 1.1 to 5 bar has been performed.

For this generic burner setup, the influence of the operating pressure on the flame transfer function is small, with the most prominent effect being a reduction of the global phase decline with pressure that can be well correlated with a flame length reduction. This reduction can be mainly attributed to the influence of non-adiabatic conditions. As the pressure rises, the relative heat loss to the rather cold combustor walls is reduced and the flame temperature rises. A model has been

presented that captures the influence of this heat loss on the turbulent flame speed and that delivers a good approximation of the flame length and also of the observed lean blow-off characteristics.

Other effects observed are a slight shift of the global FTF amplitude peak to higher frequencies for rising pressure and an interesting feature in the phase - the phase plots at all investigated operating conditions are almost identical up to a limit frequency of 120 Hz and show a distinct separation above that limit. A thorough investigation reveals that the superposition of a flame length fluctuation and the conventional convective velocity perturbations of the flame are responsible for that effect. Furthermore, some information on the linearity is given in appendix A, with the main outcome being that saturation effects observed at high frequencies and excitation amplitudes are due to the formation of ring vortex structures in the flow and the influence of these structures on the flame.

A model has been developed that is able to reproduce the global as well as the local behaviour of the measured transfer functions with a high accuracy. This model consists of three parts:

1. A time delay between the transfer function reference location at the burner exit and the flame. Velocity perturbations induced by the acoustics are generated at the burner nozzle and convected into the flame, where they modulate the heat release.
2. A second order dynamics part as an extension to the time delay. This part is applied to model the global peak observed in the measured amplitudes between 100 and 350 Hz. Together with the time delay of the first part, the 180° phase shift of this term that occurs at the frequency of the amplitude peak yields a phase plot well matching the measured phase behaviour.
3. While the first two parts represent the global - large scale - transfer function behaviour, the local - small scale - behaviour with amplitude maxima and minima and variations in the phase gradient is generated by vorticity fluctuations of the swirled flow that are superimposed on the velocity perturbation represented by the first and second part.

The underlying dynamics leading to the second part of the model are not yet understood in detail, empirically derived parameters are thus used to characterise the behaviour. However, the behaviour observed in the second part might be related to the large length and weak stabilisation of the investigated flames and may disappear or become negligible for larger swirl numbers.

Power laws have been found to represent the pressure-dependent behaviour of the flame transfer functions. This is not surprising, since a power law also governs the relative heat loss to the walls. Individual laws have been found for flame length, global time delay and other free model parameters. Using these correlations, it is not only possible to reproduce the transfer functions measured, but also to extrapolate to pressures that were not investigated. Of benefit here is the property of power laws that scaling depends on pressure ratios and not pressure differences. In order to extrapolate to realistic engine pressures, one does not necessarily have to reach that pressure in combustion experiments, but only approach it up to a sufficiently small factor.

9.2 Industrial Burner

A second burner derived from an industrial aero-engine design has been investigated in perfectly premixed mode, with the fundamental difference to the generic burner being a lifted flame stabilised at some distance downstream of the burner exit in the combustor. A strong pressure dependence of the axial flame location has been observed for this configuration, and with it a strong variation of the global time delay. This finding confirms that the FTF phase drop scales with the time delay from the burner exit to the dominant reaction zone.

After a modification to take the lifted flame with its large distance to the burner exit into account, the model developed for the generic burner has also been applied here. As a second modification, the empirical fit of the second order dynamics part has been extended by an additional parameter. The global amplitude peak related to the second order dynamics model lies at lower frequencies around 100 Hz

for the industrial burner. As a consequence, also the related parameter values differ from the generic burner configuration. The influence of the vorticity fluctuation is smaller, which can be explained by the strong swirl dissipation in the combustor before the flow is entering the flame.

A major benefit of the industrial burner is that it does also allow an operation in "technically" premixed mode to investigate the influence of mixture fraction perturbations on the flame dynamics. As found in the respective flame transfer functions, that influence remains restricted to the low frequency region. Mixture fraction perturbations are formed at the fuel injector and subsequently convected with the flow through the burner and into the flame. While the additional distance from the injector to the burner exit is responsible for an additional time delay of the mixture fraction wave, the small convective wavelength and the highly dispersive flow quickly diminish the flame response for high frequencies. As the consequence, the "technically" premixed transfer functions show a strong phase decline at low frequencies - where the mixture fraction perturbations constitute the dominant effect - and both amplitude and phase plots approach the perfectly premixed transfer functions at high frequencies.

General considerations lead to limit values of amplitude (0) and phase ($\pi/2$) for frequencies approaching zero. However, the measured transfer functions show large deviations from that limit values. These deviations are caused by systematic errors due to the strong sensitivity of the OH*-chemiluminescence on the air excess ratio and a (weaker) influence of the latter on the measured hot wire signal.

Based on the perfectly premixed transfer functions, estimations of time delay and dissipation in the mixing section and an additional calibration of the OH*-chemiluminescence signal as a function of the air excess ratio, a model extension has been introduced that allows to

- separate the systematic errors of the OH* and velocity signals from the measurement to obtain the undistorted transfer function, to

- isolate the pure influence of the mixture fraction perturbation as the difference between the two premixing modes in the form of a mixture fraction transfer function and to
- set up a model that is able to capture that influence of the mixture fraction perturbation.

Especially the last step is of interest here, since it reveals that the mixture fraction perturbations seem to follow the same flame dynamics that lead to the global amplitude peak observed already in perfectly premixed mode.

As found for the generic burner, the influence of pressure on the flame transfer functions reduces to the pressure-dependence of the flame form and location. With the lifted flame moving closer to the burner exit with rising pressure, both time delay and dissipation of the mixture fraction wave decrease. As the consequence, the phase drop is reduced and the limit frequency, where the mixture fraction fluctuations lose their influence on the flame dynamics, shifts to higher values.

APPENDIX

A Linearity

In this section, results on the linearity of the measured flame transfer functions are given. Linearity in this context denotes the invariance of the measured FTF concerning different excitation amplitudes - the transfer factor of heat release output to acoustic excitation input stays constant for both amplitude and phase. Usually, the FTF shows a linear behaviour for relative excitation amplitudes $u'/\bar{u} \ll 1$ and runs into saturation for $u'/\bar{u} = \mathcal{O}(1)$. This saturation is caused by the physical limits of the flame response: A lower heat release limit is $\dot{Q} = 0$ - the flame can only extinguish, but never absorb energy. An upper boundary is defined by the limited flame speed - the limited capability of the flame to convert fresh mixture into reaction products. However, in existing combustion systems saturation effects causing deviations from linearity are observed well before reaching these physical limits. Harper [HJN+01] determines a critical relative heat release $\dot{Q}'/\overline{\dot{Q}}$ of about 20 to 40%, also Bellows [BL04] observes heat release saturation starting at around 20%.

Usually, the FTF is implemented into an acoustic low order model to predict the eigenfrequencies and amplitude growth rates of a combustion system. These LOMs are linear models that predict the behaviour at the onset of the instability, when the amplitudes are infinitely small. It does thus make sense to use a FTF measured in the linear regime that resembles the behaviour at the small amplitudes of interest. Note also that the Rankine-Hugoniot equations 1.7 used to implement a flame transfer function into a low order model are linearised relations, large amplitudes would require a review of the validity of these equations.

FTF saturation is an issue if the limit cycle amplitude of a system is to be investigated - see [Pan04] for example. For that case, the energy supplied by the flame is in balance with the acoustic losses by transmission and damping. A model using a linear FTF without saturation effects would overestimate the oscillation amplitude or even be unable to describe any limit cycle and could produce considerable errors concerning eigenfrequency and mode shape.

To determine the range of linearity of the measured FTFs and their saturation behaviour, a variation of the excitation amplitude $u'/\bar{u}$ was performed at several excitation frequencies. The results are plotted in figure A.1. With the exception of a small amplitude deviation at the lowest frequency of 20 Hz and low excitation, almost perfectly constant FTF values are measured for both amplitude and phase up to a frequency of 160 Hz and an excitation amplitude of 27%[81]. Only for the highest frequency investigated of 320 Hz a saturation effect can be demonstrated. Both amplitude and phase plots show a bend at about 10 - 15% excitation amplitude and a linear trend above this critical value. As expected, the FTF amplitude decreases with rising $u'/\bar{u}$, and the corresponding phase values show an increase.

In terms of a global time delay model, the phase increase observed for rising excitation amplitudes at 320 Hz represents a reduction of the time delay or a flame activity zone closer to the burner exit. Additional high speed camera images of the flame at different frequencies and excitation amplitudes have been recorded to confirm this behaviour, the resulting amplitude images are shown in figure A.2. While almost no effect of the excitation amplitude can be seen at a frequency of 80 Hz, the expected decrease of the flame length is clearly visible at 320 Hz.

The work of Külsheimer [KB02] can give an explanation of the observed frequency-dependent behaviour. He investigated swirled and jet flames for varying excitation frequencies and amplitudes and found a critical value for the beginning of ring vortex formation in the combustor flowfield at the burner exit depending on both excitation frequency and amplitude. The results are plotted in figure A.3. Külsheimer found the critical pulsation limit Pu_{crit} and the Strouhal number Sr to correlate following a hyperbolical law of the form

$$Pu_{crit} \cdot Sr = \left.\frac{u'_{rms}}{\bar{u}}\right|_{crit} \cdot Sr = const. \tag{A.1}$$

[81] At 160 Hz, the maximum amplitude obtained is 17% due to unfavourable acoustics at that frequency. Generally, the excitation amplitude is limited by the rig acoustics, the maximum open area of the pressure valves defining the maximum siren massflow and the operating limits of the burner.

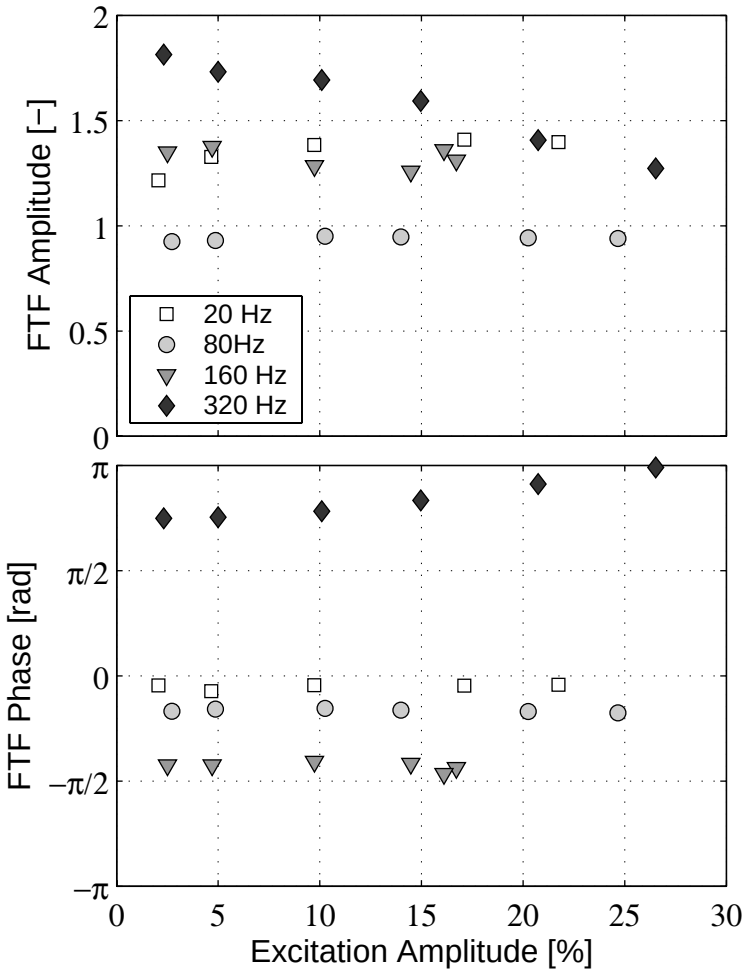

Figure A.1: Linearity of the FTF amplitude and phase for operating point TD1-P6 at 3 bar and $\lambda = 1.47$.

However, a power law like

$$Pu_{crit}\ [\%] = 7.79\ Sr^{-0.54} \tag{A.2}$$

gives a much better fit of his measured data, illustrated by the black line in figure A.3. The critical limit divides the plot into two regions with quasi-steady behaviour in the lower left and the formation of ring vortices in the upper right part.

The saturation effect observed in the 320 Hz amplitude and phase plots of figure A.1 can now be explained by the occurrance of periodic ring vortices that cause a disturbance of the flame shape and thus a deviation from the quasi-steady behaviour in the linear regime.

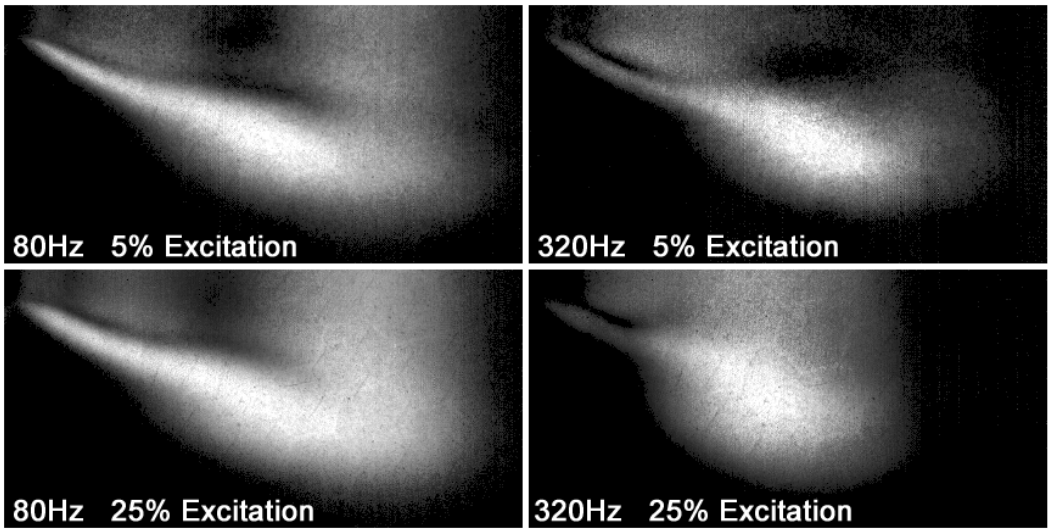

Figure A.2: Amplitude images for different excitation frequencies and amplitudes, operating point TD1-P6 at 3 bar and $\lambda = 1.47$.

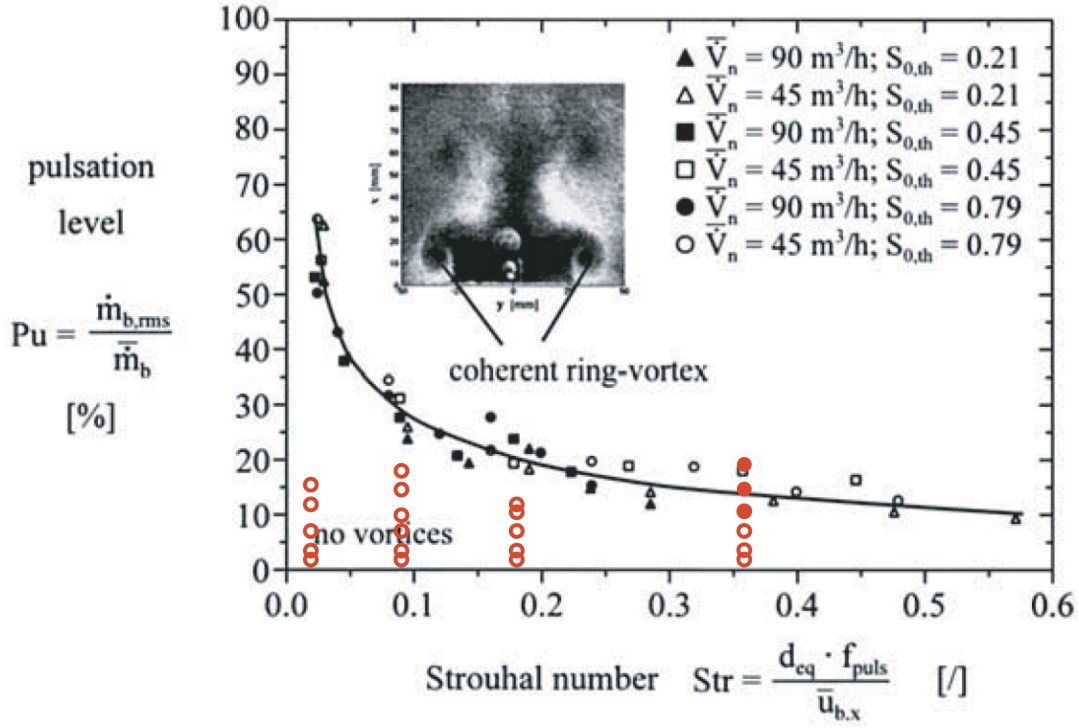

Figure A.3: Limit for the occurrance of coherent ring vortex structures for acoustically excited swirl flames. Illustration taken from [KB02]. Red: operating points from this work, circles: linear regime, dots: saturation.

These vortices increase the radial extension of the reaction zone by folding the flame front, the flame length is reduced and the reaction is completed earlier. As a consequence, the 320 Hz FTF phase moves towards smaller time delays for rising excitation amplitude as observed in figure A.1.

Up to 320 Hz excitation frequency, the operating points investigated here lie in the linear regime below the critical line. At 320 Hz and an amplitude of about 10 - 15%, the critical line is crossed and coherent ring structures are appearing that cause the nonlinear flame disturbance. To illustrate that, the results from this work have been plotted into Külsheimer's diagram.[82] Red circles denote the linear FTF conditions, while the points at 320 Hz showing saturation are plotted as red dots. As seen from the diagram, the onset of saturation at 320 Hz does coincide with Külsheimers observation of the formation of ring vortex structures. This close coherence of the results validates the explanation of coherent ring vortex structures being responsible for the nonlinear FTF saturation effects observed.

[82] The Strouhal number here has been defined by the burner nozzle diameter, the excitation frequency and the mean axial burner velocity according to the formula in figure A.3. Note that an additional factor of $\sqrt{2}$ is required to compare the excitation amplitudes here to Külsheimer's *rms* values.

B Reproducibility

Figure B.1 shows the first set of flame transfer functions measured on the TD1 burner, these correspond to operating point TD1-P1. TD1-P1 has been investigated twice with independent measurements on two different days to allow for a reproducibility check.

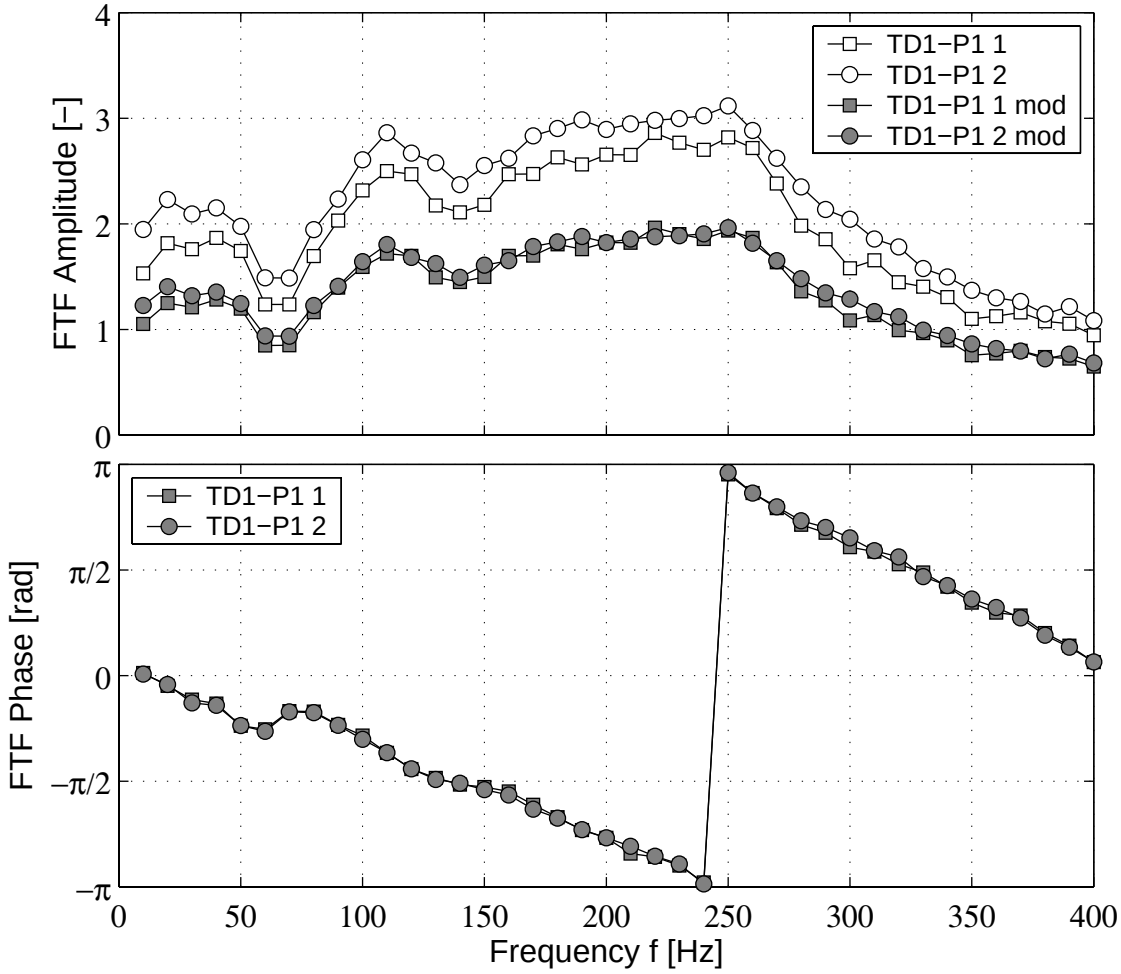

Figure B.1: Two independently measured FTFs at TD1-P1, original and modified according to section 4.2.2.

The amplitude plot shows both the original transfer functions determined with the standard photomultiplier calibration and the transfer functions measured using a modified photomultiplier calibration, as described in section 4.2.2. The term “standard calibration” does in

this context denote a linear fit to the measured data points of figure 4.4, that fit does in general not cross the coordinate origin. Alternatively, "modified calibration" stands for a linear fit through the origin of the coordinate system and thus for a strictly proportional relation between heat release of the flame and OH* chemiluminescence intensity.

Although recorded at identical conditions, the amplitude plots of the two original FTFs exhibit different magnitudes. This demonstrates the high sensitivity of the amplitude part of the transfer functions. Nevertheless, the qualitative behaviour is the same and the deviation can be reduced to a common factor independent of frequency.

Interestingly, the plots coincide almost perfectly after application of the modified photomultiplier calibration. This and the fact that the value of 1 in the low frequency limit is now approached very well leads to the conclusion that the modified photomultiplier calibration as described in section 4.2.2 represents reality and is able to compensate operating point and measurement deviations. Since the modified calibration is sufficient to achieve reproducible transfer functions and the correct behaviour in the low frequency limit, other influences - as for example deviations in the burner velocity measurement - can be excluded.

Another confirmation of the photomultiplier correction is given in [Föl06] and [FFS06], where a check of the influence of the modified photomultiplier calibration on combustor stability and eigenfrequencies has been performed with the result that the difference is usually small and that the corrected amplitudes deliver a better prediction of the stability behaviour observed in reality.

The same behaviour showing a correction of the amplitude level has been observed for the other measured transfer functions, the modified calibration factor has thus been applied for all FTFs.

Unlike the amplitude plots, the phases do not show any kind of deviations, the plots for the two repeats of TD1-P1 agree perfectly. This agreement is in line with observations of other researchers that the transfer function phase is generally more reliable than the amplitude.

Since the modified calibration does not influence the phase, a corrected phase plot is not necessary.

Note also that a normalisation of the FTF amplitude with the value of the lowest frequency measured to achieve a value of 1 in the low frequency limit as often reported[83] is not necessary here. With the above results, both reproducibility and quality of the measured TD1 transfer functions can be considered very good.

[83] [Fis04], [Kun04], [LB04], [EFS03a]

C Industrial Burner at High Frequencies

In the measured flame transfer functions of the industrial burner presented in section 6.2, an erroneous behaviour was observed with a positive gradient of the phases at high frequencies. That behaviour is investigated here in more detail.

Figures C.1 and C.2 show the amplitude and phase plots of the measured flame transfer functions. Unlike figures 6.3 and 6.4, the FTF data for the full range of excitation frequencies up to 400 Hz are presented here. At a frequency of about 280 Hz, the usual behaviour of a global phase decline with frequency is reversed and the phases start to rise again.

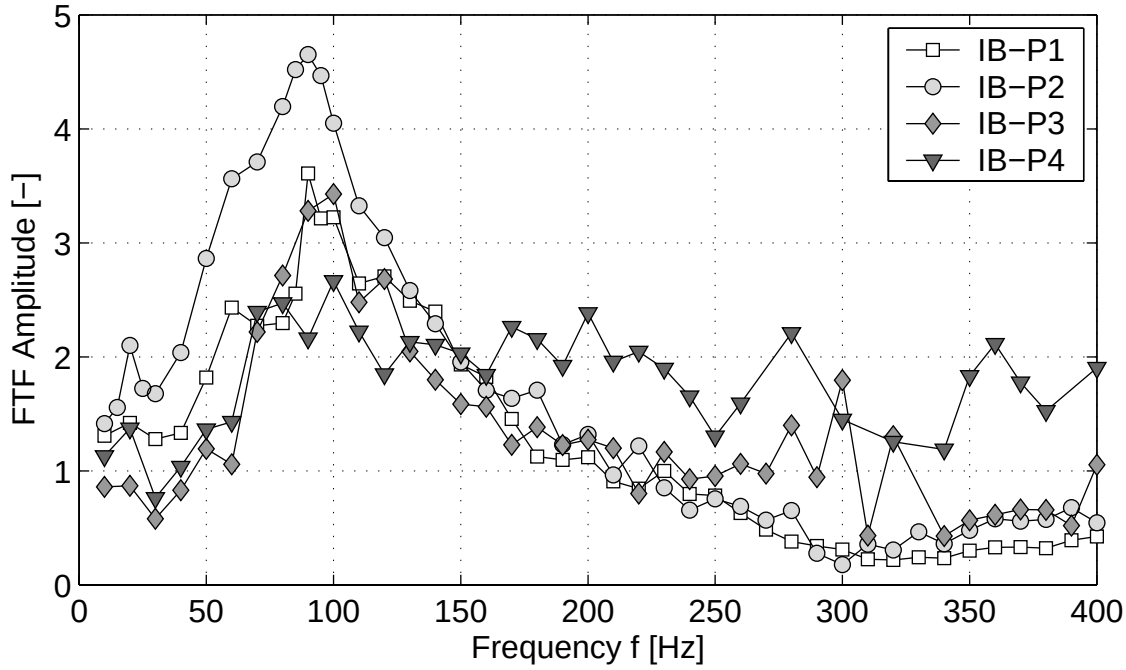

Figure C.1: Transfer function (FTF_{PP}) amplitude plots for the industrial burner, perfectly premixed mode, operating points as specified in table 2.

As seen in figure C.3 for IB-P1 as example, the OH* chemiluminescence intensity amplitude recorded by the photomultiplier becomes very low above 250 Hz. At a frequency of 280 Hz, the corresponding photomultiplier phase plot bends upwards while the CTA phase

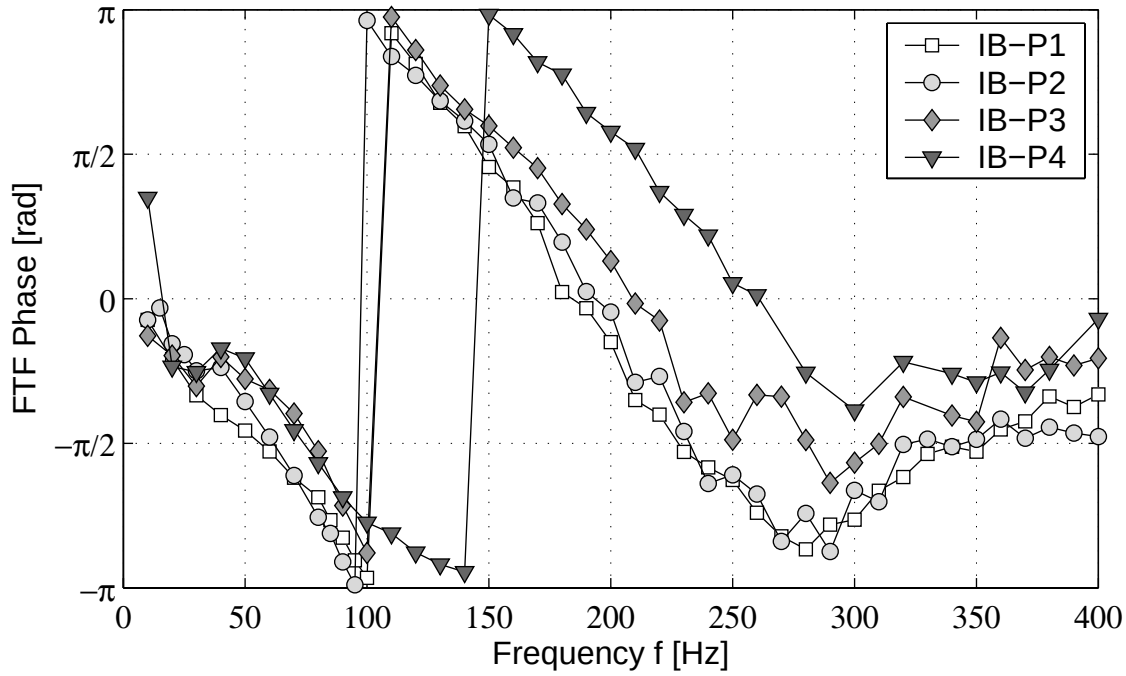

Figure C.2: Transfer function (FTF_{PP}) phase plots for the industrial burner, perfectly premixed mode, operating points as specified in table 2.

continues to decline, thus resulting in the observed FTF behaviour. The origin of this behaviour does however not lie in the flame transfer function itself, but is associated with the low chemiluminescence intensity response and the high pressure amplitude at the flame location. In the case observed here, the amplitude of the pressure oscillation $\hat{p}/\overline{p}$ amounts to about 1.2% [FES04]. According to equation 4.19, the recorded intensity fluctuation does then lose its correlation with the heat release and becomes dominated by the pressure oscillation as soon as $\hat{\dot{Q}}/\overline{\dot{Q}}$ declines below about 0.9%. As shown in the photomultiplier amplitude of figure C.3, that limit is reached at about the frequency where the phase bend is initiated. Note that $\hat{I}/\overline{I}$ is shown in figure C.3 and not $\hat{\dot{Q}}/\overline{\dot{Q}}$. Due to the complex-valued nature of both terms and their unknown phases an exact match can not be expected, but the loss of correlation is limited to the amplitude range

$$0 \leq \frac{\hat{I}}{\overline{I}} \leq \frac{\hat{\dot{Q}}}{\overline{\dot{Q}}} + \frac{\hat{p}}{\overline{p}} \qquad \text{or} \qquad 0 \leq \frac{\hat{I}}{\overline{I}} \leq 1.75\frac{\hat{p}}{\overline{p}}\,. \tag{C.1}$$

Note also that the photomultiplier amplitude peak at 350 Hz in figure C.3 is induced by the pressure oscillation, this frequency corresponds to the acoustic $\lambda/2$ mode of the combustor with very high pressure amplitudes at the flame location. The FTF phase plots do thus not return to their original behaviour related to the heat release oscillation.

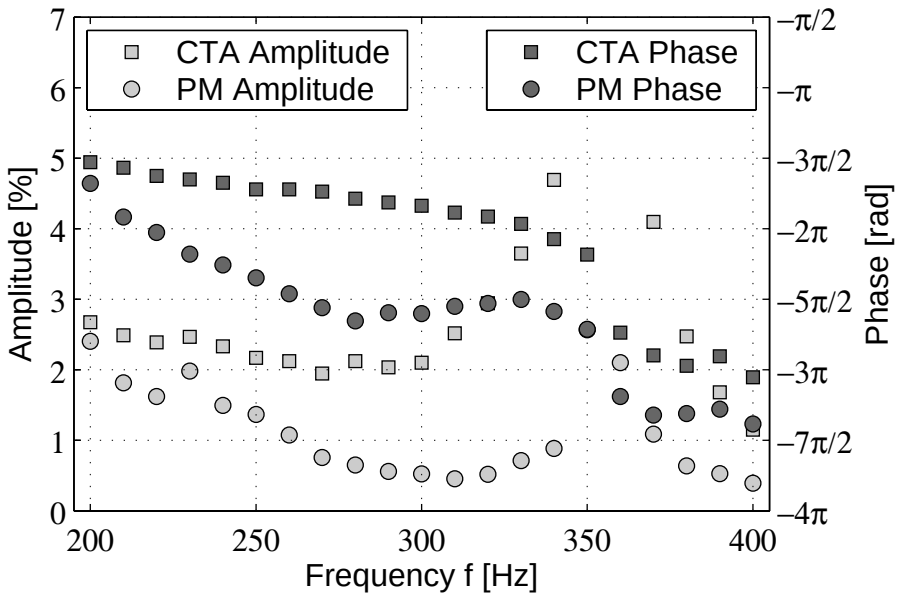

Figure C.3: Amplitude and phase plots of CTA and photomultiplier fluctuations for IB-P1.

Even though the correlation is lost not until 280 Hz, significant errors due to the influence of $p'/\overline{p}$ must be expected before, thus rendering the FTF results above about 200 Hz questionable. However, given the knowledge of $p'_F/\overline{p}_F$ at the flame location in amplitude and phase[84], the erroneous measured transfer function $TF_{OH/CTA}$

$$TF_{OH/CTA} = \frac{\frac{I'_{OH*}}{\overline{I}_{OH*}}}{\frac{u'_{CTA}}{\overline{u}_{CTA}}} \tag{C.2}$$

[84] Not available here.

can be corrected according to

$$FTF_{PP} = \frac{\frac{\dot{Q}'}{\overline{\dot{Q}}}}{\frac{u'_B}{\overline{u}_B}} = \frac{\frac{I'_{OH^*}}{\overline{I}_{OH^*}} + 0.75\,\frac{p'_F}{\overline{p}_F}}{\frac{u'_{CTA}}{\overline{u}_{CTA}} + 0.69\,\frac{p'_{CTA}}{\overline{p}_{CTA}}} \tag{C.3}$$

by making use of equations 4.12 and 4.19. In complex notation, equation C.3 reads

$$FTF_{PP} = \frac{\frac{\hat{I}_{OH^*}}{\overline{I}_{OH^*}}\,e^{i\varphi_{OH^*}} + 0.75\,\frac{\hat{p}_F}{\overline{p}_F}\,e^{i\varphi_{p_F}}}{\frac{\hat{u}_{CTA}}{\overline{u}_{CTA}}\,e^{i\varphi_{CTA}} + 0.69\,\frac{\hat{p}_{CTA}}{\overline{p}_{CTA}}\,e^{i\varphi_{p_{CTA}}}}\ . \tag{C.4}$$

In equations C.3 and C.4, also the pressure influence on the hot wire measurement is compensated. If possible, the occurrence of high pressure amplitudes at the CTA and flame locations should be avoided though by choosing the setup accordingly.

A confirmation of the validity of the assumption that the pressure fluctuation is responsible for the strange phase behaviour is provided by two observations:

- The TD1 measurements do not show a positive phase gradient - the associated pressure amplitudes at the flame location are much lower and amount to $p'/\overline{p} \approx 0.1\%$.
- More importantly, a comparison to FTF measurements of the same burner on an atmospheric rig in kerosene operation up to a frequency of 600 Hz [EFS03a] does also not show a positive phase gradient although the measured FTFs are very similar to the ones obtained in gas operation here. Since the pressure amplitudes are limited to very low values by the short open-ended combustor in the atmospheric rig, their high values in the high pressure rig can indeed be held responsible for the positive phase gradient.

The positive phase gradient at high frequencies is also observed for the TP mode transfer functions. For the sake of completeness, also figure 7.3 is reproduced here with the full range of excitation frequencies up to 400 Hz.

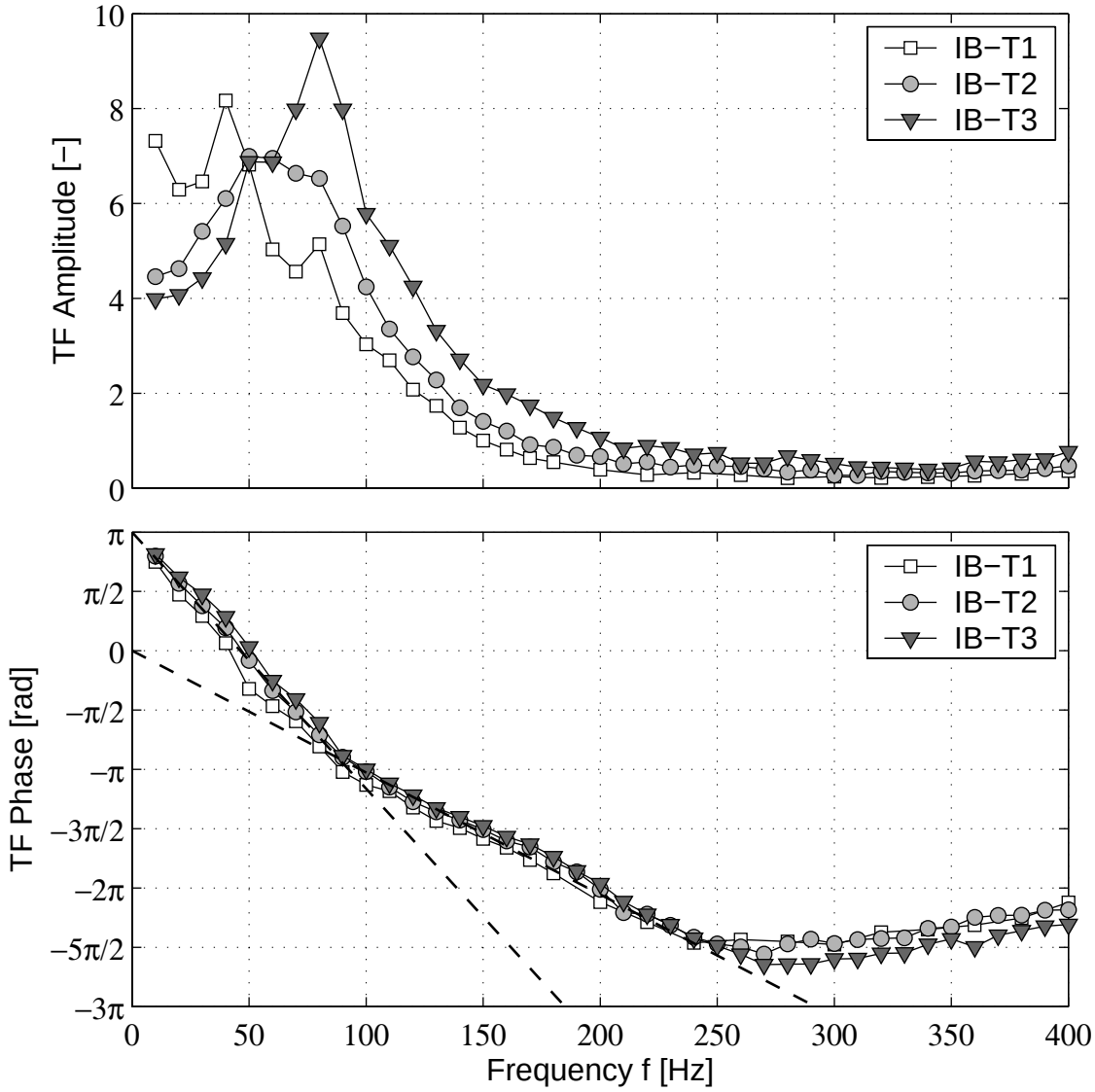

Figure C.4: Transfer function ($TF_{OH/CTA}$) plots for the industrial burner, technically premixed mode, operating points as specified in table 2.

D Transfer Function Naming

In table 15, an overview of the naming to be used for transfer functions and the associated time delays throughout this work is given. Especially when technical premixing is concerned, a number of terms appear that are clarified here. Also, different terms for modelled and measured transfer functions need to be distinguished.

As discussed in sections 4.1.3 and 4.2.3, a flame transfer function measured in technically premixed mode does not directly represent the response of the heat release to a velocity perturbation. This is reflected in the naming - TF is used instead of FTF and the subscript points out that the raw signals from the photomultiplier and the hot wire probe are concerned. If the systematic errors SE_{OH} and SE_{CTA} imposed by the mixture fraction fluctuation on the measured signals are compensated as presented section 8.3.1, the true flame transfer function FTF_{TP} is obtained. The influence of the mixture fraction fluctuation FTF_{λ} does then represent the difference between technical and perfect premixing. To determine FTF_{TP} and FTF_{λ}, the transport of perturbations from the fuel injector to the burner exit is of interest, as modelled by $TF_{IB,u}$ for acoustic and $TF_{IB,\lambda}$ for convective transport. In section 8.3.2, the influence of the mixture fraction perturbations is modelled, yielding $FTF_{\lambda,M}$ and subsequently $FTF_{TP,M}$.

In perfectly premixed mode, the measured quantities do directly represent the heat release and the burner velocity, no systematic errors exist[85] and a differentiation between measured and true flame transfer functions is not necessary. The PP mode transfer functions determined experimentally are denoted FTF_{PP} and occasionally also FTF_{u} to point out their exclusive dependence on the burner velocity fluctuation. A number of models have been introduced to take various effects of the velocity fluctuation on the flame into account - these are FTF_{τ}, FTF_{D} and FTF_{S}. In the general case these influences are summarised in the modelled PP mode flame transfer function $FTF_{\tau,D,S}$, also denoted $FTF_{PP,M}$.

[85] With the exception of distortions at very high pressure amplitudes as described in sections 4.1.4, 4.2.4 and appendix C.

The global time delay of an experimental transfer function derived from a linear fit of the phase is denoted τ_G, with further indices specifying the type of the fitted transfer function by using the naming convention described above. Note that the influence of the mixture fraction perturbation on the heat release FTF_λ and its distorting influence on the chemiluminescence signal SE_{OH} are controlled by the same time delay $\tau_{G,\lambda}$.

In the model, the time delay between burner exit and flame is given by τ_M.[86] Of importance are also the time delay τ_I resulting from the convection between fuel injector and burner exit and τ_S capturing the convection between air swirler and burner exit.

For the industrial burner configuration, an additional time delay τ_{BE} has been specified to account for the convection in the combustor from the burner exit to the root of the lifted flame. That value is extended by τ_S to form τ_{SE}, which is needed for the determination of FTF_S.

[86] Note that also the parameters of FTF_D have an influence on the phase drop, due to the phase shift of 180° at the resonance frequency of FTF_D.

Table 15: Flame transfer function naming conventions.

Influence of	Applicability premix mode		Determination from		Characteristic time delay	
	TP	PP	Experiment	Model	Experiment	Model
Measured transfer function TP mode	√	–	$TF_{OH/CTA}$	–	$\tau_{G,\,OH/CTA}$	–
Systematic error $\lambda \rightarrow OH^*$	√	–	SE_{OH}	–	$\tau_{G,\lambda}$	–
Systematic error $\lambda \rightarrow CTA$	√	–	–	SE_{CTA}	–	τ_I
Flame transfer function TP mode	√	–	FTF_{TP}	$FTF_{TP,M}$	$\tau_{G,TP}$	–
Mixture fraction	√	–	FTF_{λ}	$FTF_{\lambda,M}$	$\tau_{G,\lambda}$	$\tau_{M,\lambda}\,(\tau_F)$
Flame transfer function PP mode	√	√	FTF_{PP}	$FTF_{PP,M}$	$\tau_{G,PP}$	–
			FTF_{u}	$FTF_{\tau,D,S}$	τ_G	
Time delay	√	√	–	FTF_{τ}	–	τ_M
Higher order flame dynamics	√	√	–	FTF_{D}	–	–
Swirl-induced velocity fluctuations	√	√	–	FTF_{S}	–	τ_S
Acoustic transport fuel injector → burner exit	√	–	–	$TF_{IB,u}$	–	–
Convective transport fuel injector → burner exit	√	–	–	$TF_{IB,\lambda}$	–	τ_I
Convective transport burner exit → flame root (Industrial burner only)	√	√	–	–	–	τ_{BE}
Convective transport swirler → flame root (Industrial burner only)	√	√	–	–	–	τ_{SE}

References

[Aue05] Auer, M.: *Einfluss fluktuierender Brennstoff- und Luftmassenströme auf die Dynamik einer Drallflamme*, Technische Universität München, Lehrstuhl für Thermodynamik, Diss., November 2005

[BDL88] Bloxsidge, G. J. ; Dowling, A. P. ; Langhorne, P. J.: Reheat buzz: An acoustically coupled reheat combustion instability - Part 2, Theory. In: *Journal of Fluid Mechanics* 193 (1988), S. 445–473

[BG70] Becker, R. ; Günther, R.: The Transfer Function of Premixed Turbulent Jet Flames. In: *13th International Symposium on Combustion* (1970), S. 517–526

[BHL93] Buechner, H. ; Hirsch, C. ; Leuckel, W.: Experimental Investigations on the Dynamics of Pulsated Premixed Axial Jet Flames. In: *Combustion Science and Technology* 94 (1993), S. 219–228

[BK97] Büchner, H. ; Külsheimer, C.: Studies on frequency-dependent mixing and reaction behaviour of pulsating pre-mixed swirl burner flames. In: *Gaswärme International* 46 (1997), February, Nr. 2, S. 122–129

[BL04] Bellows, B. ; Lieuwen, T.: Nonlinear Heat-Release/Acoustic Interactions in a Gas Turbine Combustor. In: *Proceedings of the ASME IGTI Turbo Expo, Vienna, Austria, June 14-17*, 2004

[BQ90] Boyer, L. ; Quinard, J.: On the Dynamics of Anchored Flames. In: *Combustion and Flame* 82 (1990), S. 51–65

[Bue92] Buechner, H.: *Experimentelle und theoretische Untersuchungen der Entstehungsmechanismen selbsterregter Druckschwingungen in technischen Vormisch-Verbrennungssystemen*, Universität Karlsruhe, Diss., 1992

[CB76] Comte-Bellot, G.: Hot-Wire Anemometry. In: *Annual Review of Fluid Mechanics* 8 (1976), S. 209–231

[CC56] Crocco, L. ; Cheng, S. I.: *Theory of combustion instability in liquid propellant rocket motors*. Butterworths Science Publication, London, 1956. – AGARD Monograph No.8

[Chu52] Chu, B.: On the Generation of Pressure Waves at a Plane Flame Front. In: *4th International Symposium on Combustion* (1952), S. 603–612

[CKL98] Cho, S. ; Kim, J. ; Lee, S.: Characteristics of thermoacoustic oscillation in a ducted flame burner. In: *Proceedings of the 36th Aerospace Sciences Meeting and Exhibit*, 1998. – AIAA 98-0473

[CL03] Cho, J. H. ; Lieuwen, T. C.: Modelling the Response of Premixed Flames to Mixture Ratio Perturbations. In: *Proceedings of the ASME Turbo Expo, Atlanta, Georgia, USA, June 16-19*, 2003

[Cor92] Correa, S. M.: A Review of NOx Formation Under Gas-Turbine Combustion Conditions. In: *Combustion Science and Technology* 87 (1992), S. 329–362

[CSC+03] Cheung, W.S. ; Sims, G.J.M. ; Copplestone, R.W. ; Tilston, J. R. ; Wilson, C. W. ; Stow, S. R. ; Dowling, A. P.: Measurement and Analysis of Flame Transfer Function in a Sector Combustor under High Pressure Conditions. In: *Proceedings of the ASME Turbo Expo, Atlanta, Georgia, USA, June 16-19*, 2003

[CW59] Collis, D. C. ; Williams, M. J.: Two-dimensional convection from heated wires at low Reynolds numbers. In: *Journal of Fluid Mechanics* 6 (1959), S. 357–384

[Dar93] Darmofal, D. L.: The Role of Vorticity Dynamics in Vortex Breakdown. In: *24th AIAA Fluid Dynamics Conference*, 1993

[DDC00] Ducruix, S. ; Durox, D. ; Candel, S.: Theoretical and Experimental Determinations of the Transfer Function of a Laminar Premixed Flame. In: *28th International Symposium on Combustion* Bd. 28, The Combustion Institute, 2000, S. 765–773

[Dow97] Dowling, A. P.: Nonlinear Self-Excited Oscillations of a Ducted Flame. In: *Journal of Fluid Mechanics* 346 (1997), S. 271–290

[Dow99] Dowling, A. P.: A Kinematic Model of a Ducted Flame. In: *Journal of Fluid Mechanics* 394 (1999), S. 51–72

[DV92] Dandy, D. S. ; Vosen, S. R.: Numerical and Experimental Studies of Hydroxyl Radical Chemiluminescence in Methane-Air Flames. In: *Combustion Science and Technology* 82 (1992), S. 131–150

[Eck04] Eckstein, J.: *On the Mechanisms of Combustion Driven Low-Frequency Oscillations in Aero-Engines*, Technische Universität München, Lehrstuhl für Thermodynamik, Diss., December 2004

[EFH+05] Eckstein, J. ; Freitag, E. ; Hirsch, C. ; Sattelmayer, T. ; von der Bank, R. ; Schilling, T.: Forced Low-Frequency Spray Characteristics of a Generic Airblast Swirl Diffusion Burner. In: *Journal of Engineering for Gas Turbines and Power* 127 (2005), Nr. 2, S. 301–306

[EFHS06] Eckstein, J. ; Freitag, E. ; Hirsch, C. ; Sattelmayer, T.: Experimental Study on the Role of Entropy Waves in Low-Frequency Oscillations in a RQL Combustor. In: *Journal of Engineering for Gas Turbines and Power* 128 (2006), Nr. 2, S. 264–270

[EFS03a] Eckstein, J. ; Freitag, E. ; Sattelmayer, T.: Transfer Function Data for the TM-LP Module, Mainstage / ICLEAC Project of the European Community Competitive and Sustainable Growth Programme. 2003. – Forschungsbericht. Restricted Access

[EFS03b] Eckstein, J. ; Freitag, E. ; Sattelmayer, T.: Transfer Function Data for the TM-LP Module, Mainstage and Pilots / ICLEAC Project of the European Community Competitive and Sustainable Growth Programme. 2003. – Forschungsbericht. Restricted Access

[FAGG96] Fleifil, M. ; Annaswamy, A.M. ; Ghoniem, Z. ; Ghoniem, A.F.: Response of a Laminar Premixed Flame to Flow Oscillations: A Kinematic Model and Thermoacoustic Instability Results. In: *Combustion and Flame* 106 (1996), S. 487–510

[FCJM05] Fu, Y. ; Cai, J. ; Jeng, S. ; Mongia, H.: Confinement Effects on the Swirling Flow of a Counter-Rotating Swirl Cup. In: *Proceedings of ASME Turbo Expo, Reno-Tahoe, Nevada, USA, June 6-9*, 2005

[FEHS06] Freitag, E. ; Eckstein, J. ; Hirsch, C. ; Sattelmayer, T.: Pressure Influence on the Flame Transfer Function of a Premixed Swirling Flame. In: *Proceedings of ASME Turbo Expo, Barcelona, Spain, May 8-11*, 2006

[FES02a] Freitag, E. ; Eckstein, J. ; Sattelmayer, T.: Mixing Process Periodicity Investigations for a Generic LP Burner / ICLEAC Project of the European Community Competitive and Sustainable Growth Programme. 2002. – Forschungsbericht. Restricted Access

[FES02b] Freitag, E. ; Eckstein, J. ; Sattelmayer, T.: Mixing Process Periodicity Investigations for a Generic LPP Burner / ICLEAC Project of the European Community Competitive and Sustainable Growth Programme. 2002. – Forschungsbericht. Restricted Access

[FES04] Freitag, E. ; Eckstein, J. ; Sattelmayer, T.: Periodic Results for a Generic LP Burner under Elevated Pressure / ICLEAC Project of the European Community Competitive and Sustainable Growth Programme. 2004. – Forschungsbericht. Restricted Access

[FFS06] Freitag, E. ; Föller, S. ; Sattelmayer, T.: Prediction of the Stability Behaviour of a Combustor Using a Low Order Model and Measured Flame Transfer Functions. In: *8th Asia-Pacific International Symposium on Combustion and Energy Utilization*, 2006. – October 10-12, 2006, Sochi, Russian Federation

[Fis04] Fischer, A.: *Hybride, thermoakustische Charakterisierung von Drallbrennern*, Technische Universität München, Lehrstuhl für Thermodynamik, Diss., April 2004

[FJ68] Feldman Jr., K. T.: Review of the literature on Rijke thermoacoustic phenomena. In: *Journal of Sound and Vibration* 7 (1968), Nr. 1, S. 83–89

[FKS04] Fritz, J. ; Kröner, M. ; Sattelmayer, T.: Flashback in a Swirl Burner with Cylindrical Premixing Zone. In: *Journal of Engineering for Gas Turbines and Power* 126 (2004), Nr. 2, S. 276–283

[Föl06] Föller, S. *Untersuchung des Flammenstabilitätsverhaltens mittels eines optimierten akustischen Brennermodells.* Semesterarbeit, Technische Universität München, Lehrstuhl für Thermodynamik. March 2006

[FPRS01] Flohr, P. ; Paschereit, C. O. ; van Roon, B. ; Schuermans, B.: Using CFD for Time-Delay Modeling of Premix Flames. In: *ASME TURBO EXPO, New Orleans, Louisiana, June 3-7*, 2001

[Fre00] Freitag, E. *Konstruktion eines Versuchsstandes zur Untersuchung von akustischen Verbrennungsschwingungen.* Semesterarbeit, Technische Universität München, Lehrstuhl für Thermodynamik. May 2000

[Gay74] Gaydon, A.: *Spectroscopy of Flames.* Chapman and Hall, London, 1974

[GC86] Garland, N. L. ; Crosley, D. R.: On the Collisional Quenching of Electronically Excited OH, NH and CH in Flames. In: *Twenty-first Symposium (International) on Combustion/The Combustion Institute* Bd. 21, 1986, S. 1693–1702

[GHK+04] Gentemann, A. ; Hirsch, C. ; Kunze, K. ; Kiesewetter, F. ; Sattelmayer, T. ; Polifke, W.: Validation of Flame Transfer Function Renconstruction for Perfectly Premixed Swirl Flames. In: *Proceedings of ASME Turbo Expo, Vienna, Austria, June 14-17*, 2004

[GLR+78] Goldschmidt, V. W. ; Leonard, R. G. ; Riley, J. F. ; Wolfbrandt, G. ; Baade, P. K.: Transfer Function of Gas Flames: Methods of Measurement and Representative Data. In: *ASHRAE Transactions* 84 (1978), S. 466–476

[Gün05] Güntner, H. *Akustische Messungen an einem Prüfstand.* Semesterarbeit, Technische Universität München, Lehrstuhl für Thermodynamik. May 2005

[GP07] Gentemann, A. ; Polifke, W.: Scattering and Generation of Acoustic Energy by a Premix Swirl Burner. In: *Proceedings of ASME Turbo Expo, Montreal, Canada*, 2007

[GSM+05] Goldmeer, J. ; Sanderson, S. ; Myers, G. ; Stewart, J. ; D'Ercole, M.: Passive Control of Dynamic Pressures in a Dry, Low NOx Combustion System Using Fuel Gas Circuit Impedance Optimization. In: *Proceedings of ASME Turbo Expo, Reno-Tahoe, Nevada, USA, June 6-9*, 2005

[Hab00] Haber, L. C. *An investigation into the origin, measurement and application of chemiluminescent light emission from premixed flames.* Diplomarbeit, Virginia Polytecnic Institute and State University. 2000

[Had71] Hadvig, S.: Combustion Instability System Analysis. In: *Journal of the Institute of Fuel* (1971), S. 550–558

[Had73] Hadvig, S.: Combustion-Driven Oscillations. In: *ASME Publication*, 1973

[HJN+01] Harper, J. ; Johnson, C. ; Neumeier, Y. ; Lieuwen, T. ; Zinn, B.: Experimental Investigation of the Nonlinear Flame Response to Flow Disturbances In a Gas Turbine Combustor. In: *Proceedings of the 39th AIAA Aerospace Sciences Meeting and Exhibit, Reno, NV, January 8-11*, 2001

[HML+01] Higgins, B. ; McQuay, M. Q. ; Lacas, F. ; Rolon, J. C. ; Darabiha, N. ; Candel, S.: Systematic Measurements of OH Chemiluminescence for Fuel-Lean, High-Pressure, Premixed, Laminar Flames. In: *Fuel* 80 (2001), S. 67–74

[HSP+05] Hirsch, C. ; Sattelmayer, T. ; Polifke, W. ; Fanaca, D. ; Reddy, P.: Influence of the Swirler Design on the Flame Transfer Function of Premixed Flames. In: *Proceedings of the ASME IGTI Turbo Expo, Reno, Nevada*, 2005

[HV03] Haber, C. L. ; Vandsburger, U.: A Global Reaction Model for OH* Chemiluminescence Applied to a Laminar Flat-Flame Burner. In: *Combustion Science and Technology* 175 (2003), S. 1859–1891

[HVSK00a] Haber, L. C. ; Vandsburger, U. ; Saunders, W. R. ; Khanna, V. K.: An examination of the relationship between chemiluminescent light emissions and heat release rate under non-adiabatic conditions. In: *Proceedings of the IGTI ASME Turbo Expo, May 8-11, Munich, Germany*, 2000. – 2000-GT-0121

[HVSK00b] Haber, L. C. ; Vandsburger, U. ; Saunders, W. R. ; Khanna, V. K.: An Experimental Examination of the Relationship between Chemiluminescent Light Emissions

and Heat-release Rate under Non-Adiabatic Conditions. In: *Symposium on Active Control Technology for Enhanced Performance Operational Capabilities of Military Aircraft, Land Vehicles and Sea Vehicles, Braunschweig, Germany*, 2000

[HY04] Huang, Y. ; Yang, V.: Bifurcation of flame structure in a lean-premixed swirl-stabilized combustor: transition from stable to unstable flame. In: *Combustion and Flame* 136 (2004), February, Nr. 3, S. 383–389

[KB02] Külsheimer, C. ; Büchner, H.: Combustion Dynamics of Turbulent Swirling Flames. In: *Combustion and Flame* 131 (2002), S. 70–84

[KEH85] Keller, J. J. ; Egli, W. ; Hellat, J.: Thermally Induced Low-Frequency Oscillations. In: *Journal of Applied Mathematics and Physics* 36 (1985), S. 250–274

[KFS03] Kröner, M. ; Fritz, J. ; Sattelmayer, T.: Flashback Limits for Combustion Induced Vortex Breakdown in a Swirl Burner. In: *Journal of Engineering for Gas Turbines and Power* 125 (2003), S. 693–700

[Kha01] Khanna, V. K.: *A Study of the Dynamics of Laminar and Turbulent Fully and Partially Premixed Flames*, Virginia Polytechnic Institute and State University, Diss., July 2001

[KHS04] Kunze, K. ; Hirsch, C. ; Sattelmayer, T.: Transfer Function Measurements on a Swirl Stabilized Premix Burner in an Annular Combustion Chamber. In: *Proceedings of ASME Turbo Expo, Vienna, Austria, June 14-17*, 2004

[Kie00] Kiesewetter, F.: *Charakterisierung eines Drallbrenners durch numerische Strömungssimulation*, Technische Universität München, Lehrstuhl für Thermodynamik, Diplomarbeit, September 2000

[Kin14] King, L. V.: On the Convection of Heat from Small Cylinders in a Stream of Fluid: Determination of the Convection Constants of Small Platinum Wires with Applications to Hot-Wire Anemometry. In: *Philosophical Transactions of the Royal Society of London. Series A.* 214 (1914), S. 373–432

[Kip10] Kipling, J. R.: *If.* In: Rewards and Fairies, 1910

[Kon05] Konle, H. *Messung von Flammentransferfunktionen unter Druckvariation.* Diplomarbeit, Technische Universität München, Lehrstuhl für Thermodynamik. October 2005

[Kun04] Kunze, K.: *Untersuchung des thermoakustischen Flammenübertragungsverhaltens in einer Ringbrennkammer*, Technische Universität München, Lehrstuhl für Thermodynamik, Diss., January 2004

[KVSB02] Khanna, V. K. ; Vandsburger, U. ; Saunders, W. R. ; Baumann, W. T.: Dynamic Analysis of Swirl Stabilized Turbulent Gaseous Flames. In: *Proceedings of ASME TURBO EXPO, Amsterdam, The Netherlands, June 3-6*, 2002

[Lan88] Langhorne, P.J.: Reheat buzz: An acoustically coupled reheat combustion instability - Part 1, Experiment. In: *Journal of Fluid Mechanics* 193 (1988), S. 417–443

[Lau05] Lauer, M. *Untersuchung des druckabhängigen Verlaufs von Flammentransferfunktionen.* Diplomarbeit, Technische Universität München, Lehrstuhl für Thermodynamik. October 2005

[LB03] Lohrmann, M. ; Büchner, H.: Influence of the Air Preheating Temperature on the Flame Dynamics of Kerosene-LPP Swirl Flames. In: *European Combustion Meeting*, 2003

[LB04] Lohrmann, M. ; Büchner, H.: Scaling of Stability Limits in Lean-Premixed Gas Turbine Combustors. In: *Proceedings of the ASME IGTI Turbo Expo, Vienna, Austria, June 14-17*, 2004

[LBZK03] Lohrmann, M. ; Büchner, H. ; Zarzalis, N. ; Krebs, W.: Flame Transfer Function Characteristics of Swirl Flames for Gas Turbine Applications. In: *Proceedings of the ASME Turbo Expo, Atlanta, Georgia, USA, June 16-19*, 2003

[LDH90] Langhorne, P.J. ; Dowling, A.P. ; Hooper, N.: A Practical Active Control System for Combustion Oscillations. In: *Journal of Propulsion and Power* 6 (1990), S. 324–330

[Len80] Lenz, W.: *Die dynamischen Eigenschaften von Flammen und ihr Einfluß auf die Entstehung selbsterregter Brennkammerschwingungen*, Universität Karlsruhe, Diss., 1980

[Lie03] Lieuwen, T.: Modeling Premixed Combustion - Acoustic Wave Interactions: A Review. In: *Journal of Propulsion and Power* 19 (2003), September - October, Nr. 5, S. 765–781

[LZ98] Lieuwen, T. ; Zinn, B. T.: The Role of Equivalence Ratio Oscillations in Driving Combustion Instabilities in Low NOx Gas Turbines. In: *27th International Symposium on Combustion* (1998), S. 1809–1816

[MC77] Marble, F. E. ; Candel, S. M.: Acoustic disturbance from gas non-uniformities convected through a nozzle. In: *Journal of Sound and Vibration* 55 (1977), Nr. 2, S. 225–243

[MD90] Munjal, M. L. ; Doige, A. G.: Theory of a Two Source-Location Method for Direct Experimental Evaluation of the Four-Pole Parameters of an Aeroacoustic Element.

In: *Journal of Sound and Vibration* 141 (1990), Nr. 2, S. 323–333

[Mer56a] Merk, H. J.: Analysis of Heat-Driven Oscillations of Gas Flows. I General Considerations. In: *Applied Scientific Research, Section A* 6 (1956), S. 317–335

[Mer56b] Merk, H. J.: Analysis of Heat-Driven Oscillations of Gas Flows. II On the Mechanism of the Rijke Tube Phenomenon. In: *Applied Scientific Research, Section A* 6 (1956), S. 402–420

[Mer56c] Merk, H. J.: An Analysis of Unstable Combustion of Premixed Gases. In: *6th Symposium on Combustion* Bd. VI, 1956, S. 500–512

[Mer57a] Merk, H. J.: Analysis of Heat-Driven Oscillations of Gas Flows. III Characteristic Equation for Flame-Driven Oscillations of the Organ-Pipe Type. In: *Applied Scientific Research, Section A* 7 (1957), S. 175–191

[Mer57b] Merk, H. J.: Analysis of Heat-Driven Oscillations of Gas Flows. IV Discussion of the Theoretical Results Concerning Flame-Driven Oscillations. In: *Applied Scientific Research, Section A* 7 (1957), S. 192–204

[Mer58] Merk, H. J.: Analysis of Heat-Driven Oscillations of Gas Flows. V Influence of Heat Transfer in the Burner Ports on the Stability of Combustion of Premixed Gases. In: *Applied Scientific Research, Section A* 8 (1958), S. 1–27

[Mor05] Morel, A. *Erstellung eines thermo-akustischen Modells für eine Versuchsanlage.* Semesterarbeit, Technische Universität München, Lehrstuhl für Thermodynamik. 2005

[Mug80] Mugridge, B. D.: Combustion Driven Oscillations. In: *Journal of Sound and Vibration* 70 (1980), Nr. 3, S. 437–452

[Mun87] Munjal, M. L.: *Acoustics of Ducts and Mufflers.* John Wiley & Sons, 1987

[NPMW98] Najm, H.N. ; Paul, P.H. ; Mueller, C.J. ; Wyckoff, P.S.: On the Adequacy of Certain Experimental Observables as Measurements of Flame Burning Rate. In: *Combustion and Flame* 113 (1998), S. 312–332

[Pan04] Pankiewitz, C.: *Hybrides Berechnungsverfahren für thermoakustische Instabilitäten von Mehrbrennersystemen*, Technische Universität München, Lehrstuhl für Thermodynamik, Diss., May 2004

[PBP+03] Pieringer, J. ; Brandt, M. ; Polifke, W. ; Griebel, P. ; Siewert, P. ; Bombach, R. ; Inauen, A. ; Kreutner, W.: Anwendung von Modellen der turbulenten Flammengeschwindigkeit auf einen vorgemischten Strahlbrenner. 21. Flammentag Cottbus : VDI, 2003, S. 629–635

[PD54] Putnam, A. A. ; Dennis, W. R.: Burner Oscillations of the Gauze-Tone Type. In: *Journal of the Acoustic Society of America* 26 (1954), Nr. 5

[Pet00] Peters, N.: *Turbulent Combustion*. Cambridge University Press, 2000 (Cambridge Monographs on Mechanics)

[PHS68] Price, R. ; Hurle, I. ; Sugden, T.: Optical study of the generation of noise in turbulent flames. In: *Proceedings of the Combustion Institute* 12 (1968), S. 1093–1102

[PKS01] Polifke, W. ; Kopitz, J. ; Serbanovic, A.: Impact of the Fuel Time Lag Distribution in Elliptical Premix Nozzles on Combustion Stability. In: *7th AIAA/CEAS Aeroacoustics Conference, Maastrich, NL*, 2001

[PPD01] Polifke, W. ; Paschereit, C.O. ; Döbbling, K.: Constructive and Destructive Interference of Acoustic and Entropy Waves in a Premixed Combustor with a Choked Exit. In: *International Journal of Acoustics and Vibration* 6 (2001), Nr. 3, S. 135–146

[PPSM99] Paschereit, C.O. ; Polifke, W. ; Schuermans, B. ; Mattson, O.: Measurement of Transfer Matrices and Source Terms of Premixed Flames. In: *Proceedings of the ASME International Gas Turbine and Aeroengine Congress, Indianapolis, Indiana, USA*, 1999

[RJ98] Richards, G. A. ; Janus, M. C.: Characterization of Oscillations during Premix Gas Turbine Combustion. In: *Journal of Engineering for Gas Turbines and Power* 120 (1998), Nr. 97-GT-244, S. 294–302

[RR05] Richards, G. A. ; Robey, E. H.: Effect of Fuel System Impedance Mismatch on Combustion Dynamics. In: *Proceedings of ASME Turbo Expo, Reno-Tahoe, Nevada, USA, June 6-9*, 2005

[Sat00] Sattelmayer, T.: Influence of the Combustor Aerodynamics on Combustion Instabilities from Equivalence Ratio Fluctuations. In: *Proceedings of the ASME IGTI Turbo Expo, Munich, Germany, May 8-11*, 2000

[SBG+04] Schuermans, B. ; Belluci, V. ; Güthe, F. ; Meili, F. ; Flohr, P. ; Paschereit, C. O.: A Detailed Analysis of Thermoacoustic Interaction Mechanisms in a turbulent Premixed Flame. In: *Proceedings of ASME Turbo Expo, Vienna, Austria, June 14-17*, 2004

[Sch95] Schmid, H. P.: *Ein Verbrennungsmodell zur Beschreibung der Wärmefreisetzung von vorgemischten turbulenten Flammen*, Universität Karlsruhe, Diss., 1995

[Sch03] Schuermans, B.: *Modeling and Control of Thermoacoustic Instabilities*, Ecole Polytechnique Federale de Lausanne, Diss., 2003

[Sch04] Schabreiter, H. *Vorbereitung, Durchführung und Auswertung einer Messkampagne am Hochdruckversuchsstand.* Semesterarbeit, Technische Universität München, Lehrstuhl für Thermodynamik. 2004

[Sch05] Schinkel, C. *Konstruktion und Aufbau eines CTA-Versuchs.* Semesterarbeit, Technische Universität München, Lehrstuhl für Thermodynamik. 2005

[SDC03] Schuller, T. ; Durox, D. ; Candel, S.: A Unified Model for the Prediction of Laminar Flame Transfer Functions: Comparisons between Conical and V-Flame Dynamics. In: *Combustion and Flame* 134 (2003), S. 21–34

[SF00] Scarinci, T. ; Freeman, C.: The Propagation of a Fuel-Air Ratio Disturbance in a Simple Premixer and its Influence on Pressure Wave Amplification. In: *Proceedings of the IGTI ASME Turbo Expo, May 8-11, Munich, Germany*, 2000. – 2000-GT-0106

[SFD04] Scarinci, T. ; Freeman, C. ; Day, I.: Passive Control of Combustion Instability in a Low Emissions Aeroderivative Gas Turbine. In: *Proceedings of ASME Turbo Expo, Vienna, Austria, June 14-17*, 2004

[SG92] Schadow, K. C. ; Gutmark, E.: Combustion Instability Related to Vortex Shedding in Dump Combustors and Their Passive Control. In: *Progress in Energy and Combustion Science* 18 (1992), S. 117–132

[SLBF05] Schuermans, B. ; Lübcke, H. ; Bajusz, D. ; Flohr, P.: Thermoacoustic Analysis of Gas Turbine Combustion Systems Using Unsteady CFD. In: *Proceedings of ASME Turbo Expo, Reno-Tahoe, Nevada, USA, June 6-9*, 2005

[Son50] Sondhauss, C.: Über die Schallschwingungen der Luft in erhitzten Glasröhren und in gedeckten Pfeifen von ungleicher Weite. In: *Annalen der Physik und Chemie* 79 (1850), S. 1–34

[SP03a] Sattelmayer, T. ; Polifke, W.: Assessments of Methods for the Computation of the Linear Stability of Combustors. In: *Combustion Science and Technology* 175 (2003), Nr. 3, S. 453 – 476

[SP03b] Sattelmayer, T. ; Polifke, W.: A Novel Method for the Computation of the Linear Stability of Combustors. In: *Combustion Science and Technology* 175 (2003), Nr. 3, S. 477 – 497

[SPP99] Schuermans, B. ; Polifke, W. ; Paschereit, C. O.: Modeling Transfer Matrices of Premixed Flames and Comparison with Experimental Result. In: *Proceedings of the ASME International Gas Turbine and Aeroengine Congress, Indianapolis, Indiana, USA*, 1999

[Str78] Strutt, J. W.: The Explanation of Certain Acoustic Phenomena. In: *Nature* 18 (1878), S. 319–321, (Lord Rayleigh)

[SVK+98] Seume, J. R. ; Vortmeyer, N. ; Krause, W. ; Hermann, J. ; Hantschk, C.-C. ; Zangl, P. ; Gleis, S. ; Vortmeyer, D. ; Orthmann, A.: Application of Active Combustion Instability Control to a Heavy Duty Gas Turbine. In: *Journal of Engineering for Gas Turbines and Power* 120 (1998)

[SZ85] Smith, D. A. ; Zukoski, E. E.: Combustion Instability Sustained by Unsteady Vortex Combustion. In: *AIAA/SAE/ASME/ASEE 21st Joint Propulsion Conference*, 1985. – Monterrey, CA, AIAA 85-1248

[TSI] Temperature Compensation of Thermal Sensors / TSI Incorporated (TB16). – Technical Bulletin

[Tur00] Turns, S. R.: *An Introduction to Combustion.* Boston : McGraw-Hill, 2000

[TVP03] Truffin, K. ; Varoquie, B. ; Poinsot, T.: Measurements of Transfer Functions Using Large Eddy Simulations: Theoretical Framework and First Tests. In: *10th International Congress on Sound and Vibration, Stockholm, Sweden*, 2003, S. 785–793

[VDI02] VDI: *VDI Wärmeatlas, Berechnungsblätter für den Wärmeübergang*. Springer-Verlag Berlin Heidelberg New York, 2002 (9. Auflage). – ISBN 3-540-41201-8

[WD81] Westbrook, C.K. ; Dryer, F.L.: Simplified Reaction Mechanism for the Oxidation of Hydrocarbon Fuels in Flames. In: *Combustion Science and Technology* 27 (1981), S. pp 31 – 43

[WLTS98] Walsh, K. T. ; Long, M. B. ; Tanoff, M. A. ; Smooke, M. D.: Experimental and Computational Study of CH, CH* and OH* in an Axisymmetric Laminar Diffusion Flame. In: *Twenty-Seventh International Symposium on Combustion*, 1998, S. 615–623

[Wol05] Wolf, M. *Experimentelle Bestimmung von Flammentransferfunktionen für einen Vormischbrenner*. Semesterarbeit, Technische Universität München, Lehrstuhl für Thermodynamik. June 2005

[Wäs05] Wäsle, H.: *Experimental Investigation of the TD1 Swirl Burner*. 2005. – Internal Communication

[ZDB03] Zhu, M. ; Dowling, A. P. ; Bray, K. N. C.: Study of Flame Transfer Function with Three Dimensional Calculations. In: *Proceedings of the ASME Turbo Expo, Atlanta, Georgia, USA, June 16-19*, 2003